Development of an advanced DC-polarisation/AC-impedance cyclic test to evaluate the corrosion of electrically-conductive coating/substrate systems

This dissertation submitted in partial fulfilment of the requirements for the degree of Doctor of Philosophy

BY

Fahima Indeir

Department of Materials Science and Engineering

March 2017

Declaration

I declare hereby that the work presented in this thesis is original and is my own work, except as some of the information in this thesis, however, is taken from the research of others to provide support of the data in the present work. To the best of my knowledge, clear references to these sources have in all cases been provided. There is no portion of the work referred to in the thesis has been submitted in support of an application for another degree or qualification of this or any other university or other institute of learning.

Fahima Indeir
Sheffield
March 2017

Dedication

To my beloved

Mom and the memory of my Dad,

may Allah (SWT) grant them the highest place

in Jannah

Acknowledgments

First and foremost, I thank the Almighty Allah (SWT) whom I believe for his ultimate guide and infinite mercy for enabling me for the successful completion of this project and my life in general.

I would like to express my heartfelt gratitude and sincere thanks to my principal supervisor, Dr. Adrian Leyland for his kind supervision throughout the course of my research. I could not have completed this thesis without his guidance, invaluable support, constant encouragement and 'patience'. I would like to express my sincere gratitude to Prof. Allan Matthews for his kind support and supervision.

I would like to express my appreciation to the academic and secretary staff at both the Department of Materials Science and Engineering and The University of Sheffield. Special thanks go to the technical staff for their assistance and training.

I would like to express my gratitude and appreciation to my family (specially my nephew Mohamed Enafati and my brother in Law Mohamed Ezutrini) and my friends back home for their immense support despite the distance.

Last, but of course not least, my special thanks go to my dearest friends, Nadia and her family, Seham and her family, Josephine, Abtesam, Noor, Kalthoom, Dalal, Aysha, Reem, Thoria, Fatoma and Nouf for their motivation, support, help and understanding my most difficult times. Many thanks to all the past and present my research colleagues in RCSE group and MSE department, Husein, Omar, Fash, Ray, Yonghao, Lian, Xinggyang, Wei-Yu, Chang, Ming, John, Yin, Tao, Jay, Lynne, Gorkem and Nora. I would like to express how much I value the lovely time spent together discussing, sharing experiences and exploring ideas.

I shall express regret to those whose names are not mentioned above, but their help and support are deeply acknowledged.

THANK YOU ALL 🌹
Fahima Indeir

Abstract

In this work, an advanced (AC)DC/OCP/AC cyclic test regime has been developed (and validated experimentally) as a new tool for the evaluation of the corrosion behaviour of metallic substrates and/or electrically-conductive coatings. Incorporation of concurrent solution pH measurement with the advanced (AC)DC/OCP/AC technique developed in this work, qualifies this approach to be applied in different industrial applications, such as in aircraft, nuclear and biomedical sectors. It provides opportunities to evaluate objectively the detailed corrosion behaviour in shorter exposure times (as little as 1 day) compared to the widely-used and accepted (but highly subjective) salt spray test (SST) and to conventional (periodically repeated but laborious) electrochemical impedance spectroscopy (EIS) evaluation at open circuit potential (E_{OCP}).

The (AC)DC/OCP/AC cyclic test provides valuable information concerning the corrosion behaviour of uncoated Al 6082 alloy (repeat tests are performed, to eliminate test protocol variables and improve the robustness of the test). The three examples of prototype PVD Al-based nanostructured coatings (AlCr, AlCr(N) and AlCrTi), deposited on 17/4 PH steel, were then evaluated from a scientific perspective, to acquire a fundamental understanding of their performance and degradation with time. The results are shown in two main sets; i) electrochemical results obtained at E_{OCP} and six repeated cycles of (AC)DC/OCP/AC cyclic testing and ii) solution pH results during continuous monitoring of the cyclic electrochemical test procedure. AlCrTi coating showed the best corrosion resistance after application of six successive DC/OCP cycles as a sacrificial protection for the substrate, followed by the AlCr(N) and AlCr coatings. However, the repassivation behaviour exhibited by the AlCr(N) coating after breakdown during extreme DC polarisation, may suggest an advantage to use this coating preferably in aerospace applications because of its strong ability to self-heal. This might be promising for

future coating materials for corrosion protection where cadmium or hard chromium needs to be replaced. In addition, the structural and chemical composition of these samples was characterised using SEM and EDX analysis. Conventional open circuit potential (E_{OCP}) and potentiodynamic polarisation scans were also employed, to determine the 'as-received' corrosion behaviour.

Table of Contents

List of Figurs

List of Tables

Acronyms

DC   Cathodic polarisation

AC   Impedance measurement

EIS   Electrochemical Impedance Spectroscopy

SST   Salt Spray Testing

OCP   Open Circuit Potential

SEM   Scanning Electron Microscopy

EDX   Energy Dispersive X-Ray

XRD   X-Ray Diffraction

PVD   Physical Vapour Deposition

EB   Electron Beam

PA   Plasma Assistance

CPE   Constant Phase Element

EC   Electrical Circuit

REAP   Rapid Electrochemical Assessment of Paint

SCE   Saturated Calomel Electrode

R_1 1st run of (A)DC/OCP/AC cyclic testing on 1st sample of Al 6082 alloy

R_2 2nd run of (A)DC/OCP/AC cyclic testing on 2nd sample of Al 6082 alloy

R_3 3rd run of (A)DC/OCP/AC cyclic testing on 3rd sample of Al 6082 alloy

Chapter One

Introduction and Objectives

1.1   Introduction

Surface modification and coating technologies have developed rapidly in recent years and are now increasingly widely used due to the availability of new coating methods which can improve the surface properties of engineering materials and components (such as morphology, composition, structure, cohesion and adhesion), in ways which were previously unachievable. Wear and corrosion degradation are still major issues, as they reduce the service life of many components in automotive and aerospace, where safety is of the utmost priority [1].

Electroplated cadmium coatings display excellent sacrificial and barrier corrosion resistance, thus providing long-term protection of steel. However, cadmium and its compounds are severely restricted from use in corrosion resistance applications due to high toxicity and associated safety and environmental concerns. In addition, a variety of alternative coatings to cadmium (which have been employed by the aerospace industry) include zinc, zinc alloys, aluminium and aluminium alloy coatings. Aluminium-based coatings are environmental friendly and widely used in corrosion resistance of steel for automotive and aerospace industries, due to their electrochemical potentials similar to that of cadmium (and which can be adjusted to suit different steel substrates).

Al-based coatings employed to provide corrosion resistance to steel are designed to focus mainly on obtaining coating passivity in the corrosive environments to which the steel might be exposed. However, the coating may then act cathodically with respect to the steel substrate which could be prone to localised corrosion at low (or high) pH due to existing (or developing) coating defects that may allow the corrosive media to reach the coating/substrate interface [2, 3].

In recent years, environmentally friendly vacuum deposition techniques such as Plasma-Assisted Physical Vapour Deposition (PAPVD) have been established as a means to improve the performance of Al-based coatings by incorporating sacrificial/anodic elements in the coating structure [4]. PVD techniques can produce alloy films using both interstitial and (low miscibility) substitutional alloying elements, which are important factors in promoting nanocrystalline or glassy phase components in metallic films [5]. Pure Al-based coatings deposited by PVD techniques are already used as non-toxic alternative to cadmium on steel and titanium (IVD-Al) [6], but suffer high sensitivity to localised degradation. Thus, incorporating alloying elements such as Cr, Ti and Mo may modify and improve the composition and properties of the oxide passive film, thereby enhancing the resistance to corrosion by localised degradation of the passive film on Al-based coatings (primarily by limiting the adsorption of chloride ions that could lead to the initiation of pits due to local breakdown of the passive film [5, 7-9]).

The Technical Challenge

A rapid evaluation technique is required that can provide accurate, quantitative results that may reveal additional (or complimentary) information on the corrosion behaviour and/or wear performance of PVD metallic nano-structured coatings, before they are selected and deployed by end users in various industrial applications. Since it is difficult to measure complex corrosion and wear interactions for moving parts in actual service conditions (and for the purposes of quicker and more precise down-selection of candidate coating systems) in practice it would be highly desirable to apply an offline, laboratory method which can reliably assess the anticipated in-service degradation behaviour of coatings in a shorter time than conventional corrosion test techniques allow. Conventional methods such as the salt spray test (SST), and immersion tests coupled with the (increasingly used) electrochemical impedance spectroscopy (EIS) technique, are currently very popular but can be time consuming in their execution (SST) and/or interpretation (EIS), for evaluating the corrosion behaviour of coatings prior to their selection for use in serial production. Salt spray testing offers many well-established benefits, such as a standardised protocol for conducting the test, evaluating the results and a basic simplicity of test procedure; however, the method has been criticized for its inability to provide quantitative performance data and for often being unrepresentative of the results seen in the non-idealised, commercial conditions of practical use [10].

Electrochemical impedance spectroscopy offers many benefits, such as the ability to determine numerical data for coating corrosion damage, make detailed investigation of the mechanisms of electrochemical reactions in the corrosion process (and their evolution) and measure changes in dielectric media and charge transfer characteristics between various coating systems, to explore the relative distribution of coating defects (and their evolution with exposure time) [10, 11]. Nevertheless, to gain comprehensive information regarding the temporal evolution of coating degradation, EIS evaluations still need to be carried out repetitively (and in 'real time') during coating exposure to the corrosion environment, to construct a detailed map of the degradation and failure processes.

Current State-of-Art Methods

Kendig and co-workers [12] have developed a Rapid Electrochemical Assessment of Paint (REAP) protocols which relies on two electrochemical tests, to predict the longer term salt spray test life to estimate the time-to-failure of paint coated mild steel. The tests can be made rapidly, almost within 24 h. The test procedures were conducted on scribed panels of automotive coating on mild steel over 24 h using a combination of EIS testing and DC cathodic polarisation to -1.5 V vs. Normal (Standard) Hydrogen Electrode (NHE).

Hollaender et al. [13, 14] used rapid cycles of electrochemical testing that combined AC (EIS) and DC (cathodic polarisation) measurements, initially for the testing of coated metal surfaces in food packaging applications.

4

Suay and co-workers [15-18] subsequently adapted this test for paints on steel surfaces, with considerable success, while Poelman and co-workers applied the same rapid electrochemical approach on an epoxy coated aluminium substrate [19].

The test consists of three main steps: (i) an EIS measurement (AC) step, to establish the initial state of the coating; (ii) a DC cathodic polarisation step, where the coating is cathodically polarised to stimulate coating disbondment (this also tends to create an alkaline environment, as discussed later); and (iii) after a period of recovery to reach open circuit potential (E_{OCP}), an EIS measurement is run to assess the current state of the coating after applying the DC polarisation. However, relatively few other studies have been performed to reveal the evolution of the EIS response after application of repetitive DC cathodic polarisation which aims to degrade the coating and coating/metal substrate interface by producing H_2 gas and OH$^-$ ions (that promote pore formation and coating disbondment) [20-24]. The application of (a sufficiently negative) cathodic potential will cause electrolysis of the solution to take place and different cations (such as H$^+$ and Al$^+$) will be attracted to the cathode and reduction reactions will take place, producing H_2 gas, whilst different anions (such as OH$^-$ and Cl$^-$) will be attracted to the anode, where oxidation reactions will take place, producing chlorine gas. Nevertheless, since the hydroxide ions remain in solution, the overall pH of the whole system will tend towards alkalinity [25-27]:

$$H_2O_{(l)} + e^- \rightarrow 1/2H_{2(g)} + OH^-_{(aq)} \qquad (1.1)$$
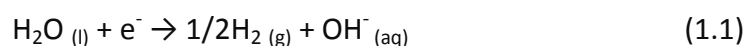
Testing of Electrically-Conducting Coatings

The applicability of such cyclic testing to metallic, electrically-conducting films has until now not been systematically investigated. Before carrying out the main aim of this work (i.e. to extend studies on these rapid evaluation techniques to electric alloy conductive metallic PVD coatings), it is essential to study the evolution of solution pH during the various stages of the test cycle since the pH may increase significantly due to the high concentration of OH^- produced from electrolysis of the solution caused by the applied DC cathodic polarisation.

Aluminium and its alloys are widely used in industry, since they provide versatile properties such as low weight and high strength (when alloyed and heat treated), good corrosion resistance (in neutral pH) and wear resistance that, although poor for pure aluminium, can be significantly improved by the addition of suitable alloying elements and/or by surface modification treatments, such as anodising. For these reasons, the corrosion behaviour of aluminium and its alloys in aggressive media has been extensively studied [28].

Al-based coatings (deposited on steels and other engineering metal-alloy substrates) can in principle be used both as a physical corrosion barrier and as a sacrificial anode to a steel substrate [29, 30]. However, the mechanical properties of such materials (and hence their friction and wear behaviour) have historically been rather poor [31, 32]. Recently developed Al-based nanostructured metallic coatings with modified and improved corrosion resistance and (importantly) better wear performance can now be deposited using advanced techniques such as

Plasma-Assisted Physical Vapour Deposition (PAPVD) [5]. This deposition method is employed to enhance the mechanical properties, thermal stability and corrosion protection of metal surfaces; for example, PVD ceramic coatings are now widely used to increase the in-service lifetime (and performance and/or product quality) of tools and engineering components in a wide range of industrial sectors [33, 34]. As the metallic coatings sector continues to grow and new advanced deposition techniques are developed to substitute for, or ideally replace, 'problem' coatings (such as electroplated cadmium or hexavalent hard chrome), it is becoming increasingly necessary to find rapid test protocols to efficiently evaluate (and thereby optimize) the corrosion behaviour of new coating system candidates. However, aluminium and its alloys are very reactive metals and can be vulnerable to corrosion particularly in aqueous environments of low or high pH, where the protective oxide layer is easily lost. Activation (or passivation) can take place, depending on the potential, pH and Cl^- ion concentration. In highly alkaline solutions containing a high concentration of OH^-, the dissolution process takes place readily [35].

1.2 The Need for a Rapid Corrosion Evaluation Technique for Metallic Coatings

From a scientific perspective (and also an economic point of view), it is highly desirable to develop a rapid evaluation technique for corrosion behaviour, to acquire a fundamental understanding of the coating performance function and degradation with time for new coatings before their use in real applications. Broadly speaking, the need for rapid evaluation of corrosion behaviour has four

main reasons. Three of these reasons are based on societal issues regarding i) human life and safety, ii) the cost of corrosion, and iii) conservation of materials. The fourth reason is that corrosion is inherently a difficult phenomenon to understand, and its study is in itself a challenging and interesting pursuit [36].

Therefore, before extending studies on coatings assessment by conventional evaluation techniques (that take a long period of time to obtain the result), it is essential to focus on conducting experiments with rapid corrosion techniques for the purpose of evaluation and comparison of results in a short period of time. However, the results still need to be indicative of the likely 'real time' performance of the coated system in service — and this remains a scientifically and technically challenging task to fulfil.

1.3 Research Aim & Objectives

Despite all adopted electrochemical evaluation techniques to date, the challenge to obtain comprehensive information regarding the electrochemical corrosion behaviour of electrically-conductive (metallic) coating/substrate combinations during advanced (AC)DC/OCP/AC multi-cyclic testing in a short time (i.e. no more than 24 h) remains-and the aim of this research was to develop a new cyclic corrosion test to satisfy this challenge.

The main objectives of the research to achieve this aim were defined as follows:

- Develop, adapt (and establish valid test protocols for) an advanced (AC)DC/OCP/AC cyclic testing capable of providing detailed information crucial for understanding of the corrosion behaviour underlying the

electrochemical characteristics of uncoated Al 6082 alloy and PVD Al-based coatings on a steel substrate.

- Study the effect of solution pH on the electrochemical dissolution of Al 6082 alloy and of PVD Al-based coatings using (AC)DC/OCP/AC cyclic testing.

- Prove the validity and repeatability of advanced (AC)DC/OCP/AC cyclic testing by carrying out repeated solution pH and hydrogen permeation measurements on Al 6082 alloy over several full test cycles.

- Investigate and correlate the temporal and spatial evolution of individual solution pH with applied electrochemical parameters on uncoated Al 6082 alloy and PVD Al-based coatings on a steel substrate.

1.4   Thesis Outline

Seven chapters are included into this thesis describing the research work in order to meet the above aim & objectives. The structure is as the following:

Chapter 1 This Chapter introduced Al-based coatings deposited by PVD technique and explains why PVD Al-based coating is a non-toxic alternative to cadmium on steel. A review of current State-of Art cyclic accelerated corrosion tests and of the need for a rapid corrosion evaluation technique is given.

Chapter 2 provides a comprehensive overview of the background and a literature review on electrochemical corrosion behaviour of aluminium and PVD Al-based coatings is also discussed.

Chapter 3 reviews the history of the development of electrochemical accelerated corrosion evaluation techniques for coated steel; mainly the advanced (AC)DC/OCP/AC cyclic testing is presented and the need for test improvements is explained.

Chapter 4 describes the experimental equipment and test procedures employed in this work with fundamentals and principles of each test method

briefly explained. The corrosion behaviour of uncoated Al 6082 alloy and PVD Al-based coatings is studied using electrochemical methods including: Open Circuit Potential (OCP), Potentiodynamic Polarisation (PTD), Electrochemical Impedance Spectroscopy (EIS) and advanced (AC)DC/OCP/AC cyclic testing. These methods give some indication of the corrosion protection offered by the coatings and how they compare to each other. The chapter presents the design of the experimental procedure of advanced (AC)DC/OCP/AC cyclic testing. Coating characterisation techniques used in this work such as X-Ray Diffraction (XRD), Scanning Electron Microscopy (SEM), and Energy Dispersive X-Ray (EDX) analysis are explained.

Chapter 5 covers the results and discussion of three experimental repeats (R_1, R_2 and R_3) using an advanced (AC)DC/OCP/AC cyclic testing that has been developed on (firstly and electrically-conductive, but uncoated Al 6082 alloy with incorporation of solution pH measurement). Evaluation of the corrosion behaviour of Al 6082 alloy and an estimation of the test validity and repeatability from the achieved results are explained.

Chapter 6 presents the results and discussion of the corrosion behaviour of three different PVD Al-based coatings with incorporated real time solution pH measurement using advanced (AC)DC/OCP/AC cyclic testing. Comparison between the coating results and the ability to discriminate between different coating behaviours is addressed and the conclusions and recommendations of this thesis for future work are also provided.

Chapter Two

Background and Literature Review

2.1 Electrochemical Corrosion Behaviour of Aluminium

Corrosion in its simplest definition is the process of a metal returning to its original thermodynamic state. Most commonly used metals tend to return to their original state (ore) when they are taken from the earth, before being refined non-spontaneously into engineering components. To refine pure metal from its ore (which is thermodynamically stable) requires a large amount of energy in order to extract the metal, usually by chemical or electrolytic reduction. In contrast, once the metal is refined (thermodynamically unstable) it will spontaneously try to revert to its stable state [37, 38]. The counteracting process is illustrated in Figure 2.1 [37].
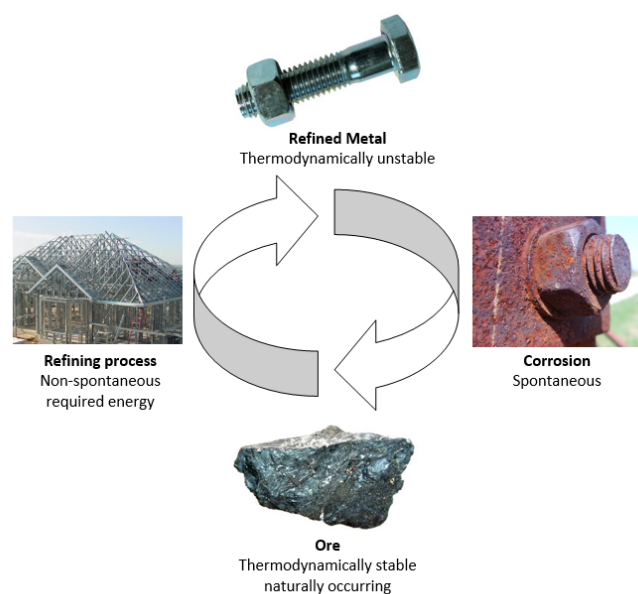
Figure 2.1: Cycle of counteracting refining and corrosion [37].

Corrosion in nature is an electrochemical process occurring through two or more electrode reactions (oxidation and reduction reactions). The corrosion process is an electrochemical degradation occurring at a metal/electrolyte interface, where the electrons are released by the metal (oxidation) and gained by elements (reduction) in the corroding electrolyte. The total rate of oxidation reactions must be equal to the reduction reactions taking place, to ensure a balance of charges between electrodes [37].

Aluminium is one of the most prevalent engineering metal after steel, used widely since 1950 [39]. Aluminium has low atomic mass, high electronegativity and an ability to transfer three electrons per atom, which make it potentially attractive as sacrificial anode for corrosion protection for other metals. Aluminium and its alloys have high corrosion resistance, due to a native thin protective oxide film that forms on its surface by its reaction with the air. However, once aluminium is immersed in aqueous solution containing 'aggressive anions' or highly alkaline solution the dissolution of the native oxide film occurs. In an acidic solution (or in a high alkaline solution also, in the case of pure aluminium) the oxide film may dissolve completely. Aluminium and its alloys have high corrosion resistance under ambient conditions, due to the formed thin protective surface oxide film. This colourless, protective, nascent oxide film is built up from two superimposed layers with a total thickness of between 4 and 10 nm when formed spontaneously in contact with air or with an oxidising medium; however, it will be significantly thicker at elevated temperatures or in the presence of moisture [39, 40], as shown in Figure 2.2 [39].

Superficial contamination:
Adsorbed water
Residues of rolling oil
Residues of degreasing agents

External film:
Hydrated
boehmite or
bayerite

Amorphous and compact oxide
Initial thickness 2–4 nm

Intermetallic phase
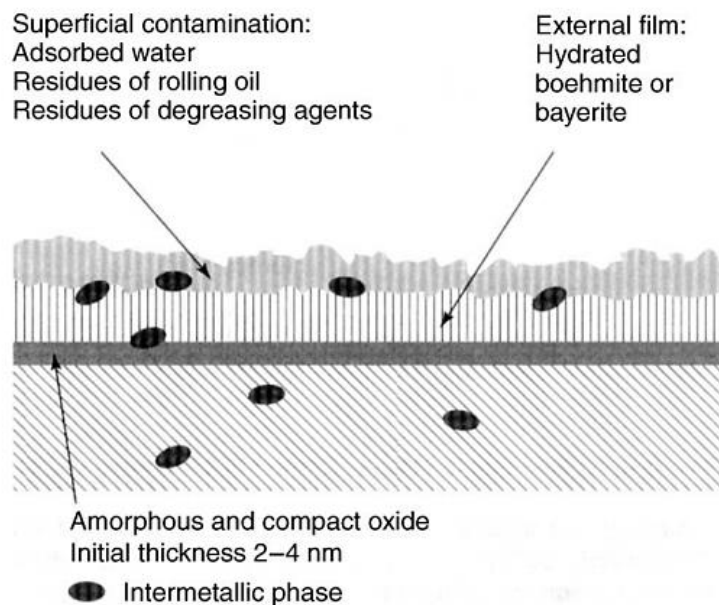
Figure 2.2: Aluminium oxide film layers [39]

Aluminium oxide films generally exhibit a nonhomogeneous surface (and very low thermal/electrical conductivity) compared to the parent aluminium substrate. The oxide film is chemically (and mechanically) rather weak and can be rather influenced by moist, humid environments to exhibit localised (pitting) corrosion. The oxide film can also undergo another formation in direct contact with water creating an amorphous, black and porous oxide/hydroxide film. Pure aluminium is inherently more corrosion resistant than its alloys (which tend to contain secondary, precipitate phases), but the use of pure aluminium is limited in engineering applications due to its low mechanical strength [37, 39, 41-43].

The presence of native oxide film of aluminium should be considered in the corrosion of aluminium that proceeds by comprising a partial anodic reaction (oxidation) and a partial cathodic reaction (reduction). So, in order to follow the mechanism underlying the corrosion behaviour of aluminium, it is necessary to

explore what partial reactions prevail in the overall corrosion rate. In the presence of a native oxide film the anodic dissolution reaction of Al can be classified into a direct dissolution reaction via ejection of Al^{3+} ion through the film and an indirect dissolution reaction via consecutive formation and dissolution of the film [44].

The dissolution reaction of aluminium in acidic and alkaline solutions can be written in the partial anodic and cathodic reactions. The cathodic reaction at low pH (strongly acidic) is discharge of proton (H^+) while the common cathodic reaction at high pH (strongly alkaline) is the reduction of water to H_2 gas and OH^- ions:

$$H^+ + e^- \rightarrow 1/2\, H_2 \tag{2.1}$$

$$H_2O + e^- \rightarrow 1/2H_2\uparrow + OH^- \tag{2.2}$$

The anodic reactions occurring in the dissolution of aluminium at acidic and alkaline solutions respectively are:

$$Al + 3H^+ \rightarrow Al^{3+} + \frac{3}{2}H_2 + 3e^- \tag{2.3}$$

$$Al + 4OH^- \rightarrow Al(OH)_4^- + 3e^- \tag{2.4}$$

The overall equations for both reactions and solutions can be written as follows:

$$Al + 3H^+ \rightarrow Al^{3+} + \frac{3}{2}H_2 \tag{2.5}$$

$$Al + H_2O + 3OH^- \rightarrow Al(OH)_4^- + \frac{3}{2}H_2 \tag{2.6}$$
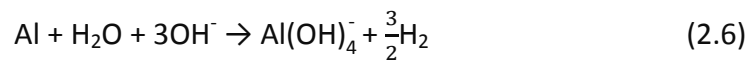
MacDonald et al. [45] proposed several mechanisms for the anodic reaction that correspond to the dissolution of Al metal to aluminate ions in alkaline solution, through a stepwise addition of OH^- ions, as in following reactions:

$$Al + OH^- \rightarrow Al(OH)_{ads} + e^- \tag{2.7}$$

$$Al(OH)_{ads} + OH^- \rightarrow Al(OH)_{2,ads} + e^- \tag{2.8}$$

$$Al(OH)_{2,ads} + OH^- \rightarrow Al(OH)_{3,ads} + e^- \qquad (2.9)$$

$$Al(OH)_{3,ads} + OH^- \rightarrow Al(OH)_4^- + ss \qquad (2.10)$$
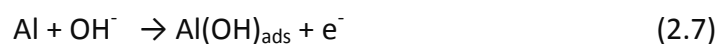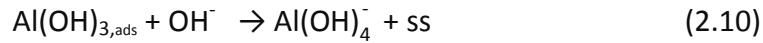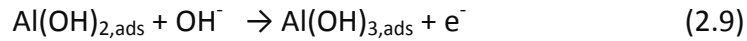
Where (ss) represents a surface site of the aluminium substrate.

A very similar mechanisms to that of Al metal oxidised to aluminate ions has been proposed by Chu and Savinell [46], involving Al dissolution reactions:

$$Al \rightarrow Al^{3+} + 3e^- \qquad (2.11)$$

$$Al^{3+} + 3OH^- \rightarrow Al(OH)_3 \qquad (2.12)$$

$$Al(OH)_3 + OH^- \rightarrow Al(OH)_4^- \qquad (2.13)$$
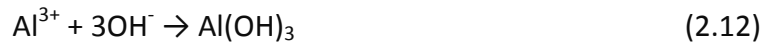
However, under alkaline solution (high pH) conditions the direct dissolution of aluminium involves direct ejection of aluminium ions (reaction 2.11) can never occur because Al^{3+} ions are not stable thermodynamically in alkaline solution [44].

However, aluminium dissolving in an alkaline solution may remain covered by hydrated oxide film. The dissolution of aluminium by OH^- ions leads to the formation of a porous bi-layer consisting of amorphous $Al(OH)_3$ and crystalline Al_2O_3 on the surface of aluminium substrate. The combination of this bi-layer can reduce the corrosion rate of aluminium, but it cannot fully protect it from aggressive environments [47]. Therefore, Moon and Pyun [48] divided the anodic reaction (2.4) into electrochemical reaction as following:

$$Al + 3OH^- \rightarrow Al(OH)_3 + 3e^- \qquad (2.14)$$
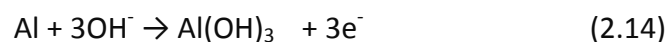
They suggested that the reaction (2.14) is limited by electrochemical formation of $Al(OH)_3$ film at $Al/Al(OH)_3$ interface by diffusion of OH^- ions into the passive film

towards Al substrate. $Al(OH)_3$ is chemically dissolved to form aluminate ions (reaction 2.13) by OH^- ions attack at the $Al(OH)_3$/electrolyte interface [44, 49, 50].

Perrault [51] assumed the formation of aluminium hydride intermediate ions, in which cathodically formed hydrogen reacts with Al to form hydride (AlH_3) at the surface of the electrode which thereafter is anodically oxidised by OH^- ions to form aluminate ions:

$$Al + 3H \rightarrow AlH_3 \qquad\qquad (2.15)$$

$$AlH_3 + 7OH^- \rightarrow Al(OH)_4^- + 3H_2O + 6e^- \qquad\qquad (2.16)$$
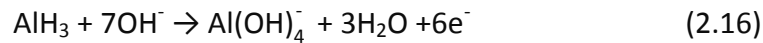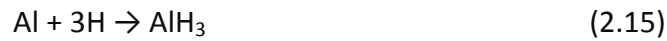
Adhikari et al. [52, 53] proved that the transition of the dissolution mechanism being observed occurs when the solution pH is close to the neutrality, where the formation of AlH_3 takes place and increases the solution pH to alkalinity. Also, they reported that the minimum corrosion potential of the anodic reaction of aluminium hydride to form aluminate ions is -1.9 (V vs. Ag/AgCl) [52].

However, if the dissolution of the hydroxide film proceeds sufficiently, the dissolution rate will be suppressed by the enrichment of aluminate ions. Aluminate ions tend to accumulate at the passive film/electrolyte interface to form a viscous layer (gel), which hinders the diffusion of OH^- ions towards the $Al(OH)_3$/electrolyte interface [54-56]. This can cause the repassivation (growth of the passive film) with applied anodic potential on the surface, which is enhanced by the electric field. The formation rate of the passive film dominates over its competing dissolution rate; thereby, a zero value of repassivation rate implies that the rate of formation is equal to the rate of the dissolution, so the passive film hardly grows [57].

2.2 Potential/pH diagrams (E-pH)

Electrochemical thermodynamics show that the anodic reaction of corrosion may take place only when the potential of the metal electrode is more positive than its equilibrium potential and the cathodic reaction of the oxidant reduction is more negative than its equilibrium potential [58]. Nevertheless, the corrosion of metal in aqueous solution not only depends on the electrode potential but also on the acidity or alkalinity of the solution (i.e. the solution pH). Then the thermodynamic prediction is illustrated by a so-called Pourbaix diagram, first developed by Marcel Pourbaix in 1938 [59]. The E-pH diagram is a graph representing the thermodynamic stability of metal and its corrosion products as a function of electrolyte pH and potential. E-pH diagrams are used widely for studies of corrosion, electrolysis, electrical cells, electroplating, hydrometallurgy and water treatment, since they are electrochemical maps that can provide information on predominant species (e.g. ions, oxides or hydroxides), in equilibrium, for a given pH and potential. An electrochemical process can be measured as a potential and the acidity or alkalinity of the species involved can be measured in terms of pH [37, 58, 60].

2.2.1 E-pH diagram of aluminium

The E-pH diagram of aluminium species shown in Figure 2.3 [61] is a schematic diagram which includes the water and oxygen lines that illustrate the passivation region of $Al(OH)_3$ at neutral pH and the corrosion regions at higher and lower pH that extend to very low potentials, and the corrosion resistance depends therefore

on a dense and continuous oxide film. Four species containing the aluminium element can be considered, that is, two solid species Al and $Al(OH)_3$ and two ionic species Al^{3+} and $Al(OH)_4^-$ ions. E-pH diagrams show the possible corrosion reactions thermodynamically, but cannot predict the corrosion rate [36, 39, 60, 61].
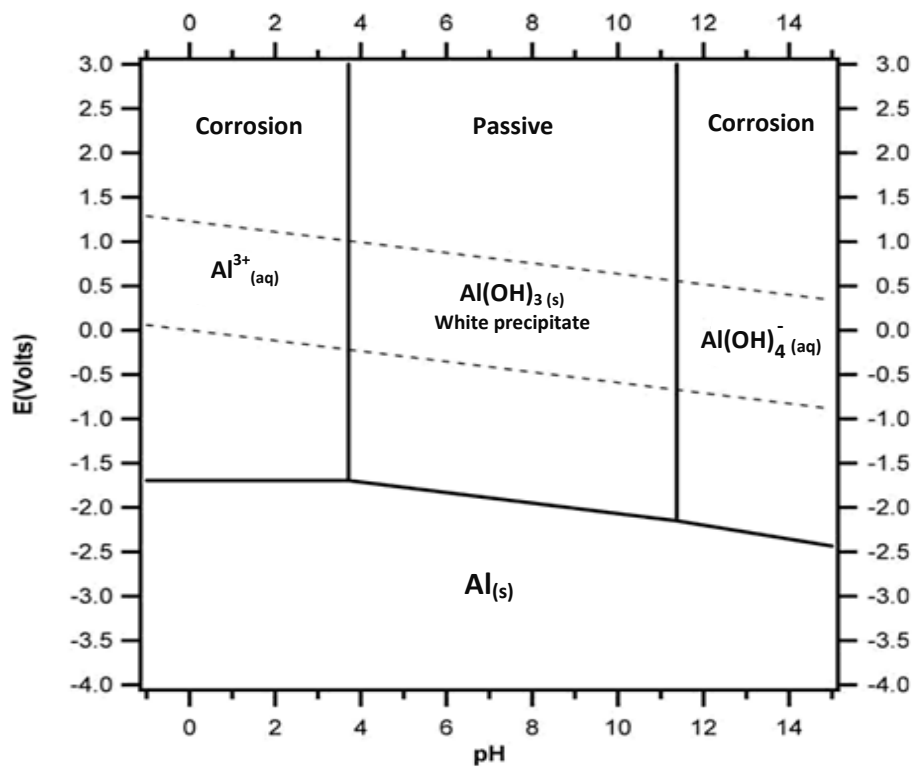
Figure 2.3: E-pH diagram of pure aluminium species at 25C° [61]

Figure 2.4 [62] shows the solubility diagram for aluminium hydroxide $Al(OH)_3$.The solubility boundary indicates the thermodynamic equilibrium that exists between the dominant aluminium species in solution at a given pH and solid $Al(OH)_3$. The minimum solubility of $Al(OH)_3$ is about 0.03 mg Al/L at a pH about 6.3 and increases as the solution pH becomes more alkaline or acidic. In alkaline solution the aluminium hydroxide formed electrochemically can dissolve chemically to

aluminate ions via OH$^-$ ion attack at the passive film/electrolyte interface, through

reaction (2.13) [44, 62].
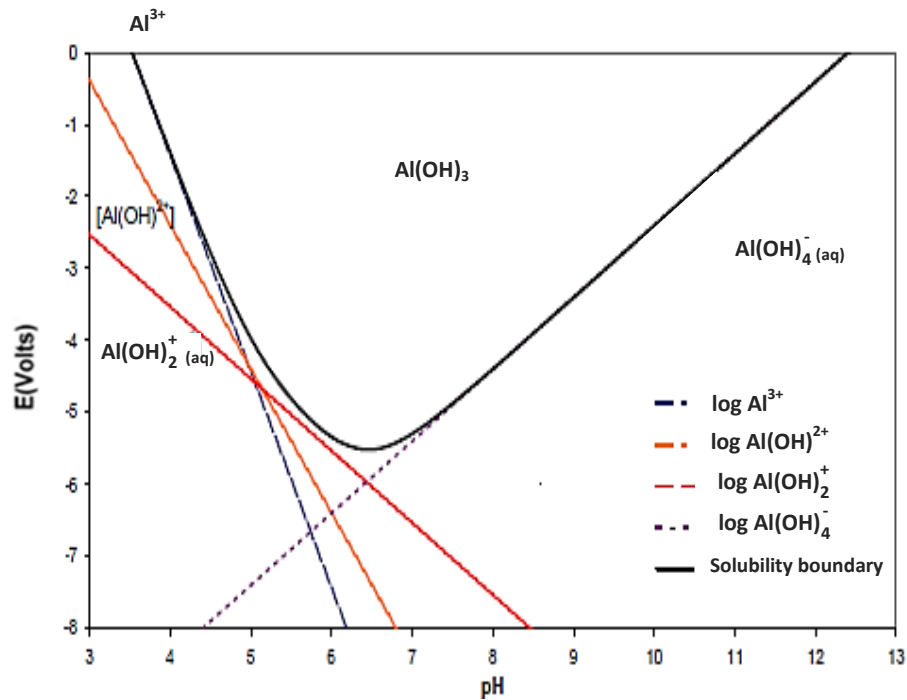
Figure 2.4: pH-dependent solubility diagram of aluminium hydroxide Al(OH)$_3$ [62].

Measurements of aluminium potential at all values of pH should take into account

of the following points [39]:

- the corrosion potential E_{corr} and the pitting corrosion potential E_{pit} are very
  close to each other
- pitting corrosion takes place only in the range of pH in which the oxide
  layer is totally insoluble
- uniform cathodic attack is a disastrous corrosion event, that may dissolve
  up to 10 mm.h^{-1} under cathodic polarisation,
- immunity is theoretically unattainable at pH values above 9 because, at
  potentials low enough to enter the region of immunity of aluminium,
  water is no longer stable and hydrogen will be released.

The electrochemical behaviour of aluminium is defined by the influence of the natural oxide film that controls the corrosion resistance of the metal. The measured potential of aluminium corresponds to the mixed potential between the oxide film and the metal itself. The potential of the aluminium substrate cannot be measured because, in oxidising media such as water, the oxide film will form almost immediately (within 1 ms or even less) [39].

In evaluating the corrosion behaviour of aluminium, the pitting potential does not have the same importance as for steel. Figure 2.5 [39] shows schematically that the polarisation curve for aluminium do not have the same shape as for steel. There is no region of passivity, because aluminium is a naturally passivating metal. Corrosion on aluminium will progress as pitting in aqueous media near to neutral pH. Corrosion current measurements can give some indication of the corrosion rate, but do not reveal anything about the morphological features of corrosion.
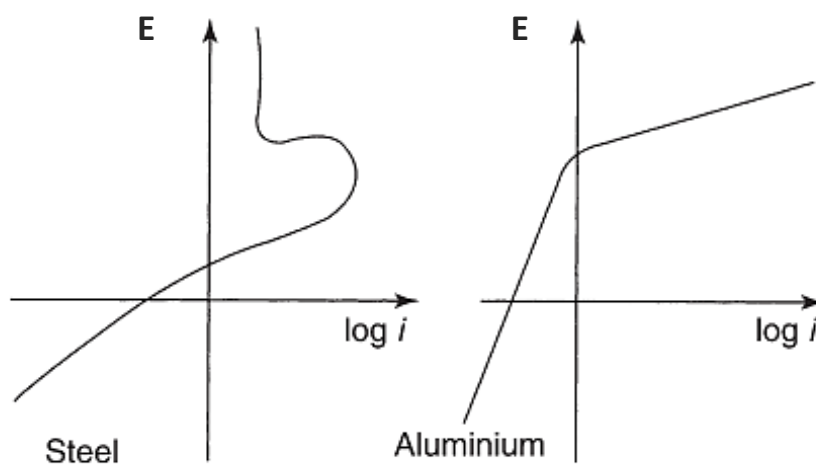
Figure 2.5: Schematic polarisation curves of steel and aluminium [39].

2.3   Pitting Corrosion in Aluminium

Pitting corrosion is the most common localised corrosion phenomenon of aluminium in media with a pH close to neutral which basically covers all natural environments such as surface water, seawater, and moist air [63, 64]. This type of corrosion is always highly visible because the corrosion pits are covered with white, voluminous precipitates of $Al(OH)_3$ on the metal surface. Pitting corrosion is a very complicated process, and is not totally understood even today. The one well-known aspect of pitting corrosion however, is the conditions under which it is initiated and propagates. The evolution of pits in aluminium is observed in NaCl solutions during anodic polarisation at the pitting potential as shown schematically in Figure 2.6 [65]. In the pit, aluminium dissolves anodically into the pit electrolyte partially hydrated to Al^{3+}, whereby hydrolysis of a portion of these cations to $AlOH^{2+}$ acidifies the pit electrolyte, causing hydrogen reduction in the pit and producing hydrogen bubbles which locally agitate the electrolyte before they escape from the pit interior. During transport of Al^{3+} through the pit mouth into the bulk of the electrolyte, an intermediate deposition of a veil of solid hydroxide may occur, followed by aluminate re-dissolution. The acidity of the pit electrolyte is such that repassivation of the pit interior is excluded at least when the pit electrolyte is saturated with respect to hydrated aluminium chloride [39, 65].
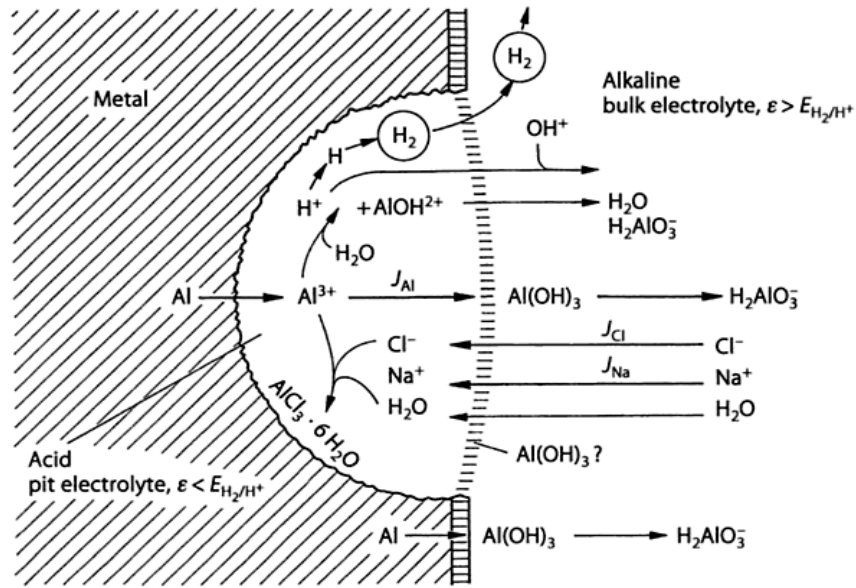
Figure 2.6: Mechanisms of pitting corrosion of aluminium in NaCl solution [65].

2.3.1 Initiation and propagation of corrosion pits

Passive films are prone to localised corrosion caused by anions that can incorporate into the passive film and initiate pitting corrosion at weak sites. The pitting potential E_{pit} of aluminium is a potential of passivation breakdown in which an acceleration of the corrosion process occurs by incorporation of various species present within pits such as metal cations, metal hydroxide, Cl^- and H^+. Acidification within pits as a result of hydrolysis is generally recognized to be a critical factor [66]. The possibility of pitting corrosion by Cl^- ions attack as described by the following reactions [47, 67]:

$$Al_2O_3 + 6Cl^- + 6H^+ \rightarrow 2AlCl_3 + 3H_2O \qquad (2.17)$$

$$Al(OH)_3 + Cl^- \rightarrow Al(OH)_2Cl + OH^- \qquad (2.18)$$

$$Al(OH)_2Cl + Cl^- \rightarrow Al(OH)Cl_2 + OH^- \qquad (2.19)$$

$$Al(OH)Cl_2 + Cl^- \rightarrow AlCl_3 + OH^- \tag{2.20}$$

$$AlCl_3 + Cl^- \rightarrow AlCl_4^- \tag{2.21}$$
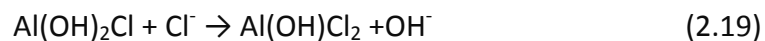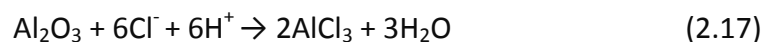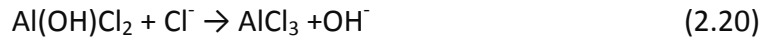
The adsorption of chloride ions into the passive film at weak points will cause formation of micro-cracks a few nanometres wide. In the propagation stage, initiated pits will continue to propagate in the floor of the pit. According to the following reactions [39, 61], pits will propagate:

- Reduction reactions of hydrogen and oxygen at the cathode area surrounding the pit are important; i.e. reactions (2.1) and (2.2).

- anodic aluminium oxidation reaction (2.3) at the anode floor pits.

The solution pH will decrease due to the production of H^+ and Al^{3+} ions at the floor of the pit. The pit floor environment changes to become anodic and, to balance the positive charge, Cl^- ions will be attracted and transported into the pit. As a result, HCl acid will form inside the pit, causing acceleration of pit propagation. The reduction reaction will produce OH^- ions, thus increasing alkalinisation around cathodic sites [68]. As mentioned previously, Al^{3+} ions are highly concentrated in the floor of the pit and will diffuse outwards from the pit opening, where they meet the high pH condition of the surrounding cathode area and react with the OH^- ions to form insoluble $Al(OH)_3$ that will precipitate. The micro-bubbles of hydrogen gas formed in the pit push the $Al(OH)_3$ to the pit opening, where it forms insoluble white pustules around the pit [39, 67].

2.4   Passivity

One form of corrosion protection is the use of metals or alloys which have inherently low corrosion rates in solution due to a naturally-occurring passive oxide film. As noted by Macdonald, [69] "passivity is the key to our metals-based civilization". Most common metals, such as iron, titanium, aluminium, chromium and nickel (and their alloys) have active-passive behaviour as they occur in nature as their ores. A thin layer can be formed on the metal surface in most cases where active-passive behaviour occurs. The oxide thin film is generally more resistant to the environment than the underlying metal. The electrochemical basis of passive film formation after an active-passive transition, found in the anodic polarisation curve, is shown in Figure 2.7 [37].
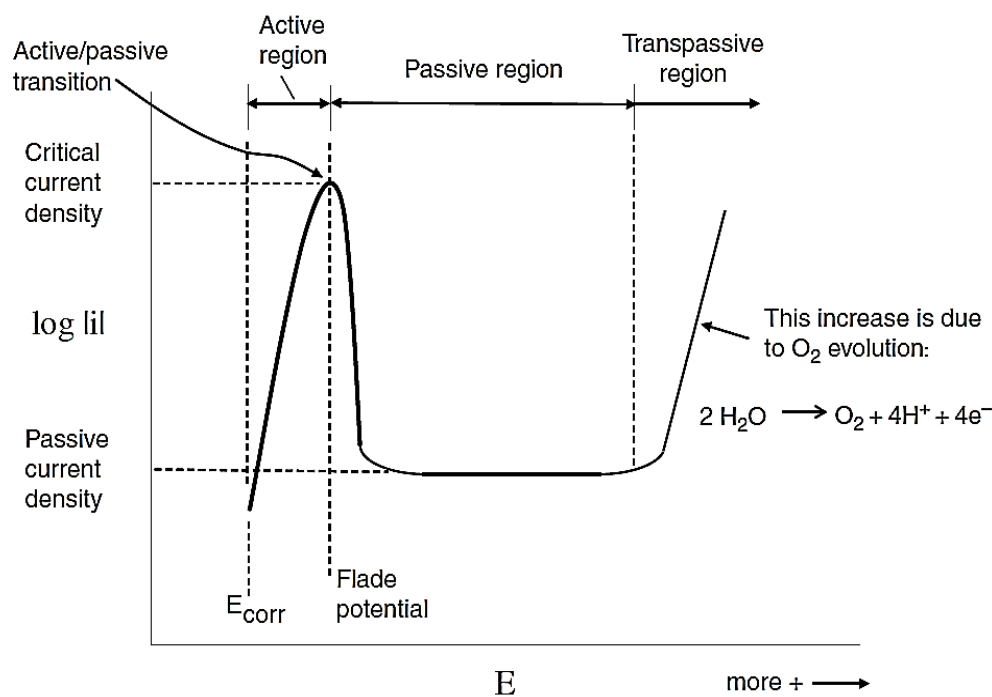
Figure 2.7: Schematic diagram of anodic polarization curve for metal exhibiting active-passive behaviour [37].

The curve starts at the open circuit potential and moves in the anodic direction with increasing current in the active region. However, the polarisation affects the current at a certain potential called the Flade potential. Further increases in potential cause a decrease in the current on the metal's surface. As the potential is increased further, the corrosion basically stops because a passive film is being formed at the metal surface. In this case the metal is undergoing an active-passive transition. As the passive film continues to form, the metal enters the passive region of anodic polarisation. The current density in this region is called the "passive current density", while at the Flade potential it is called the "critical current density for passivation". With further increase in potential, the current will increase, but this increase is due to the evolution of oxygen, not to metallic corrosion. This region is called the transpassive region, where breakdown of the passive film takes place and the corrosion current density starts to increase again with increasing potential [37, 70, 71].

2.5 Passivity breakdown

While repassivation kinetics of metals greatly reduces the dissolution rate, they cannot completely protect the metal surface from corrosion. In particular, passivating films are frequently related to the susceptibility to localized types of corrosion such as pitting, crevice corrosion and stress corrosion cracking (SCC). The occurrence of each of these types of corrosion requires the initial breakdown of passivity, in which the passive layer is ruptured and the underlying metal becomes exposed to the environment [71, 72].

2.5.1 Passivity of aluminium

Aluminium and its alloys are important structural metals because of their excellent corrosion resistance. Aluminium is naturally passive and, therefore, does not usually need to be passivated. The dissolution potential of aluminium in most aqueous media is of the order of 660 mV standard electrode potential with respect to this same electrode. Aluminium (like all passive metals) is covered with a continuous and uniform natural oxide film, corresponding to the formula Al_2O_3, which is formed spontaneously in oxidising media according to the reaction [39, 59]:

$$4Al_{(s)} + 12H_2O_{(l)} + 3O_{2\,(g)} \rightarrow 2Al_2O_{3\,(s)} + 12H^+_{\,(aq)} + 12\,OH^-_{\,(aq)} \qquad (2.18)$$
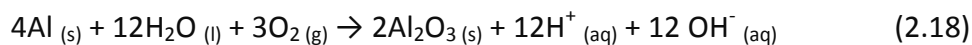
2.6 Influence of Alloying on the Dissolution Potential of Aluminium

Transition metal alloying elements (in aluminium alloys and coatings) bring improvements of wear and corrosion properties. Transition metal elements disrupt the kinetics of localised corrosion and/or facilitate formation of an improved protective passive film [30]. Formation of nitrides is known to bring a positive effect for high temperature resistance to aluminium alloy. Figure 2.8 [37] shows the influence of alloy elements on the dissolution potential of aluminium alloys in both directions. Some of these elements can increase the nobility when added to the aluminium (such as copper, manganese and silicon), by shifting the potential of aluminium in the high potential direction (anodic direction) to cause a decrease in corrosion current density.
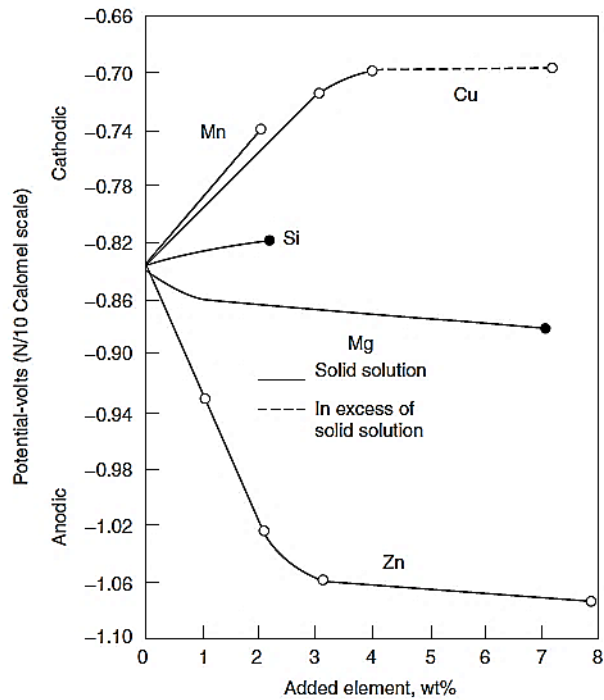
Figure 2.8: Influence of alloying elements on dissolution potential of aluminium [37].

However, addition of electronegative potential elements (such as magnesium and zinc) can shift the aluminium potential in the low potential direction (cathodic direction) and cause an increase in corrosion current density. The result shows that aluminium alloy OCP value will be inversely proportional to the percentage Mg. However, corrosion current density is increasing as the Mg % increased.

Baldwin et al. [73] concluded that the corrosion resistance of sputtered aluminium alloy coatings alloying with 20 wt. % Mg would yield the best anodic protection to the steel substrate. Further increases of Mg in the aluminium alloy coating more than 20 wt. % could potentially initiate selective de-alloying, as Al is nobler than Mg. Molybdenum added as tertiary element into Al-Cr alloy coatings ennobled both the open circuit potential and the pitting potential. Al-Cr-Mo alloy coatings required

27

relatively high Cr content more than 20% (and 15-18 % of Mo) to effectively increase resistance to corrosion. This type of aluminium alloy coating would form a passive film instantaneously even exposed in 1M HCl. Primary Mo enrichment facilitates formation of an improved chromium oxide passive film and widens the passive region of anodic polarization [74].

Aluminium alloys can easily oxidise when Al is existing in solid solution or as intermetallic (IM) phases [41]. Although IM phases may have a dissolution potential rather different from that of the solid solution, they have no influence on the dissolution potential of aluminium. However, they may give rise to intergranular corrosion, exfoliation corrosion, or stress corrosion cracking resulting in localised micro-galvanic cells if localised at, or close to, grain boundaries — as in (for example) titanium addition to Al-Si alloy [39, 41, 75-77]. Titanium addition to Al-Si alloy causes IM separation in the compositional form of titanium aluminide $TiAl_3$. $TiAl_3$ phase that formed inside the Al matrix constructs cathodic regions of localised galvanic cells inside the Al matrix. The intermetallic $TiAl_3$ behaves as a cathode and the nearby Al matrix behaves anodically and therefore dissolves [78].

2.7   Electrochemical Polarisation

For metallic corrosion to take place there must be current flow. Since the corrosion reactions involve the transfer of electrons between the metal and the solution, the rates of these reactions are proportional to the measured electric current [79]. The electrochemical cell is an electric circuit comprising elements controlled by Ohm's law (I = E/R). If cell resistance was infinite, the potential could be calculated, and

there would be no corrosion in this case. If cell resistance was zero the potentials of both half-cells would approach each other and the corrosion rate would in principle be infinite. In the 'real' case (of intermediate resistance in the circuit), the potentials of each half-cells will move slightly towards each other as current flows; the flow of electrons between the anodic and cathodic sites generates a net current (I), resulting in a local electrochemical potential in the media. This change or shift in potential is called polarisation (η); polarisation is anodic, when the anodic processes on the electrode are accelerated by moving the potential in the positive (noble) direction, or cathodic, when the cathodic processes are accelerated by moving the potential in the negative (active) direction [36, 39, 79, 80]. The relationship between the polarisation reactions of aluminium for each half-cell, in relation to the corrosion potential and current, is represented schematically in Figure 2.9 [39].
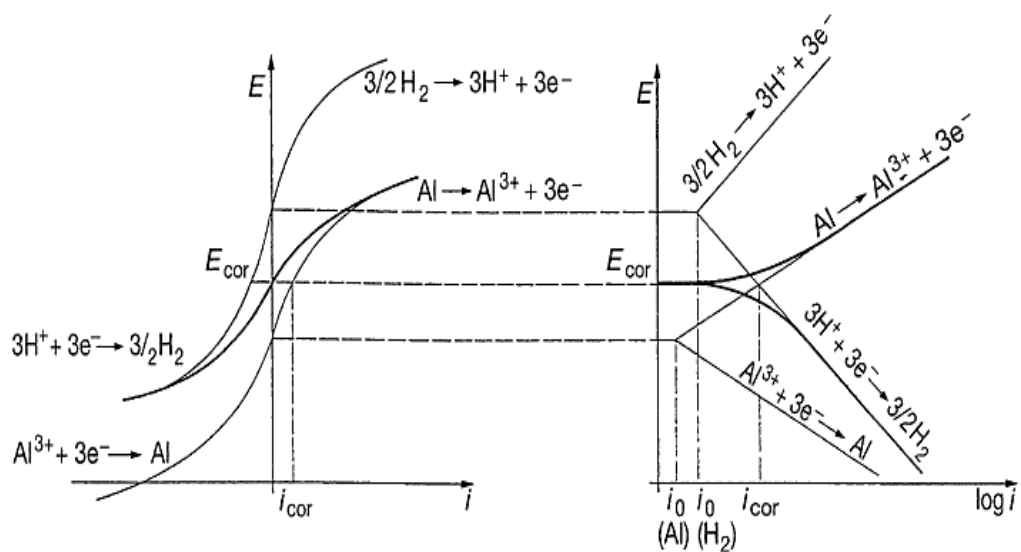
Figure 2.9: Anodic and cathodic polarisation curves of aluminium [39].

There is little advantage in plotting these curves completely, because only the area around the corrosion potential is useful for measuring corrosion current i_{corr} [39]. Corrosion occurring in aqueous media can be measured by electrochemical techniques based on polarisation — these being mainly Tafel extrapolation and linear polarisation measurements. Tafel extrapolation measures the corrosion rate from the linear slopes of anodic and cathodic current curves in the vicinity of the corrosion potential. In the case of aluminium (Figure 2.9), the anodic polarisation curve has no linear portion, and the cathodic part must be used, with the condition that hydrogen reduction takes place [39, 81].

2.7.1 Electrochemical polarisation corrosion testing

Corrosion testing with polarisation methods basically consists of imposing a potential on the sample under study, while determining the resulting current or voltage response. This may be achieved by using either a direct current (DC) or an alternating current (AC) source. A typical instrument for carrying out polarisation measurements (as used in this study at our Lab) is illustrated in Figure 2.10. It comprises an electrochemical cell setup consisting of an electrolyte solution, three electrodes (working, counter and reference electrodes) and electrochemical instrumentation to carry out polarisation measurements in which a potentiostat/galvanostat power controller is used to pass current through the working electrode and an auxiliary (counter) electrode, while monitoring the potential of the working electrode against a reference electrode.
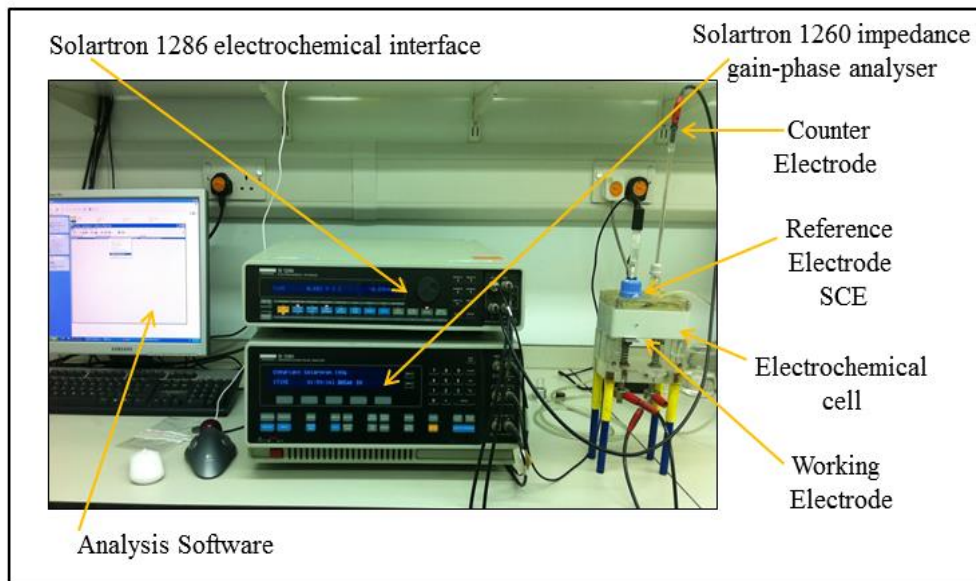
Figure 2.10: Polarization measurement apparatus and electrochemical cell.

Most often, the types of polarisation measurement that are useful in understanding the behaviour of metal and alloy systems in aqueous environments are the anodic and cathodic polarisation curves. An anodic polarisation test can be conducted in which the current is constantly measured as a gradual increase in potential occurs. The anodic reaction will be increased; on the other hand the cathodic reaction will be decreased. Anodic polarisation is also useful in investigating the active-passive behaviour that most actively corroding metals exhibit. Cathodic polarisation is often used to accelerate the rate of reduction reactions and develop local alkalinity that disbonds and degrades coatings (this forms part of the rationale of rapid testing procedures developed in this work). Where a constant potential in the negative direction is applied, electrolysis of the solution should take place. Dissolution occurring due to the effects of cathodic reactions at the passive film/metal substrate interface is known as cathodic disbondment [82].

2.7.2   DC cathodic polarisation

High solution pH "alkalinisation" is the main reason for dissolution at the passive film/metal interface due to the chemical attack by OH^- ions [44, 83]. The loss of adhesion known as cathodic disbondment is due to water reduction that produces H^+ ions that permeate into the passive film and reduces to H_2 gas, which promoting the physical disbondment with the contribution of OH^- ions that causes chemical dissolution [18, 84, 85]. The application of DC cathodic polarisation causes cathodic degradation through electrolysis of the electrolyte [82, 86].

Electrolysis is the process by which ionic substances are decomposed (broken down) into simpler substances by passage of an electric current through them from a DC direct current battery or power supply. The substances must be ions, free to move and dissolve in water (or be molten). During electrolysis, reduction reactions occur at the cathode (which attracts positively charged ions, cations) and oxidation reactions at the anode electrode (which attracts negatively charged ions, anions) and these are discharged to give the products, which may be solid or gaseous. In general, when an aqueous solution of an ionic compound is electrolysed, a metal or hydrogen gas is produced at the cathode. At the anode, a gaseous non-metal, for example oxygen or chlorine may be evolved [87]. The electrode reactions and products of the sodium chloride solution (brine) are shown in Figure 2.11 [87].
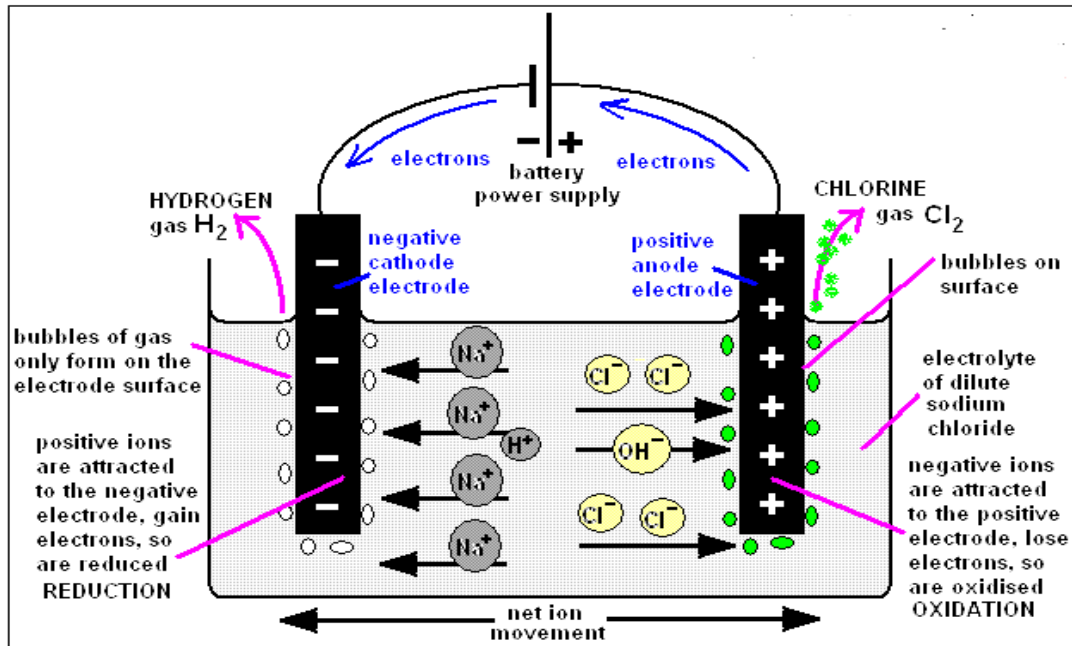
Figure 2.11: The electrolysis of sodium chloride solution (brine) [87].

An aqueous solution of sodium chloride contains four different types of ions. These are:

- o Ions from sodium chloride : Na^+ (aq) and Cl^- (aq)

- o Ions from water : H^+ (aq) and OH^- (aq)

During the electrolysis of dilute sodium chloride solution the Na^+ and H^+ ions are attracted to the cathode. The Cl^- and OH^- ions are attracted to the anode.

– **At the cathode:**

The positive charges (H^+ and Na^+) are attracted to the cathode electrode. H^+ ions reduce to H_2 gas (H^+ ions gain electrons more readily than Na^+ ions).

$$Na^+ + e^- \rightarrow Na \qquad\qquad E^{\circ}_{Na^+/Na} = -2.713 \text{ V}$$

$$H^+ + e^- \rightarrow H_2 \qquad\qquad E^{\circ}_{H^+/H_2} = 0 \text{ V}$$

Also at the cathode (because it is much easier to reduce water than Na$^+$ ions), the only product formed at the cathode is hydrogen gas.

$$2H_2O + 2e- \rightarrow H_2 + OH^- \qquad E^\circ_{H_2/H_2O} = -0.828 \text{ V}$$
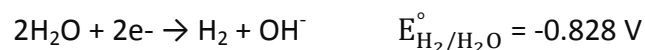
- **At the anode:**

The negatively charged ions (Cl$^-$ and OH$^-$) are attracted to the anode electrode. OH$^-$ ions release electrons and are oxidised to form water and O$_2$ gas, while Cl$^-$ ions remain in the solution.

$$4OH^- \rightarrow 2H_2O + O_2 + 4e^- \qquad E^\circ_{O_2/OH^-} = -0.40 \text{ V}$$

$$2Cl^- \rightarrow Cl_2 + 2e^- \qquad E^\circ_{Cl_2/Cl^-} = 1.358 \text{ V}$$

By contrast, during the electrolysis of concentrated sodium chloride solution, at the cathode electrode H$^+$ ions reduce to hydrogen gas as during diluted NaCl solution. The only difference is that at the anode, Cl$^-$ ions are much more probably oxidised than OH$^-$ ions. It would seem to be easier to oxidise OH$^-$ ions (E°_{ox} = -0.40 V) than Cl$^-$ ions (E°_{ox} = 1.358 V); however, because of the concentration-kinetic factor wins out, the much higher concentration of Cl$^-$ ions over OH$^-$ ions leads to the oxidation of the chloride ion to form chlorine gas [87, 88]. Table 2.1 [36] illustrates the standard reduction potentials for most typical half-reactions encountered in electrochemistry.

Table 2.1: Standard Reduction of Half-Cell Potentials

Half-Reaction	E^0_{red}
$O_3(g) + 2\ H^+ + 2\ e^- \rightleftharpoons O_2(g) + H_2O$	2.07
$H_2O_2 + 2\ H^+ + 2\ e^- \rightleftharpoons 2\ H_2O$	1.776
$Au^+ + e^- \rightleftharpoons Au$	1.68
$PbO_2 + 4\ H^+ + 2\ e^- \rightleftharpoons Pb^{2+} + 2\ H_2O$	1.467
$Cl_2(g) + 2\ e^- \rightleftharpoons 2\ Cl^-$	1.3583
$O_2 + 4\ H^+ + 4\ e^- \rightleftharpoons 2\ H_2O$	1.229
$Pt^{2+} + 2\ e^- \rightleftharpoons Pt$	1.2
$H_2O_2 + 2\ e^- \rightleftharpoons 2\ OH^-$	0.88
$Hg^{2+} + 2\ e^- \rightleftharpoons Hg$	0.851
$Ag^+ + e^- \rightleftharpoons Ag$	0.7996
$Hg_2^{2+} + 2\ e^- \rightleftharpoons Hg$	0.7961
$Cu^+ + e^- \rightleftharpoons Cu$	0.522
$O_2 + 2\ H_2O + 4\ e^- \rightleftharpoons 4\ OH^-$	0.401
$Cu^{2+} + 2\ e^- \rightleftharpoons Cu$	0.3402
$2\ H^+ + 2\ e^- \rightleftharpoons H_2$	0.0000...
$Fe^{3+} + 3\ e^- \rightleftharpoons Fe$	−0.036
$Pb^{2+} + 2\ e^- \rightleftharpoons Pb$	−0.1263
$Sn^{2+} + 2\ e^- \rightleftharpoons Sn$	−0.1364
$Ni^{2+} + 2\ e^- \rightleftharpoons Ni$	−0.23
$Co^{2+} + 2\ e^- \rightleftharpoons Co$	−0.28
$Fe^{2+} + 2\ e^- \rightleftharpoons Fe$	−0.409
$Cr^{3+} + 3\ e^- \rightleftharpoons Cr$	−0.74
$Zn^{2+} + 2\ e^- \rightleftharpoons Zn$	−0.7628
$Mn^{2+} + 2\ e^- \rightleftharpoons Mn$	−1.04
$Al^{3+} + 3\ e^- \rightleftharpoons Al$	−1.706
$Mg^{2+} + 2\ e^- \rightleftharpoons Mg$	−2.375
$Na^+ + e^- \rightleftharpoons Na$	−2.7109
$K^+ + e^- \rightleftharpoons K$	−2.924

2.8 Hydrogen Damage

It is well known that atomic hydrogen, and not the H_2 molecule is the smallest atom of the periodic table and as such it is small enough to diffuse readily through a metallic structure, and can cause corrosion phenomena under the general term of cracking which relates to its penetration into metals and alloys [36]. When the crystal lattice is in contact or is saturated with atomic hydrogen, the mechanical properties of many metals and alloys are diminished. Nascent atomic hydrogen can be produced as a cathodic reaction, either during natural corrosion processes or

forced by cathodic protection, when certain chemical species are present. This hydrogen damage is very dangerous and close to stress corrosion cracking (SCC), but is caused only by hydrogen atoms and molecules and tensile stresses. Hydrogen can enter metals and alloys either from a gas or a liquid phase. The mechanism of entering from the gas phase includes adsorption of H_2 or other gas containing hydrogen (such as H_2S), its dissociation into adsorbed H atoms (H_{ads}) on the surface and the diffusion into the metal structure. In the liquid phase, H_{ads} is formed as a result of an electrochemical reaction in acidic solution:

$$H_3O^+_{(aq)} + e^- \rightarrow H_{ads} + H_2O_{(l)} \qquad\qquad (2.22)$$

Hydrogen atoms that originate from the cathodic reaction of H^+ ions are very active and easy to diffuse into a metal lattice. Inside the metallic lattice, hydrogen atoms can combine to form H_2 gas, the accumulation of which can cause hydrogen blister formation because of the large hydrogen molecular pressure that results. The internal pressure of H_2 increases to a level at which cracks initiate and propagate [89]. The methods that produce hydrogen are numerous; one of the easiest and fastest ones is electrolysis of an aqueous solution by producing hydrogen on the cathode electrode. Cathodic hydrogen evolution represents the most important reaction to produce hydrogen as fuel. The biggest problem facing hydrogen producers is to find a suitable metal or alloy that works as a cathode with low hydrogen overpotential (electrode damage) to reduce the cost of replacement and, at the same time, is stable enough for long-term electrolysis [90, 91]. Hydrogen damage in metals can occur in three different ways [89]:

- Formation of hydrogen atoms and their adsorption on metal surface.

- Diffusion (penetration) of adsorbed hydrogen atoms into metallic lattice.

- Accumulation of hydrogen atoms inside metals, leading to increased internal pressure, and thus to blistering or cracks.

2.8.1 Electrochemical hydrogen permeation

The permeation of hydrogen (diffusion) into metals has been widely studied by electrochemical permeation tests [92, 93]. The diffusion of hydrogen in metals is a significant problem met by engineering components in industry. This phenomenon must be studied closely to give a better understanding of its mechanisms. Permeation of hydrogen is strongly influenced by the local hydrogen ion concentration [94]. Due to the ionic behaviour of passive films, hydrogen absorbed into the passive film must be considered as being present as a charged species and very low hydrogen diffusion coefficients are expected in them [95]. It is well known that the passive layer can act as an effective barrier against hydrogen entry into metals, depending on exposure time and on the electrochemical conditions of the electrode surface. Hydrogen can be easily absorbed into, and retained by, metals via processes such as fabrication, welding, corrosion, electrodeposition coatings and cathodic polarization [96]. The electrochemical hydrogen permeation into metals depends on the surface preparation, defects and surface oxidation and passivation state. Hydrogen permeation can be measured by a current density that is expected to be proportional to the hydrogen flux [95, 97]. Figure 2.12 [97] shows hydrogen evolution with time during and after cathodic polarisation.
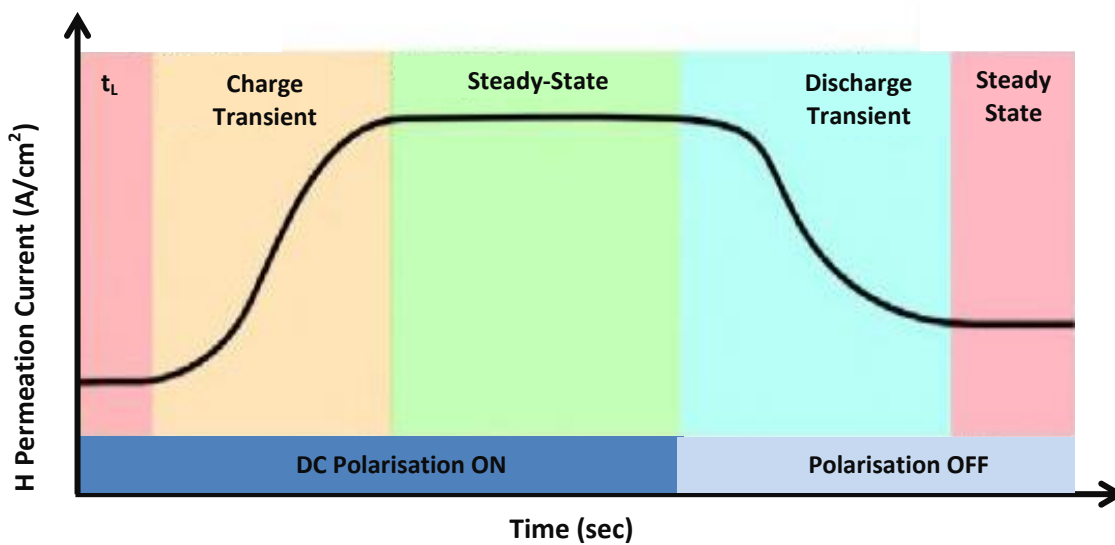
Figure 2.12: Schematic diagram of the overall process of hydrogen permeation current development with time during and after DC polarisation [97].

The time lag (t_L) is the time required to obtain a steady-state of hydrogen flow through the metal interstitial sites, after a sudden change of experimental conditions [95]. The hydrogen permeation curve is a function of time during and after DC cathodic polarisation (potentiostatic process). It was usually illustrated that the typical hydrogen permeation flux curves have a clear region of charging transient. This transient will begin at some low current and then rise as the first diffusion of hydrogen atoms into the metal takes place. Hydrogen atom is more reactive than the ion because it is more unstable. This rising current transient will become constant (steady-state current), where hydrogen atoms reach a saturation level. Once the metal surface is saturated with hydrogen atoms (H_{abs}), hydrogen will no longer diffuse easily into the metal and would preferentially form hydrogen gas H_2. The discharge transient (with decreasing current), starts after the DC polarisation is terminated. Continuation of discharging results in a decrease in

current until reaching the steady-state level. If a steady-state is not reached, but a peak is observed, this can be assumed to be due to the production of voids within the metal structure, or to changes in the surface film [97, 98]. Hydrogen affects the properties of a metal when its absorbed concentration equals or exceeds a threshold hydrogen concentration.

The protective surface oxide layer generally present on active metal exposed to air (or aqueous media) can hinder hydrogen absorption into the metal. This retardation could be due to the lower diffusion coefficient for hydrogen in the oxide compared to the metal [96]. Generally, the accepted reactions for H^+ ion evolution can be written as follows:

$$1) \quad H^+{}_{(aq)} + e^- \rightarrow H_{ads} \quad\quad\quad\quad (2.23)$$

followed by either the chemical reaction

$$2) \quad H_{ads} + H^+{}_{(aq)} + e^- \rightarrow H_{2\,(g)} \quad\quad\quad (2.24)$$
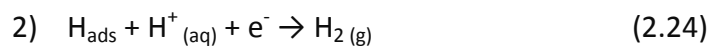
or the electrochemical reaction

$$3) \quad 2H_{ads} \rightarrow H_{2\,(g)} \quad\quad\quad\quad\quad (2.25)$$

and accompanied by the following reaction

$$4) \quad H_{ads} \rightarrow H_{abs} \quad\quad\quad\quad\quad (2.26)$$

For this sequence, the reduction reaction of H^+ ion (2.23) would be expected to be rapid since the energy of H_{ads} on a metal surface is large. However, the concentration of H_{ads} at the surface would be decreased since the rate of H_{abs} via the reaction 4 (2.26) would also be expected to be rapid (as the permeability of a passive film is high), and can proceed by the mechanism illustrated schematically in Figure 2.13 (a) [99]. Consequently, the rate of the reactions 2 and 3 (2.24 and 2.25) would be slow and low since both are dependent on the availability of H_{ads} concentration at the surface.
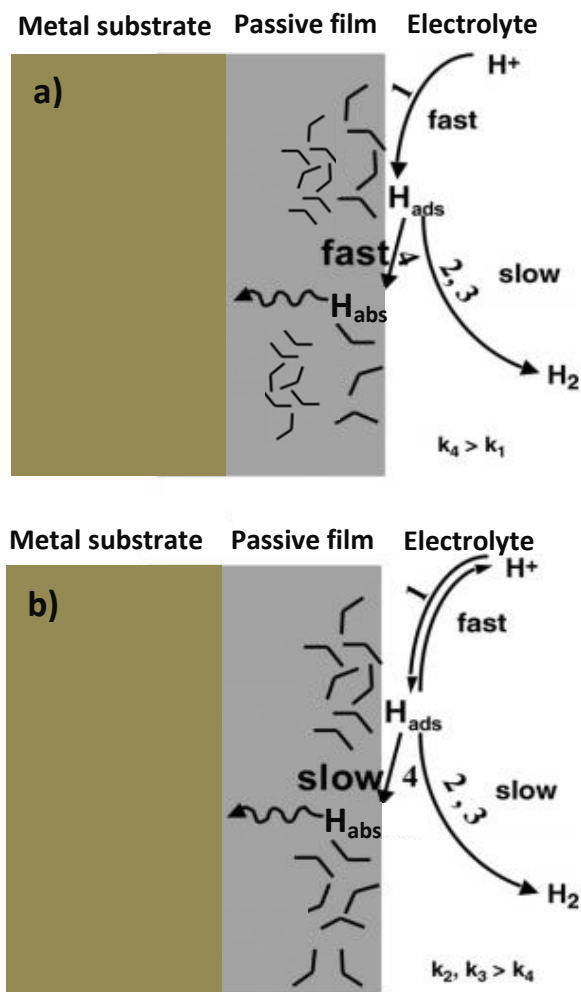
Figure 2.13: Schematic diagrams for the mechanism of hydrogen evolution at the passive film/electrolyte interface, after [99].

The protective passive films would slow down hydrogen absorption into the metal. Thus, the rate of the reactions 2 and 3 would be higher than the reaction 4 and the reaction 1 would be irreversible with the following current/potential relationship formula 2.27 [99]:

$$I = 2Fk_1[H^+] \exp\left\{-\frac{\alpha_{1F}}{RT}E\right\} \tag{2.27}$$

Where, k_1 is the rate constant for reaction 1, which is dependent on H^+ ions concentration and can proceed by the mechanism illustrated schematically in Figure 2.13 (a) [99].

Hydrogen permeation into the passive film is a complex process involving three mechanisms: diffusion, absorption and trapping. Qin et al. [100] created simulation models that describe the hydrogen permeation process through a passive film. They proposed a diffusion only model (D), diffusion and trapping model (DT), diffusion and absorption model (DA), and a combination model (DAT) as shown in Figure 2.14.
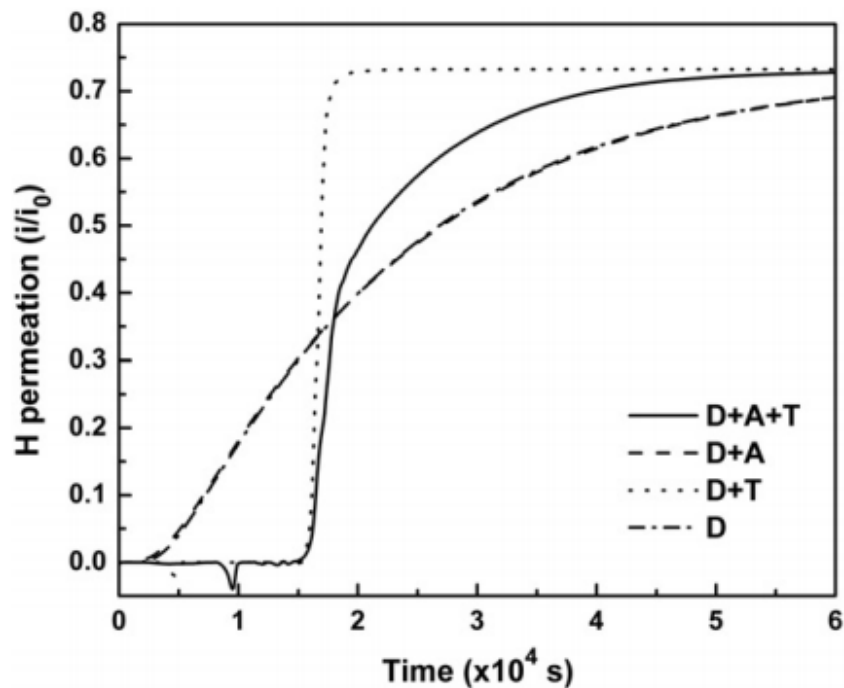
Figure 2.14: Types of models that describe hydrogen permeation though a passive film [100].

These models were numerically simulated by finite element method and compared with hydrogen permeation curves, values of the parameters associated with permeation (such as diffusion coefficients, absorption and desorption rate constants), passive film structure and chemical composition, the presence of oxygen vacancies, the types of impurities and their concentration, the permeability characteristics of the passive film, the passive film thickness, porosity and uniformity and environmental parameters (such as electrochemical potential and temperature) [96, 99-101]. Thus, the hindrance of hydrogen permeation by a passive film can be due to a combination of low hydrogen adsorption at the passive film surface and/or slow hydrogen transport in the passive film. Therefore, it can be seen in Figure 2.13 (b) that the rate constants of k_2 and k_3 for reactions 2 and 3 are greater than the rate constant k_4 of the reaction 4.

The distribution and diffusion of hydrogen in a metal could be calculated by Fick's first low of diffusion, according to the permeation rate of hydrogen. The concentration of hydrogen atoms inside the metal surface is C_0, which can be calculated by first converting current measurements into flux of hydrogen atoms. Where the saturation current is measured in amperes (which is coulombs of charge passed per second), the permeation of hydrogen atoms diffusing into the metal may now be measured. In the steady-state (saturated level), the maximum concentration of hydrogen in metal C_0 (mol cm^{-3}), can be calculated from the following equation:

$$C_0 = \frac{I_{max} L}{FD} \tag{2.27}$$

where $I_{\max}$ is the permeation current density (A cm^{-2}) at the steady state; L (cm) is the specimen thickness; F is the Faraday constant (96500 A s) and D (cm^2 s^{-1}) is the hydrogen diffusion coefficient in the specimen at 298 K [97, 102, 103].

2.9 Protective Coatings

A countless number of environments cause corrosion of structures and engineering components, and therefore various approaches exist for the protection of metallic substrates. Most of these approaches are governed by the use of either organic or metallic barrier coatings and are based on matching the requirements of the application with the combination of properties that can be offered by different coatings. The selection of a coating process for a specific application depends on several factors, including the corrosion resistance that is required, the expected lifetime of the coated material, the number of parts being produced, the production rate that is required, and environmental considerations. The function that a coating will provide is based on the material's content and design compared to the required need for protection. It is essential to express the requirements in a way that can be directly compared to the known properties and characteristics of coatings and coating processes. A coating may be prone to identical conditions and not improve or protect the substrate [1, 104, 105]. Typical steps of the coating selection procedure and the process employed are shown in Figure 2.15 [1].
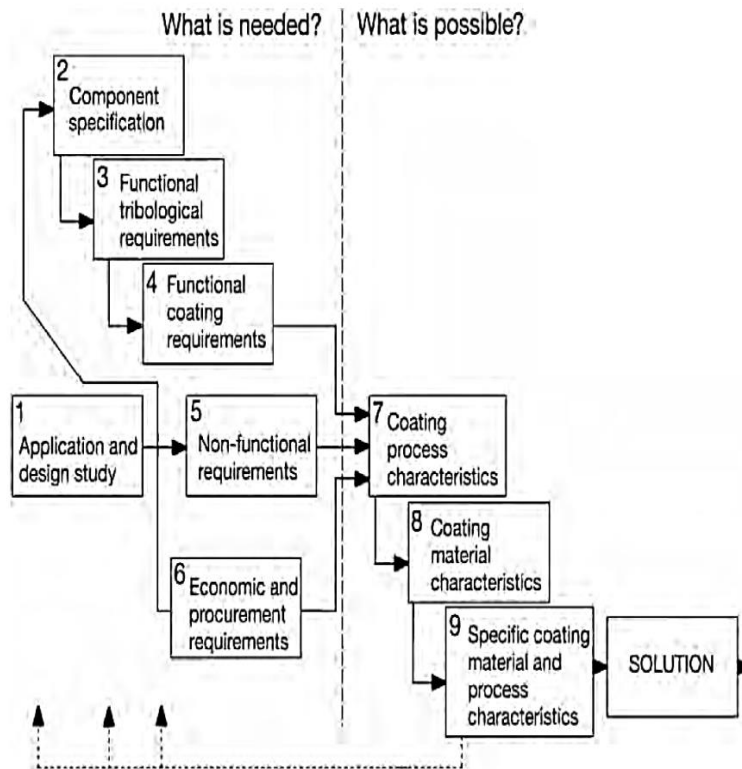
Figure 2.15: Methodology for coating and processes selection [1].

2.10 Advanced Methods for Coating Corrosion Protection of Steel

Most of the time, environmental degradation resistance is provided by a coating system applied to a metal substrate that acts as a back support, providing mechanical strength and fracture toughness. Historically, development of improved corrosion and wear resistant coatings can be defined as a combination of one or more dissimilar materials applied to a metal substrate. Corrosion and wear resistance are of significant concern in many industries, as they shorten the service life of many engineering components. Therefore, study of the factors that influence coating durability includes chemical composition, morphology, structure and adhesion [106]. The most common techniques that have been widely employed to

impart corrosion resistance are chromate conversion coatings and cadmium or zinc electroplating. These types of coating exhibit excellent mechanical and corrosion resistance properties and also improve engineering paint adhesion and lubricity characteristics; they have been used in the aerospace industry for many years [107]. However, many such coatings are banned under strict regulation due to the toxic nature of materials and deposition processes threaten human health and the environment [108, 109]. PVD coating technology has the highest potential, where the market share of PVD segment will be worth $294.6 million in 2016 with compound annual growth rate (CAGR) of 7.2% [110].

2.10.1 Physical vapour deposition coating

PVD coatings are vital for surface modification of various tools and engineering components. In general, PVD of engineering coating is conducted through four commercially main deposition processes: ion vapour deposition (IVD), magnetron sputtering, cathodic arc evaporation and plasma-assisted electron-beam PVD (ion plating) in vacuum or low pressure chamber and a coating is deposited on a substrate surface by condensation of atoms or molecules of metal vaporised from a solid or liquid state [111]. PVD coating technique accomplished to deposit coatings thickness from few nanometres (nm) to few microns (µm). There are several alternative coating methods used for thin-film deposition or coating such as chemical vapour deposition (CVD), thermal spraying, electroplating, etc. [111]. However, nowadays most PVD processes can be done using processes involve generation of an electrical discharge, in order to create ion bombardment during

deposition, which is known generically as plasma-assisted (PAPVD). In the context of metallic coatings PAPVD is used widely for depositing very thin coatings of aluminium on substrates for decorative and optical applications.

2.10.2 PVD processing

2.10.2.1 Ion vapour deposition

Ion vapour deposition (IVD) is a physical vapour deposition process for applying metallic coatings on various metallic steel substrates, mainly pure aluminium for corrosion protection of steels and titanium alloys. In the early 1960s, IVD was first applied by Mattox [111]. Many researchers started to eliminate cadmium (and some zinc coatings) with alternative non-toxic aluminium coating. IVD processing employed resistive evaporation using Al wire feed onto a ceramic boride crucible.

The IVD process uses evaporation (either resistive or electron-beam) and a high voltage applied to a cathode, to produce uniform adherent aluminium coatings on metallic substrates. A DC cathodic potential of (500 to 1500 V) is typically applied to the substrate. Aluminium is evaporated from resistively heated elements or from an aluminium slug by electron beam evaporation. The IVD-Al coating does not affect the mechanical properties of the substrate and (with shot peering after deposition) can provide precise thickness control on a wide range of shapes. IVD-Al coating is non-toxic and can be used in a wide range of applications and is particularly effective as a replacement for cadmium coatings. However, the disadvantage of IVD-Al coating is that it often has structural defects (such as pores

and columnar microstructure) which may result in insufficient corrosion resistance for the metallic substrate [112].

2.10.2.2 Electron beam evaporation

Electron beam evaporation is a physical vapour deposition process whereby an intense, high-voltage electron beam is generated from a heated tungsten filament and accelerated these electrons using electronic and/or magnetic fields to deflect the beam. E-Beam evaporation is a preferred vacuum technique for deposit highly dense metallic films. Electron-Beam evaporation eliminates many disadvantages of IVD process such contamination from the crucible, heaters and adjusting the relative low input power levels, which makes it difficult to deposit pure films at appropriate rates. E-Beam evaporation method can deposit materials which are difficult to deposit by IVD, such as reactive, low vapour pressure, refractory and insoluble material mixtures [113]. Materials including low vapour pressure metals (such as platinum), refractory metals (such as tungsten) and alloys can be evaporated. Since the electron beam method concentrates large amounts of heat on a very small area, high rates of deposition can be obtained, and a factor which is of commercial significance in thick, metallic coating production [112].

When the electron beam hits the surface of target material, the high kinetic energy is transformed efficiently into thermal energy. The energy given off by a single electron is quite small and the heating is accomplished simply by advantage of the vast number of electrons hitting the evaporant surface. The achieved energy level is quite high, often more than ten million watts per square centimetre. The power

supply for this operation is a high voltage DC power supply and the applied acceleration voltage is typically (10 to 20 KV) [114].

2.10.2.3 Sputter deposition

According to Mattox [111] the first sputter deposited films were reported by Wright in 1877. Sputtering, in contrast to evaporation, is a non-thermal vapourisation process where atoms are physically ejected from a solid surface by bombarding it with energetic atoms/molecules which are usually gaseous ions accelerated from plasma. Sputter deposition is performed under vacuum conditions (typically less than 10^{-5} mbar base pressure and 10^{-3} operating pressure) and uses a glow discharge to generate energetic species, which bombard the material to be deposited (target) and cause atoms to be ejected from its surface by transfer of momentum. Sputtering techniques are generally categorised as, cold cathode DC diode sputtering, DC triode sputtering, DC magnetron sputtering, AC sputtering and Radio Frequency (RF) sputtering. Sputtering provides a number of advantages including: i) excellent coating thickness uniformity; ii) large area vapour sources; iii) no droplet formation; iv) no spitting, v) deposition of insulating films; and vi) deposition of refractory materials [115, 116].

2.10.2.4 Magnetron sputtering

Magnetron sputtering is the most widely used of sputtering methods and was developed to overcome the limitations of traditional sputter deposition methods such as low deposition rate, low ionisation efficiency and excessive substrate heating by electrons [117, 118]. Extra magnetic field lines parallel to the target

surface restrain the secondary emitted electron motion in the vicinity of target or cathode. The magnetic field South Pole is located at the central axis of target whereas North Pole is formed at the outer edge (or vice versa), as illustrated in Figure 2.16 [119]. A Lorentz force (FL) induced by the magnetic field traps emitted electrons and confines them in a 'racetrack' between the target poles. This leads to an increment in sputter rate, corresponding to a higher degree ionization [114, 119].
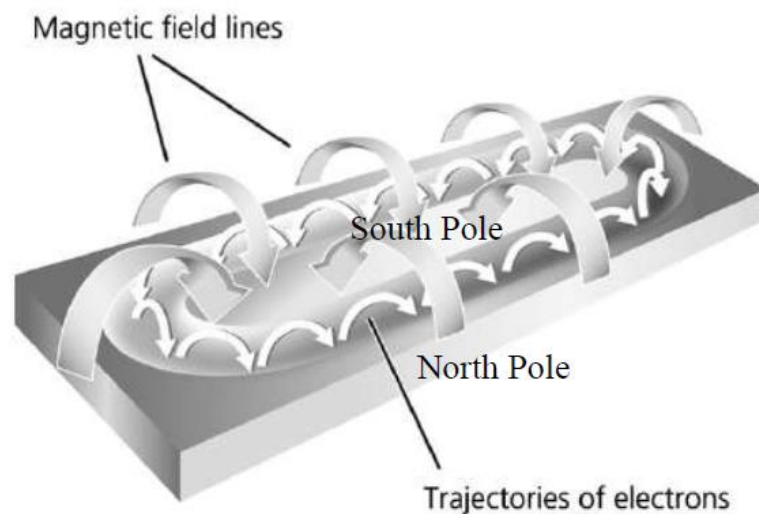
Figure 2.16: Schematic diagram of magnetron sputtering [119].

2.10.3 PVD coating microstructure

All industrial or academic research in magnetron sputtering deposition involves two or more elements simultaneously. The microstructure, crystal structure, grain size and texture of films are influenced by deposition parameters. Properties of protective coatings are strongly influenced by the microstructure. The two critical factors are ion bombardment energy and sputtering rate must be controlled for the

growth of the desired thin film microstructure [120]. The structure zone model (SZM) was first introduced by Thornton relating microstructure growth to the ratio of the experimental temperature to the melting [121].

Following on studies of these models by researchers have been based on either deposition methods or bias voltage to identify growth pattern of thin film microstructures. Kelly and Arnell proposed a structure zone model particularly for CFUBMS method. The authors outlined a new approach to determine the effect of temperature, high ion flux and ion energy each individually on the microstructure. This model considers three variables which are homologous temperature, ion-to-atom ratio and substrate bias voltage. Results shows this deposition method usually produces either fully dense or dense columnar coating structure [118].

Sanchette et al. [122] successfully deposited microcrystalline Al-Cr and Al-Ti coatings. Grain size of coatings decreased when percentage of foreign elements Cr increased from 5 at.% to 40at.% or 25 at.% to 60 at.% for Ti. Nitrogen (N_2) injected into PVD chamber with mixture of argon (Ar) resulted transition of microcrystalline to amorphous structure. A fully amorphous coating was obtained at around 5 vol.% of N_2 injection for AlTi (11 at.%) and AlCr (10 at.%) coatings system. The authors also report amorphization occurred at low 2 vol.% N_2 injection as Ti increment to 23 at.% or 13 at.% for Cr [5, 8, 122, 123]. Nitrogen—stabilized amorphous coating and dense Al-Cr coating theory were supported by research conducted by Creus et al [5]. Also Creus et al [124] deposited a range of PVD Al-based coatings composed of pure aluminium, Al-Cr, Al-N, Al-Ti, Al-Zr, Al-Mn, Al-Mo, Al-Si, Al-Ni, Al-V, Al-Zn, Al-Y,

Al-Ce, Al-Gd and Al-Mg on glass substrates by magnetron sputtering and (more recently) EBPVD techniques. The following alloys: Al-Cr, Al-N, Al-Ti, Al-Zr, Al-Mn, Al-Mo, Al-Si, Al-Ni and Al-V were all found to improve the resistance of Al to localised corrosion.

Chapter Three

Accelerated Corrosion Evaluation Techniques for Coated Steel

3.1   Introduction

As the demand for improved corrosion resistant of coatings increases, users of coatings require improved testing and quality control procedures to be introduced to determine how long coatings will resist corrosion of the metal substrate on which they are applied [125-128]. It is becoming increasingly necessary to develop rapid evaluation and screening techniques that can estimate the likely corrosion behaviour of coatings before using them in actual applications. However, it is impractical for coating manufacturers to wait weeks, months or even years for completion of outdoor exposure tests [15, 128]. At the beginning of the 20th century accelerated corrosion testing was first developed to induce quicker deterioration of coating systems based on the application of specific "stresses" (e.g. temperature, salt, humidity, UV light) at higher levels than might be expected to occur under natural exposure [129]. Electrochemical evaluation techniques and, principally, electrochemical impedance spectroscopy (EIS) are now widely used to evaluate the changes that take place in the protective properties of coatings during their exposure to aggressive media [24, 130].

It is however, highly desirable to have a new rapid evaluation technique that can reliably estimate the corrosion behaviour of engineering coatings in a shorter period of time [131]. For example, EIS gives useful numerical information about coated system degradation characteristics [132], but still involves the periodic interrogation of corroding coating/substrate system in real time. Recently, a rapid accelerated technique has been developed by Hollaender et al. [13, 14] called the AC/DC/AC test; this can provide a rapid assessment of the corrosion behaviour of organic surfaces and particularly of paint coatings which led to this test being successfully adopted by Suay et al., 2003 [85] to evaluate liquid painted steel.

3.2   Corrosion evaluation techniques

3.2.1   Salt Spray Testing

3.2.1.1   *Background of salt spray testing*

Conventionally, characterising and evaluating the corrosion behaviour of the coating is performed through accelerated testing techniques, in which the time to failure is considerably less than that expected for real applications and conditions. In 1914, Salt Spray Testing (SST) was first used as an evaluation technique for bulk materials corrosion testing [125]. SST was formalised as the ASTM B117 standard in 1939 [133], and is one of the most widely accepted accelerated testing methods (particularly by industry) to evaluate the corrosion behaviour of coatings. SST causes the degradation of the bulk materials and coatings or their failure in shorter time periods than natural conditions without, in most cases, changing fundamentally the failure mechanisms [134]. SST is performed under controlled

conditions and any alterations in the appearance of the coating during exposure are monitored as a function of time by a trained observer. A frequent and strong criticism of the salt spray test is that the results obtained are qualitative, and not completely independent of the operator. So far, a direct correlation between natural and SST degradation is not clear; therefore, SST is generally only used for comparative ranking of different alloys and coatings. The method is based on the principle that corrosion can only occur if electrolyte and oxidant species are present at the metal surface. Nevertheless, ASTM B117 is generally accepted as valid corrosion test technique due to its standardised protocols for conducting the test exposure and evaluating the results, its procedural simplicity and the ability to discriminate between 'good' and 'bad' coatings [10, 23, 126, 134-136].

3.2.1.2   Salt spray test procedure

ASTM B117 provides a standardised protocol of test procedure, which involves continuous exposure to a fog or mist of 5 wt. % NaCl solution at 35°C. Other chemicals may also be added to the electrolyte to simulate other corrosive environments, such as acid rain or industrial atmospheres [125]. Salt spray testing has been criticised for its inability to provide a quantitative results of corrosion damage and for a lack of reproducibility from one test to other. Figure 3.1 [125] shows a schematic of a typical chamber used for salt spray testing.
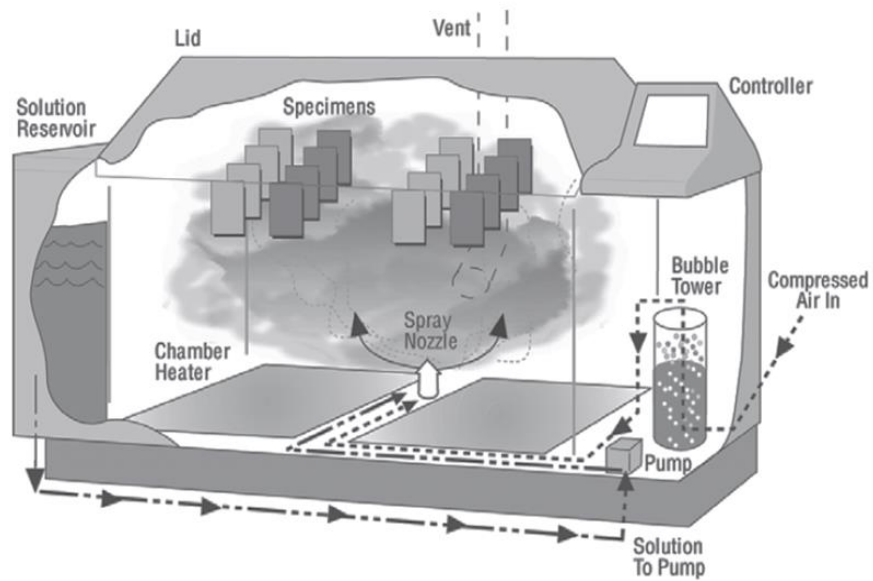
Figure 3.1: Schematic of a typical salt spray chamber [128].

3.2.2   Electrochemical Impedance Spectroscopy EIS test

3.2.2.1   Background of EIS

Since corrosion is an electrochemical process, electrochemical techniques are frequently employed to study and understanding the corrosion process. However, electrochemical testing techniques, such as Electrochemical Impedance Spectroscopy (EIS) are very common use in evaluating corrosion behaviour of coating over [137, 138]. EIS is a powerful, proven and non-destructive technique that can provide valuable information with regard to the details of corrosion rate, electrochemical reactions and detection of localised corrosion [139-142]. Impedance is a measure of the ability of the electric circuit to resist of the current flow [143].

The activity of EIS has been used in the early of 20th century by Finkelstein [144] characterise the dielectric response of the oxide film. A few years later, Cole, K.S.

[145] found that the capacitance was a function of frequency from the analysis of cell membranes. The relationship between the frequency exponent of impedance and a constant phase angle was also observed by Fricke in 1932 [144].

Cole, K. S. and Cole, R. H. in 1941 [145], reported the frequency dependent dielectric constant in a Nyquist plot (imaginary part and real part of dielectric constant as y and x axis, respectively), which is so called 'Cole-Cole plot' . They also suggested the use of a Constant Phase Element (CPE) for non-ideal data. Furthermore, in the next decade, the double-layer structure was explored by Frumkin and Grahame, and provided a fundamental understanding of EIS technique use and le to the development of the Equivalent Circuit (EC) modelling approach by Randle and Warburg [146].

3.2.2.2   Fundamental theory of EIS

In EIS tests, small amplitude AC signals are applied (usually of the order of 10 mV) over a wide range of frequencies (10^{-2} Hz to 10^{5} Hz) the resulting impedance calculated [34, 147]. The results obtained from EIS scans are commonly represented as a plot of real component (Z') vs. imaginary (Z") component of the spectrum of impedance (complex plots) and impedance modulus |Z| vs. frequency, or impedance phase angle vs. frequency (Bode plots). The impedance Z can be calculated as follows [138]:

$$Z (j\omega) = Z' + jZ'' \qquad\qquad (3.1)$$

Electrochemical impedance spectroscopy has become a popular tool in materials research including the study of rates of electrochemical reaction of corrosion, mass transfer, microstructure, etc. [138, 143].

The interpretation of EIS results can be made by calculating the values of electric circuit elements from a model equivalent circuit. There is a correlation between the elements of the EC and the structure of (and resulting corrosion properties) of the coating system [134, 135, 148]. Figure 3.2 [127] shows schematically the equivalent circuit for a general case of a permeable coating under attack by an electrolyte.
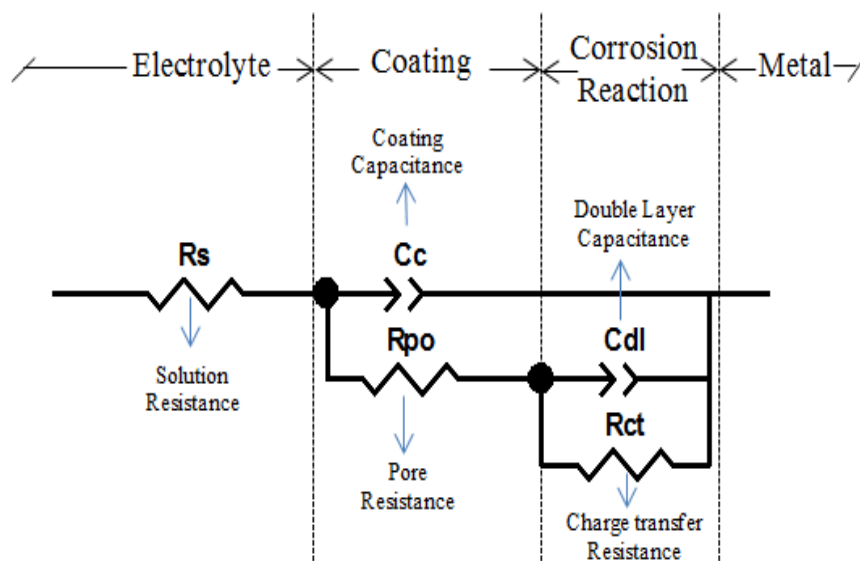
Figure 3.2: Schematic general equivalent circuit EC of coated metal surfaces [130].

3.2.2.3 Equivalent circuit interpretation

Generally, EIS data analysis requires an appropriate equivalent circuit which, in principle, comprises basic electrical elements (such as resistors and capacitors), attributable to the physical and electrochemical properties of the studied system

[132, 143]. The EC shown in Figure 3.2 is typically used for a corroding metallic coating which, comprises the following elements: solution resistance R_s, pore resistance R_{po}, charge transfer resistance R_{ct}, constant phase element CPE_c (representing the coating capacitance) and constant phase element CPE_{dl} (representing the double layer capacitance) . CPEs in the equivalent circuit describe the distribution of relaxation times, due to inhomogeneities present at the solid/liquid interface [149]. This non-ideal behaviour may arise from coating heterogeneities such as surface roughness and local changes in composition or structure. In such a case the coating cannot be simply described by discrete resistive or capacitive electrical elements and CPEs thus provide better circuit fitting results. The impedance of a CPE (Z_{CPE}) is defined by:

$$Z_{CPE} = \frac{1}{C\,(j\omega)^n} \tag{3.2}$$

Where C is the capacitance and n is the power that relates to the extent of heterogeneity generally attributed to the fractal geometry, inhomogeneity and sample porosity. The exponent n is an adjustable parameter that lies in the range (1 ≤ n ≤ 0). When the value of n approaches unity, the CPE is equivalent to a pure capacitor, if n approaches to 0, the CPE is equivalent to pure resistance, but with an n exponent closer to 0.5, the CPE value is indicative of diffusion processes and consequently, the CPE indicates a Warburg diffusion component [149-151].

R_{po} and CPE_c are related to the coating characteristics [23, 151, 152]; R_{po} represents the resistance to current flow through the pores, which can provide a measure of coating porosity and deterioration:

$$R_{\text{po}} = \frac{\rho d}{A} \qquad\qquad (3.3)$$

where ρ is the electrical resistivity of the electrolyte in the pores, *d* is the coating thickness and A is the total surface occupied by the pores. R_{po} thus tends to decrease with immersion time, as the electrolyte penetrates through the pores and/or columnar structure of the coating and reaches the coating/metal substrate interface (increasing the effective surface area in contact with the electrolyte). The decrease in pore resistance value can also be related to an increase in area *A* which relates to an increase in the number of pores (or in their size) if the coating is damaged. However, R_{po} can also be seen to increase with immersion time under certain circumstances, probably due to the deposition of corrosion products that can block the pores [150, 151].

The coating capacitance C_c is a measure of coating integrity and can be determined by the composition and structure of the coating material:

$$d = \varepsilon_r \varepsilon_0 A/C \qquad\qquad (3.4)$$

Here, ε_o is the permittivity of free space (8.854 x 10^{-12} F/m); ε_r is the permittivity constant of the coating material, *A* and *d* are the coating surface area and the thickness, respectively [23, 34, 151-153].

The charge transfer resistance R_{ct} and double layer capacitance C_{dl} represent the corrosion process of the coating at the coating/metal interface. R_{ct} is associated with charge transfer behaviour of the metal substrate. A C_{dl} exists at the electrode/electrolyte interface. This double layer is formed as ions from the solution approach the electrode surface. The magnitude of the C_{dl} is affected by

many variables include: electrode potential, type of ion, ions concentration, roughness of the electrode surface, ionic oxide layers and the electrolyte temperature [150, 154, 155]. The C_{dl} in Figure 3.3 can be charged and discharged like any other capacitor [154].
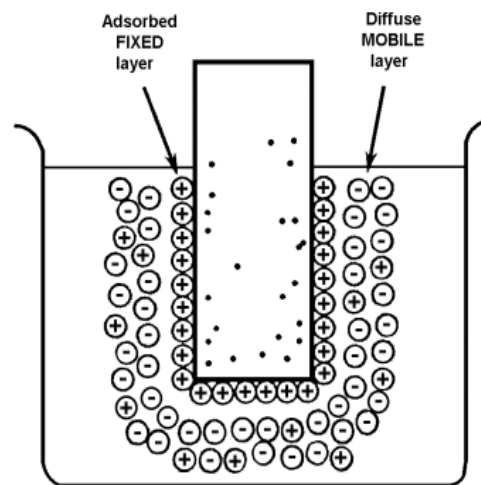
Figure 3.3: Schematic diagram of double layer capacitor [159].

3.2.3 Rapid Electrochemical Assessment of Paint (REAP)

Since not even conventional accelerated corrosion evaluation techniques are quick enough, several more rapid techniques have been developed in recent years to introduce aggressive conditions to accelerate the coating degradation. This has been driven the development of unconventional accelerated corrosion test techniques that can provide quantitative indications of corrosion damage in considerably less time than conventional test techniques.

In 1996, Kendig et al. [12] first proposed a rapid (about 24 h) electrochemical method that could combine EIS measurement with DC cathodic polarisation to

determine the 'time-to-failure' of a painted mild steel substrate. Since then his approach has been verified and expanded by other researchers [14, 85]. A Rapid Electrochemical Assessment of Paint (REAP) was proposed by Kendig, which is now being considered by ASTM as a standard, under ASTM G01.11, on electrochemical measurements in corrosion testing of painted steel [156]. REAP is a procedure designed to estimate the long-term corrosion resistance of coated metals using short-term electrochemical tests. It involves running a series of experiments (of about 24 h duration) on two or more samples.

3.2.3.1   REAP experimental procedure

In REAP testing the electrochemical cell shown in Figure 3.4 a) [157] was used to carry out the test. The evaluation of corrosion behaviour of the painted metal samples using REAP testing involves a combination of wide-frequency AC (as an electrochemical impedance spectrum (EIS) and DC cathodic polarisation over 24 h. The REAP testing procedure involves running a number of tests on at least two paint samples (preferably more). To evaluate the relative time to failure and rank the coating samples, a scribed sample with 2 x 2 cm right angle cross must be created, and the other sample remaining unscribed in case of testing two samples (Figure 3.4 b) [12]. The flat painted metal sample is fitted to a cell that contains a saturated calomel electrode (SCE) as a reference electrode, while the counter electrode can be graphite, platinum or any noble metal and the cell is filled with 0.5 M NaCl solution with an exposed area of 56 cm^2.
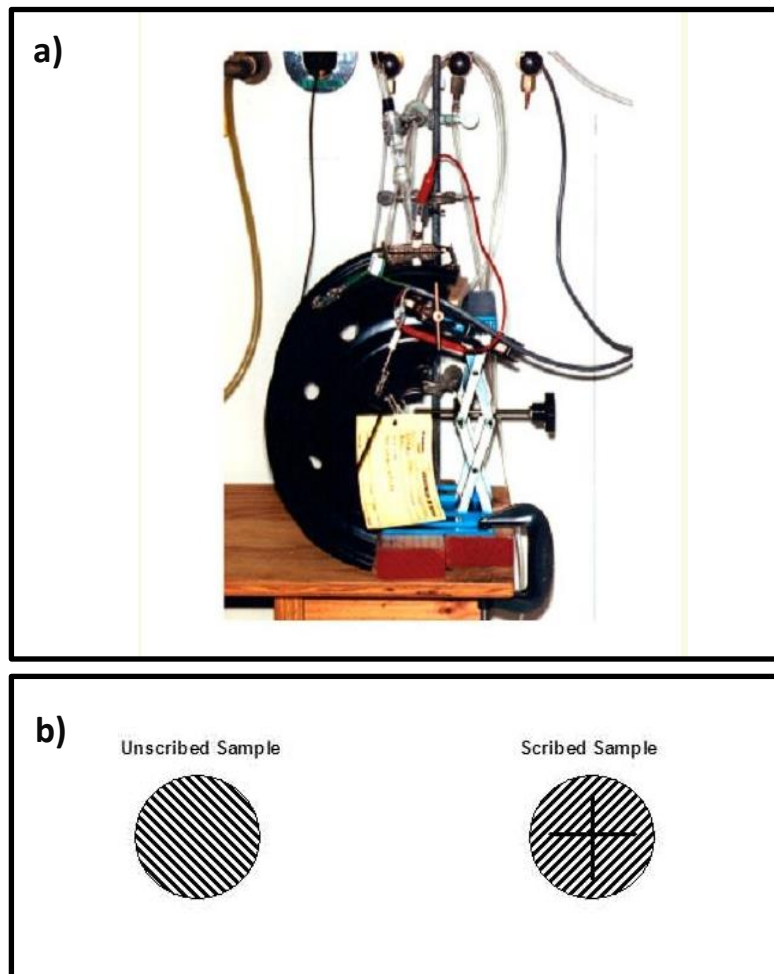
Figure 3.4: REAP experiment; a) rapid electrochemical assessment of paint cell [158] and b) painted metal samples [12]

Figure 3.5 [12] shows the schematic diagram of REAP testing, comprising the following steps :

I. Measuring the corrosion potential of the painted sample immediately after the cell is filled with salt solution.

II. EIS_0 at 0 h; an initial electrochemical impedance measurement to evaluate the effectiveness of the paint as a barrier before applying DC cathodic polarisation.

III. DC cathodic polarisation measurement -1.05 V (vs. SCE) , for 24 h applied to the scribed paint, to accelerate the disbonding of the coating.

IV.   EIS$_f$ at 24 h, to evaluate the efficiency of the coating ability to remain
      adherent under conditions of electrochemically accelerated corrosion, after
      applied DC cathodic polarisation for 24 h.
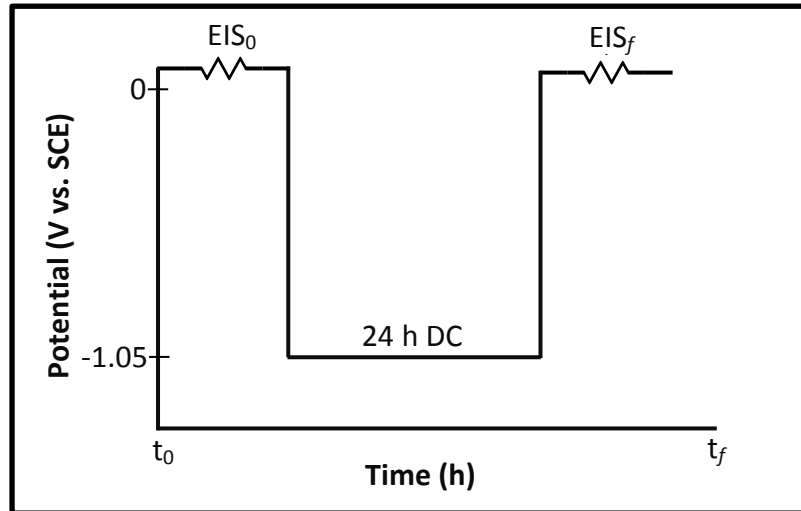
Figure 3.5: schematic diagram of REAP test procedure [12].

The results were then compared to conventional salt spray test results. The
outcome results of such comparative test method were an observed formula that
predicted the relative time to failure (TTF) of the coatings as a function of the
corrosion resistance (R_{cor}) measured after 24 h, the coating disbondment rate *dx/dt*
and coating permeability to the electrolyte [12, 128, 157].

3.2.4   REAP data analysis

3.2.4.1   Measuring coating disbondment rate dx/dt

The disbondment rate can be determined by the following relationship:

   dx/dt = Avg. width scribe mark (mm)/ total time (h)   (3.5)

After applied REAP testing for 24 h, the scribed painted sample is removed from
the cell and directly rinsed in deionised water and dried. Any loose coating around

the scribe is removed using a sharp edge, to make sure the damaged coating areas are completely removed. The average width can be measured using a ruler to measure the loosened coating area in several places. The default value of 10^{-4} mm/h is used in Kendig's standard, whenever no significant 'pullback' is observed [158].

3.2.4.2 REAP impedance (EIS) data ($C_{c,0}$, $C_{c,24}$ and R_{cor})

Analysis of EIS data of painted metal samples is achieved using a suitable equivalent circuit. The fitting results of the EIS data at 0 h as a starting point and the fit for the EIS data at 24 h as a final point. The considered elements of the electric circuit are coating capacitance at 0 and 24 h ($C_{c,0}$ and $C_{c,24}$). But for the corrosion resistance R_{cor} the value obtained at 24 h should be taken in to the account.

The obtained coating capacitance C_c is used to estimate the water uptake of the coating (i.e. the permeability) as volume percent (%v), which can be calculated from the following formula:

$$\%v = 100 \frac{log(C_{c,0}/C_{c,24})}{log(80)} \qquad (3.6)$$

The measured three REAP parameters (dx/dt, %v and R_{cor}) can predict the time-to-failure (TTF) of coating. Therefore, higher values of dx/dt and %v lead to shorter failure time, while higher values of R_{cor} lead to longer failure time. Considering the relative TTF in REAP testing can be used to compare several different types of coatings, which can reveal noticeable differences in disbondment rate. It is assumed that the 'best' coatings with lowest disbondment rate would be associated

to the low water uptake and high corrosion resistance [158]. It was found that the TTF is directly proportional to that obtained from salt spray test results [128].

3.3 (AC)/DC/AC cyclic testing

Hollaender et al. [13, 159] in 1997 used repeated cycles of electrochemical testing that combined DC cathodic polarisation and AC (EIS) measurements, initially for the testing of organically-coated metal surfaces in food packaging applications in a repeated sequence of (AC)/DC/AC procedures; this was successfully adopted by Suay et al. [85], 2003 on a liquid painted steel. In 2005, Poelman et al. [19], extended Suay's approach to investigate painted coatings on aluminium substrates.

3.3.1 Fundamentals of the (AC)/DC/AC cyclic testing

The (AC)/DC/AC test developed by Hollander is based on the influence of the cathodic reaction of water electrolysis that occurs when the potential is more negative than (-1V) vs. SCE[159]. Cathodic reactions at the coating/substrate interface produce H_2 gas and OH^- ions, which promote coating degradation. Evolving H_2 gas bubbles can lead to physical delamination, which gives rise to coating damage (reflected by the variations in EIS spectral response) [135]. When the cathodic reaction is terminated (and H_2 gas evolution has taken place), the normal electrochemical corrosion reactions of the coating system take place in the presence of an electrolyte with production of iron oxide and hydroxides [22, 148]. Figure 3.6 [160] shows the physical effect of the (AC)/DC/AC test on the coating.
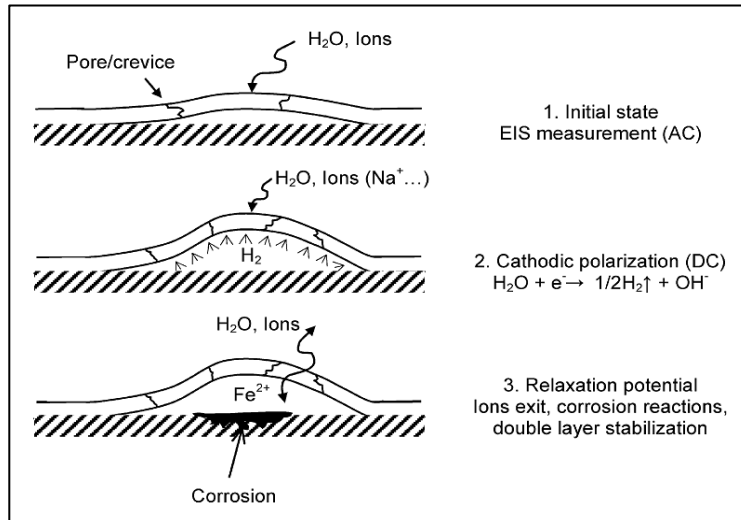
Figure 3.6: Schematic of the physical effects of (AC)/DC/AC cyclic testing on a coating [163]

The electrochemical cell setup used in AC/DC/AC experimental procedure is the same electrochemical cell used in REAP testing under the same conditions as described in the previous section. A schematic diagram of the (AC)/DC/AC test procedure is shown in Figure 3.7 [15]; it is used in repeated cycles for an extended period of time (almost 24 h) to accomplish the accelerated degradation of painted coating systems on steel. The (AC)/DC/AC test procedure consists of the following steps:

I.   Initial EIS step: AC measurement at the resting potential monitoring the painted metal system state at Open Circuit Potential (OCP) before applied DC cathodic polarisation.

II. DC cathodic polarisation step: which driven by applied a constant cathodic voltage (-2 V) for 20 min.

III. OCP step: potential relaxation for 3 h until the painted metal system reaches a new steady-state after DC cathodic polarisation.

IV.   Final EIS step: AC measurement is again applied to determine the new state of the painted metal system after the applied DC cathodic polarisation and relaxation cycle.
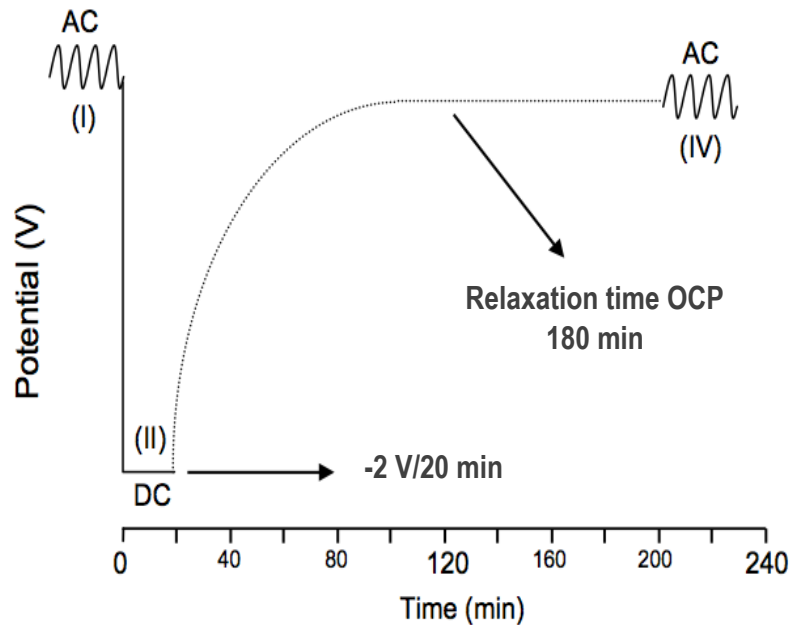
Figure 3.7: Schematic diagram of (AC)/DC/AC test procedures vs. time [15].

The test sequence (II-IV) is repeated several times in a very short time (almost 24 h) until the coating system is significantly damaged. This is a significant improvement when compared to traditional periodic EIS interrogation and conventional salt spray tests each of which require weeks or months of cumulative testing to give meaningful results. Depending on the coating quality, the number of cycles of (AC)/DC/AC could be increased and/or the relaxation time reduced (or extended) whilst the accelerated failure of the coating system is monitored periodically by the applied impedance measurements [22, 41, 135, 148, 160].

3.3.2   (AC)/DC/AC data analysis from the point of view of Suay's study

Experimental results of (AC)/DC/AC testing obtained by EIS measurements, DC cathodic polarisation measurements and potential relaxation OCP, which are fitted using a suitable equivalent circuit are shown in Figure 3.8 [85] and the potential relaxation time data is explained using the graph in Figure 3.9 [41].

The equivalent circuit below was used by Suay to model AC/DC/AC impedance data, where (R_s = electrolyte resistance, R_{po} = pore resistance, CPE_c = constant phase element of coating capacitance, R_p = polarisation resistance and CPE_{dl} = constant phase element of the double layer capacitance [85].
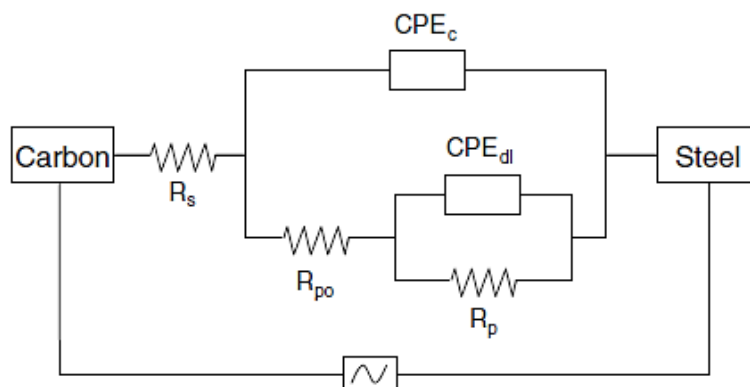
Figure 3.8: The equivalent circuit used to model AC/DC/AC impedance data [85].

During DC cathodic polarisation electrolysis of 3.5 wt. % NaCl solution occurs and the following process will take place during this step [35]:

a. Different cations (eg. H^+, Al^+) will be attracted to the cathode electrode and accumulate at the electrode/electrolyte interface, which can lead to a high concentration of the positive ions that may (depending on the film integrity)

pass through the paint film, due to the high negative potential imposed on the metallic substrate. This passage of positive ions through the paint film can cause its deterioration and initiate pore formation.

b. If the electrolyte passes through the coating and reaches the coating/metal substrate interface then cathodic reactions will take place producing H_2 gas and OH^- ions. This can depend on many coating properties (such as permeability to ions, adherence to the substrate and susceptibility of the coating to form cracks because of its rigidity on the substrate). Evolution of H_2 gas in this circumstance will cause physical deterioration of the coating and OH^- ions will increase the solution pH (alkalinity) at the coating/metal substrate interface.

Other information that the AC/DC/AC test can provide is from the evolution of open circuit potential (relaxation potential with time) after DC cathodic polarisation. However, the relaxation potential with time was added to the test procedure for the first time by Suay and co-workers [85]. When cathodic polarisation is terminated, the coated metal potential may be seen to relax according to two types of typical trend, depending on the quality of the coating (Figure 3.9) [41].
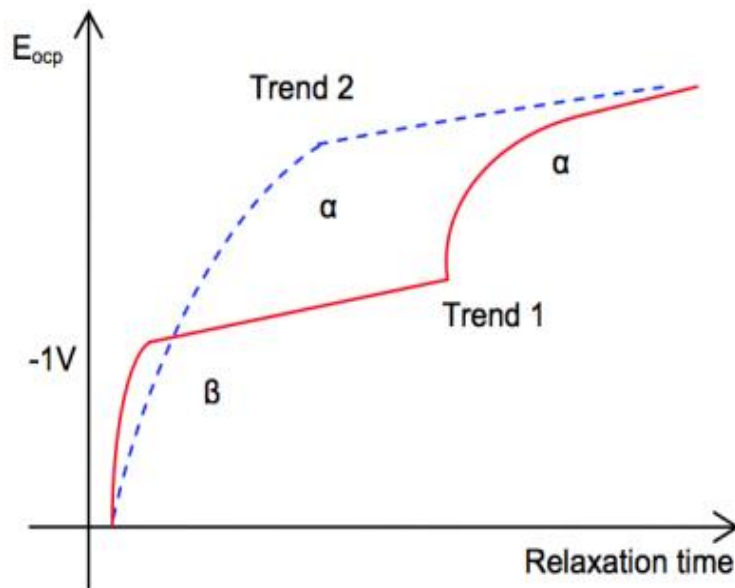
Figure 3.9: Typical trends of relaxation time OCP of organic coated steel [41].

a) Strongly degraded coating systems (trend 1), show two relaxation times (OCP) designated α and β. If the cathodic reactions were taking place at organic coating/metallic substrate interface, the potential will first show a rapid relaxation potential (β) beyond -1V. Afterwards, a second relaxation potential (α) represents the ion and electrolyte expulsion from the damaged coating.

b) Less degraded coating systems (trend 2), show just one relaxation time to OCP (α) which corresponds to ion and electrolyte expulsion from the coating and cathodic reactions in this case did not occur at the organic coating/metallic substrate interface [41, 152].

3.4 Development of (AC)DC/AC Test protocol for Metallic Coatings

3.4.1 Aim of the test development in this work

With the increasing demand for improved metallic engineering coatings for corrosion resistance, attempts to develop a nature (and variability) of test regime under static corrosion cell conditions before several advanced metallic coated steel are then will be evaluated and compared. However, the scientific literature gives little or no attention and consideration to the effect of experimental parameters such as solution pH on the rate of degradation of organic coated steels using the current (AC)DC/AC protocols; this in turn lends this technique to be considered imprecise and not fully trusted for practical results. Hence, the results obtained so far from (AC)DC/AC tests involve many assumed explanations with fictional physical interpretation. Therefore, it was very important in this work to take into account considerations to perform such a test method in a reliable, repeatable way, which importantly can give more precise details for electrochemical corrosion process at the coated steel/electrolyte interface during every step of test procedure to evaluate (and discriminate between) different compositions of metallic coating and substrate. Currently the use of (AC)DC/AC is limited only to the (rather subjective) evaluation of non-conductive coating materials on steel. In this work conducting the advanced (AC)DC/AC cyclic testing would be the first attempt for evaluating the electrochemical corrosion behaviour of conductive material rather than non-conductive material. This approach would appear to offer unique advantages over other   available corrosion techniques.

3.4.2 Experimental requirements and electrochemical cell design

A critical problem for any experimental analysis is the validity of the data determined. In proper use of experimental procedures protocols by numerous engineering experimental designers is a common occurrence [161]. Developing an experimental protocol that can enhance the validity, reliability and clarity of corrosion data leads to much easier analysis and interpretation of obtained results [162]. For a long-time of using the (AC)DC/AC technique for evaluating the corrosion degradation of organic coated steels, the understanding of obtained results was incomplete because of the missing measurement of changes occurring during the DC step and the measurement of solution pH evolution during the test procedure, despite such factors being strongly indicative of the development coating permeability and inducing the degradation of organic coating on steel. However, in order to avoid misleading interpretations, modifications on the electrochemical cell design for measuring the effect of solution pH was the first target in this work. Therefore, the experimental procedure was carried out using a pH meter with probe that was integrated with the electrochemical cell construction, in which connection to pH software for monitoring and recording of solution pH allowed real time test measurements.

Chapter Four

Experimental Techniques

4.1   Introduction

This chapter describes the techniques used to evaluate the corrosion behaviour of Al 6082 alloy and PVD Al-based coatings; specifically, a newly developed (AC)DC/AC cyclic test method used for the first time to evaluate the corrosion behaviour of metallic, electrically conducive coating materials, incorporating parallel studies of the role of solution pH. Two main experimental sets were carried out to achieve the objectives of this thesis. First, the corrosion behaviour of Al 6082 alloy and different PVD Al-based coatings (AlCr, AlCr(N) and AlCrTi) deposited on 17/4 PH stainless steel substrate was evaluated using advanced (AC)DC/OCP/AC cyclic testing. Potentiodynamic (PTD) polarisation, Open Circuit Potential (OCP) and Electrochemical Impedance Spectroscopy (EIS) were studied. Second, the effect of solution pH on the electrochemical reactions was simultaneously recorded while conducting the electrochemical tests (E_{OCP} and (AC)DC/OCP/AC). In addition, the experimental work involved coating characterisation (phase composition, structure and corrosion properties of the samples above coating) which was investigated 'as received' and after six successive cycles of (AC)DC/OCP/AC using Scanning Electron Microscopy (SEM) and Energy Dispersive X-Ray (EDX) analysis.

4.2 Experimental Materials

Different metallic, electrically conductive systems were investigated in this work, including; uncoated Al 6082 alloy (to establish test protocols and repeatability) and PVD Al-based coatings (AlCr, AlCr(N) and AlCrTi) deposited on 17/4PH stainless steel substrate (to demonstrate the ability of the optimised test protocol to discriminate between different behaviour of electrically-conductive coatings).

a) The substrate

In this work the steel substrate used is a well-known martensitic stainless steel precipitation hardening 17/4 PH. The name comes from the key addition of 17% chromium and 4% copper due to an ability to obtain a combination of high strength, hardness and fracture toughness through flexible heat treatment paths (whilst maintaining high corrosion resistance) 17/4 PH steel is used widely in various industrial sectors, such as aircraft structures, steam turbine components, energy applications, offshore oil and gas and load-bearing applications in marine sector. 17/4 PH steel is significantly more noble than (for example) mild steel and M2 tool steel. The nobility of 17/4 PH can be attributed to the chromium and nickel content in its composition, which (depending on heat treatment) raises the electrochemical potential of the 17/4 PH steel to less negative values. A summary of the chemical composition (wt. %) of 17/4 PH steel substrate is presented in the Table 4.1 [37].

Table 4.1: The chemical composition of 17/4 PH steel [37].

Substrate	Fe	C	Mn	P	S	Si	Cr	Ni	Cu
wt. %	Balance	0.07	1	0.04	0.03	1	15.0-17.5	3.0-5.0	3.0-5.0

b) Al 6082 alloy

Aluminium 6082 alloy was employed to evaluate its corrosion behaviour for the first attempt of using advanced (AC)DC/OCP/AC cyclic testing. Al 6082 alloy selected to be evaluated because it is a well proven medium strength alloy with excellent corrosion resistance that satisfies the requirements of most applicable alloy and number of specifications that used in automotive and aerospace applications [161]. It also provides the opportunity to test the effects of a dielectric oxide layer, without the complication of galvanic coupling of a coating to a steel substrate. Figure 4.1 shows the Al 6082 alloy test used for this work disc (diameter 30 mm). Samples were ground and polished to achieve a mirror surface finish (Ra ≈ 0.40 μm), then ultrasonically cleaned in isopropanol for 10 minutes. A summary of the chemical composition (wt. %) of Al 6082 alloy is given in Table 4.2. [162].

Figure 4.1: Al 6082 alloy disc sample.

Table 4.2: Chemical composition of Al 6082 alloy [167].

Element	at. %
Silicon (Si)	0.70 – 1.30
Magnesium (Mg)	0.60 – 1.20
Manganese (Mn)	0.40 – 1.00
Iron (Fe)	0.0 – 0.50
Chromium (Cr)	0.0 – 0.25
Zinc (n)	0.0 – 0.20
Titanium (Ti)	0.0 – 0.10
Copper (Cu)	0.0 – 0.10
Others (in total)	0.0 – 0.15
Aluminium (Al)	Balance

The effect of alloying elements such as Mg included in Al alloys is in improving the corrosion resistance even though its electrode potential is more negative than that of Al (this is primarily) because Mg stabilises and increases the thickness of the naturally-occurring oxide film. The addition of Mn to Al alloys controls the grain size, which in turn results in a harder alloy. Adding Si, Cr and Ti improves the corrosion resistance because of their nobility [67, 78].

c) PVD Al-based Coatings

Figure 4.1 shows the PVD Al-based coatings disc with diameter 25 mm, which used for this study. PVD Al-based coatings AlCr and AlCr(N) were deposited on 17/4 PH substrate discs of 25 mm diameter by electron beam (EB) plasma-assisted (PA) physical vapour deposition (PVD) using a twin-EB PAPVD system (modified Tecvac IP70L) with separate Al and Cr vapour sources. An AlCrTi coating was also deposited using multi-target magnetron sputtering (three pairs of horizontally-opposed Al, Cr and Ti sputter targets). The previously ground and polished 17/ PH steel substrate was ultrasonically cleaned in acetone and isopropyl for 10 minutes

and dried. In the EBPVD process, the substrate was attached to a rotating holder about 170 mm from the rotation axis to ensure better homogeneity in coating thickness and composition of deposited material. The distance of the crucible-substrate was constant at 25 cm.
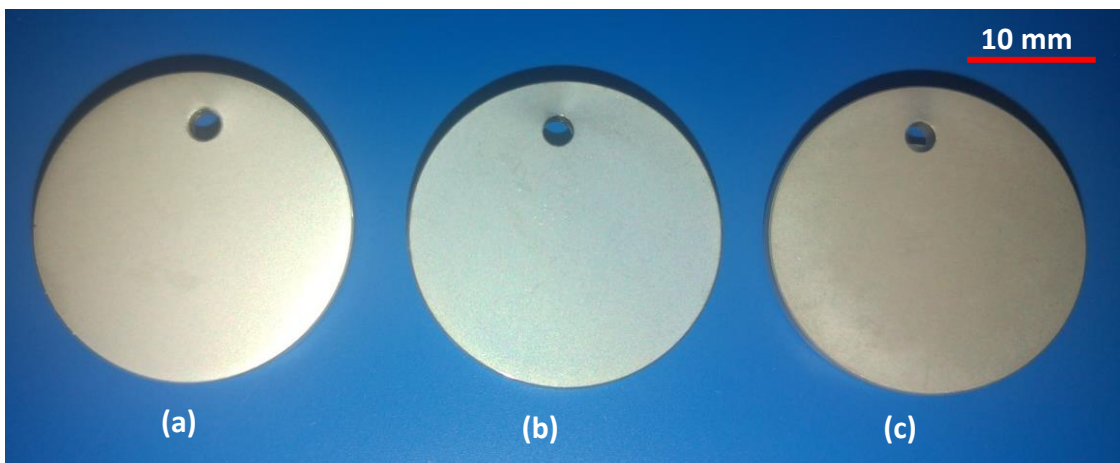
Figure 4.2: PVD Al-based coatings a) AlCr, b) AlCr(N) and c) AlCrTi.

EBPVD coatings of AlCr and AlCr(N) were deposited at 300° C, while the sputtered AlCrTi coating was deposited at 180° C substrate temperature. The deposition of was in pressure of an ionised argon gas at about o.3 Pa for AlCr, 0.5 Pa for AlCr(N) and AlCrTi in total mass flow about 45 ml/min. The deposition of AlCr coated 17/4 PH steel used in this study was carried out by mixing of vapour flux of evaporant source pure materials (80 at. % Al and 20 at.% Cr) from two separate crucibles by controlling the current flow in both crucibles and monitoring the actual evaporating rates via optical emission spectroscopy (OES) of single spectra line that generated in ionised vapour flux. Whilst, the deposition of AlCr(N) coated 17/4 PH steel was carried out by mixing of vapour flux of evaporant source of pure materials (75 at.% Al and 15 at.% Cr) in the presence of a partial pressure of nitrogen gas at flow rate

of 5 ml/min. Whereas, the deposition of AlCrTi coated in this study was carried out by mixing of vapour flux of evaporant source pure materials (75 at. % Al, 15 at. % Cr and in addition 5 at.% Ti). The AlCrTi coatings were deposited on the 17/4 PH steel substrate by magnetron sputtering using 6 targets of pure metals so 2x Al targets, 2x Cr targets and 2x Ti targets. The workpiece voltage was 30V and the base pressure 5 x 10^{-3} mbar. The addition of Ti promotes the formation of a TiO_2 layer over Al_2O_3 resulting in superior corrosion resistance. The chemical composition and deposition conditions of three PVD Al-based coatings are presented in table 4.3.

Table 4.3: Chemical composition and deposition condition of PVD Al-based coatings

Sample coating	Process Temperature (° C)	Actual Al at. %	Actual Cr at. %	Actual N at. %	Actual Ti at. %
AlCr	300° C	80	20	0	0
AlCr(N)	300° C	75	20	5	0
AlCrTi	180° C	75	20	0	5

4.3   Microstructural Analysis Preparation

Evaluation of surface morphology of Al 6082 alloy and of cross-sections of the PVD Al-based coatings was carried out by successive grinding with 120, 240, 800, 1200 and 2500 grit emery paper, followed by polishing with diamond paste (6 and 1 μm). The mounting of PVD Al-based coating cross-sections was carried out by non-ferrous cutting wheel prior to the hot mounting in carbon conductive epoxy resin.

4.4   Coating phase analysis and structural characterisation

4.4.1   X-Ray Diffraction XRD

X-Ray diffraction is a commonly used technique in determining the phase composition of Al 6082 alloy and PVD Al-based coatings. A Siemens D5000 X-Ray diffractometer with (Cu Kα radiation, λ = 1.54 Å) operated at 40 kV acceleration

voltage and 30 mA filament current was used to obtain XRD patterns. Standard coupled θ-2θ scans were set up in a 2θ range of 20° to 90° with 0.02° step size and 1 sec dwell per step.

4.4.2 Scanning Electron Microscopy SEM

The surface morphology of Al 6082 alloy and PVD Al-based coatings as received and after exposure to six cycles of DC/OCP were characterised using Scanning Electron Microscopy (SEM, JEOL-6400) with an operating voltage of 20 kV.

4.4.3 Energy Dispersive X-Ray (EDX) Spectroscopy

The chemical composition of Al 6082 alloy and PVD Al-based coatings as received and after exposure to six cycles of DC/OCP was determined using (SEM, JEOL-6400) linked to INCA software® that operated the EDX spectroscopy, which is used to determine and quantify the coating composition. The function of EDX linescan-profile is used to study the distribution of the distribution of constituent elements on both surface and cross-sectional images.

4.5 Electrochemical Cell and Electrolyte

Electrochemical tests were carried out in a conventional three-electrode electrochemical cell, with the coated sample as the working electrode. An area of 0.432 cm^2 is exposed to the electrolyte using an inert O-ring fixed underneath the corrosion cell; a platinum rod was used as the counter electrode and saturated calomel electrode SCE of (Hg/Hg$_2$Cl$_2$/KCl sat.) was used as the reference electrode. This cell consists of a (electro-) chemically inert container, which is attached to the coating surface and with an electrolyte capacity of 0.2 l. The electrolyte (3.5 wt. %

NaCl neutral salt solution), was prepared by dissolving 34 g of reagent grade sodium chloride in 920 ml deionised water, following ASTM G44-99 standard test procedure used for electrochemical testing [163]. Fresh solution was used during all electrochemical experiments which were maintained at room temperature under laboratory conditions at all times.

4.5.1 Measurement of solution pH

The solution pH of the electrolyte was measured during the E_{OCP} and (AC)DC/OCP/AC cyclic testing using potentiometer pH meter HANNA-210® using a glass probe (HI-1131) filled with neutral KCl solution buffered pH 7 and contains Ag/AgCl wire forms the electrical connection and the pH data was monitored and collected using proprietary National Instruments software.

4.6 Corrosion Evaluation Techniques

4.6.1 Open circuit potential

Open circuit potential (E_{OCP}) measurement is the simplest electrochemical technique for evaluation and study of changes in corrosion behaviour with increasing exposure time. E_{OCP} can measure the potential of the working electrode respect to the reference electrode, when no external polarisation or current flows from or to it. The fundamental principle of E_{OCP} is that a shift in potential in the cathodic direction is a sign of active corrosion, while a shift in the anodic direction is an indication of ennoblement (passivation or film formation). All coated samples were monitored for 3 h E_{OCP} to study their corrosion potential with respect to the reference electrode; E_{OCP} measurements were carried out using a Solatron SI 1286 potentiostat. Furthermore, stable E_{OCP} measurements can be employed as an initial

(starting) potential before conducting any other tests (such as potentiodynamic polarisation and Electrochemical impedance spectroscopy EIS) or as a means to establish a relaxation time for provoke coating system after applied DC cathodic polarisation, when conducting advanced (AC)DC/OCP/AC cyclic testing.

4.6.2   Potentiodynamic polarisation

Potentiodynamic polarisation (PTD) measurement is the most commonly used electrochemical corrosion technique [164]. PTD measurements were used to evaluate the corrosion behaviour of the coated samples in anodic polarisation scans by determining the corrosion current density (i_{corr}). The potential is scanned from (or near to) the OCP potential to a more anodic potential. The corrosion current density increases after the scanning system passes the corrosion potential, then the coating starts to corrode. A Solatron SI 1268 electrochemical interface potentiostat was used for PTD measurements to determine the corrosion rate. All coated samples were polarised at a scan rate of (1.667 mV/s) from -300 mV vs. OCP to 0 mV (vs. SCE) in 3.5 wt. % NaCl solution. In PTD measurements, the corrosion current represents the rate in ($\mu A/cm^2$), at which anodic and cathodic reactions are taking place on the working and counter electrodes. The current density is expressed in terms of the current per unit area of working electrode and can be determined using the obtained polarisation curves based on Tafel extrapolation. The current corrosion density can be expressed as function of polarisation (η) by the following relationship:

$$\eta = \beta \, log \frac{i}{i_0} \qquad\qquad (4.1)$$

Where $\eta = E_{applied} - E_{OCP}$, β is the Tafel slope, i the applied current density and i_0 the change in current density. Polarisation increases with increasing corrosion current density.

The corrosion potential (E_{corr}), corrosion current density (i_{corr}), and anodic/cathodic linear Tafel slopes (βa and β_c) were identified and calculated using the CorrWare software® supplied and marketed by Scribner Associates, Inc. Polarisation resistance (R_p) was determined by the following equation:

$$R_p = \frac{\beta_a \text{ X } \beta_c}{2.3 \text{ x } i_{corr} \, (\beta_a + \beta_c)} \qquad (4.2)$$

To estimate the corrosion rate of the coated sample, Faraday's law (eq.4.3) can be employed such that, in terms of the mass loss rate:

$$CR = \frac{M}{nF\rho} i_{corr} \qquad (4.3)$$

Where CR is the corrosion rate (mm/yr), M atomic weight of metal (g), n is the number of electrons transferred in the dissolution reaction, F is Faraday's constant (93,485 C/mol), ρ is metal density (g/cm^3) and i_{corr} is the corrosion current density (μA/cm^2).

4.6.3 Electrochemical impedance spectroscopy

In recent years, electrochemical impedance spectroscopy (EIS) has been developed and used for measuring and studying the electrochemical corrosion process and mechanisms. EIS can provide quantitative measurements on corrosion resistance of coated metals. In this work a Solatron SI 1286 electrochemical interface and SI 1260 Impedance/Gain Phase Analyser that shown in Figure 2.10 p31 were used to perform electrochemical impedance tests. A sinusoidal AC perturbation of 10mV AC

signal was applied to the working electrode at (previous potential mode) over a range of frequencies from 10^{-2} to 10^{5} Hz [140, 165]. Obtained EIS data were presented in terms of Bode plots (log of |Z| and phase angle as functions of log frequency f). The impedance spectra were collected and analysed using Z-plot® and Z-view® software (Scribner Associates).

4.7 First use of advanced (AC)DC/OCP/AC for evaluation the corrosion of metallic material.

The experimental equipment and modified electrochemical cell with pH kit used in this work are illustrated in Figure 4.3.
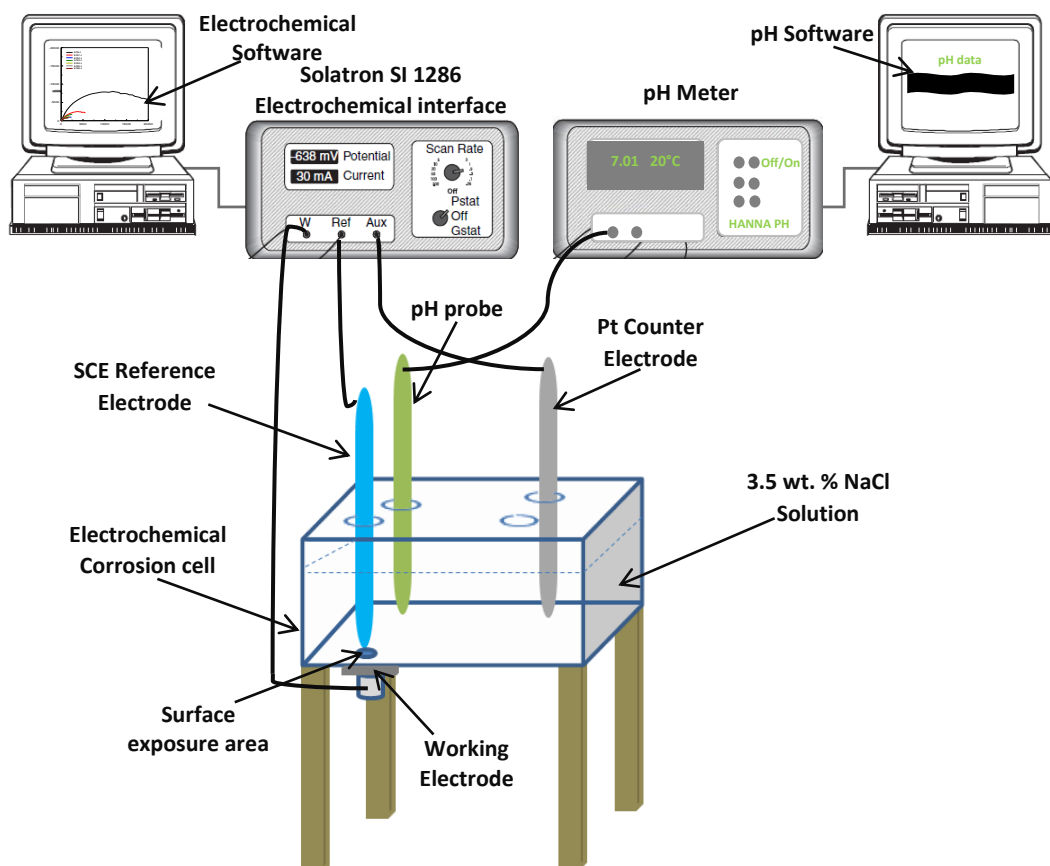
Figure 4.3: Schematic modified electrochemical cell configuration for advanced (AC)DC/OCP/AC cyclic testing coupled with solution pH measurement kit.

Measuring solution pH and collecting data after composed solution pH measuring kit to electrochemical experimental design were carried out with the same parameters and procedure of (AC)DC/OCP/AC cycling testing that used to evaluate the organic coated steel.

In this work (AC)DC/AC cyclic test procedure (Figure 3.7) [15] was developed by augmented with an incorporating solution pH measurement as shown in Figure 4.4, in order to study the effect of solution pH on the degradation of the coating concurrently with conducting the advanced (AC)DC/OCP/AC cyclic test procedure, which perform as the following steps:

I. 2 h open circuit potential E_{OCP} exposure to 3.5 wt. % NaCl solution prior to starting (AC)DC/OCP/AC test ensures that a steady-state is established for the potential.

II. AC_i step: an initial EIS measurement applied respect to the reference electrode SCE to establish as-received state of the coating system before applying DC cathodic polarisation for 15 minutes.

III. DC_n step: A high cathodic potential -2V vs. SCE is applied for 20 minutes for where electrolysis process generates hydrogen evolution and OH^- ions.

IV. OCP_n step: A stabilisation period following the application of DC cathodic polarisation, where the sample is left to relax at its resting potential for 3h, to reach E_{OCP} after applied DC cathodic polarisation.

V. AC_n step: The same initial (AC) step is repeated to obtain information on the new steady-state OCP condition of the sample after applied DC cathodic polarisation.

Where, n is the number of applied cycle.
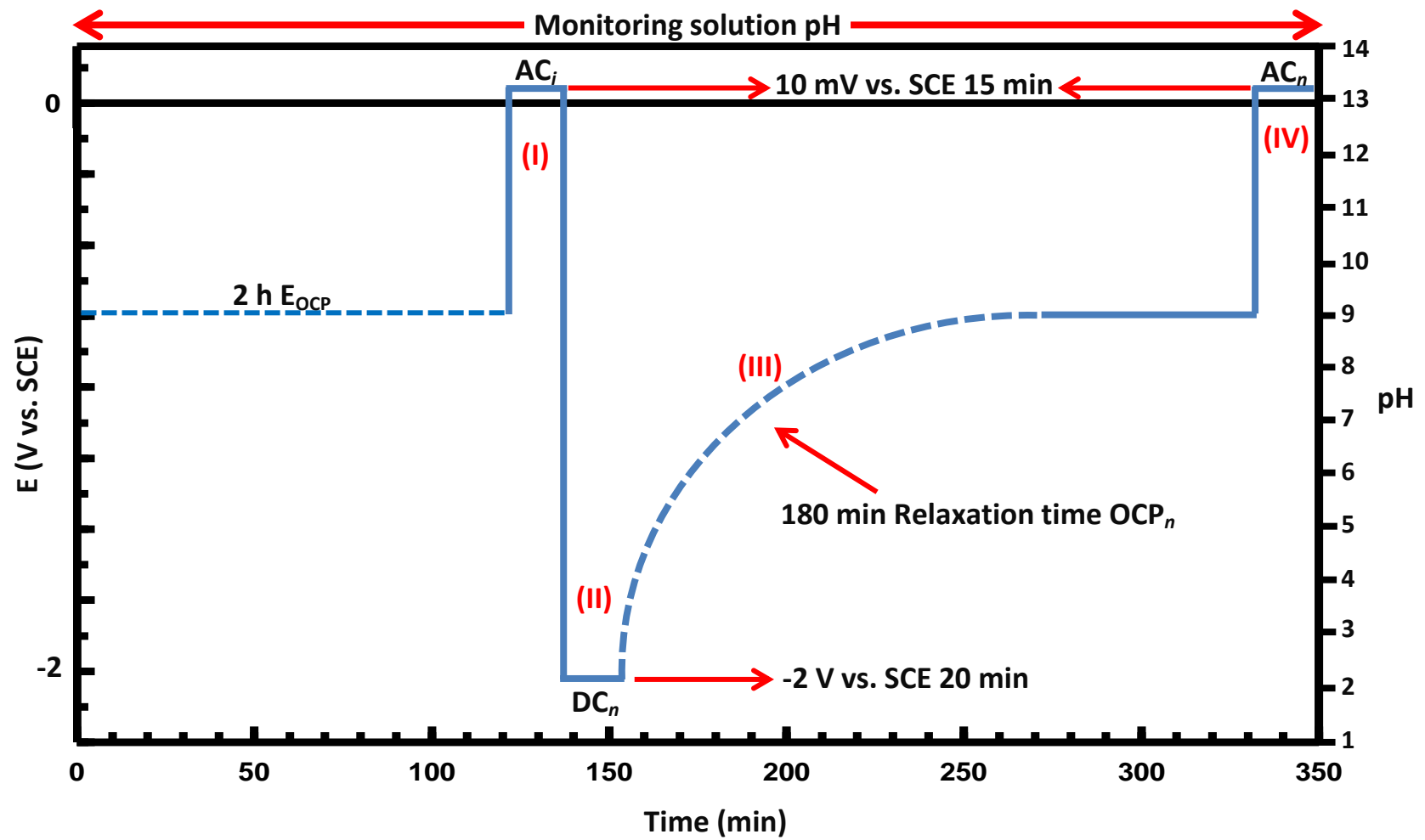
Figure 4.4: Schematic diagram of advanced (AC)DC/OCP/AC test procedure with incorporating solution pH measurement (after Ref.[15]).

The sequence of DC/OCP/AC was repeated six times (for around 24h in total) to trace the degradation path of the sample using an AC impedance spectra obtained after each DC-polarisation/OCP-relaxation cycle. The examination of changes at the electrolyte/metal interfaces, under the effect of fluctuating pH during the applied (AC)DC(OCP)/AC cyclic test procedure were measured by pH probe.

For performing the repeatability of the advanced (AC)DC/OCP/AC cyclic testing, experiments were carried out on three trial samples of Al 6082 alloy to ensure that the electrochemical corrosion process during (AC)DC/OCP/AC cyclic testing for each sample is having the same manner under the same conditions with measuring solution pH and presenting same results. Therefore, reason for performing the repeatability tests was to check the accuracy and reliability of the test parameters, procedure and instruments before extending to assess other metallic coatings in particular the complex metallic coatings.

Al 6082 alloy sample was selected in this study to be tested for the first attempt of using an advanced (AC)DC/OCP/AC cyclic testing to evaluate the electrochemical corrosion behaviour at the conductive material/electrolyte interface. However, the reason behind the selecting such "commercial Al-alloy" as a sample is the simplicity need for conducting and interpretation of the obtained results, rather than selecting a complex conductive material (such as an electrically conductive metallic coated metallic substrate), that consists of three different layers includes: (i) metallic substrate (ii) metallic coating and (iii) native oxide film. Therefore, selecting simple conductive metal would be better for the first use of the advanced

(AC)DC/OCP/AC technique to obtain an easy and better understanding of the electrochemical corrosion behaviour process and to be reliable to evaluate the complex samples.

In order to verify the validity and reliability concerns of (AC)DC/OCP/AC cyclic testing, the repeatability of the test was carried out on Al 6082 alloy for three runs. Thus, the first run was designed as R_1, the second run R_2 and the third run R_3. The (AC)DC/OCP/AC test procedure consisted of a sequential combination of DC cathodic polarisation, OCP potential relaxation time and AC impedance spectroscopy measurement (EIS), applied over successive six cycles on Al 6082 alloy sample for period of time almost 24 h.

Chapter 5

Development of advanced (AC)/DC/OCP/AC cyclic testing to evaluate the corrosion behaviour of uncoated electrically-conductive substrates

5.1 Introduction

The aim of the work in this chapter was to establishing a reliable and repeatable accelerated test protocol to evaluate the corrosion behaviour of electrically-conductive substrates carried out simultaneously, with solution pH measurement. Incorporating real time pH solution measurement concurrent to (AC)DC/OCP/AC test procedures can provide information that would be useful to follow the mechanism underlying the corrosion of the metal, to gain insights regarding the electrochemistry of the corrosion processes through every step of the test procedure. However, the literature lacks information on the effects of experimental parameters such as solution pH simultaneously with cyclic electrochemical test procedures and little or more information exists on the corrosion behaviour of electrically-conductive substrates and/or coatings in the types of accelerated cyclic test regimes previously investigated.

(AC)DC/OCP/AC cyclic testing was carried out in three samples of Al 6082 alloy by three different runs (R_1, R_2 and R_3). The obtained test results retrieved from the experimental work are carried out and presented into two main sets; I) electrochemical results obtained at E_{OCP} and repeated (six-cycles) of

(AC)DC/OCP/AC cyclic testing and ii) solution pH results during continuous monitoring of electrochemical test procedure. In addition, the structure and composition of these samples were examined using XRD, SEM and EDX. The results are later used to evaluate the electrochemical corrosion behaviour of Al 6082-alloy samples induced by the DC/OCP cycles, to try to establish a correlation between the obtained test results of (AC)DC/OCP/AC and the parallel solution pH measurement.

5.2 Phase Composition Analysis and structural Characterisation

5.2.1 Phase composition analysis

The phase composition analysis was conducted by x-ray diffraction as described in Chapter 4. In Figure 5.1 the XRD pattern of Al 6082 alloy exhibits two high intensity peaks at 38° and 45° and a very weak peak at 84°, are indicative to FCC-aluminium. Other weak peaks are observed at 34° for Mn, 37° and 43° for Mg and at 40° for Si.
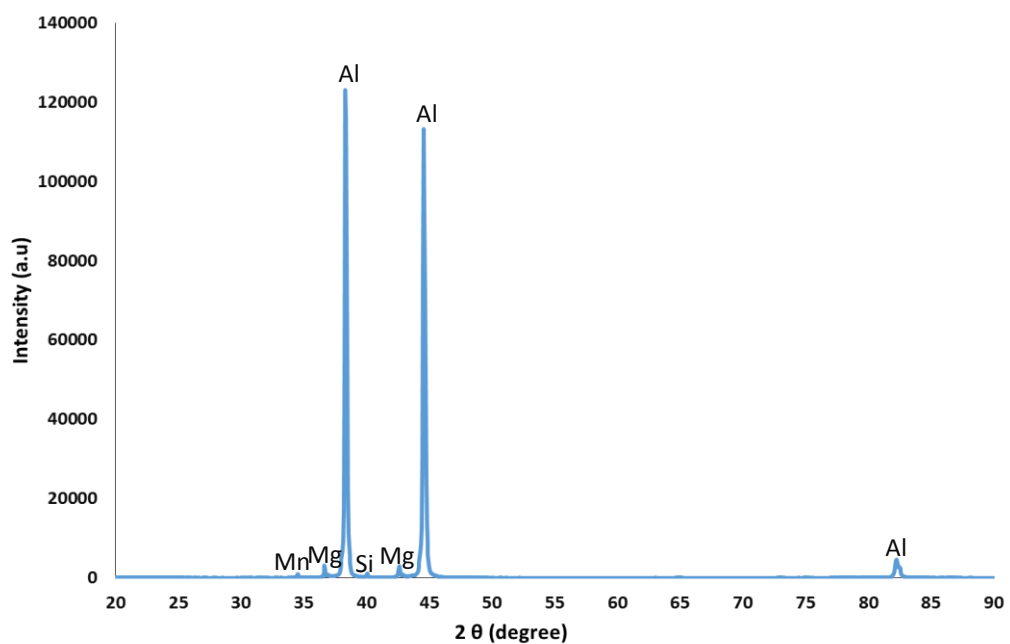
Figure 5.1: X-ray diffraction pattern of Al 6082 alloy.

5.2.2 Structural characterisation

Three Al 6082 alloy samples were analysed by SEM and EDX in order to identify their structural characteristic (surface morphology and composition) before and after six applied cycles of DC/OCP when exposed to 3.5 wt. % NaCl solution. The SEM micrograph and EDX analysis of the as-received Al 6082 alloy sample are shown in Figure 5.2 (a-b) respectively. The SEM micrograph exhibits a surface morphology free from any pits or cracks; some small polishing scratches are visible on the surface, which were formed during the sample preparation. The EDX spectrum of as-received Al 6082 alloy (with inserted table of the chemical composition) is presented in the Figure 5.2 (b).
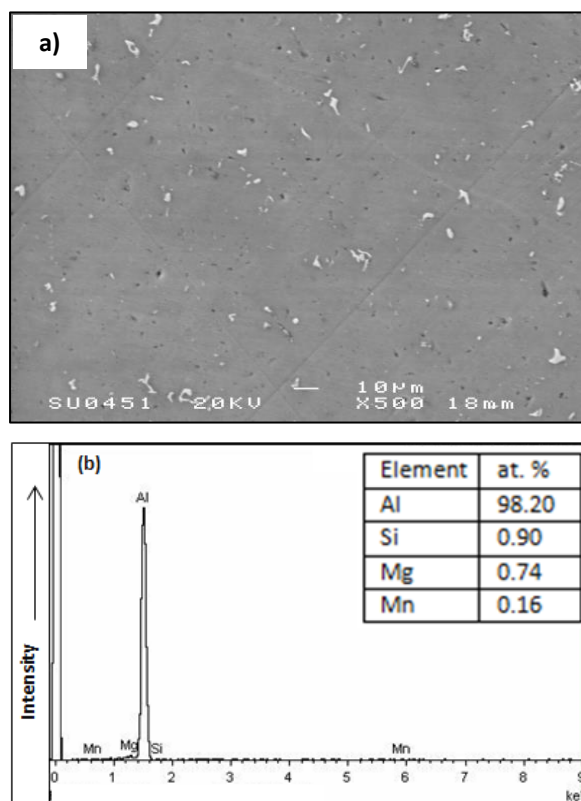
Figure 5.2: SEM & EDX analysis of as-received Al 6082 alloy a) SEM surface plane micrograph, b) EDX spectrum analysis with inserted table of chemical composition.

EDX analysis exhibited highest intensity peak for Al with 98.20 at % and small peaks of Mg, Mn and Si.

Figure 5.3 (a-d) shows the SEM micrograph with EDX analysis of corroded Al 6082 alloy during the first run R_1 after six successive DC/OCP cycles. Figure 5.3 (a) shows the SEM micrograph of the surface morphology that reveals some corrosion features and products of pits and crevice corrosion surrounded with white precipitation of $Al(OH)_3$. The corresponding EDX spectral analysis of corroded Al 6082 alloy during R_1 is presented in Figure 5.3 (b) with inserted Table of the chemical composition. From the inserted table it can be observed that that highest content is observed for Al about 65.13 at. % and O about 33.43 at.% which emphasizes the existence of corrosion products such as $Al(OH)_3$, which appear as white pustules around the pits.

Figure 5.3 (c) shows the SEM micrograph overlaid with EDX linescan-profile of ~ 150 μm length. Figure 5.3 (d) shows the revealed EDX linescan-profiles for the constituent elements of corroded Al 6082 alloy after six successive DC/OCP cycles. The profile analysis indicates a high signal intensity of Al which emphasizes that Al is the main element in the alloy lattice, while low signal intensity observed around the pits is associated with redeposited aluminium in hydroxide form. The Mg, Mn, and Si signal intensities are very low and indistinguishable with the energy resolution of the EDX detector. In contrast, no signal is observed from the EDX detector over the pits, which can be related to the deep cavities that the pits caused.
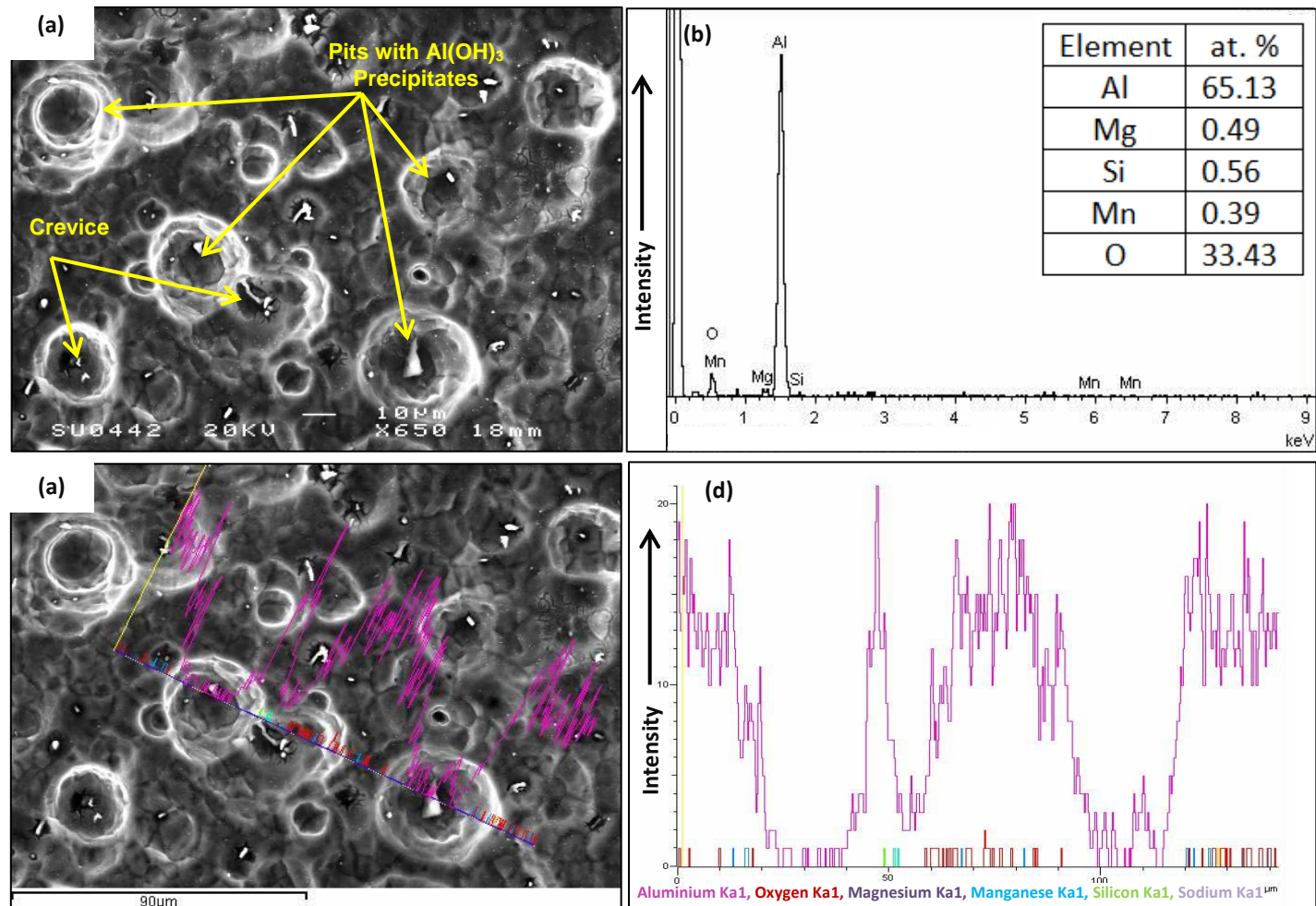
Figure 5.3: SEM & EDX analysis of corroded Al 6082 alloy during R_1 after six successive DC/OCP cycles a) SEM surface plane micrograph, (b) EDX spectrum analysis with inserted table of chemical composition, c) SEM micrograph overlaid with EDX linescan-profile and d) EDX linescan-profile of the distribution of constituent elements.

The SEM micrograph with EDX analysis of corroded Al 6082 alloy during the second run R_2 after applied six DC/OCP cycles are presented in Figure 5.4 (a-d). The Figure 5.4 (a) shows the SEM micrograph of the surface morphology Al 6082 alloy during R_2 that reveals more pits and crevices corrosion surrounded with much more white precipitation of $Al(OH)_3$. Some mud cracks on the surface plane are also revealed. The corresponding EDX spectra analysis of corroded Al 6082 alloy during R_2 after six successive DC/OCP cycles is presented in Figure 5.4 (b) with inserted table of the chemical composition. From the inserted table it can be observed that the content of Al and O are high, which emphasizes the re-deposition of $Al(OH)_3$ layer after Al dissolved in R_2 is high than that in R_1. This explains that Al 6082 alloy during R_2 is corroded more than Al 6082 alloy during R_1 after six successive DC/OCP cycles (if they compared).

SEM micrograph presented in Figure 5.4 (c) shows the overlaid with EDX linescan-profile of ~ 150 μm length. The EDX linescan-profile in Figure 5.4 d reveals the constituent elements of corroded Al 6082 alloy, which exhibits a high signal intensity of Al which emphasizes the main element in the alloy lattice is Al, while low signal intensity observed around the pits associated with aluminium deposited in hydroxide. Very low signal intensities are observed and indistinguishable with the energy resolution of the EDX detector associated with the Mg, Mn, and Si. In contrast, no signal observed from the EDX detector over the pits, which can be related to the cavity that pits caused.
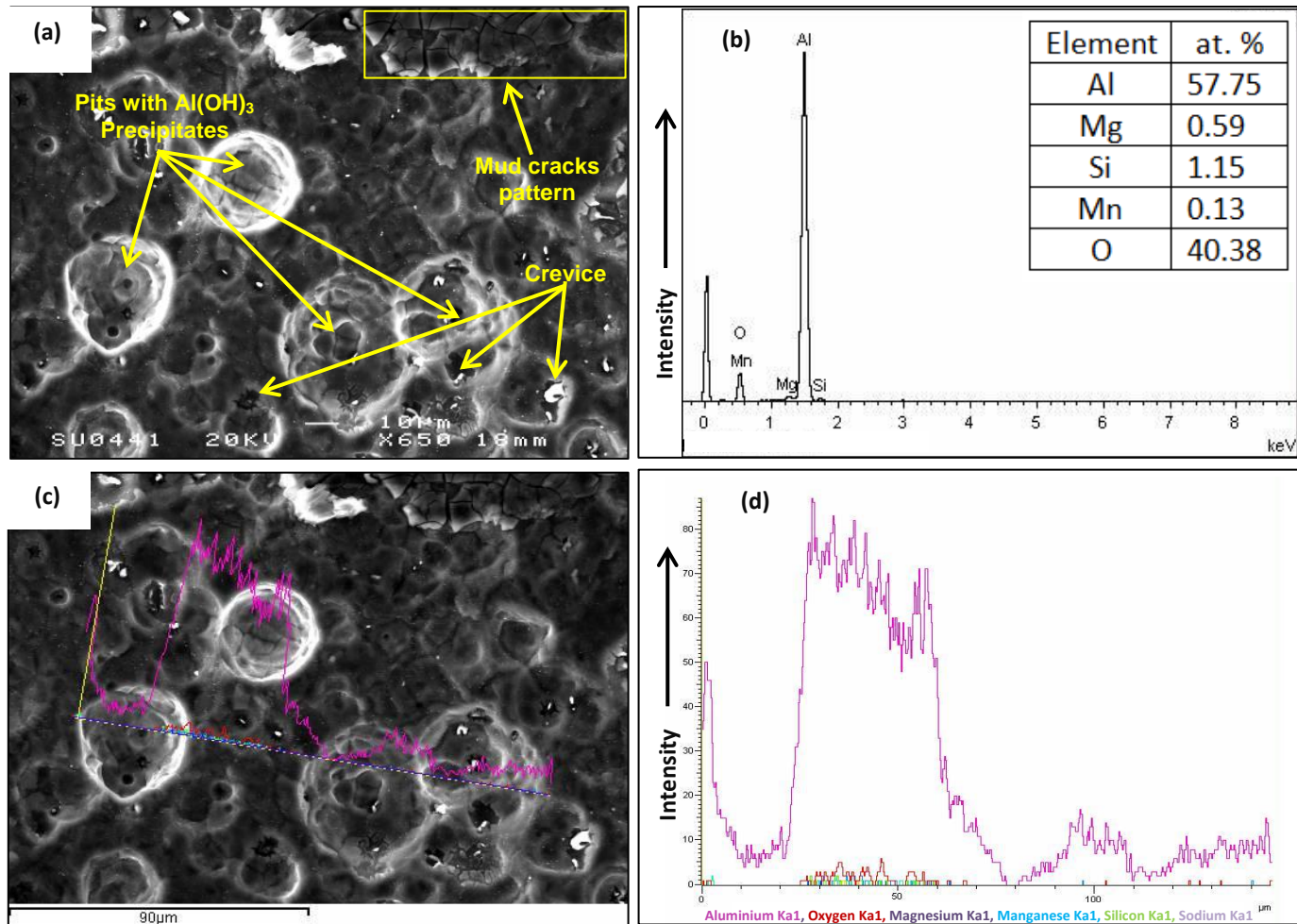
Figure 5.4: SEM & EDX analysis of corroded Al 6082 alloy during R_2 after six successive DC/OCP cycles a) SEM surface plane micrograph, (b) EDX spectrum analysis with inserted table of chemical composition, c) SEM micrograph overlaid with EDX linescan-profile and d) EDX linescan-profile of the distribution of constituent elements.

Figure 5.5 (a-d) shows the SEM micrograph with EDX analysis of corroded Al 6082 alloy during the third run R_3 after applied six DC/OCP cycles. In Figure 5.5 (a) the SEM micrograph of the surface morphology reveals significant corrosion feature of mud cracked pattern surface with big cavities caused by pit and crevice corrosion. From the inserted table in Figure 5.4 (b) the chemical composition of corroded Al 6082 alloy during R_2 after six applied DC/OCP cycles exhibits the highest content of Al and O, which emphasizes the existence of corrosion products such as $Al(OH)_3$.

Figure 5.4 (d) shows the EDX linescan-profiles for constituent elements of corroded Al 6082 alloy during R_3 that reveals fluctuations of high and low signal intensity of Al which influenced due to the cracked pattern of the surface while the low signal intensity observed for O which can be associated to oxides. The Mg, Mn, and Si signals intensity are very low and indistinguishable with the energy resolution of the EDX detector. In contrast, no signal observed from the EDX detector over the pits, which can be related to deep cavities that pits may cause.

It can be concluded that the SEM micrograph and EDX analysis exhibited significant degradation to all samples after six successive DC/OCP cycles. The most corroded sample is observed during R_3 followed by R_2 and R_1, which can be attributed to the high dissolution rate of aluminium.
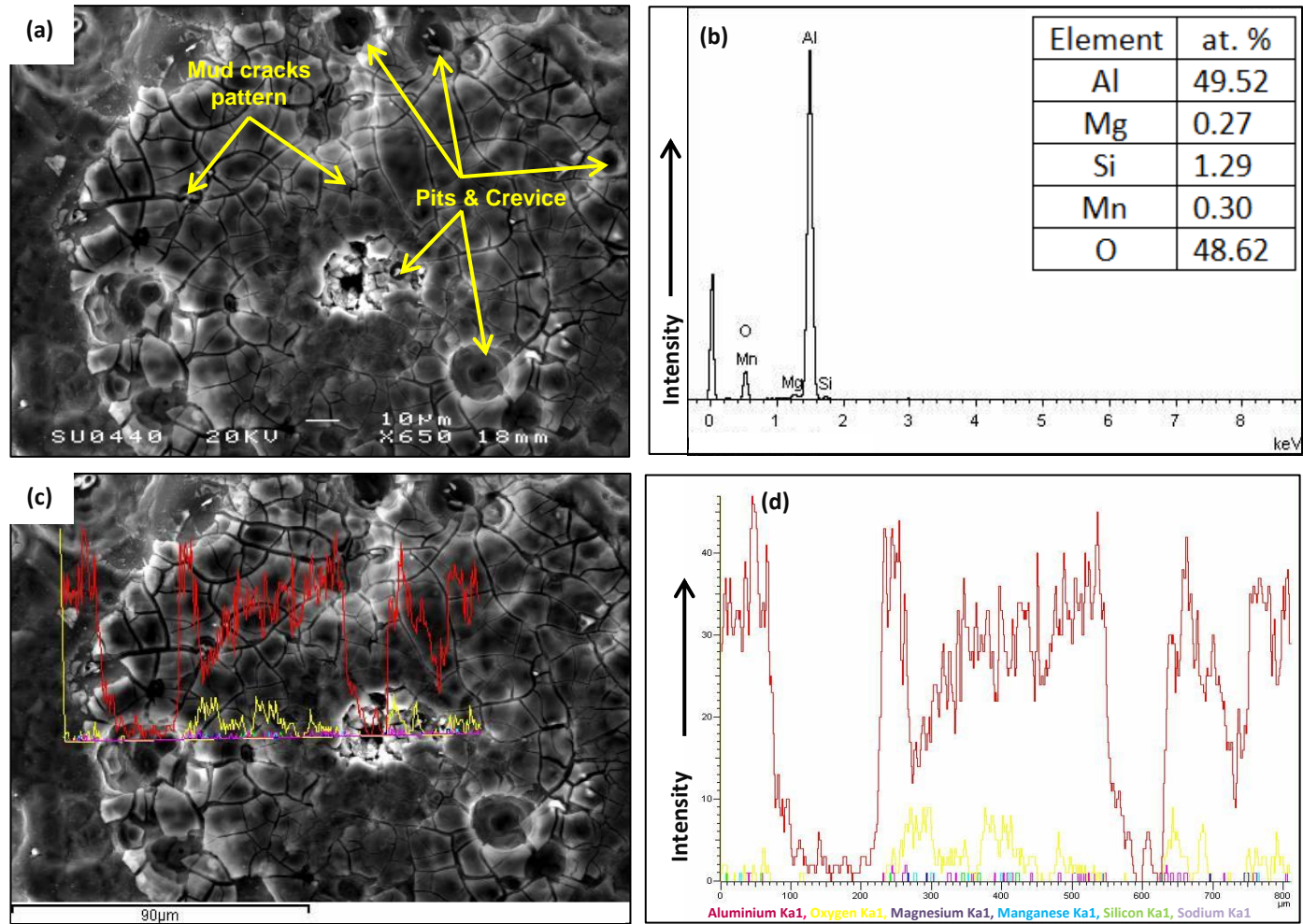
Figure 5.5: SEM & EDX analysis of corroded Al 6082 alloy_ during R_3 after six successive DC/OCP cycles a) SEM surface plane micrograph, (b) EDX spectrum analysis with inserted table of chemical composition, c) SEM micrograph overlaid with EDX linescan-profile and d) EDX linescan-profile of the distribution of constituent elements.

5.3 Electrochemical evaluation testing

5.3.1 Open circuit potential E_{OCP}

Figure 5.6 shows the E_{OCP} of Al 6082 alloy while a steady-state value after 2 h exposure to 3.5 wt. % NaCl solution. E_{OCP} applied for 2 h to measure the corrosion potential of the Al 6082 alloy electrode, which recorded to be around -0.748 V. vs SCE. Based on the consideration for conducting electrochemical measurements such as potentiodynamic polarisation and advanced (AC)DC/OCP/AC cyclic testing; E_{OCP} was carried out for few hours prior to starting any electrochemical measurements. This ensures that a steady-state is established for the potential value to avoid any initial fluctuation in potential, which may affect their results (see inset in Figure 5.6).
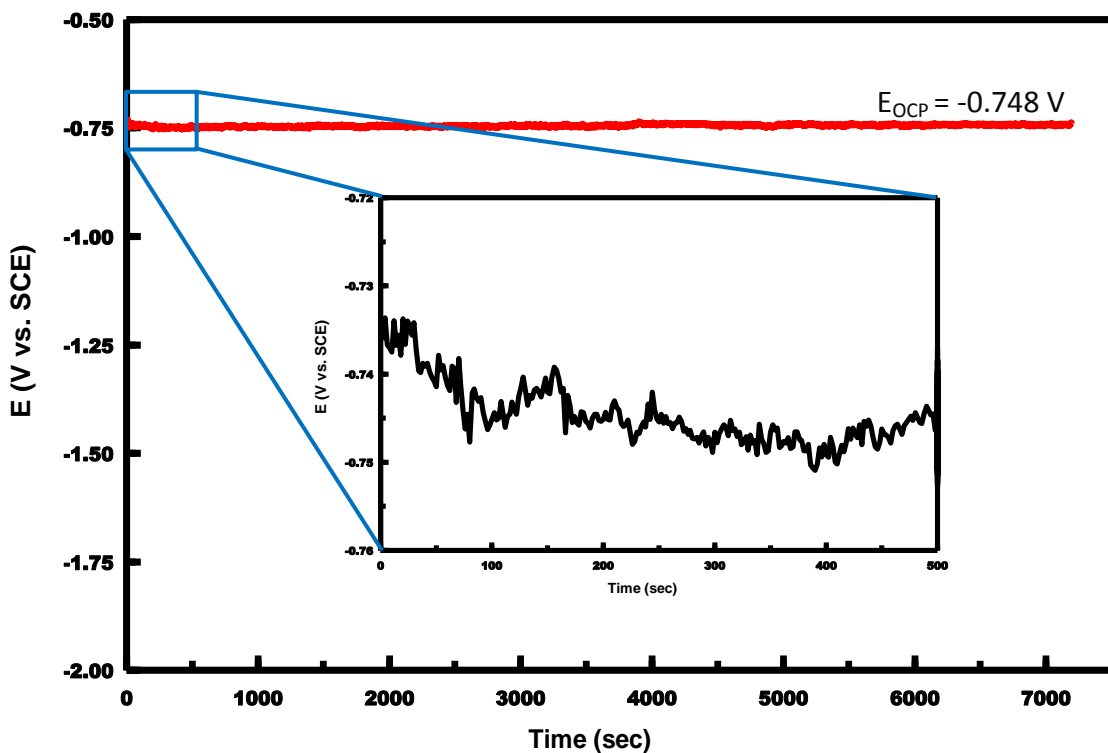
Figure 5.6: Change of open circuit potential E_{OCP} of polished Al 6082 alloy during 2 h exposure time to 3.5 wt. % NaCl solution.

5.3.2   Potentiodynamic polarisation measurement (PTD)

Potentiodynamic polarisation behaviour and corresponding parameters derived from the polarisation curve of Al 6082 alloy after 2 h E_{OCP} exposure time to 3.5 wt. % NaCl solution are presented in Figure 5.7 and Table 5.2 respectively.
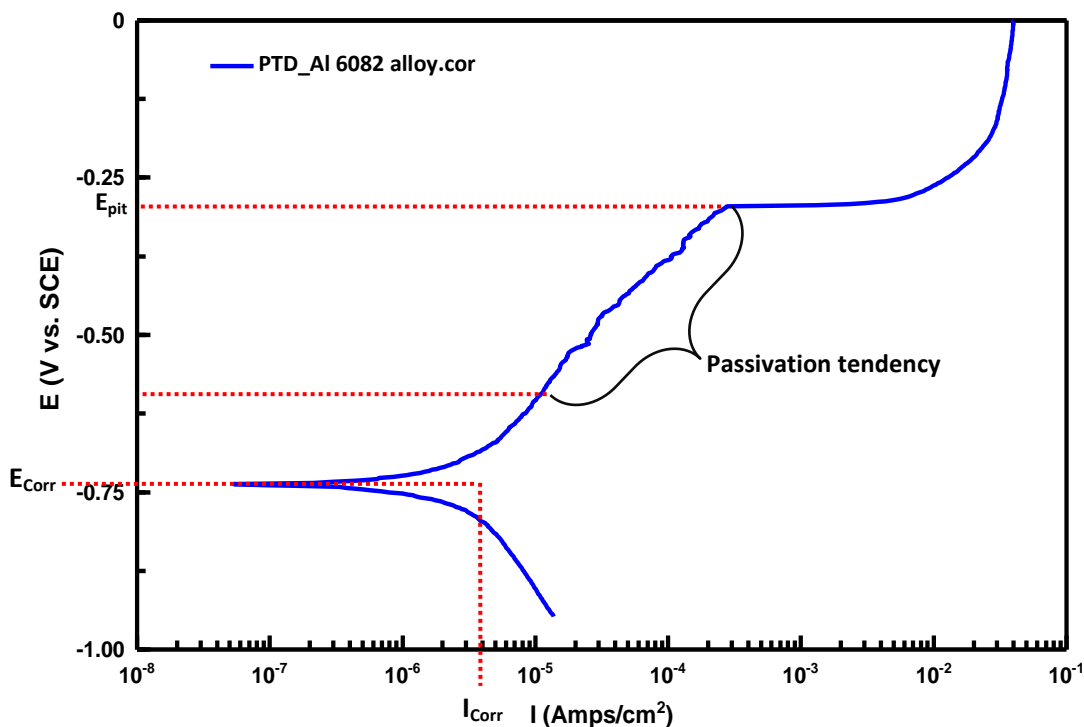
Figure 5.7: Potentiodynamic polarisation curve of Al 6082 alloy after 2 h E_{OCP} exposure time to 3.5 wt. % NaCl solution.

Table 5.1: Open circuit potential E_{OCP} and potentiodynamic data of Al 6082 alloy.

Material	E_{OCP} (mV)	E_{corr} (mV)	I_{corr} ($\mu A/cm^2$)	E_{pit} (mV)	β_a (mV/decade)	β_b (mV/decade)	R_p ($K\Omega cm^{-2}$)
Al-alloy	-748	-747	8.96	-295	482.8	747.6	8.5

The obtained polarisation curve for Al 6082 alloy exhibits a strong period of passivation tendency from -587 to -295 mV (vs. SCE) followed by a gradual increase in the current density, representing the initiation of the pits at pitting potential (E_{pit}) of -295 mV (vs. SCE) and at a corrosion current density of 0.3 $\mu A/cm^2$. The pitting

98

corrosion was preceded by uniform thinning of the passive film. After reaching the pitting potential the current density continued to increase slightly with increasing potential. It was found necessary to explore the initial potential behaviour of each sample for better understanding of the mechanisms underlying the evolution of electrochemical corrosion of aluminium. Variations in the formation and dissolution of the passive film on the surface of the Al 6082 alloy substrate during the 2 h E_{OCP} pre-test stage lead to differences in the development of the oxide layer, resulting in variations in passive film permeability [44]. Figure 5.8 inset shows how the initial potential behaviour of three samples of Al 6082 during three different runs R_1, R_2 and R_3 after 2 h E_{OCP} fluctuated between passivation and dissolution processes for the first few minutes of exposure.
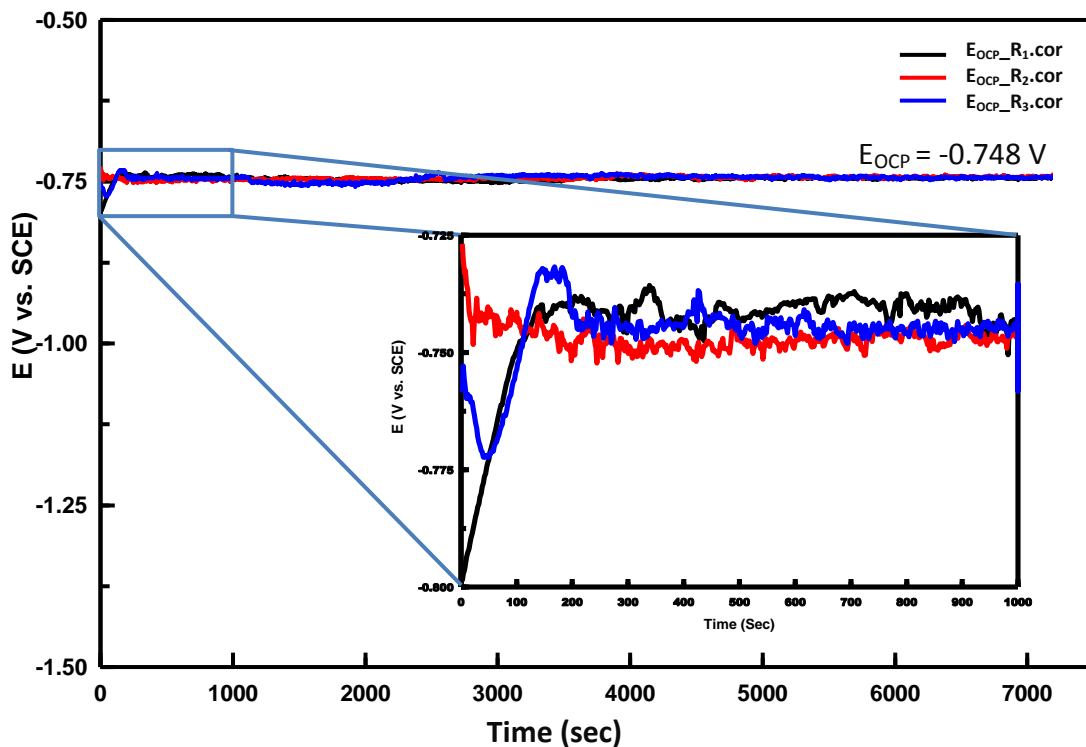
Figure 5.8: Fluctuations in E_{OCP} recorded during 2 h exposure to 3.5 wt. % NaCl solution for three samples of Al 6082 alloy during three runs R_1, R_2 and R_3. **Inset**: Variability in of the initial potential behaviour during R_1, R_2 and R_3.

Thus, during E_{OCP} during R_1, the initial potential instantly increased in anodic potential from an initial value of -0.802 V (vs. SCE) to -0.748 V in less than 2 minutes (110 sec), and remained steady at this value until the end of the 2 h E_{OCP} test. The rapid initial increase in potential can be attributed to the initial growth of an $Al(OH)_3$ film on the surface [47, 55]. The formation of aluminium hydroxide proceeds by the partial anodic dissolution of Al to Al^{3+} by reaction 2.11 (see section 2.1, p15), and the electrons produced are consumed by the partial cathodic reaction of water reduction to its constituent hydrogen and hydroxide ionic components reaction 2.2 p.14. Hence, Al^{3+} ion reacts with an OH^- ion to form insoluble precipitate of $Al(OH)_3$ by reaction 2.12 (see section 2.1, p15). The overall reaction can be written as the follows:

$$2Al + 6H_2O \rightarrow 2Al(OH)_3 + 3H_2 \qquad (5.1)$$
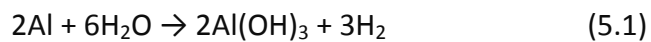
The potential during E_{OCP} during R_2 instantly decreased from an initial potential of -0.721 V (vs. SCE) to -0.748 V after approximately 20 sec, and it remained steady at this potential with minor fluctuations until the end of the E_{OCP} test. In this case, the immediate decrease in potential can be attributed to the electrochemical dissolution of the (very thin) of native Al_2O_3 oxide film that formed during sample preparation. Chao et al. [166] theoretically assumed that the removal of Al^{3+} ions into solution is responsible for the observed electrochemical dissolution of the native oxide film. Strictly speaking however, the removal of the Al_2O_3 film is not due to oxide film dissolution, but to the removal (ejection) of Al^{3+} ions from the oxide film lattice towards the solution, generating aluminium vacancies in the film, which

leads to a porous structure. The ejected Al^{3+} ions will then react with OH^- ions in solution and form passive film of $Al(OH)_3$ (reaction 2.12 p15); the remaining oxygen in the lattice of the oxide film is removed, by cathodic hydrogen reacting with oxygen to form water (simultaneous to the removal of Al^{3+} ions) [55, 57].

In contrast, the potential during E_{OCP} during R_3 decreased almost instantaneously towards the cathodic direction from an initial potential of -0.757 V (vs. SCE) to -0.776 V, over a period of approximately 40 sec. The decrease in potential can in this case be ascribed to the dissolution of aluminium by Al^{3+} ion removal from the aluminium substrate. Afterwards, a rapid increase in potential towards the anodic direction is observed, which can again be attributed to the growth of a passive film $Al(OH)_3$ by the chemical reaction 2.12. Ultimately the anodic increase reached an over potential of -0.732 V vs. SCE (higher than the E_{OCP} value) then rapidly decreased in cathodic direction in few seconds back to E_{OCP} -0.748 V vs. SCE and remained steady at this potential (with minor fluctuations) until the end of the experiment. The initial overshoot and subsequent rapid decrease in potential can be attributed to transpassive dissolution, which is closely related to passive film breakdown and localised corrosion phenomena, due to the metal electrode potential becoming higher than E_{OCP} [167].

It can be seen that the potential value during E_{OCP} (Figure 5.8) and during six successive relaxation times Figure 5.23 during R_1, R_2 and R_3 converted to the same value of potential about -0.748 V vs. SCE, which suggests a similar type of passive film formation, but these may possess different surface morphology and thickness

which can influence subsequent DC cathodic polarisation behaviour. Aluminium

hydroxide precipitates often form gels, which crystallise and gradually change to

Al_2O_3 with time, resulting in the formation of passive film by the following reaction:

$$2Al(OH)_3 \rightarrow Al_2O_3 + 3H_2O \qquad\qquad (5.2)$$

Although, this passive oxide film can reduce the corrosion rate of the aluminium

substrate, but it cannot fully protect it from aggressive species (such as Cl^- and OH^-

ions) when exposed to a corrosive solution. For example chloride ions can easily

diffuse through the passive film causes dissolution of the underlying aluminium

substrate and resulting in pitting corrosion [161, 168, 169]. Nevertheless, the

passive film formed after 2 h E_{OCP} and after six successive relaxation times (Figure

5.22) during three runs R_1, R_2 and R_3 is probably pure alumina. The surface

morphology and thickness of the passive film can be modelled and predicted using

the formula (3.4), p59, by fitting electrochemical impedance spectroscopy data

(capacitance and 'n' parameter), which will be discussed later in this Chapter.

5.3.3 Evolution of EIS spectra after six successive DC/OCP cycles

EIS (AC measurement) is non-destructive electrochemical technique applied to

reveal specific effects on the electrochemical corrosion process at the metal

electrode/electrolyte interface without any morphological changes. Figure 5.9 (a-c)

shows the Nyquist plots of characterised EIS spectra obtained at 2 h E_{OCP} "EISi" and

six successive DC/OCP cycles "EIS1-EIS6" during three runs (R_1, R_2 and R_3

respectively).
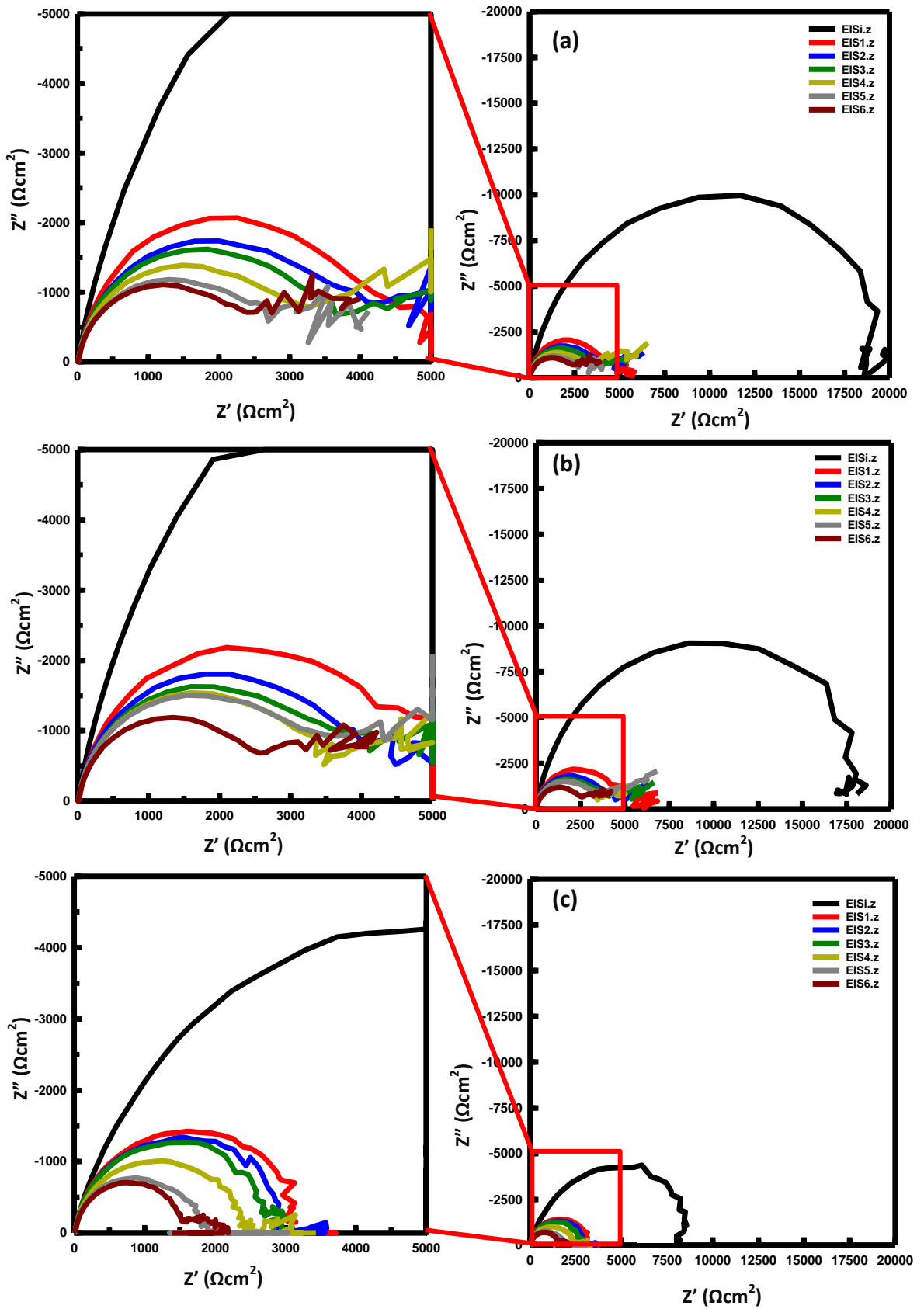
Figure 5.9: Nyquist plots for Al 6082 alloy at E_{OCP} & after successive six cycles of DC/OCP during a) R_1, b) R_2 and c) R_3.

Different EIS spectra were generated after 2 h E_{OCP}, EISi and EIS1-EIS6 during R_1, R_2 and R_3 exhibits one semicircle with large radius for the most of the frequency range, which can be attributed to charge transfer resistance R_{ct} (corrosion resistance). Visually, the radius of the semicircle during R_1 is the largest, followed by those one during R_2 and R_3, which suggests that the passive film formed after 2 h E_{OCP} during R_1 has high charge transfer resistance R_{ct} (i.e. highest corrosion resistance). A significant decrease in semicircle radius is seen after the first DC/OCP cycle is applied. This is related to a significant decrease in R_{ct} [132], which can in turn be attributed to a high rate of dissolution of the passive film formed during 2 h E_{OCP}. Probably, it was completely removed and formed a new passive film less protection to the corrosion (low charge transfer resistance) during relaxation time OCP1. Nyquist plots feature six slightly depressed semicircles with smaller radius in the high frequency range and a diffusional tail tends to appear in the low frequency range after six successive DC/OCP cycles (ESI1-EIS6) for all test repeats. The decrease in the radius of the semicircles can be explained by a progressive reduction in charge transfer resistance due to the lower corrosion resistance of the passive films that formed during each relaxation time (OCP1-OCP6). The repassivation process during OCP1-OCP6 occurred in progressive stronger alkaline solutions, where OH^- ions attack slows the growth of the passive film and leads to less protective passive film formation on the surface of aluminium substrate.

As mentioned above, the film can reduce the corrosion rate of the aluminium substrate, but does not provide adequate protection from pitting corrosion caused

by the inward diffusion of aggressive anionic species such as Cl^- ions, which form soluble complexes by the reactions 2.17-2.21 p22-23 [44, 54, 170]. In the very low frequency range a diffusional tail which tends to appear in most cases indicates the initiation of metastable pitting corrosion [47].

By comparing the Nyquist plots obtained during R_1, R_2 and R_3, it can be concluded that the EIS spectra indicate similar degradation behaviour overall, but with different semicircle radius at each step in each repeated cycle. It can be observed that the semicircle radii of EIS spectra during R_1 are apparently the largest, followed by those during R_2 and then at R_3. This can be related to the highest charge transfer resistance of the passive film that formed on this bulk sample after 2 h E_{OCP} during R_1, which is probably due to its low permeability and high thickness.

Figure 5.10 (a-c) shows Bode plots (phase angle vs. frequency) obtained after 2 h E_{OCP} "EISi" and repeated six DC/OCP cycles "EIS1-EIS6" during R_1, R_2 and R_3 respectively. The Bode plots exhibit typical resistive-capacitive (RC) behaviour featuring constant phase angle (i.e. complete peak) over a wide frequency range (10^{-1}-10^4 Hz) for EISi-EIS6 as indicated by the semicircle (and depressed semicircles in the corresponding Nyquist plots. A diffusional tail in the low frequency range (below 0.1 Hz) is visible; this probably due to the diffusion process of corrosion products. It can be seen that the Bode plots exhibit a high phase maximum angle θ_{max} and a broadening of the peak at EISi, which is indicative of a low dissolution rate of the passive film (highly resistive behaviour).
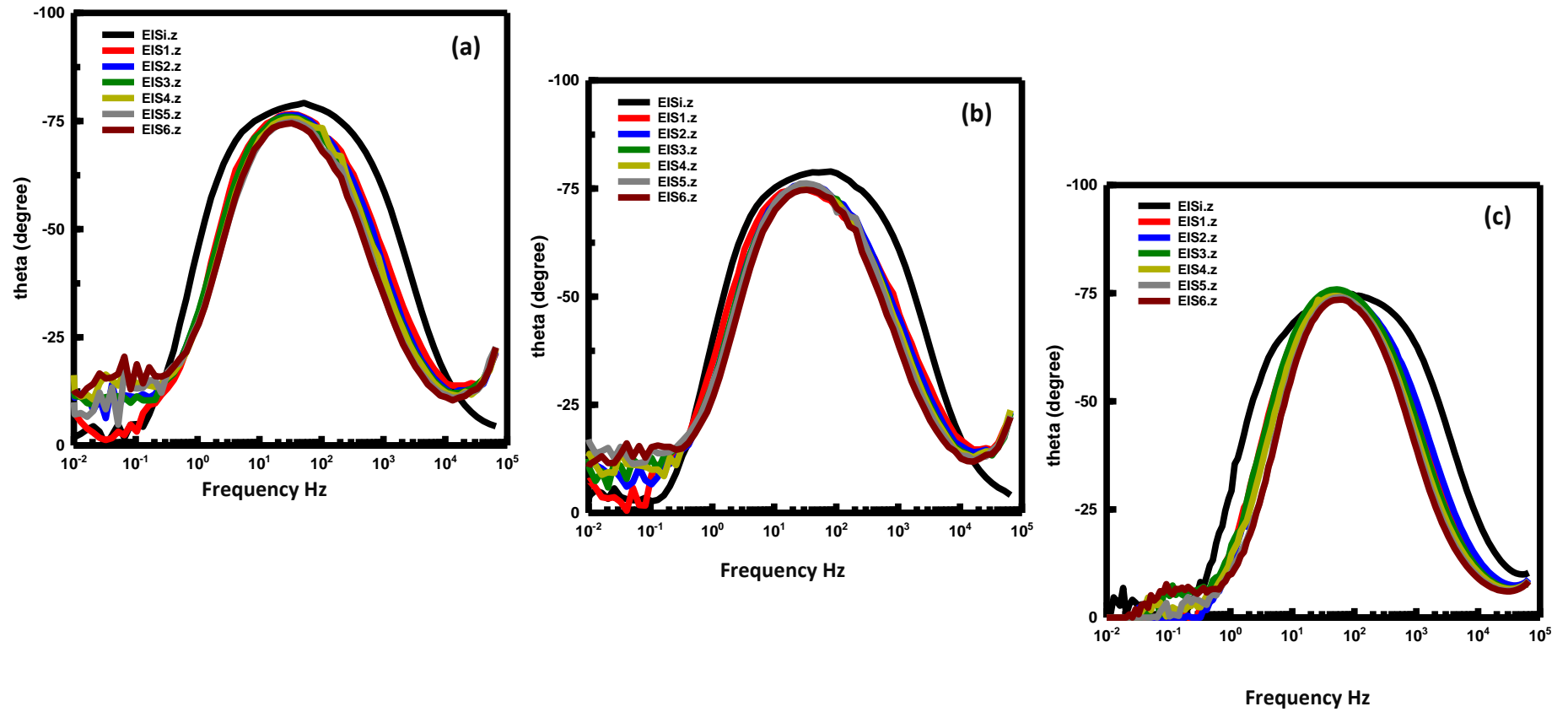
Figure 5.10: Bode plots (phase angle vs. frequency) for Al 6082 alloy at 2 h E_{OCP} & after successive six cycles of DC/OCP during a) R_1, b) R_2 and c) R3.

However, the maximum phase angle during EISi is observed to be the highest at R_1 (-79.3°) compared with -77.7° and -73.1° for R_2 and R_3 respectively, as well as the broadening of the peak being the widest at R_1 followed by R_2 and R_3, from which it can be deduced that the passive film for R_1 is the most corrosion resistant followed by R_2 then R_3. A decrease in θ_{max} and a narrowing of the phase-angle peak with the increasing the number of DC/OCP cycles is observed during EIS1-EIS6, which can also be related to a progressive decrease in charge transfer resistance of the passive film.

Figure 5.11 (a-c) shows the Bode plots (impedance modulus vs. frequency) obtained at 2 h E_{OCP} "EISi" and after six successive DC/OCP cycles (EIS1-EIS6) during R_1, R_2 and R_3 respectively. It can be seen that all impedance modulus |Z| spectra contain a linear slope at high frequencies (1-10^3 Hz) indicating that |Z| increases inversely to the frequency. The slope decreases for frequencies less than 1 Hz and reaches a plateau in the frequency range below 0.1 Hz in EISi during R_1, R_2 and R_3. The slopes for EIS1-EIS6 tend to plateau at a frequency less than 1 Hz but are still increasing slightly, a with diffusional tail in the low frequency range <0.1 Hz, which probably related to the diffusion process of corrosion products. The highest value of |Z| at EISi is observed at 2.3 x 10^{-4} Ωcm^2, 1.7 x 10^{-4} Ωcm^2 and 7.5 x 10^{-3} Ωcm^2 during R_1, R_2 and R_3 respectively, which can be attributed to the high corrosion resistance of the passive film the formed during 2 h E_{OCP} compared to |Z| at EIS1-EIS6.
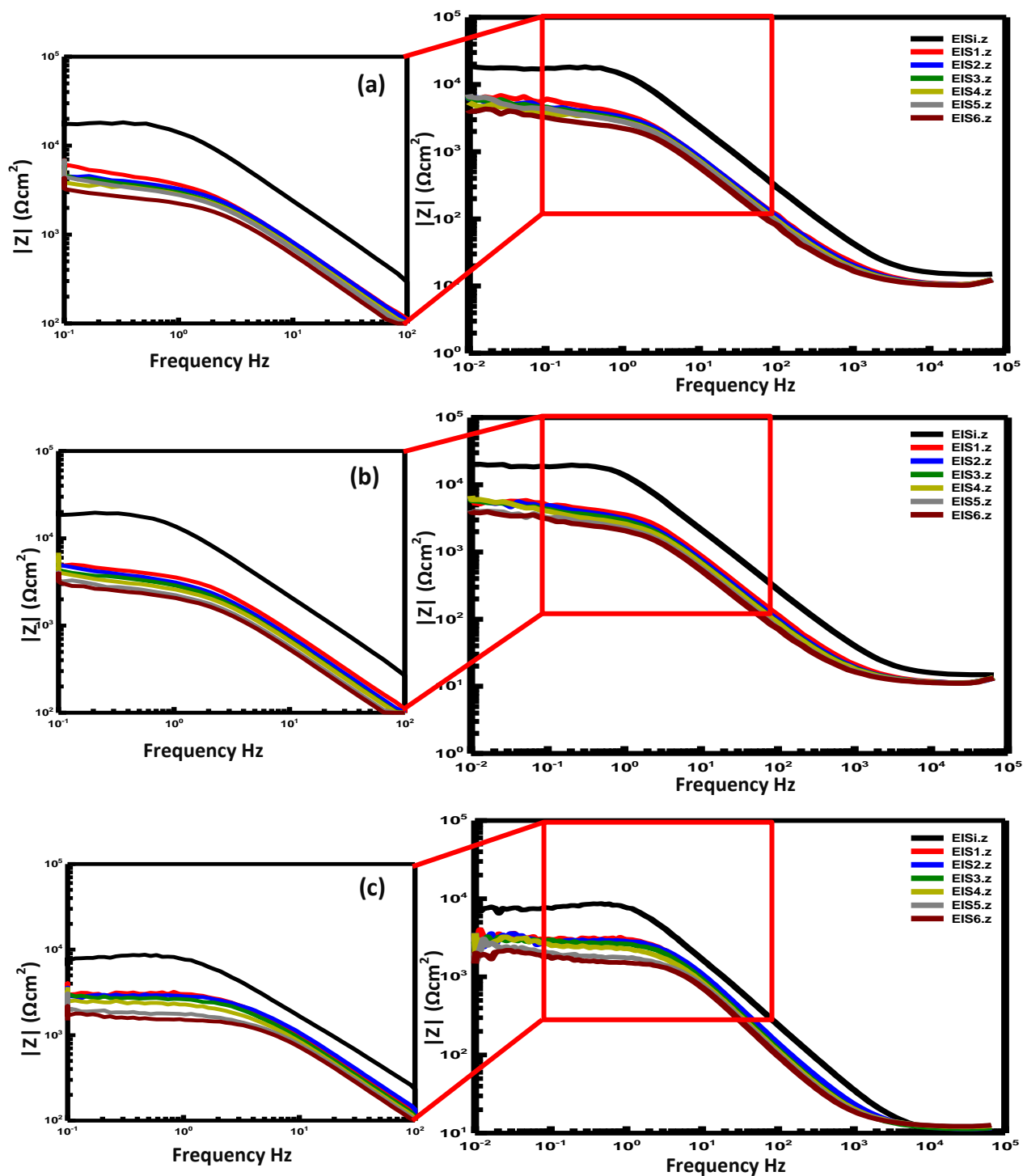
Figure 5.11: Bode plots (impedance modulus vs. frequency) of Al 6082 alloy at 2 h E_{OCP} & after successive six cycles of DC/OCP during a) R_1, b) R_2 and c) R_3.

It can clearly be observed that the |Z| value during EISi during R_1 is the highest, followed by R_2 and R_3, which can be related to the high charge transfer resistance of the passive film during R_1.

After applied first DC/OCP cycle the |Z| value decreased significantly to 6.9 x 10^{-3} Ωcm^2, 5.4 x 10^{-3} Ωcm^2 and 1.6 x 10^{-3} Ωcm^2 during R_1, R_2 and R_3, respectively. The decrease in |Z| indicates low corrosion resistance of the passive film formed during the relaxation time OCP1, which is probably susceptible to pitting corrosion attack. The passive film that formed during 2 h E_{OCP} is probably completely removed (chemical dissolution) by OH^- ions attack during DC1 cathodic polarisation.

During EIS1-EIS6 a slight decrease in |Z| value with increasing the number of DC/OCP is observed. This can be explained by the low corrosion resistance of the passive films formed during the relaxation time OCP1-OCP6. The repassivation process during OCP1-OCP6 was carried out in alkaline conditions where OH^- ion attack lowers the growth rate of the passive film and leads to less protective passive film formation on the surface of aluminium substrate, which susceptible to pitting corrosion during OCP relaxation time.

The impedance spectra were analysed using Z-view® software (Scribner Associates) and based on the features of the EIS spectra two different electrical equivalent circuits (EC) were constructed to analyse the electrochemical corrosion process, as shown in Figure 5.12 a & b.

The EC in Figure 5.12 a was employed to model the corrosion behaviour of the EISi spectrum after 2 h E_{OCP} during R_1, R_2 and R_3, which provided a typical resistive-

capacitive (RC) behaviour, featuring a single time constant over a wide range of frequency, suggesting the present of a highly stable passive film. This EC is composed of a solution resistance element, R_s, in series with a parallel combination of a constant phase element CPE (representing the double layer capacitance C_{dl} of the passive film) and a charge transfer element, R_{ct}, across the passive film (corrosion resistance). A similar EC (Figure 5.12 b) has also been used to model EIS spectra with an additional element of Warburg impedance element, W_R, in series with R_{ct}, selected to represent the diffusional tail.

(a)   (b)
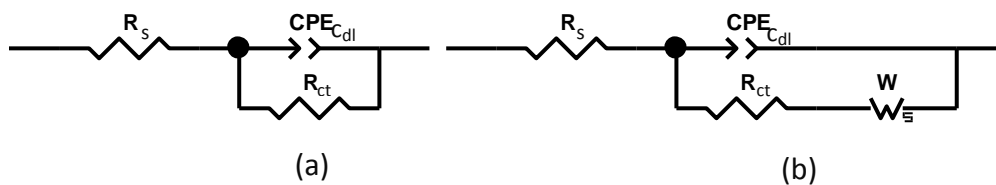
Figure 5.12: Electrical equivalent circuit used to model EIS spectra at (a) 2 h E_{OCP} and (b) after six DC/OCP cycles.

The values of the EC elements in the electric circuit used to model the EIS spectra after 2 h E_{OCP} and after six successive DC/OCP cycles are presented in Tables 5.2 to 5.4 and plotted as a function of the number of DC/OCP cycles in Figures 5.13 to 5.15 during R_1, R_2 and R_3 respectively.

Table 5.2: Fitting results of EIS spectra of Al 6082 alloy during R_1 obtained at E_{OCP} and after six successive DC /OCP cycles.

EIS spectrum	R_s (Ωcm^2)	CPE_{Cdl} (μFcm^{-2})	n	R_{ct} $(k\Omega cm^2)$	W_R $(k\Omega cm^2)$
EISi	14.81	8.73	0.92	21.3	-
EIS1	11.68	29.3	0.91	6.3	1.92
EIS2	11.62	32.4	0.91	6.1	3.61
EIS3	11.71	34.3	0.91	5.9	2.62
EIS4	11.67	34.4	0.91	5.3	3.43
EIS5	11.68	36.5	0.91	4.8	1.68
EIS6	11.59	38.1	0.91	4.6	2.56
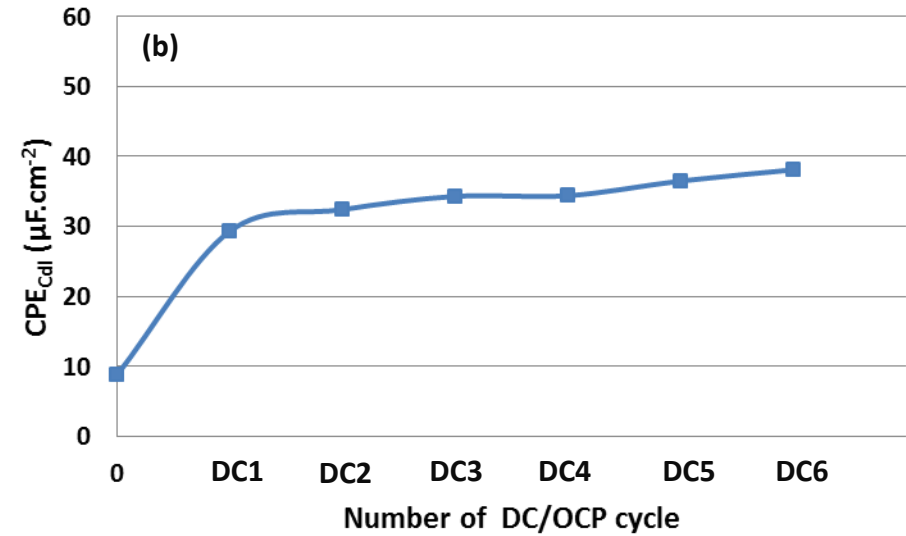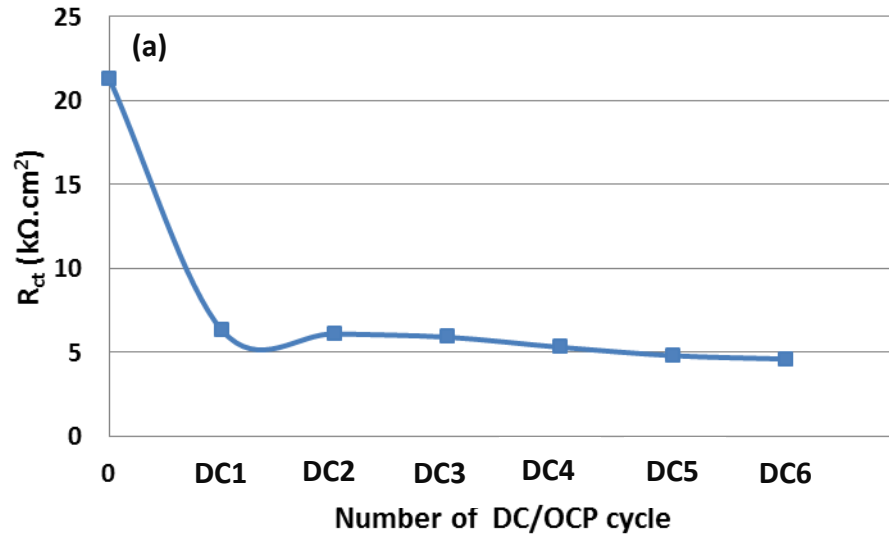
Figure 5.13: Evolution of (a) charge transfer resistance R_{ct}, (b) constant phase element representing double layer capacitance $CPEc_{dl}$ as function of DC/OCP cycle for Al 6082 alloy during R_1.

Table 5.3: Fitting results of EIS spectra of Al 6082 alloy_R_2 obtained during E_{OCP} and after six successive DC/OCP relaxation cycles.

EIS spectrum	R_s (Ωcm^2)	CPE_{Cdl} $(\mu F.cm^{-2})$	n	R_{ct} $(k\Omega cm^2)$	W_R $(k\Omega cm^2)$
EISi	14.5	10.3	0.91	18.6	-
EIS1	10.7	33.1	0.89	5.5	1.4
EIS2	10.7	34.4	0.89	4.4	2.1
EIS3	10.8	34.6	0.89	4.2	2.6
EIS4	10.8	35.4	0.89	3.7	2.2
EIS5	10.7	36.8	0.89	3.1	3.7
EIS6	10.7	40.5	0.89	2.9	1.9
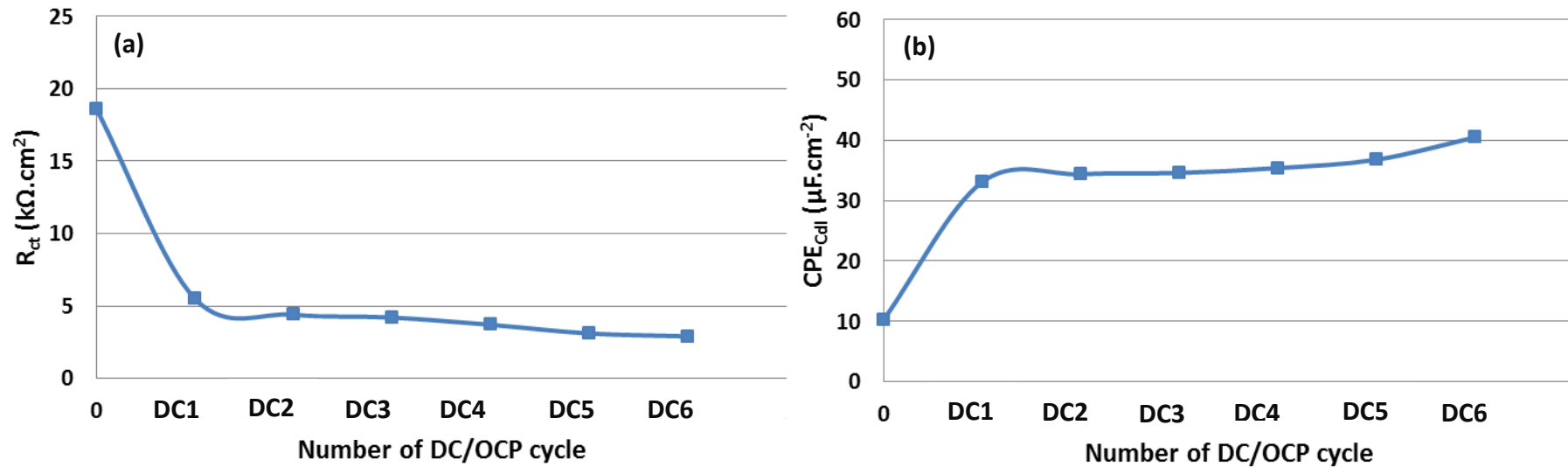
Figure 5.14: Evolution of (a) charge transfer resistance R_{ct}, (b) constant phase element representing the double layer capacitance $CPEc_{dl}$ as function of DC/OCP cycle of Al 6082 alloy during R_2.

Table 5.4: Fitting results of EIS spectra of Al 6082 alloy during R_3 obtained at E_{OCP} and after six successive DC/OCP cycles.

EIS spectrum	R_s (Ωcm^2)	CPE_{Cdl} ($\mu F/cm^2$)	n	R_{ct} ($k\Omega cm^2$)	W_R ($k\Omega cm^2$)
EISi	10.98	17.4	0.88	8.3	3.4
EIS1	11.45	43.1	0.85	3.2	1.9
EIS2	11.62	45.5	0.87	2.9	0.73
EIS3	11.58	46.3	0.88	2.8	0.29
EIS4	12.23	46.5	0.88	2.4	0.11
EIS5	12.43	47.7	0.88	1.8	0.33
EIS6	12.37	49.3	0.88	1.6	0.32
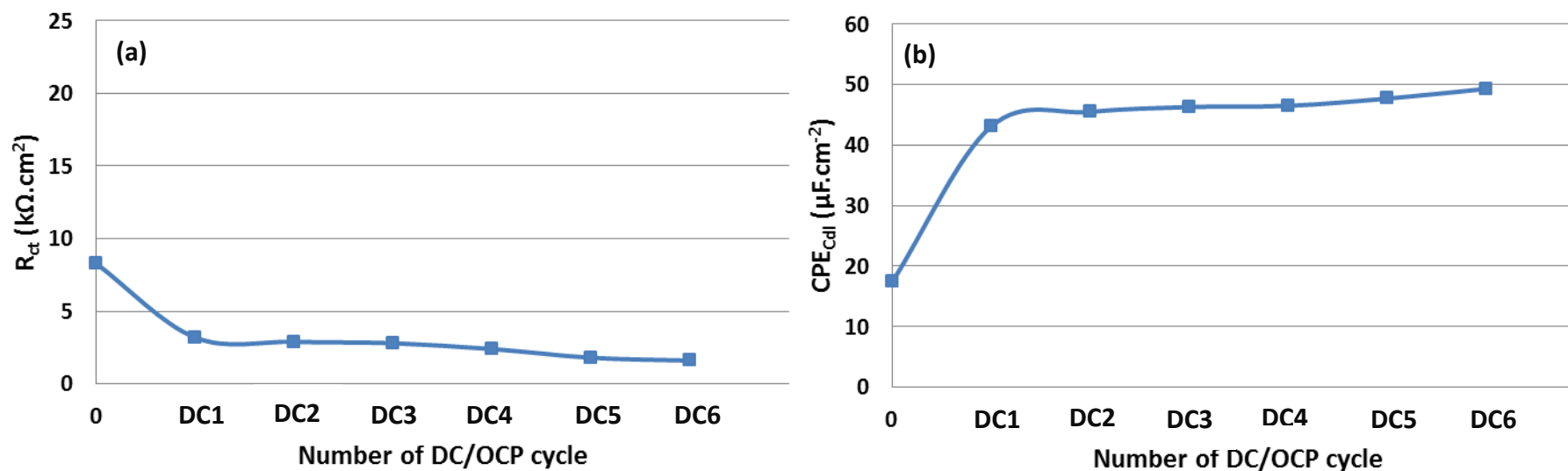
Figure 5.15: Evolution of (a) charge transfer resistance R_{ct}, (b) constant phase element representing the double layer capacitance CPE_{dl} as function of DC/OCP cycle of Al 6082 alloy during R_3.

Accordingly, the corrosion behaviour can be deduced from the charge transfer resistance R_{ct} and constant phase element CPE_{Cdl} values. A significant decrease in R_{ct} value of EISi from 21.3 to 6.3 $k\Omega cm^2$ for R_1, 18.1 to 5.5 $k\Omega cm^2$ for R_2 and 8.3 to 3.2 $k\Omega cm^2$ for R_3 after application of the first DC/OCP cycle "EIS1" is observed. This significant decrease can be explained by the high dissolution rate of the passive that formed during 2 h E_{OCP}, which is probably completely removed during cathodic polarisation DC1 and less affectively re-formed during relaxation under alkaline conditions (i.e. probably thin, porous and very susceptible to pitting corrosion). A slight decrease in R_{ct} value with increasing the number of DC/OCP cycles during EIS2-EIS6 is observed.

In contrast, an increase in CPE_{Cdl} values with increase of number DC/OCP cycles is observed. Hence, the constant phase element CPE is replaced in the EC with a pure capacitance element (C) to reflect the non-ideal capacitive behaviour, caused by factors such as surface compositional heterogeneity and roughness at the metal substrate/passive film interfaces. As described in Chapter 3 section 3.2.2.3 p58, the CPE value is controlled by the exponent n, which is an adjustable parameter related to the inhomogeneity of the sample, which always lies in the range ($1 \leq n \leq 0$). When the value of n approaches unity, the CPE is equivalent to a pure capacitor, if n approaches to 0, the CPE is equivalent to pure resistance, but with an n exponent closer to 0.5, the CPE value is indicative of diffusion processes and consequently, the CPE indicates a Warburg diffusion component [149-151]. A significant increase in CPE_{Cdl} value for EISi from about 8.7 to 29.3 μFcm^{-2} during R_1, 10.3 to 33.1 μFcm^{-2}

at R_2 and 17.4 to 43.1 μFcm^{-2} at R_3 after applied the first DC/OCP cycle "EIS1" is observed.

As can be seen in Tables 5.2 to 5.4 the Warburg impedance W_R values are varying. Low value of W_R corresponds to diffusion of Al$^+$ ions, produced by the anodic reaction of the metal surface with the bulk electrolyte and to the initiation of metastable pitting corrosion. High values of W_R can be attributed to accumulation of corrosion products such as white precipitation of Al(OH)$_3$ that covered the pits resulting in a temporary passivation as revealed in SEM micrographs (Figures 5.3, 5.4 and 5.5 a) of the corroded samples after six successive DC/OCP cycles during R_1 , R_2 and R_3, respectively.

Due to the need to perform the cyclic experimental test procedures as a continuous process, it was not possible to characterise by SEM and EDX analysis to explore the actual thickness and chemical composition of the passive layers formed after the practical conditions of 2 h E_{OCP} and during/after each the successive DC/OCP cycle. Furthermore, the extremely low thickness of the (hydrated) alumina layer, which is only a few nanometres deep, is hardly measurable using common analytical instruments. Up to now, the extensive literature on this topic failed to introduce a precise technique that can measure the thickness value of alumina layer claimed to be present. The thickness value is famously claimed to be between 2-3 nm [171], 5-10 nm [172], 7.5-15 nm [173], 25 nm [174] less than 40 nm [175] and 70-100 nm [176]. Reference [177] resorted to employing EIS data fitting (capacitance and the *n* exponent values) to determine the thickness of oxide film using the formula (3.4)

see p59. In this case, the calculated thickness is derived from the capacitance by assuming the oxide film acts as a parallel plate capacitor with the permittivity constant is $\varepsilon_r = 10$ in case of alumina, a value comparable to those typically found in literatures [178-180]. It should be said that values of permittivity constant (ε_r) of alumina between 8 and 12 have been reported in the literatures [181, 182]. The calculated alumina layer thickness as a consequence of this was between 1.6 and 2.5 nm but no consideration of factors such as porosity was made.

However, the only sensible option to indirectly obtain a defined thickness of the passive film is to employ the obtained data (capacitance and n exponent) from fitting of EIS spectra that are introduced in Tables 5.2 to 5.4 at R_1, R_2 and R_3 respectively using the aforementioned formula (3.4).

As described earlier, when the exponent n approaches unity, the CPE is equivalent to a pure capacitor, which means that the oxide film can be considered act as a parallel plate capacitor. Figure 5.16 shows the schematic diagrams of the capacitor classification according to the characteristics and properties of their insulating permittivities; (a) the parallel plate capacitor, (b) the fact of the porosity, which is in parallel to the passive film growth direction, but not parallel to the capacitor plats (and that a parallel calculation — taking account of the respective permittivities of the material and the electrolyte filled the pore), and (c) the fact if the layer formed during 2 h E_{OCP} and during six relaxations cycles is probably in practice a bi-layer of $Al(OH)_3$ and Al_2O_3, which is in series with the growth direction, but parallel to the

capacitor plates (and that series calculation — taking account of the respective permittivities of the both materials).

(a) Parallel plate capacitor

(b) Porosity parallel to the passive film growth direction

(c) bi-layer of $Al(OH)_3$ and Al_2O_3 in series with the growth direction
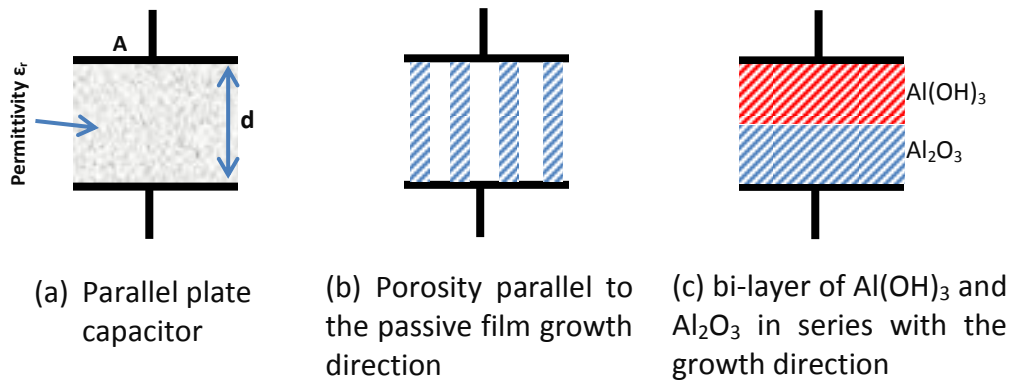
Figure 5.16: Schematic diagrams illustrate the capacitor classification according to the characteristics and properties of their insulating permittivities.

As mentioned earlier in section 5.3.2 p102-103, the ultimate passive film formed during E_{OCP} and during six successive DC/OCP cycles is probably pure alumina, where aluminium hydroxide precipitates often form gels, which crystallise and gradually change to Al_2O_3 with time, resulting in the formation of passive film by the reaction 5.2 [161, 169].

The calculations presented in Tables 5.5 and 5.6 and plotted as a function of the DC/OCP cycles shown in Figure 5.18 (a-c) were carried out to determine the likely evolution of passive film thickness based on a consideration of existence porosity or not in the passive film.

Table 5.5: The calculated thickness of the passive film (assuming pure Al_2O_3 and no porosity) formed during 2 h E_{OCP} and six successive DC/OCP cycle during R_1, R_2 and R_3.

Cycle No.	CPE_{Cdl} ($\mu F.cm^{-2}$)	R_{ct} ($k\Omega cm^2$)	n	Density D%	Porosity ρ%	Permittivity of electrolyte	Total permittivity constant ε_r	d(nm)
R_1:								
(at E_{OCP})	8.73	21.3	0.92	100	-	-	10	43.5
1	29.3	6.1	0.91	100	-	-	10	12.9
2	32.4	6.2	0.91	100	-	-	10	11.7
3	34.3	5.9	0.91	100	-	-	10	11.1
4	34.4	5.3	0.91	100	-	-	10	11.1
5	36.5	4.8	0.91	100	-	-	10	10.4
6	38.1	4.6	0.91	100	-	-	10	9.9
R_2:								
(at E_{OCP})	10.3	18.1	0.91	100	-	-	10	36.9
1	33.1	5.5	0.89	100	-	-	10	11.5
2	34.4	4.4	0.89	100	-	-	10	11.0
3	34.6	4.2	0.89	100	-	-	10	10.9
4	35.4	3.7	0.89	100	-	-	10	10.7
5	36.8	3.1	0.89	100	-	-	10	10.3
6	40.5	2.9	0.89	100	-	-	10	9.3
R_1:								
(at E_{OCP})	17.4	8.3	0.88	100	-	-	10	21.8
1	43.1	3.2	0.85	100	-	-	10	8.8
2	45.5	2.9	0.87	100	-	-	10	8.3
3	46.3	2.8	0.88	100	-	-	10	8.2
4	46.5	2.4	0.88	100	-	-	10	8.1
5	47.7	1.8	0.88	100	-	-	10	7.9
6	49.3	1.6	0.88	100	-	-	10	7.7

Table 5.6: The calculated thickness of the passive film (assuming pure Al_2O_3 and porosity "in parallel") formed during 2 h E_{OCP} and six successive DC/OCP cycles during R_1, R_2 and R_3.

Cycle No.	CPE_{Cdl} ($\mu F.cm^{-2}$)	R_{ct} ($k\Omega cm^2$)	n	Density D%	Porosity ρ%	Permittivity of electrolyte	Total permittivity constant ε_r	d(nm)
R_1:								
(at E_{OCP})	8.73	21.3	0.92	98	2	45	ε_r =(0.980 x 10) + (0.020 x 45) = 10.60	50.5
1	29.3	6.1	0.91	95.5	4.5	45	ε_r =(0.955 x 10) + (0.045 x 45) = 11.58	15.0
2	32.4	6.2	0.91	95.5	4.5	45	ε_r =(0.955 x 10) + (0.045 x 45) = 11.58	13.6
3	34.3	5.9	0.91	95.5	4.5	45	ε_r =(0.955 x 10) + (0.045 x 45) = 11.58	12.8
4	34.4	5.3	0.91	95.5	4.5	45	ε_r =(0.955 x 10) + (0.045 x 45) = 11.58	12.8
5	36.5	4.8	0.91	95.5	4.5	45	ε_r =(0.955 x 10) + (0.045 x 45) = 11.58	12.0
6	38.1	4.6	0.91	95.5	4.5	45	ε_r =(0.955 x 10) + (0.045 x 45) = 11.58	11.6
R_1:								
(at E_{OCP})	10.3	18.1	0.91	95.5	4.5	45	ε_r =(0.955 x 10) + (0.045 x 45) = 11.58	42.8
1	33.1	5.5	0.89	94.5	5.5	45	ε_r =(0.945 x 10) + (0.055 x 45) = 11.48	13.2
2	34.4	4.4	0.89	94.5	5.5	45	ε_r =(0.945 x 10) + (0.055 x 45) = 11.48	12.7
3	34.6	4.2	0.89	94.5	5.5	45	ε_r =(0.945 x 10) + (0.055 x 45) = 11.48	12.6
4	35.4	3.7	0.89	94.5	5.5	45	ε_r =(0.945 x 10) + (0.055 x 45) = 11.48	12.3
5	36.8	3.1	0.89	94.5	5.5	45	ε_r =(0.945 x 10) + (0.055 x 45) = 11.48	11.8
6	40.5	2.9	0.89	94.5	5.5	45	ε_r =(0.945 x 10) + (0.055 x 45) = 11.48	10.7
R_1:								
(at E_{OCP})	17.4	8.3	0.88	94	6	45	ε_r =(0.94 x 10) + (0.06 x 45) = 12.1	26.5
1	43.1	3.2	0.85	92.5	7.5	45	ε_r=(0.925 x 10) + (0.075 x 45) = 12.63	11.2
2	45.5	2.9	0.87	93.5	6.5	45	ε_r =(0.935 x 10) + (0.065 x 45) = 12.28	10.2
3	46.3	2.8	0.88	94	6	45	ε_r =(0.94 x 10) + (0.06 x 45) = 12.1	9.9
4	46.5	2.4	0.88	94	6	45	ε_r =(0.94 x 10) + (0.06 x 45) = 12.1	9.9
5	47.7	1.8	0.88	94	6	45	ε_r =(0.94 x 10) + (0.06 x 45) = 12.1	9.6
6	49.3	1.6	0.88	94	6	45	ε_r =(0.94 x 10) + (0.06 x 45) = 12.1	6.3

Table 5.5 presents the obtained thicknesses calculated by assuming a passive film (pure alumina) with no porosity (100% density) for R_1 R_2 and R_3. This assumption is based on the previous thickness calculations that are found in the literature [177, 183, 184], which use the formula 3.4 to fit EIS data without taking into account factors such as the permittivity constant of the electrolyte that might fill any pores that are present, which means they assumed the passive film is fully dense. The calculated thickness of the passive film formed after 2 h E_{OCP} is the largest compared to the obtained thickness of the passive film that formed after six successive DC/OCP cycles. Thus, this result suggests that (as previously speculated) the growth of the passive film formed during exposure to neutral salt solution proceeded normally (without OH^- ion that cause competing chemical dissolution but then the re-growth of the passivate film taking place during the relaxation time in each cycle where of the passive film formed in an increasingly alkaline solution (i.e. progressively highly concentration of OH^- ions) was gradually disrupted and suppressed.

In fact, the passive film (even after E_{OCP}) will definitely contain some porosity that should take into account (and that will be filled with the electrolyte). Therefore, the permittivity of the electrolyte that filled the pores in the passive film should also be considered in the calculation of the actual layer thickness. However, the effective permittivity is the summation of the permittivity of the passive film (alumina) $\varepsilon_r = 10$ and the permittivity of the electrolyte (sodium chloride) $\varepsilon_r = 45$ [185] (in parallel at a level of overall porosity that can be inferred from the exponent n in EIS data

Tables 5.2 to 5.4). However, there is an assumption that, when $n = 1$ (pure capacitor), the density of the passive film is 100%, where when $n = 0.5$ (Warburg impedance) the assumed density is 75% and when $n = 0$ the (pure resistor) the assumed density is 25%. In terms of considering porosity in alumina the calculations were carried out in parallel (Table 5.6) to simulate connected porosity.

The values of the inhomogeneity exponent n, which researchers generally attribute to the porosity of the passive film (but rarely, if ever, take account of in their subsequent thickness calculations) after different runs R_1, R_2 and R_3 that are plotted as function of number of DC/OCP cycle in Figure 5.17.
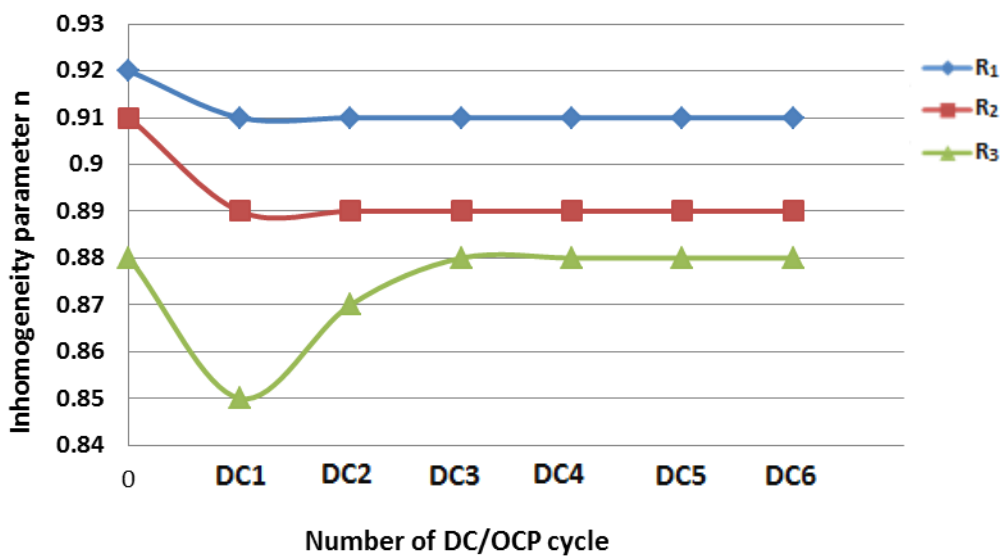
Figure 5.17: Inhomogeneity parameter as a function of number of DC/OCP cycle of the passive film at R_1, R_2 and R_3.

The highest n value is observed for the passive film that formed during 2 h E_{OCP} during R_1, R_2 and R_3. This can be explained by the passive film that formed during 2 h E_{OCP} being more compact and less defective than the passive film formed during

six successive DC/OCP cycles. It can be seen that the *n* values of the passive film formed during 2 h E_{OCP} and six successive DC/OCP cycles during R_1 are the highest followed by those during R_2 then R_3. This can be attributed to the passive film for R_1 being more compact and less defective than of the passive film during R_2 and R_3.

From the obtained results that presented in Table 5.5 and 5.6 and plotted in Figure 5.18, it can be observed that the estimated thickness value of a passive film formed during 2 h E_{OCP} is higher than the one that formed during six successive relaxation times during R_1, R_2 and R_3. Bearing in mind that any passive oxide layer is effectively removed during the DC polarisation step (and then, depending on solution pH, reform in the OCP relaxation period), this can be explained by the growth rate of the passivating film during 2 h E_{OCP} preceding unhindered in neutral salt solution without OH$^-$ ion attack. Whereas, the growth rate of the passivating film during OCP1-OCP6 is progressively hindered by increasing levels of OH$^-$ ion attack, leading to less protective passive film formation on the surface of aluminium substrate. However, the calculated thickness values in Tables 5.5 and 5.6 seem to be more sensible (to the typical values as reported in the previous literatures [172, 173, 175]), but the calculated thickness values that presented in Table 5.6 are the most sensible where an existing porosity in the passive film took in the account.

Regardless of the different thickness values obtained from calculations made using different assumptions, the values for the passive film during R_1 seem always to be thicker (and more dense) than for the passive film during R_2 and, similarly the

passive film of R_2 seems to be thicker (and more dense) than the passive film during R_3.
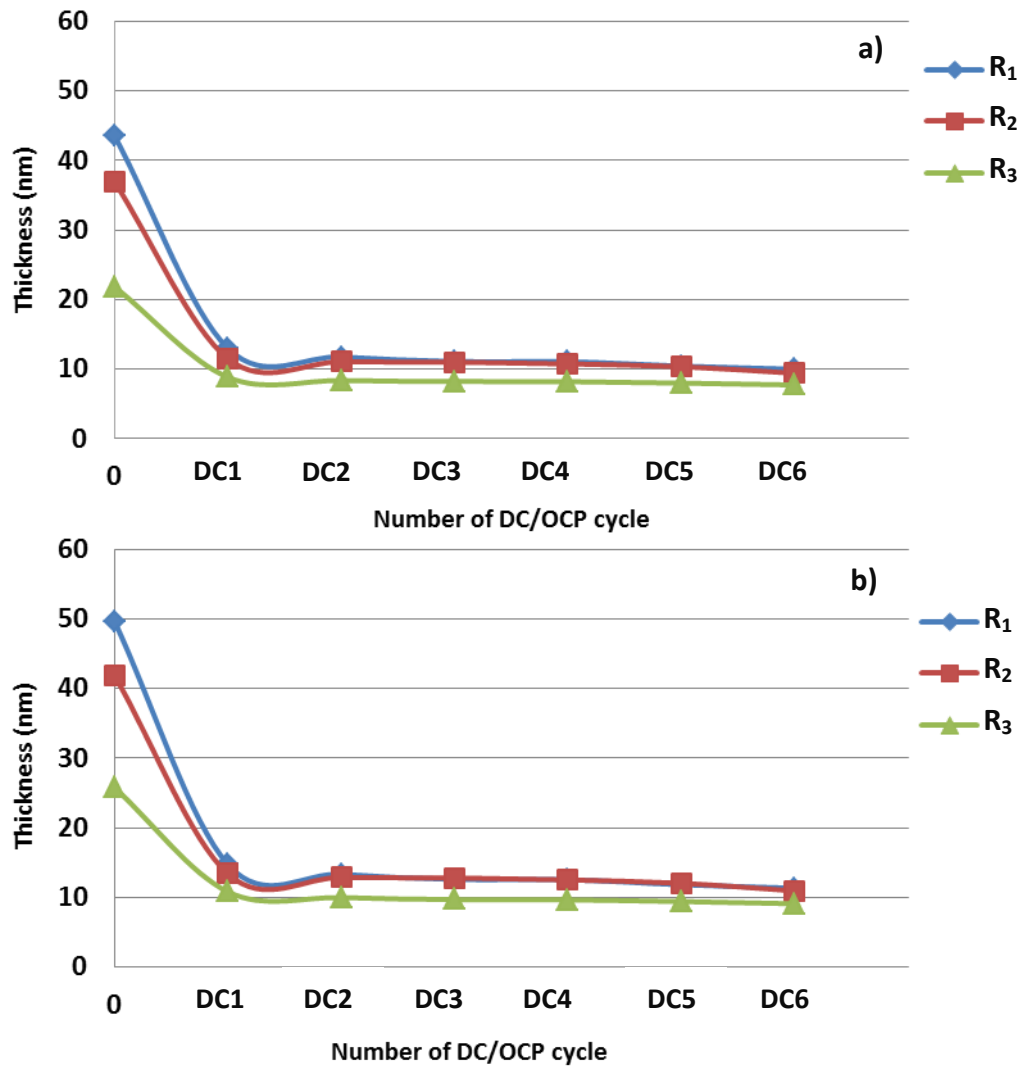
Figure 5.18: Calculated thickness of the passive film as function of DC/OCP cycle during R_1, R_2 and R_3 a) with no porosity and b) with porosity in parallel.

5.3.4 Hydrogen permeation current density during DC cathodic polarisation

In order to explore the rate of hydrogen permeation across the passive film (and how it might change during six successive DC cathodic polarisation cycles) and to study the effect of the permeability on hydrogen adsorption H_{ads}, it was necessary to study the hydrogen permeation current density during DC cathodic polarisation. As ascribed earlier Qin et al. [100] created simulation models (Figure 2.14 p41) that describe the hydrogen permeation process through a passive film. It can be say in Figure 5.19 the evolution of hydrogen permeation current density during DC1 during R_1, R_2 and R_3 shows that the diffusion model (D) appears to be linked directly to the hydrogen permeation current density transients.
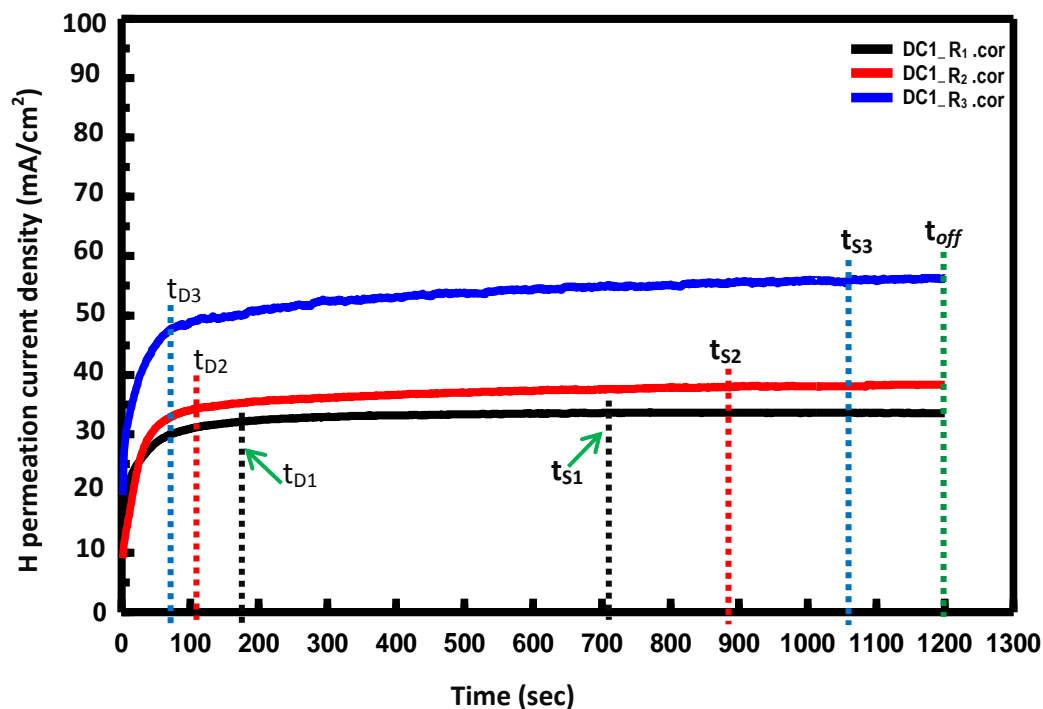
Figure 5.19: Evolution of hydrogen permeation current density during DC1 during R_1, R_2 and R_3.

It can be observed that the hydrogen permeation current density increases rapidly from an initial value (12, 11 and 19 mA/cm^{-2}) to reach a maximum diffusion rate value (31, 35 and 48 mA/cm^{-2}) at diffusion time t_{D1}, t_{D2} and t_{D3} (198, 110 and 97 sec) during R_1, R_2 and R_3, respectively. This diffusion time is consistent with the time lag in stage (I) at t_1 (198, 110 and 97 sec) of the solution pH evolution during DC1 during R_1, R_2 and R_3, respectively (see Figure 5.27 a-c p146), which will be explained broadly in a later in section 5.4.1. It can be observed that hydrogen permeation current density curves after reaching maximum diffusion rate values is slightly increasing until reaches a saturation-state at a time of t_{S1}, t_{S2} and t_{S3} (710, 890 and 1060 sec) during R_1, R_2 and R_3, respectively and remains steady until the DC cathodic polarisation step is terminated at t_{off} (1200 sec). The continued slight increase can be explained by the fact that, although the hydrogen permeation rate through the passive film is no longer increasing, the contribution of aluminate ion gel formation at the passive film/electrolyte interface continues to hinder H_{ads} diffusion towards the passive film. This is consistent with the stage (III) of the solution pH evolution during DC1 (see Figure 5.27 a-c p146) where the increase in solution pH reaches a steady-state at t_{2a} (710, 890 and 1060 sec) during R_1, R_2 and R_3 respectively, due to the aluminate ion enrichment at the passive film/electrolyte interface.

It can be observed in Figure 5.19 that the maximum diffusion rate at t_{D3} during R_3 is the highest, followed by t_{D2} during R_2 then t_{D1} during R_1 respectively, which can be related to the high permeability of the relatively porous passive film during R_3 and

to the high hydrogen ions concentration at the Al_2O_3/electrolyte interface (see stage (I) in Figure 5.27 c). According to the hydrogen evolution reactions 2.23-2.26 (see section 2.8.1 p39), a high concentration of H^+ ions at the Al_2O_3/electrolyte interface leads directly to a high level of H_{ads} since the rate of the reaction 1 (2.23) would be expected to be rapid. However, the concentration of H_{ads} would be decreased, since the rate of H_{abs} via reaction 4 (2.26) would also be expected to be rapid (due to the high permeability of the porous Al_2O_3 film).

In contrast, the maximum diffusion rate up to t_{D1} during R_1 is the lowest (and the slowest to be reached), which can be related to a low hydrogen permeation rate into the passive film due to low permeability of the Al_2O_3 film, which is in this case relatively dense, compared to the passive films during R_2 and R_3. However, the concentration of H_{ads} at Al_2O_3/electrolyte interface would still be high since the rate of reaction 4 would be expected to be slow and the rates of reactions 2 and 3 (2.24 and 2.25) would be expected to be slow, but higher than the rate of the reaction 4. The rates of reaction 2 and 3 depend on the availability of H_{ads} which in turn depends on the H^+ ion concentration at the Al_2O_3/electrolyte interface. However, after application of the first DC/OCP cycle, H^+ ion decay at the Al_2O_3/electrolyte interface would be expected, as the solution pH starts become increasingly alkaline. Therefore, the concentration of H_{ads} at the Al_2O_3/electrolyte interface would be expected to decrease with time.

Table 5.8 presents the total charge (Q_t Coulomb/cm^2) calculated after each DC cathodic polarisation during R_1, R_2 and R_3, which may be attributed to the total

hydrogen ion charge permeating into the passive as H_{ads}. Figure 5.20 shows the total charge Q_t of permeated hydrogen as function of number of DC cathodic polarisation, during R_1, R_2 and R_3 respectively.

Table 5.7: Total charges of hydrogen permeated into the passive film during DC

DC Cathodic polarisation	Q_{R1} Coulomb/cm^2	Q_{R2} Coulomb/cm^2	Q_{R3} Coulomb/cm^2
DC1	37.21	43.66	63.69
DC2	38.62	44.59	66.76
DC3	35.27	41.76	64.98
DC4	35.33	41.85	65.04
DC5	36.11	41.86	65.11
DC6	36.43	42.15	65.33
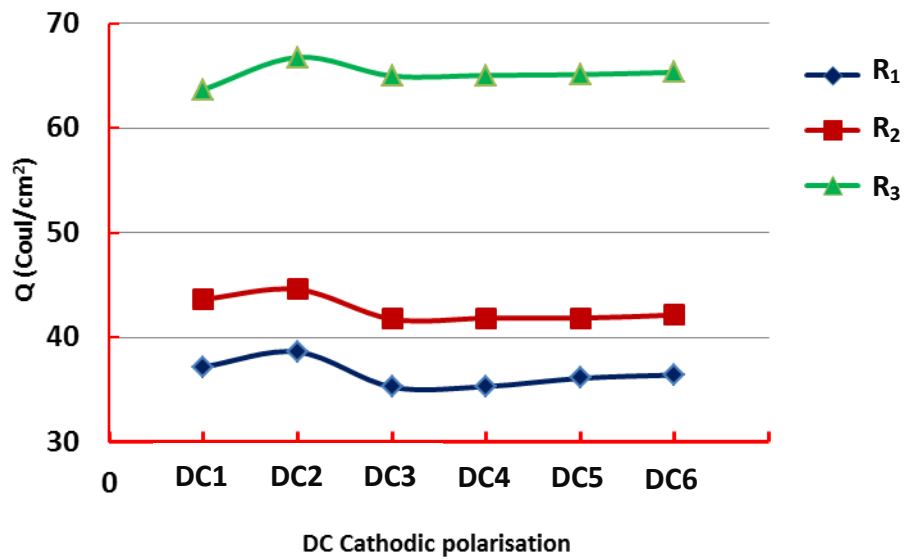
Figure 5.20: The calculated total charge of hydrogen permeated though the passive film during six DC cathodic polarisation cycles during R_1, R_2 and R_3.

It can be seen that the total charge calculated during DC2 is the highest for all three samples, which can be attributed to the higher hydrogen permeation rate through the passive film formed during OCP1 due to its high permeability, which is higher than the permeability of the passive film formed during 2 h E_{OCP} (that the DC1 test

results measure). However, the hydrogen ion decay at the Al_2O_3/electrolyte interface increases with the number of DC cathodic polarisation cycle. The total charge calculated during DC2 is higher than during DC3-DC6, due to hydrogen ion concentration at Al_2O_3/electrolyte interface being higher even though the passive films formed during OCP3-OCP6 have higher permeability than those formed during OCP2.

From Figure 5.20 it can be observed that the total charge curve during DC1-DC6 at R_1 is the lowest compared to R_2 and R_3. This can be attributed to low hydrogen permeability of the passive film, which is in this case thick and relatively dense, compared to the passive film during R_2 and R_3. Conversely, the highest total charges curve during DC1-DC6 is observed at R_3, which can be attributed to the high hydrogen permeation rate through the passive film due to high permeability of Al_2O_3 film, which is thin and highly porous, compared to the passive film during R_2 and R_1. These results are consistent with the evolution of hydrogen permeation current density curves during DC1-DC6 during R_1, R_2 and R_3 that are shown in Figure 5.21.
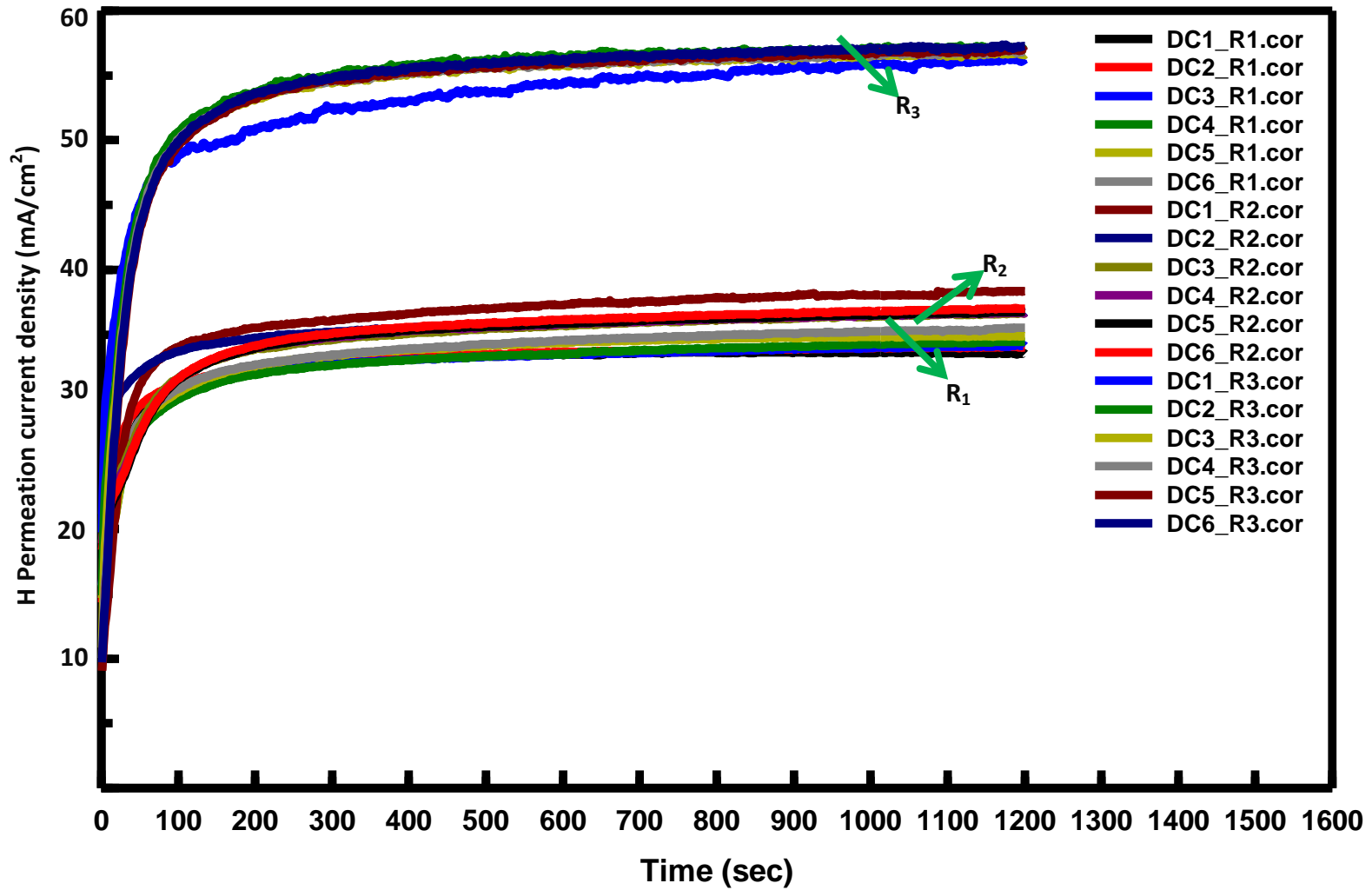
Figure 5.21: Evolution of hydrogen permeation current density curves for Al 6082 alloy during a) R_1, b) R_2 and c) R_3 and during six DC cathodic polarisations.

5.3.5 Relaxation time to reach E_{OCP} after applied DC

Typical graph of evolution of relaxation time to reach E_{OCP} after applied -2 V vs. SCE DC cathodic polarisation is shown in Figure 5.22. This graph describes the four-stages in the evolution of E, during the 3 h relaxation time of OCP1-OCP6 curves (Figure 5.16 (a-c)) during R_1, R_2 and R_3.

Stage (I) represents a slope of rapid increasing in potential from -1.5 V vs. SCE to potential beyond -1.35 V vs. SCE which can instantaneously be observed in the inflection of the current at t_1 (up to approximately 20 sec). During DC cathodic polarisation the standard potential of the cell is -2 V vs. SCE, imposed by a potentiostat. Once the imposed DC cathodic polarisation step is terminated the standard potential of the cell (E_{Cell}°) will be calculated from the standard reduction potentials at the cathode and anode electrodes. Hence the standard reduction potential at the cathode is $E_{H^+/H_2}^{\circ} = 0$ V and the standard reduction potential at the anode is $E_{Cl_2/Cl^-}^{\circ} = -1.358$ V (see Table 2.1 p35). Therefore, the standard potential for the cell E_{Cell}° can be calculated according to the following equation:

$$E_{Cell}^{\circ} = E_{red,cathode}^{\circ} - E_{red,anode}^{\circ} = E_{H^+/H_2}^{\circ} - E_{Cl_2/Cl^-}^{\circ} = 0 - 1.358 = -1.358 \text{ V}$$

Nevertheless, the rapid increase in initial potential beyond -1.35 V. vs SCE at stage (I) during all relaxation OCP1-OCP6 curves is probably due to the E_{Cell}°. The rapid initial increase in potential causes a rapid removal of aluminate gel (agitation due to the electric field) and fast supply of OH⁻ ions towards Al/electrolyte interface. The passive film formed during 2 h E_{OCP} is probably completely dissolved during DC cathodic polarisation leaving the bare Al substrate surface.
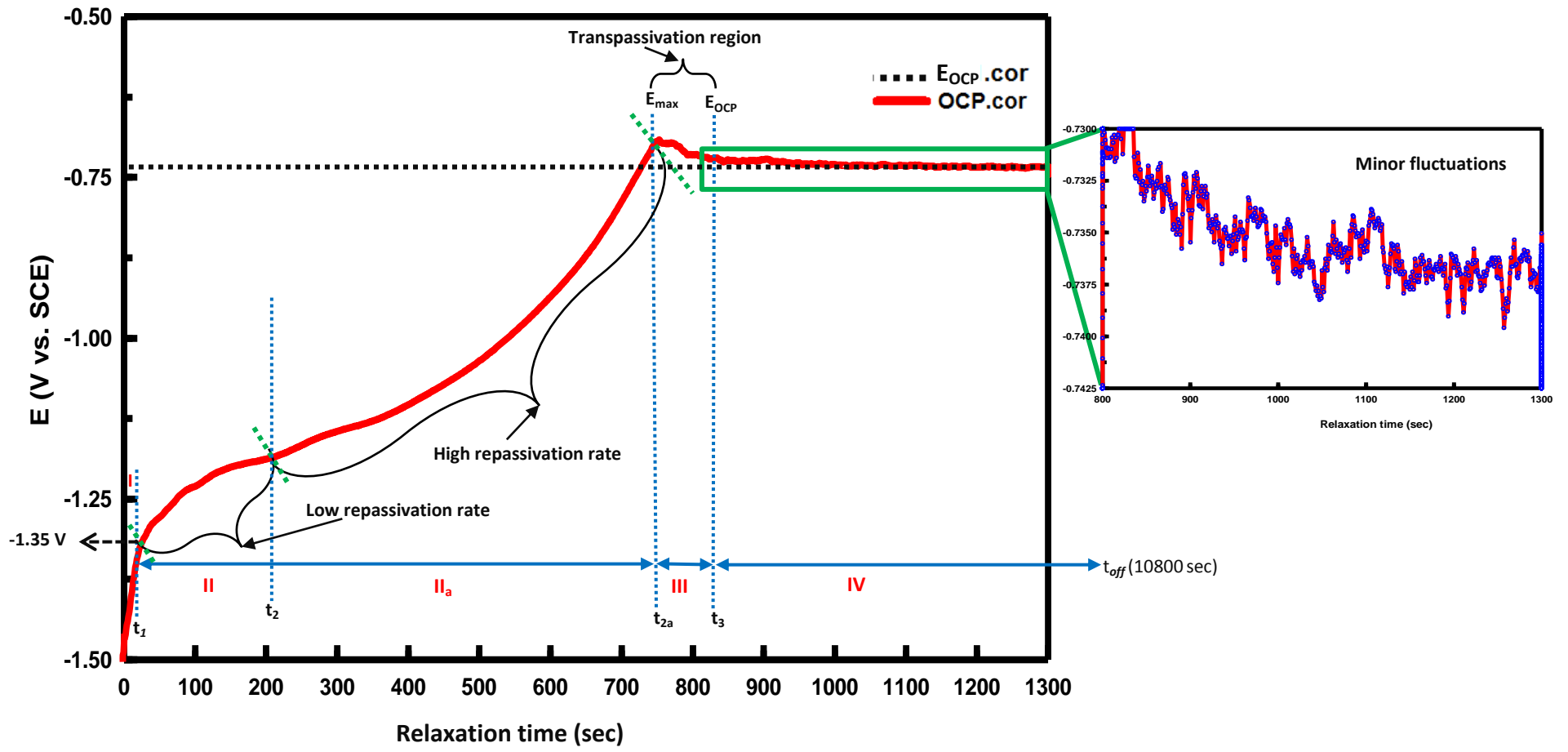
Figure 5.22: Typical graph explains the four stages variation of the evolution of relaxation time to reach E_{OCP}.

Whereas the relaxation time step carries out in alkaline solution, it can be considered an indirect aluminium dissolution by consecutive film formation and dissolution both as a partial of anodic reaction [44]. Therefore, the partial anodic dissolution reaction of Al substrate can be obtained by concurrent electrochemical $Al(OH)_3$ film formation from (reaction 2.12 p15) and chemical dissolution of $Al(OH)_3$ film (reaction 2.13 p15), which can be written as (reaction 2.4 p14). The electron that produced by the anodic reaction (reaction 2.4) will be consumed by the partial cathodic reaction of water (reaction 2.2 p14). The overall corrosion reaction of Al substrate in alkaline solution can be written as (reaction 2.6 p14) by combining the anodic partial (reaction 2.4) and cathodic partial reaction of water (reaction 2.2) [44, 57].

In the sequence of the overall corrosion reaction (reaction 2.6), aluminate ions will form at the passive film/electrolyte interface and delay the dissolution rate of the passive film by slowing down the diffusion of OH^- ions towards the $Al/Al(OH)_3$ interface, thereby enhancing the growth rate of the passive film $Al(OH)_3$.

The second stage represents an increase in anodic potential between t_1 and t_{2a}. This increase can be attributed to the recovery of the sample potential to reach its E_{OCP} value after applied -2 V vs. SCE cathodic polarisation. However, the increase in anodic potential retards the chemical dissolution of the passive film. Therefore, the film growth rate can be enhanced by the increase in anodic potential in alkaline solution [54].

It can be observed that the second stage exhibits two different regions of increasing in anodic potential. The first region represents a low increase in anodic potential in the region between t_1 and t_2. This can be associated to the low repassivation rate that can be explained by the low growth rate of the passivating film due to chemical attack by OH^- ions causing concurrent dissolution. Second, high increase in anodic potential is observed in the later stage up to E_{max} at t_{2a}. This can be associated to a higher film repassivation rate due to aluminate ion enrichment, which enhances the growth rate of passivating film by hindering OH^- ion diffusion towards the passive film/electrolyte interface.

By comparing the two regions that appear in second stage with the concurrent evolution solution pH during stage (I) and (I_a) in (Figure 5.28 a-c p153), it can be concluded that the low repassivation rate (II) is consistent with stage (I) where a slight increase in solution pH can be observed due to enriched OH^- ions and depleted aluminate ions gel after sudden increase in potential from -2 V vs. SCE to potential beyond -1.35 V vs. SCE by the electric field at the Al substrate/electrolyte interface. Whilst, the high repassivation rate (II_a) is consistent with stage (I_a) where the solution pH seems to be higher than that in stage (I), which can be related to the increase in aluminate ion concentration retards the dissolution of the growing passive film.

After reaching E_{max} at t_{2a} the potential rapidly decreases in the cathodic direction until reaching a value close to the final E_{OCP} at t_3 in stage (III). This decrease can be explained by transpassive behaviour (localised corrosion or passive film

breakdown), which is probably caused by the onset of pitting corrosion of the aluminium, where the pitting potential of aluminium corresponds to that at in which the corrosion process is accelerated by diffusion of aggressive anions (such as Cl^- ions) through the passive film [47]. The last stage (IV) represents a steady-state potential around the E_{OCP} value (with minor fluctuations persisting) until the relaxation time terminated at t_{off} (10800 sec). This fluctuation can be associated to the changes of solution pH at the passive film/electrolyte interface (see stage (II) Figure 5.28 a-c).

Figure 5.23 (a-c) shows 2 h E_{OCP} and six successive relaxation times OCP1-OCP6 to reach the E_{OCP} after successive DC cathodic polarisation during R_1, R_2 and R_3. The OCP1-OCP6 curves appear to be composed with the four-stage variation of E(V) that was described earlier in Figure 5.22. It can be observed that during OCP1-OCP6 curves during R_1, R_2 and R_3 the stage (I) represents a slope of rapid increase in anodic potential from applied -2 V vs. SCE to potential value beyond -1.35 V vs. SCE at t_1 (up to approximately 20 sec). This can be associated to the standard potential of the cell E_{Cell}°.

During first relaxation time OCP1 for R_1 the second stage represents an increase in anodic potential from potential beyond -1.35 V (vs. SCE) to E_{max} -0.703 V (vs. SCE) at 686 sec. It can clearly be observed that this increase in anodic potential exhibits two different regions.
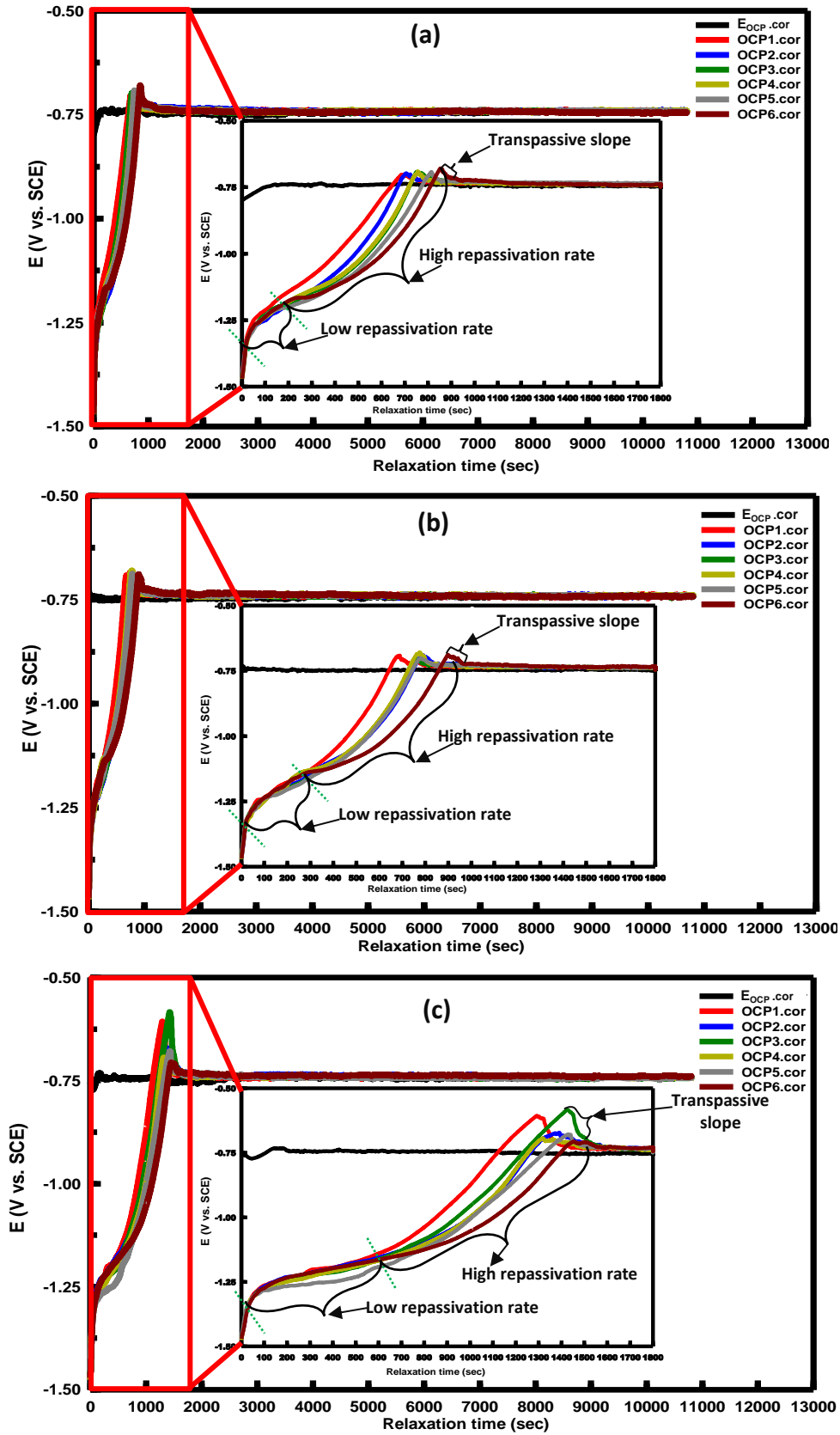
Figure 5.23: The evolutions in 2 h E_{OCP} exposure to 3.5 wt. % NaCl solution and evolution of six successive relaxation times to reach E_{OCP}, after successive six DC cathodic polarisations during a) R_1, b) R_2 and c) R_3.

First, a low increase in anodic potential follows immediately after the stage (I) up to 120 sec (which can be related to low repassivation rate). Second, a higher increase in anodic potential is observed in the later stage up to E_{max} at 686 sec (which can be related to higher repassivation rate).

After reaching E_{max} a rapid decrease in potential to E_{OCP} at 790 sec is observed at stage (III). This can be associated to transpassive behaviour of the passive film. In stage (IV) the potential remains in steady-state at E_{OCP}, with minor fluctuations until the relaxation time OCP1 terminated at t_{off}.

During R_2 during OCP1 the second stage represents an increase in anodic potential from potential beyond -1.35 V (vs. SCE) to E_{max} -0.691 V (vs. SCE) at 690 sec, which also exhibits two different regions. First, low increase in anodic potential followed immediately stage (I) up to 300 sec associated to the low repassivation rate. Second, high increase in anodic potential in the later stage to E_{max} at 580 sec is observed, which related to the high repassivation rate. In stage (III) it can be seen that after reaching E_{max} the potential rapidly decreased to E_{OCP} at 834 sec. This can be associated to the transpassive behaviour. In stage (IV) the potential remained in steady-state at E_{OCP} with minor fluctuations until the relaxation time OCP1 terminated at t_{off}.

By contrast, the second stage during OCP1 during R_3 represents an increase in anodic potential from potential beyond -1.35 V (vs. SCE) to E_{max} -0.604 V (vs. SCE) at 1298 sec. This increase exhibits two different regions. First, the low increase in anodic potential up to 800 sec following the stage (I), which related to the low

repassivation rate. Second, high increase in anodic potential in the later stage to E_{max} at 1298 sec, associated to the high repassivation rate is observed. In stage (III) after reaching the E_{max} a rapid decreased in potential to E_{OCP} at 1455 sec is observed, which can be associated to the transpassive behaviour of the passive film. Stage (IV) represents the steady-state of the potential at E_{OCP} with minor fluctuations that persists until the relaxation time OCP1 terminated at t_{off}.

It can be concluded that all stages during OCP1 have similar behaviour during R_1, R_2 and R_3, but with different period of time. Where the second stage during R_1 is observed to be the shortest followed by R_2 and R_3. This can be related to the rapid $Al(OH)_3$ film formation that formed at Al/electrolyte interface due to less OH^- ion attack, since low OH^- ions concentration can be observed from the upward spike once DC cathodic polarisation terminated. It can be observed that the upward spike during R_2 is higher than that one during R_1 and less than the upward spike during R_3, which suggests that the OH^- ions concentration is the highest for R_3, which can cause the delay of the rate growth of passive film by its chemical attack (and hence the longer timescale of OCP relaxation for this sample).

By comparing the obtained graphs in Figure 5.23 a-c during R_1, R_2 and R_3, it can be deduced that the four-stage variations during in E(V) relaxation time for OCP1-OCP6 have similar behaviour, but with different period of time during the second stage due to the different OH^- ion concentration after DC cathodic polarisation terminated. As explained earlier this stage represents an increase in anodic potential from potential beyond -1.35 V (vs. SCE) to E_{max} for relaxation times OCP2-

OCP6. This increase can be attributed to the repassivation rate of the passive film that apparently exhibits two different regions. First, the low increase in anodic potential following stage (I) (up to 200, 300 and 800 sec during R_1, R_2 and R_3 respectively), which can be related to the low repassivation rates. Second, a higher increase in anodic potential observed in the later stage to E_{max} at t_{2a}, which can be related to higher repassivation rates. The obtained values of E_{max} at t_{2a} during relaxation time OCP1-OCP6 during R_1, R_2 and R_3 are illustrated in Table 5.9.

Table 5.8: E_{max} values at t_2 during relaxation time OCP1-OCP6 during R_1, R_2 and R_3

Relaxation time	E_{max} V. vs SCE			t_2 (sec)		
	R_1	R_2	R_3	R_1	R_2	R_3
OCP1	-0.703	-0.691	-0.604	686	690	1298
OCP2	-0.697	-0.687	-0.672	707	757	1387
OCP3	-0.691	-0.703	-0.583	750	763	1426
OCP4	-0.690	-0.680	-0.693	751	780	1429
OCP5	-0.689	-0.700	-0.677	815	785	1430
OCP6	-0.678	-0.688	-0.706	856	901	1453

From Table 5.9 it can clearly be observed that the time for anodic potential to reach E_{max} during R_1, R_2 and R_3 becomes slower with increasing number of DC polarisation cycles. This can be associated to the gradual retardation of repassivation rate with increasing OH^- ion attack (that lowered the growth rate of a passivating film through competitive dissolution). The increase in OH^- ion concentration with increasing number of DC/OCP cycles can be traced back to the formation of OH^- ions during the relaxation time from the pitting corrosion reactions 2.18-2.20 p22-23. It can be seen that the increase in anodic potential to reach E_{max} value at t_2 during OCP1-OCP6 has proceeded faster for R_1 than during OCP1-OCP6 for R_2 and R_3 respectively, which can be related to the rapid growth rate of the passive film due the rapid

formation of aluminate ions. In stage (III) it can be observed that after reaching E_{max} the potential rapidly decreases to E_{OCP}. The decrease in potential can be related to transpassive behaviour of the passive film that caused by pitting corrosion attack at anodic overpotential. Stage (IV) represents a steady-state of the potential at E_{OCP} with minor fluctuations that persist until the relaxation time terminated at t_{off}.

5.4 Evolution of Solution pH During (AC)DC/OCP/AC Cyclic Testing

In order to obtain information on electrochemical corrosion behaviour at the Al 6082 alloy surface electrode/electrolyte interface during 2 h E_{OCP} exposed to 3.5 wt. % NaCl solution and during repeated of (AC)DC/OCP/AC testing over six cycles, the evolution of solution pH was monitored simultaneously. Figures 5.24 to 5.26 show the evolution of solution pH during 2 h E_{OCP} exposed to 3.5 wt. % NaCl solution and during successive repeats of (AC)DC/OCP/AC cyclic testing during R_1, R_2 and R_3 respectively. It can clearly be observed that the solution pH values during 2 h of E_{OCP} and initial impedance EISi (AC initial measurement) are steady and stable, ending with pH values of 5.6, 5.7 and 4.6 during R_1, R_2 and R_3 respectively before the DC cathodic polarisation started. A sudden downward 'spike' in solution pH is observed immediately with applied -2 V (vs. SCE) DC cathodic polarisation to the electrochemical cell. This sudden 'spike' in pH value is associated to 'hydrogen charging' of the pH probe due to the accumulation of local H^+ ions at the Al 6082 alloy/electrolyte interface. The intensity of this offset in pH value depends on the H^+ ion concentration. During DC1 the downward spike in solution pH reached value of 4.2, 4.3 (weak acidic) during R_1, R_2 respectively, and it reached a value of 3.3 (strong

acidic) during R_3. In contrast, a neutral the downward spike in solution pH value during DC2-DC6 during R_1, R_2 and R_3 is observed. This can be attributed to the low H^+ ion concentration due to hydrogen ion decay after applied DC1. During DC1 the reduction of hydrogen ion to H_{ads} by the reaction 1 (2.23 p39) would be expected to be rapid. However, the concentration of H_{ads} at the surface would be decreased since the rate of H_{abs} via reaction 4 (2.26) would also be expected to be rapid as the permeability of a passive film is high (see Figure 2.13 a p40), or slow, if the permeability of the passive film is low. Thus, the rates of reactions 2 and 3 (2.24 and 2.25 p39) respectively would be higher than the rate of reaction 4 as illustrated in Figure 2.13 (b) p40.

After the DC cathodic polarisation is terminated, the relaxation p to reach the E_{OCP} value starts with a sudden upward 'spike' in solution pH (to an alkaline value) by 'hydroxyl (and probably Chloride) charging' of the pH probe due to rapid accumulation of OH^- and Cl^- ions at the Al /electrolyte interface. It can be seen that the sudden upward 'spike' followed by a more gradual increase in solution pH to become more alkalinity. This increase can be associated to dissolution of the passive film caused by OH^- ion attack in the form of aluminate ions. After certain of time a decrease in solution pH with time is observed, which can be can be explained by the acidification of the solution pH due to the production of water and aluminium chloride ($AlCl_4^-$) complex called "Lewis acid" [186] from pitting corrosion reactions 2.14-2.18 p23 [47].
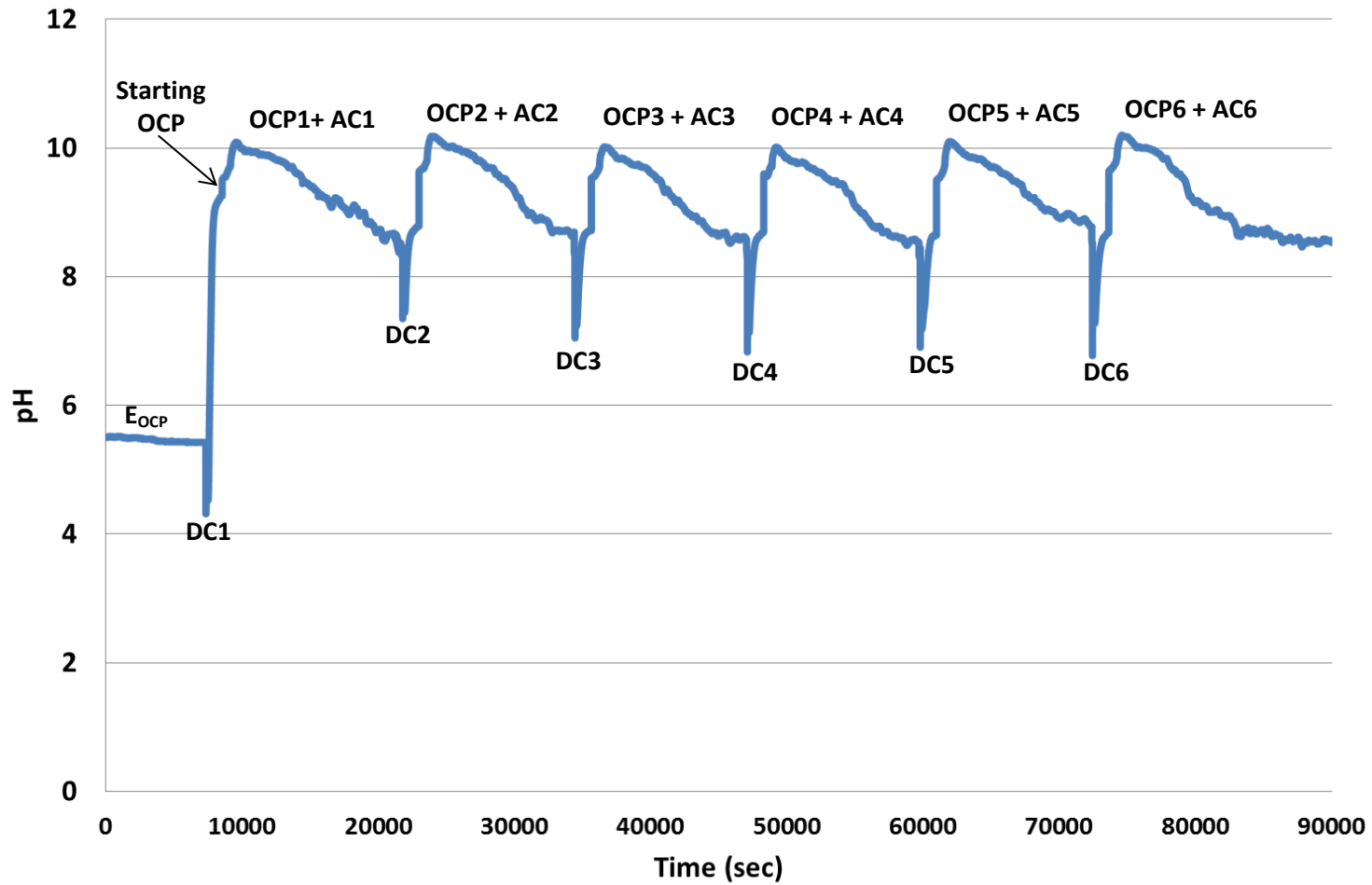
Figure 5.24: Evolution of solution pH vs. time after 2 h E_{OCP} over six successive cycles of (AC)DC/OCP/AC measurements during R_1.
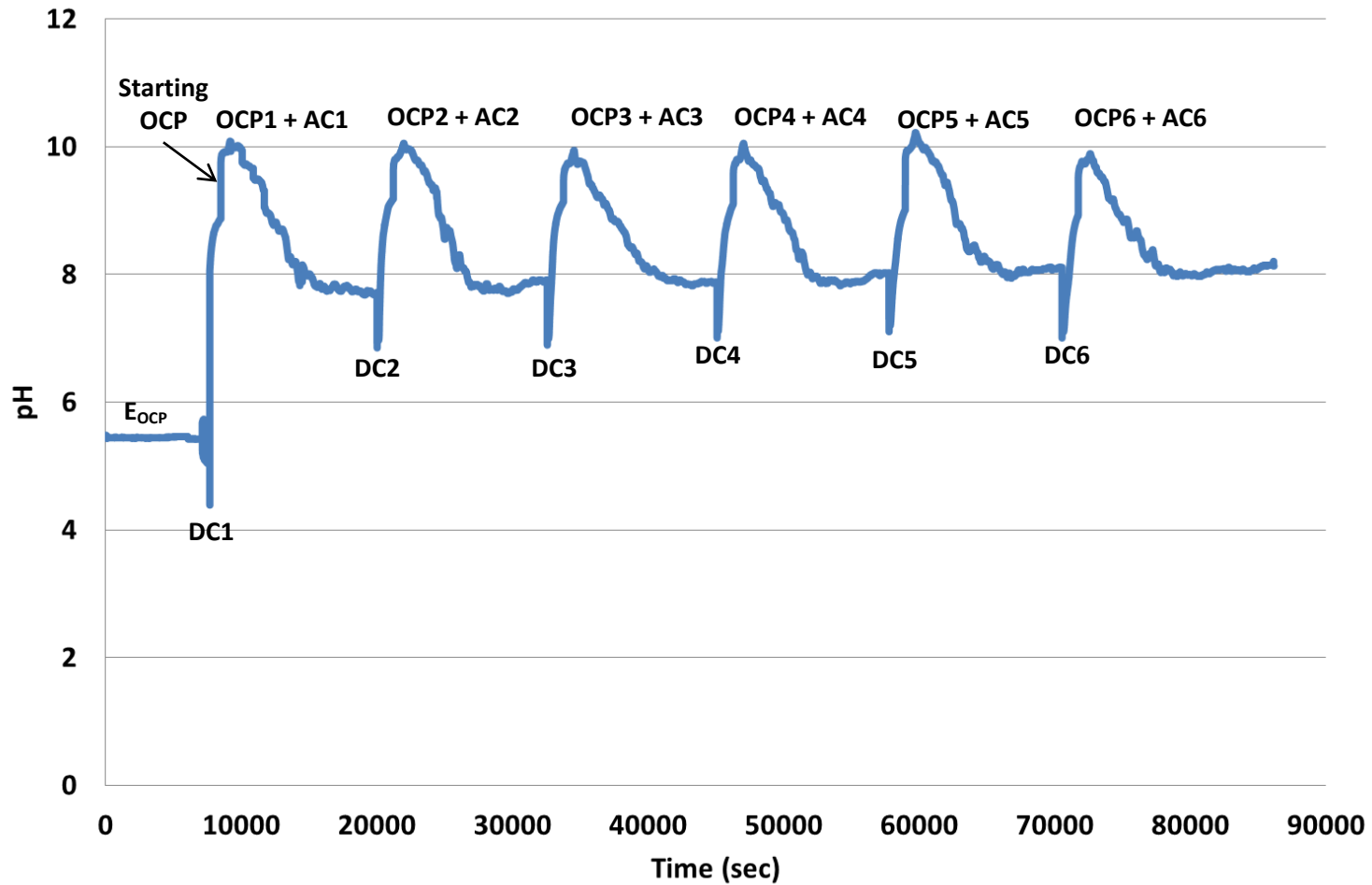
Figure 5.25: Evolution of solution pH vs. time after 2 h E_{OCP} and over six successive cycles of (AC)DC/OCP/AC measurements during R_2.
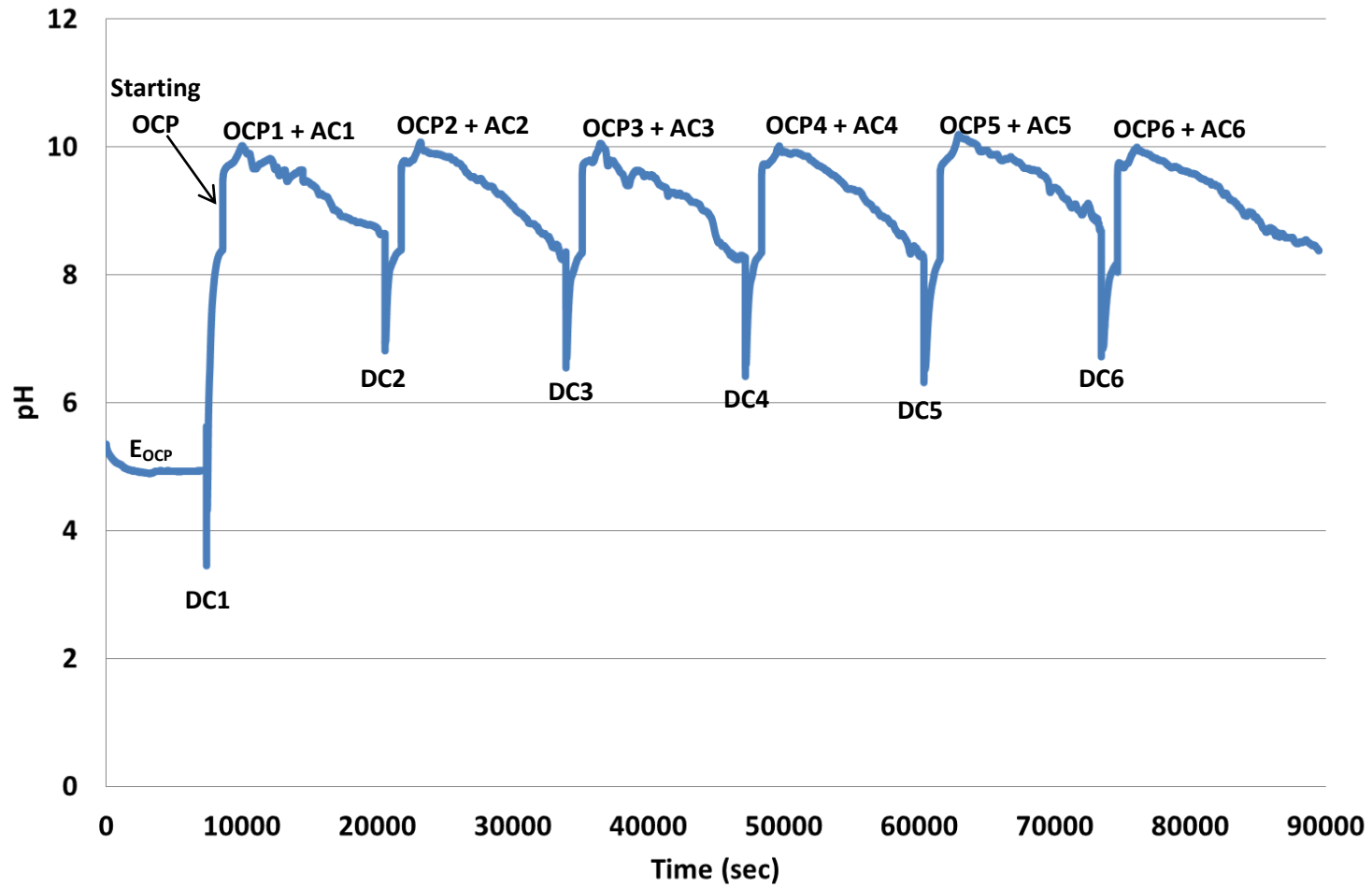
Figure 5.26: Evolution of solution pH vs. time after 2 h E_{OCP} and over six successive cycles of (AC)DC/OCP/AC measurements during R_3.

In order to follow the underlying mechanism of the electrochemical corrosion process during repeated six DC/OCP cycles, it was necessary to study the effects of evolution of solution pH during each individual cycle of DC cathodic polarisation and relaxation time to reach E_{OCP}. Figure 5.27 (a-c) illustrates the evolution of solution pH during each of the six DC cathodic polarisation cycles DC1-DC6 during R_1, R_2 and R_3, whilst Figure 5.28 (a-c) illustrates the evolution of solution pH during each of the six relaxation times OCP1-OCP6 during R_1, R_2 and R_3 (to reach E_{OCP} after each applied DC cathodic polarisation).

5.4.1 Evolution of solution pH during DC cathodic polarisation

The evolution of the solution pH during the successive -2 V DC cathodic polarisation of uncoated Al 6082 alloy samples for three runs R_1, R_2 and R_3 is presented in the three plots of Figure 5.27 (a-c). It can be seen that the evolution of solution pH during DC1-DC6 appears to be composed of three-stages in each case.

The first stage (I) corresponds to the sudden downward 'spike' in solution pH as the -2 V DC cathodic polarisation is initially applied followed immediately by a partial recovery to a somewhat higher value, which remains stable for a certain time (called hereafter the 'time-lag'). The time lag is related to the hydrogen permeation rate through the passive film up to time t_1.
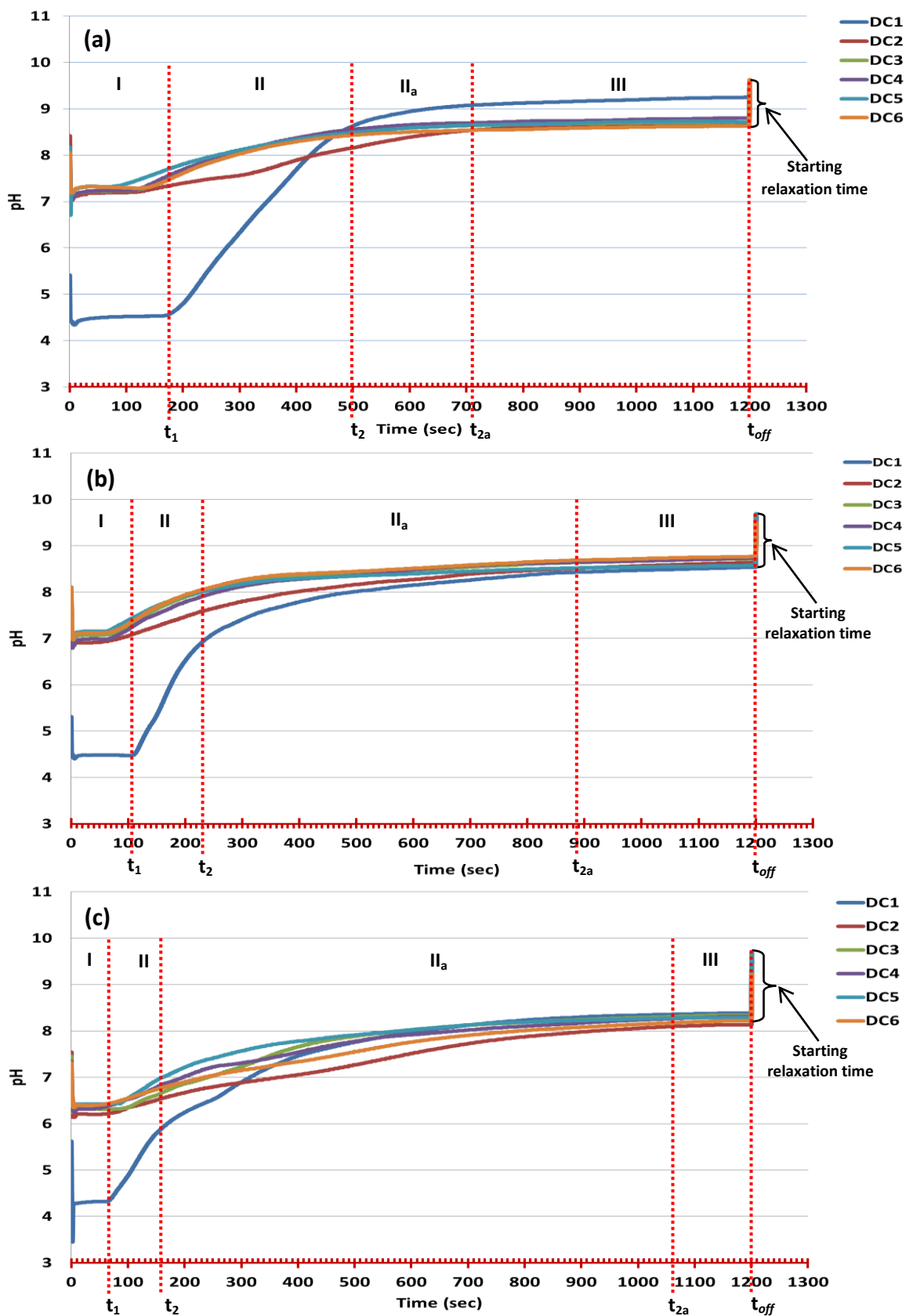
Figure 5.27: Evolution of solution pH over six successive DC cathodic polarisations during a) R_1, b) R_2 and c) R_3.

The second stage represents two different increasing rates; region (II) represents an increase of solution pH between the times t_1 and t_2, which is attributed to an increase in aluminate ion formation caused by the dissolution (and eventual complete removal) of the passive film that formed during 2 h E_{OCP} at DC1 and during the relaxation time at DC2-DC6 via OH^- ion attack.

Stage (II_a) represents the low aluminate ion formation due to low dissolution rate of aluminium substrate by OH^- ions since the dissolution of Al substrate in alkaline solution occurs by indirect dissolution via consecutive film formation and dissolution, which both considered as a partial anodic reaction. The dissolution rate of aluminium substrate will be retarded by aluminate ions enrichment [55]. Aluminate ions tend to accumulate at the Al/electrolyte interface and form viscous layer that hinders OH^- ions to diffuse towards Al/electrolyte interface, thereby showing a steady-state of solution pH value at stage (III) that persists until DC cathodic polarisation terminated at t_{off} (1200 sec) where an upward 'spike' is observed, which referred rapid accumulation of OH^- and Cl^- ions with starting up the relaxation time step.

By comparing these stages during DC1 during R_1, R_2 and R_3, it can be observed that the stage (I) represents a time lag up to t_1 of (198, 110 and 97 sec) during R_1, R_2 and R_3 respectively. Since the time lag is related to the hydrogen permeation rate into the passive film. Therefore, the long-time lag is observed for R_1, which can be attributed to the low hydrogen permeation rate into the passive film, which proceeded slowly due to low permeability of passive film, which is a thick and relatively dense as revealed earlier from EIS data. According to the hydrogen

146

evolution reactions, it can be deduced that the rate of H_{abs} via reaction 4 would also be expected to be slow due to the low permeability of passive film. However, in this case the rate of reactions 2 and 3 would be higher than the rate of reaction 4 as can be explained in Figure 2.13 b p39. Therefore, the stability of the solution pH value during the time lag up to 198 sec is related to the high concentration of H_{ads} at the passive film/electrolyte interface that would tend form H_2 gas via the slow progressive of reactions 2 and 3. However, the permeability of the passive film during R_2 is higher than that one during R_1 where the passive film during R_2 is relatively porous as revealed from EIS data. Therefore, the time lag (110 sec) is observed to be shorter than the time lag for R_1 due to the concentration of H_{ads} at the passive film/electrolyte decreasing since the rate of H_{abs} via reaction 4 would be expected to be rapid. The permeability of the passive film during R_3 is revealed from EIS data to be the highest. Nevertheless, the time lag is observed to be the shortest (97 sec). This can be consistent with hydrogen permeation current density up to t_{D1} (198 sec), t_{D2} (110 sec) and t_{D3} (97 sec) during R_1, R_2 and R_3 respectively as described earlier in Figure 5.19.

By contrast, it can be observed that the time lag during DC2-DC6 is shorter than that of DC1. This can be attributed to the high hydrogen permeation rate into the passive film due to high permeability of the passive film and/or low H^+ ion decay at the passive film/electrolyte interface. Therefore, the rate of H_{abs} via reaction 4 would be expected to be rapid as the permeability of a passive film is high.

During DC1 the stage (II) represents a slope of increasing rate of solution pH up to t_2 (500, 230 and 170 sec) during R_1, R_2 and R_3 respectively. This slope can be related to

the aluminate ion formation by dissolution of the alumina passive film formed during 2 h E_{OCP}, which is probably completely removed from Al substrate surface. For R_1 the slope appeared to be the highest and slowest followed by those during R_2 and R_3. This can be related to the structure and thickness of the alumina passive film that formed during 2 h E_{OCP} in each case. The alumina passive film (As revealed earlier from EIS data and calculated thickness) during R_1 is relatively dense and thick; therefore, the complete dissolution of the alumina film by OH⁻ ion attack takes longer time (500)), in the form of aluminate ions compared to those (220, 160 sec) during R_2 and R_3 respectively.

Stage (II_a) represents a slight increase in solution pH up to t_{2a} (710, 890 and 1060 sec) during R_1, R_2 and R_3, respectively. This slight increase can be attributed to the low rate of aluminate ion formation due to the low dissolution rate of the aluminium substrate by OH⁻ ions. The dissolution rate of aluminium substrate will be retarded by aluminate ions enrichment. The solution pH ultimately reaches a steady-state at t_3 (710, 890 and 1060 sec) during R_1, R_2 and R_3, respectively due to the formation of a viscous layer of aluminate ions as can be observed in stage (III) and it continues until DC cathodic polarisation terminated at t_{off}. It can be observed that the stage (II_a) during R_1 is the shortest, followed by those during R_2 and R_3. This can be related to the fast enrichment of the aluminate ions at the aluminium substrate/electrolyte interface (where it can be seen in stage (II) that the highest pH value at t_2 is during R_1, followed by those R_2 and R_3, depending on aluminate ion concentration.

During DC2-DC6 the second stage presents a low and slow increasing rate in solution pH up to t_{2a} (710, 890 and 1060 sec) during R_1, R_2, R_3 respectively. This can be associated to a lower level of aluminate ion formation, due to rapid dissolution of the alumina film formed during the relaxation time as well as to the progressively lower OH^- ion concentration when DC cathodic polarisation (DC2-DC6), is carried out in an alkaline solution. The dissolution rate of the aluminium substrate will be retarded by aluminate ions enrichment and then solution pH ultimately reaches a steady-state at t_3 (710, 890 and 1060 sec) in stage (III) which continues until DC cathodic polarisation is terminated at t_{off}. It can be noticed that the slope of increasing solution pH in stage (II) does not appear during DC2-DC6, which can be related to a rapid dissolution rate of the thin and porous passive film, which is (compared to the passive film formed during 2 h E_{OCP}) that formed during relaxation time. A rapid upward spike in measured solution pH is observed at t_{off}, when the DC cathodic polarisation is terminated. This can be attributed to the OH^- and Cl^- ions charging at the pH probe.

5.4.2   Evolution of solution pH during relaxation time OCP to reach E_{OCP}

Figure 5.27 (a-c) shows the six successive relaxation times OCP1-OCP6 to reach the E_{OCP} during R_1, R_2 and R_3. The evolution of solution pH appeared to be composed of two stages. The first stage corresponds to two different increasing rates in solution pH; stage (I) represents the rapid increase of solution pH up to t_1 (200, 300 and 600 sec for R_1, R_2 and R_3, respectively) which can be attributed to 'hydroxyl charging' of the pH probe due to the rapid accumulation of OH^- ions at Al/electrolyte interface.
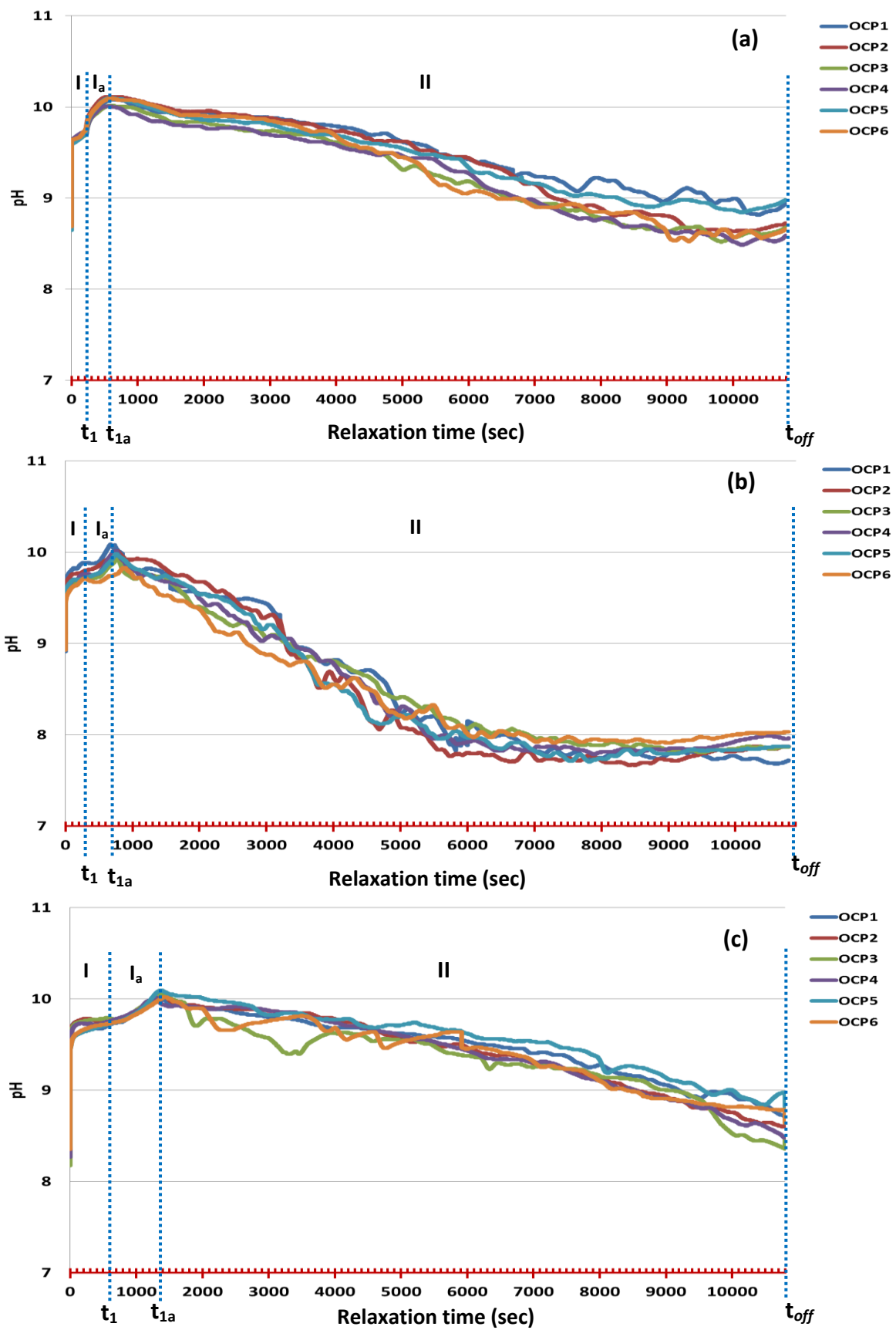
Figure 5.28: Evolution of solution pH during six successive relaxation times after applied DC cathodic polarisation during a) R_1, b) R_2 and c) R_3.

After imposed -2 V vs. SCE DC polarisation terminated the potential rapidly increased beyond to-1.5 V vs. SCE and instantly increases to potential beyond -1.35 V vs. SCE, which caused a rapid agitation to aluminate ion viscous layer and fast supply to OH^- ions towards Al/electrolyte interface. An increase in solution pH is observed up to t_1, which can be attributed to the dissolution of Al substrate in the form of aluminate ions. As mention earlier in section 5.3.5 Figure 5.21 p132 the stage (II) is attributed to the low repassivation rate region due to the OH^- ion attack that lowered the growth rate of the passive film.

Stage (I_a) represents a further increase in solution pH up to t_{1a} (620,780 and 1320) sec during R_1, R_2 and R_3 respectively. This can be related to the gradual increase in aluminate ion formation (enrichment) at Al_2O_3/electrolyte interface that retards the dissolution rate of Al substrate and enhances the growth rate of passivating film Al_2O_3. This stage is consistent with the stage (II_a) in Figure 5.22 that is attributed to the high repassivation rate region of the passive film.

Stage (II) shows a decrease in solution pH value with fluctuations until t_{off} is reached (10800 sec). The decrease can be explained by the acidification of the solution pH, which probably due to the production of water and aluminium chloride ($AlCl_4^-$) complex called "Lewis acid" [186] from the pitting corrosion.

5.5 Summary

Despite the large number of literature studies devoted to the dissolution of aluminium in alkaline media [35, 49, 52, 54, 187], one cannot determine the precise sequence of events by which the overall rate of corrosion is explained easily, because it depends on various starting parameters, such as solution pH, initial potential and presence of the native oxide film on the surface of Al substrate. Therefore, the influence of these parameters on the dissolution behaviour of Al 6082 alloy was evaluated systematically in this Chapter. The main finding of this work can be summarised in the following bullets:

- The influence of both DC cathodic polarisation and solution pH on the electrochemical corrosion behaviour of Al 6082 alloy was investigated using a cyclic test procedure that can be applied in a relatively short period of time (around 24 h).

- During the DC cathodic polarisation the mechanism of hydrogen permeation current and total charge of hydrogen permeated into the passive film are demonstrated. Meanwhile evolution of solution pH demonstrated the changes in solution pH due to aluminate ion formation caused by chemical dissolution of the passive film by OH^- ion attack. Aluminate ions gradually accumulate at Al/electrolyte interface and form a gel layer that can retard the dissolution rate of the passive film and the pH value ultimately reaches a steady-state.

– The growth rate of the new passive film formed during the relaxation time (in alkaline solution) is controlled by the competition between the rate of electrochemical film formation and rate of chemical dissolution.

– EIS data revealed how the passive film damage progressively increased after application of the first DC/OCP cycle.

– The thickness of the passive film formed after 2 h E_{OCP} and after six successive relaxation times was calculated in terms of EIS data and the assumption of the existence (or not) of porosity in the passive film.

– The progressive surface damage of Al 6082 alloy with increasing number of DC/OCP cycles can clearly be seen from the SEM micrographs of surface morphology. This observation is in accord with EIS data that confirms the significant decrease in the impedance response values (R_{ct}) and increase in capacitance values (CPEc_{dl}).

– Investigation and correlation the temporal and spatial evolution between solution pH and electrochemical characteristics on Al 6082 are confirmed.

Chapter Six

Evaluation of Corrosion Behaviour of PVD Al-based Coatings deposited on 17/4 PH steel

6.1   Introduction

In this chapter in order to obtain important new electrochemical information on complex electrically-metallic coating/substrate systems, advanced (AC)DC/OCP/AC cyclic testing with concurrent incorporation of solution pH measurement (as developed in the previous chapter) was used to evaluate three different novel PVD Al-based coatings (AlCr, AlCr(N) and AlCrTi) deposited on 14/7 PH (precipitation hardening) stainless steel substrate, in terms of electrochemical corrosion behaviour. The results obtained are retrieved from two main experimental sets that were carried out to achieve the objectives of this thesis work; i) electrochemical data obtained at initial E_{OCP} and after six successive cycles of (AC)DC/OCP/AC cyclic testing and ii) solution pH data monitored concurrently with the electrochemical test cycle. In addition, the structural and chemical composition of these coatings is characterised using SEM and EDX analysis. Conventional open circuit potential (E_{OCP}) and potentiodynamic polarisation scans are also employed, to determine the corrosion behaviour of PVD Al-based coatings coupled to a 17/4 PH steel substrate (a material used commonly for structural and load-bearing components in aircraft

applications, where toxic protective coatings such as electroplated hard chromium and cadmium are traditionally used).

6.2 Phase composition analysis

X-ray diffraction patterns of PVD Al-based coatings and their 17/4 PH substrate are presented in Figure 6.1. X-ray scans were performed with Bragg-Brentano diffraction method, over the range of 2θ from 20° to 90°.
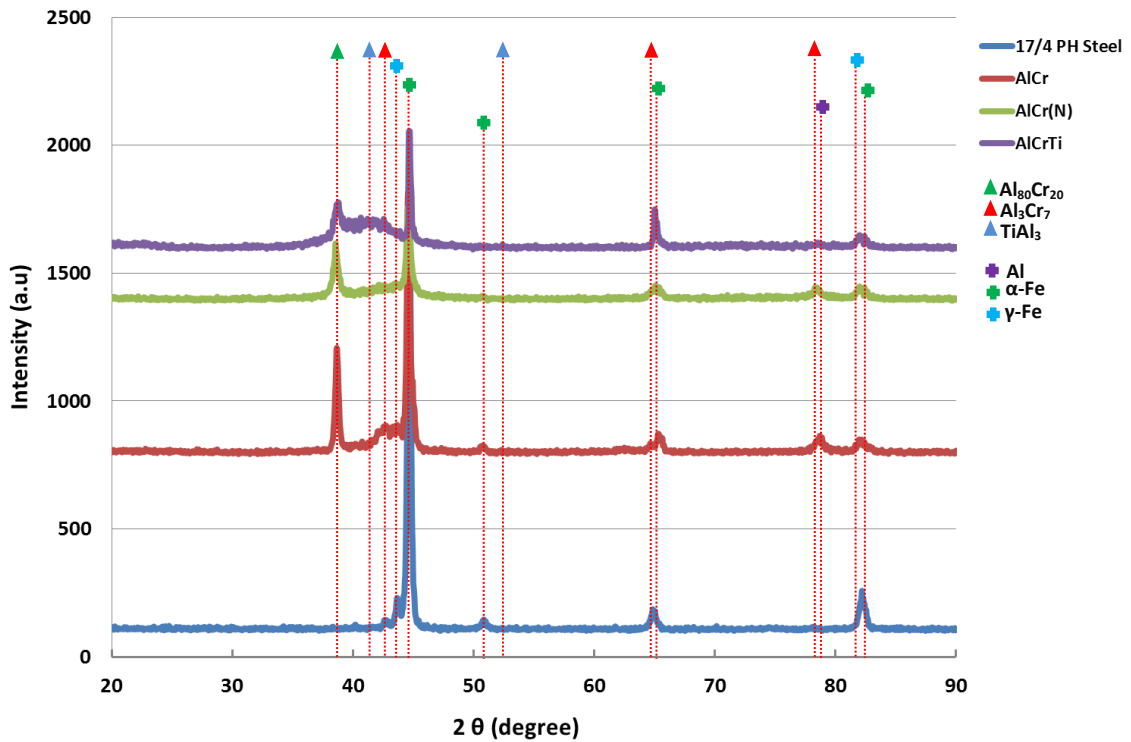
Figure 6.1: X-ray diffraction patterns of uncoated 17/4 PH steel and PVD Al-based coatings deposited on 17/4 PH steel substrate.

It can be seen that for 17/4 PH steel, there are four main peaks in the XRD pattern corresponding to the presence of α-martensite reflection Fe at around 2θ = 45°, 51°, 65°and 83°. In addition, multiple XRD peaks are positioned around 2θ = 43°and 82°, associated (to other lower intensity diffraction) probably martensite and/or delta ferrite.

For AlCr coating deposited on 17/4 PH steel, the XRD pattern exhibited peaks reflected from both structures: the substrate 17/4 PH steel as mentioned above and the coating which was probably $Al_{80}Cr_{20}$ at around $2\theta = 38°$ and Al_3Cr_7 at $2\theta = 44°$.

In AlCr(N) coating the Influence of addition of a nitrogen reactive gas flow rate on the AlCr coating can be seen: a low intensity of peak at $2\theta = 38°$ corresponding to delta $Al_{80}Cr_{20}$ intermetallic phase appeared while the peak Al_3Cr_7 at $2\theta = 44°$ has disappeared. It can be noted the intensities of peaks at $2\theta = 38°$, $2\theta = 65°$, $2\theta = 45°$ and $2\theta = 83°$, were lower indicating a reduction in coating grain size than coatings without nitrogen, (and/or partial amorphisation).

A slight change of all the detected XRD peaks were noted as titanium was added in the AlCrTi coating; the peak at $2\theta = 78°$ disappeared, which corresponds to the absence of Al_3Cr_7 phase. The peak at $2\theta = 43°$ corresponding to $TiAl_3$ phases within Al-based coating.

6.3   Composition and Structural Characterisation

Coating cross-sectional characterisation of PVD Al-based coatings deposited on 17/4 PH steel substrate as received carried out using SEM micrographs and EDX linescan-profile are shown in Figures 6.2 to 6.4.

Figure 6.2 (a-c) shows the SEM micrograph with EDX analysis of the cross-section of AlCr coating. The cross-sectional SEM micrograph (Figure 6.2 a) exhibits a thin Cr base coat (interlayer) and an AlCr top layer. The structure of the coating appears to have pores and be columnar with voids at the chromium interlayer/substrate

interface, and the average thickness of the AlCr coating is about 6.7 μm. According to the EDX linescan-profiles for the constituent elements of AlCr shown in Figure 6.3 c, the distribution of the components revealed in the AlCr cross-section indicates to the high peak intensity of Al, which emphasizes that Al is the main element (with high content about 80 at. %) in the coating composition, while the intensity peak of Cr is moderated (about 20 at. %) with the energy resolution of the EDX detector.

SEM micrograph with EDX analysis of AlCr(N) coating is shown in Figure 6.3 (a-c). A relative thick and dense cross-sectional AlCr(N) coating is shown in the SEM micrograph in Figure 6.3 a, compared to AlCr coating. The coating exhibits uniform structure of Cr base coat (interlayer) and an AlCr(N) top with good bonding to the substrate is apparent and the average thickness of AlCr(N) coating is about 7.8 μm.

EDX linescan-profiles for the constituent elements of AlCr(N) shown in Figure 6.2 c indicates to high intensity peak of Al, while the peak intensity of Cr appears to be low while the intensity of N is very low and undetectable with the energy resolution of the EDX detector.

SEM micrograph with EDX analysis of AlCrTi coating is shown in Figure 6.4 (a-c). The cross-section (Figure 6.4 a) shows a denser, thick and uniform structure compared to AlCr and AlCr(N) coatings.
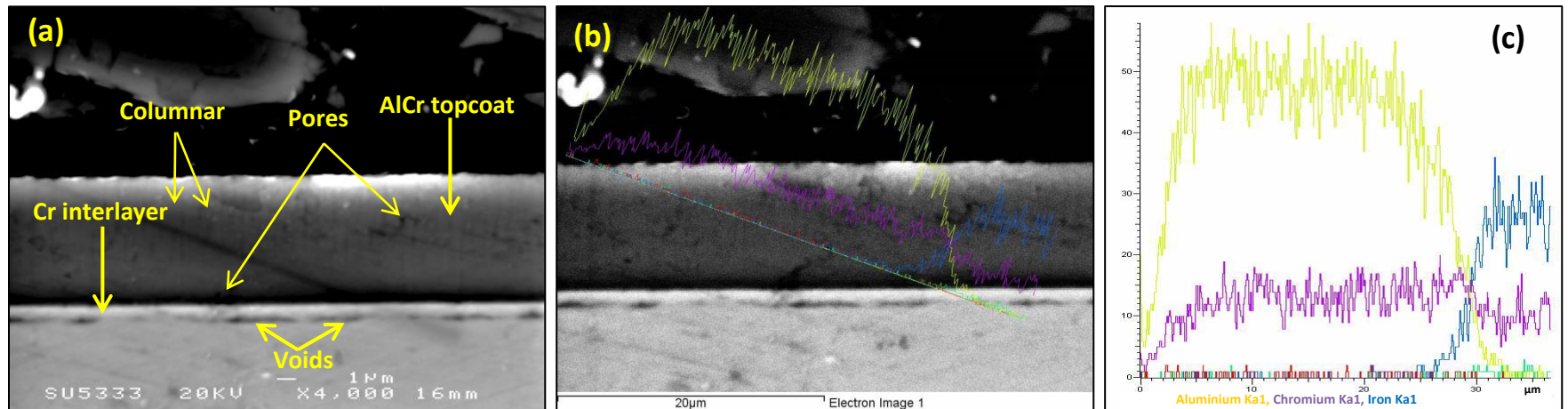
Figure 6.2: SEM & EDX analysis of cross-sectional of AlCr coating: a) SEM surface plane micrograph, (b) SEM micrograph overlaid with EDX linescan-profile and c) EDX linescan-profile of the distribution of constituent elements.
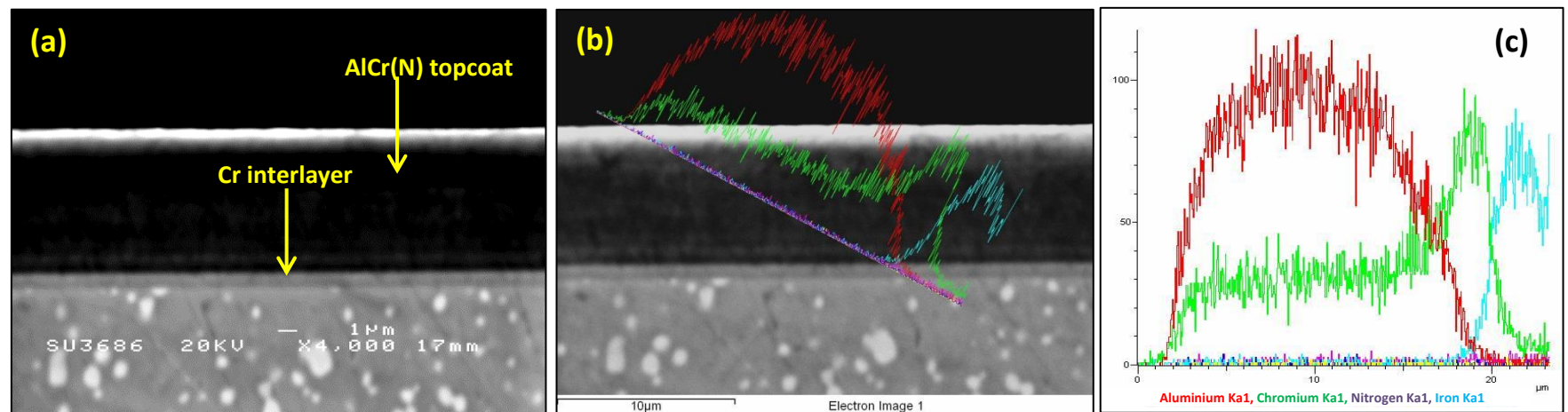
Figure 6.3: SEM & EDX analysis of cross-sectional of AlCr(N) coating: a) SEM surface plane micrograph, (b) SEM micrograph overlaid with EDX linescan-profile and c) EDX linescan-profile of the distribution of constituent elements.
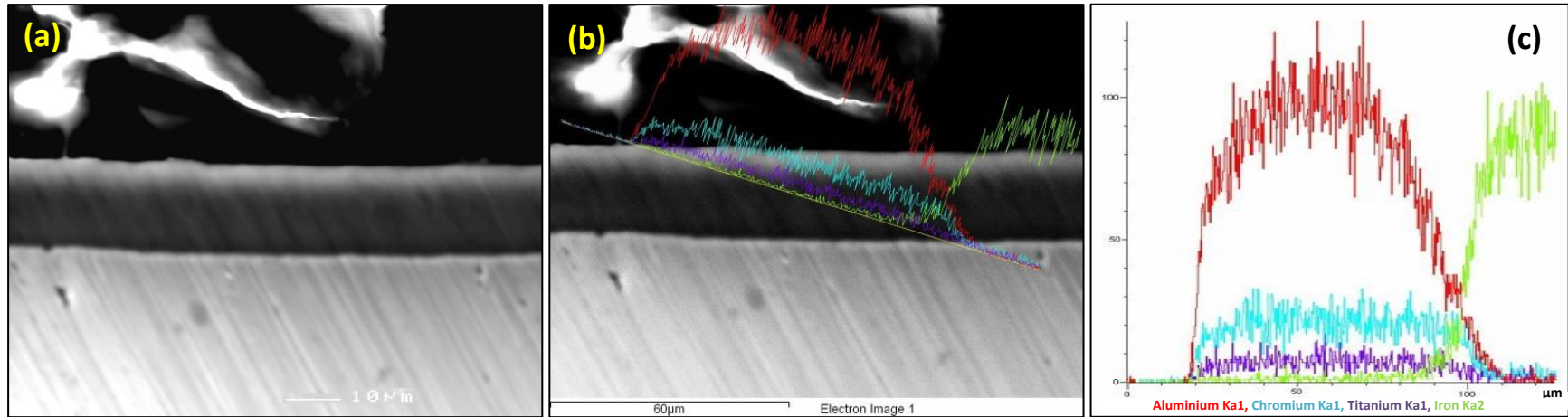
Figure 6.4: SEM & EDX analysis of cross-sectional of AlCrTi coating: a) SEM surface plane micrograph, (b) SEM micrograph overlaid with EDX linescan-profile and c) EDX linescan-profile of the distribution of constituent elements.

However, there appear to be voids at the coating/substrate interface and the average thickness of AlCrTi coating is about 10.6 μm. EDX linescan-profiles for the constituent elements of AlCrTi (Figure 6.4 c) show the distribution of the elements cross-section, which reveals high peak intensity of Al, low peak intensity of Cr while the intensity of Ti is very low and undetectable.

SEM micrographs and EDX analysis of the surface morphologies of PVD Al-based coatings deposited on 17/4 PH steel substrate as received and corroded after six successive DC/OCP cycles are shown in Figures 6.5 6.6 and 6.7.

The surface SEM micrograph analysis of as-received AlCr coating showed in Figure 6.5 a, exhibits compact structure and refinement of surface morphology. The EDX spectrum analysis (Figure 6.5 d) of the as-received AlCr coating shows high peak of Al and low peak of Cr; the chemical composition in at. % is presented in Figure 6.5 d) **inset Table**. In contrast, the corroded surface morphology of AlCr (Figure 6.5 b), exhibits significant degradation of AlCr coating, which manifested as severe pitting damage after six successive DC/OCP cycles.
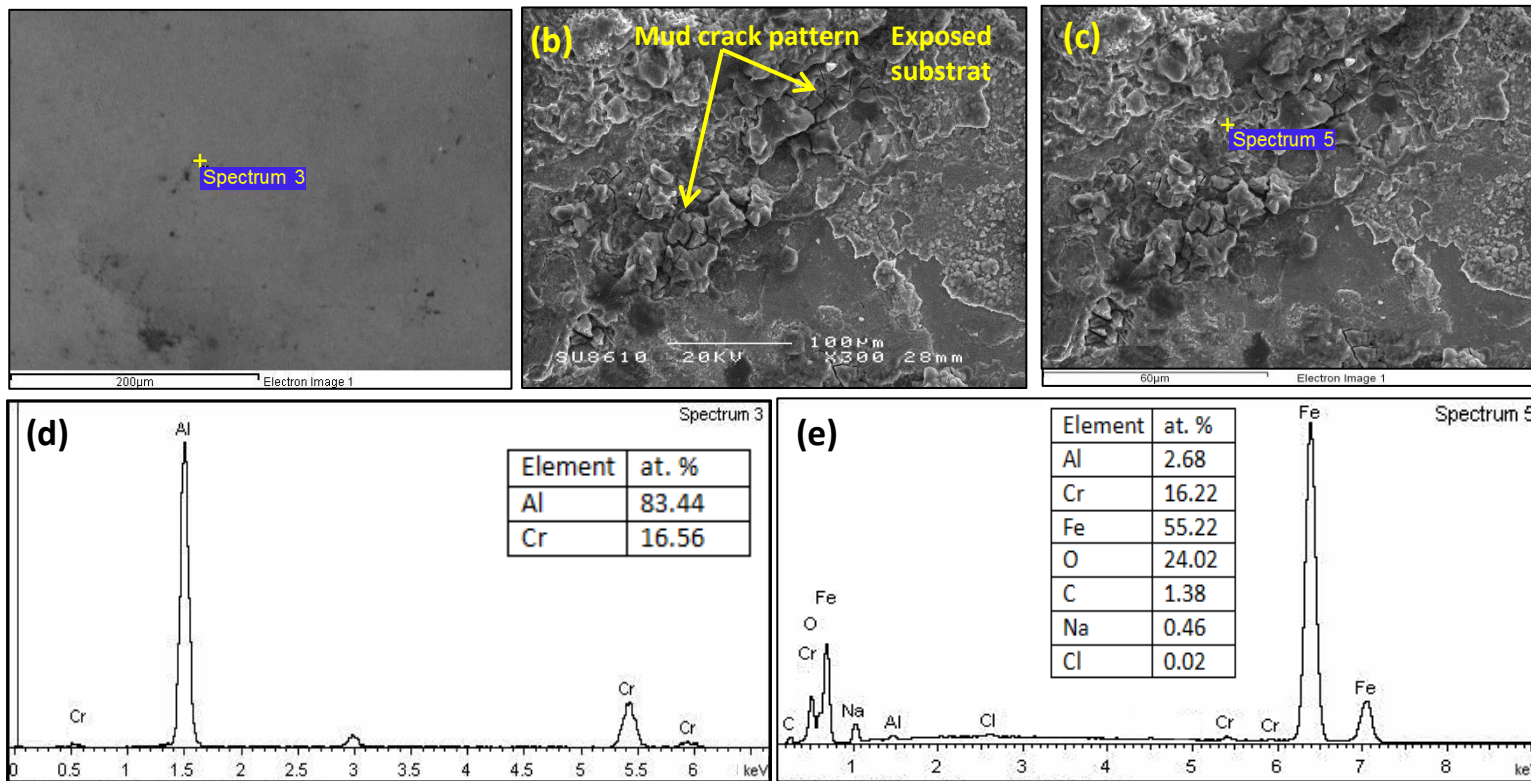
Figure 6.5: SEM micrographs of AlCr coating deposited on 17/4 PH steel: (a) surface morphology plane as-received, (b) corroded surface morphology plane, (d & E) EDX spectrum analysis with inserted table of chemical composition of as-received and corroded coating respectively.

Figure 6.5 e shows the corresponding EDX spectrum analysis of the corroded surface, which exhibits a mixture of chemical composition of AlCr coating and 17/4 PH substrate elements where stronger peaks of Fe, O and Cr are observed compared to original EDX where an intense peak of Al was revealed. This can be associated to the significant degradation of AlCr coating; the chemical composition in at. % is presented in Figure 6.5 e **inset Table**.

The SEM micrograph (Figure 6.6 a) of the surface morphology of as-received AlCr(N) coating reveals a more dense and compact structure compared to AlCr coating. The corresponding EDX spectrum analysis (Figure 6.6 d) exhibits high intensity peak of Al and low intensity peaks of Cr and N the chemical composition in at. % is presented in Figure 6.6 d **inset Table**. In contrast, Figure 6.6 b shows the SEM micrograph of the corroded surface coating after exposure to six successive DC/OCP cycles. The SEM image reveals a partial integrity of coating and exposed area of layers with some microcracks. This can be explained by coating spallation that revealed layers, which can be probably attributed to chrome oxide of 17/4 PH steel that formed on the substrate surface. According to the Figure 6.6 e the EDX spectrum analysis of the corroded surface exhibits a mixture of chemical composition between AlCr(N) coating and the substrate elements where high intensity peaks of the substrate elements Fe, Cr and O are revealed, compared to the main coating element (Al) the chemical composition of corroded surface in at. % is presented in Figure 6.6 e **inset Table**.
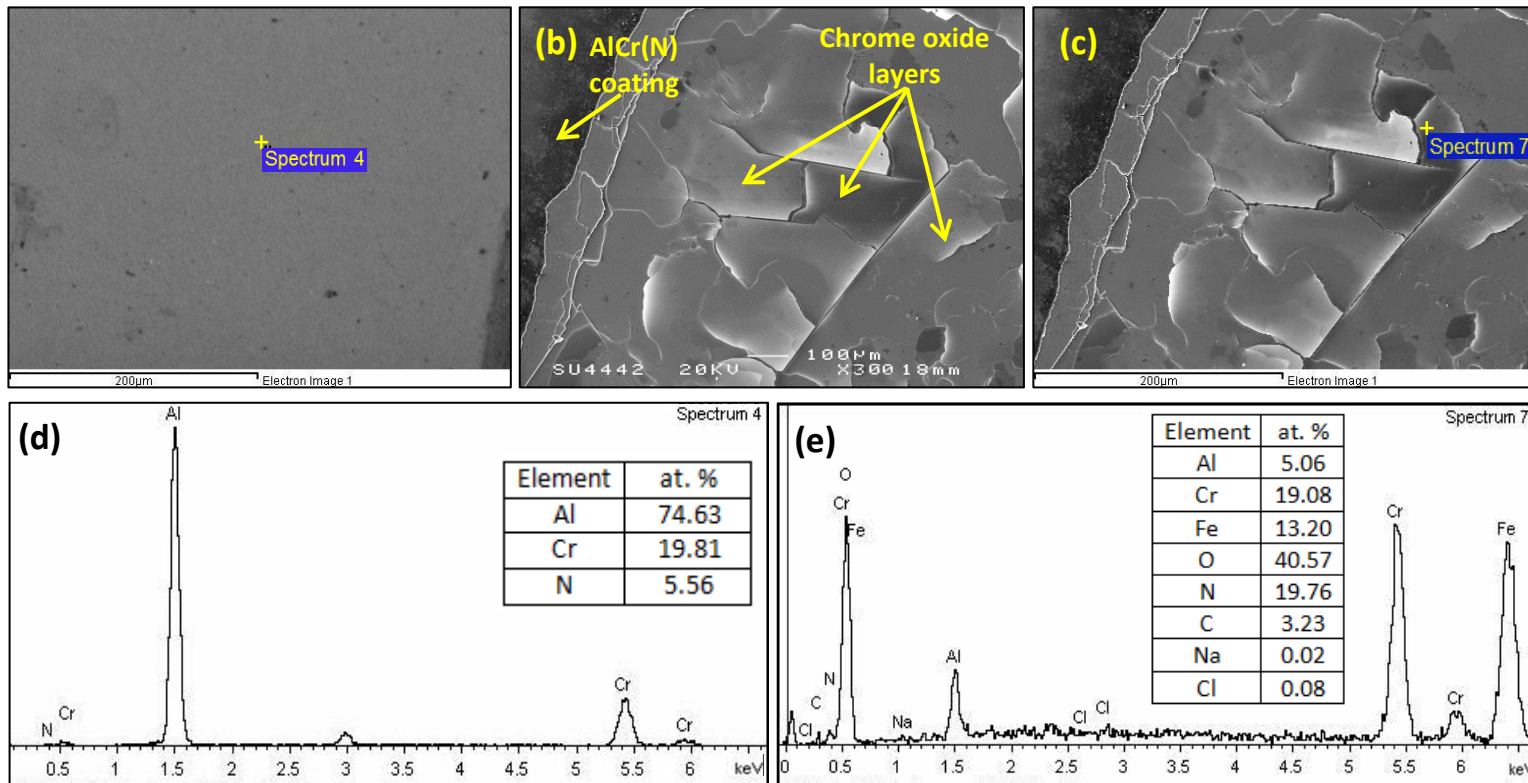
Figure 6.6: SEM micrographs of AlCr(N) coating deposited on 17/4 PH steel: (a) surface morphology plane as-received, (b) corroded surface morphology plane, (d & E) EDX spectrum analysis with inserted table of chemical composition of as-received and corroded coating respectively.

SEM micrograph of as-received surface of AlCrTi coating (Figure 6.6 a) exhibits a bimodal distribution of interconnected phases of primary aluminium matrix and titanium intermetallic content. The addition of titanium to Al-alloys causes separation in Al matrix and intermetallic phase mostly $TiAl_3$ [78]. Figure 6.6 d shows the corresponding EDX spectrum analysis of as-received AlCrTi coating, which indicates high intensity peak of Al and low intensity peaks of Cr and Ti, the chemical composition as-received AlCrTi in at. % is presented in Figure 6.6 d **inset Table**. In contrast the SEM micrograph of corroded surface (Figure 6.6 b) exhibits white precipitates of insoluble $Al(OH)_3$ accumulated at Al matrix/$TiAl_3$ boundary or boundaries. This can be explained by the intergranular corrosion that resulted from the localised galvanic attack. However, the addition of titanium into Al matrix constructs local cathodic sites. therefore intermetallic phase $TiAl_3$ behaves as a cathode, while Al matrix behaves as anode and dissolves [78].

Figure 6.6 c shows the SEM micrograph that exhibits corrosion pits that formed at the Al/$TiAl_3$ boundary, which are covered with white insoluble precipitates of $Al(OH)_3$. The EDX spectrum analysis of corroded AlCrTi coating (Figure 6.6 e) reveals high intensity peaks of Al, Cr and Ti and low intensity peaks of Fe attributed to the low coating degradation due to the contribution of the low galvanic potential difference between this coating and the 17/4 PH steel, leading to a lower driving force of galvanic corrosion. The chemical composition of corroded AlCrTi coating (in at. %) is shown in Figure 6.6 e **inset Table**. The very low intensity peak of Fe can be attributed to the slight corrosion of the metal substrate due to existence of very narrow paths in coating structure caused by pits, which can allow a small amount of electrolyte to penetrate and reach the coating/substrate interface.
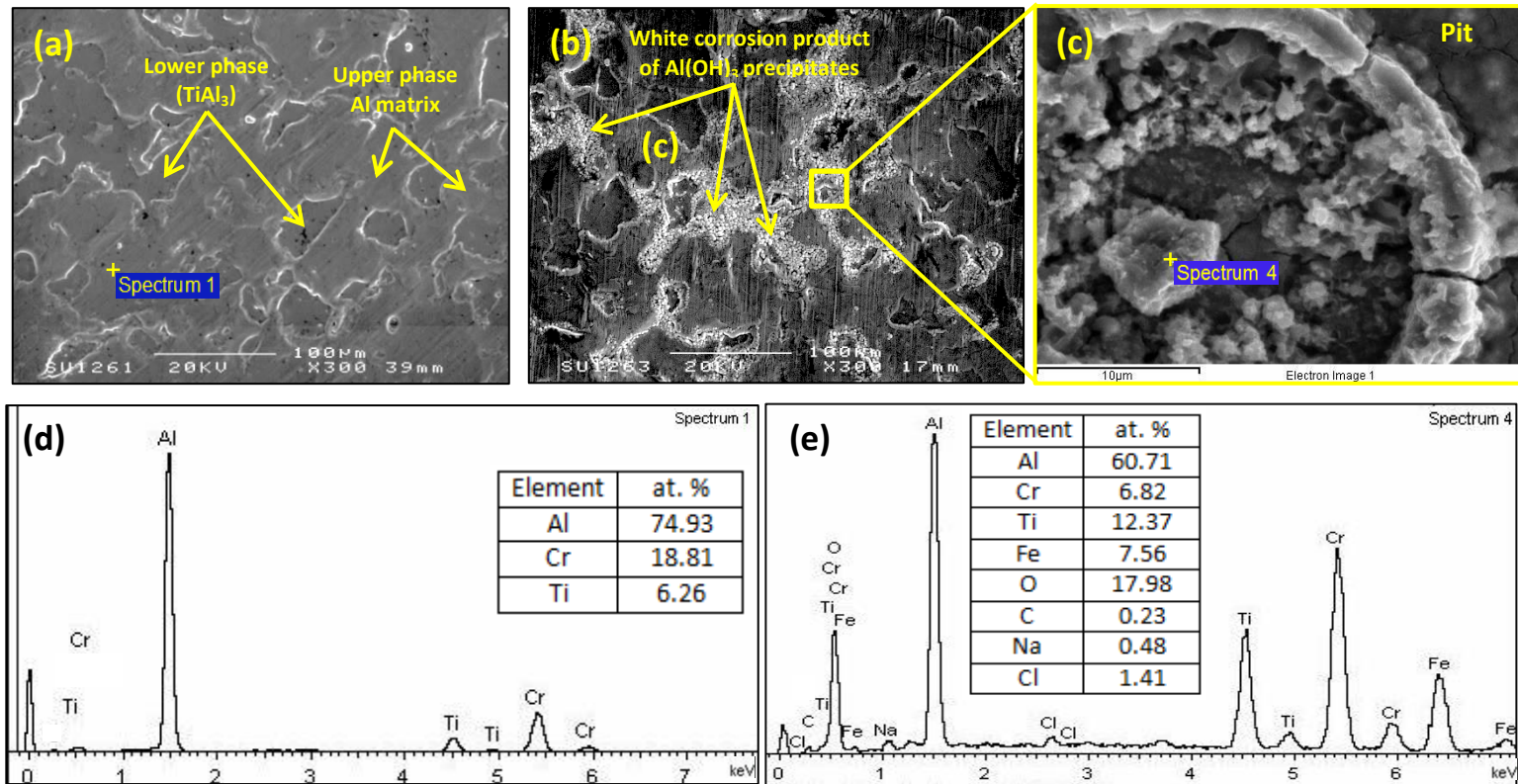
Figure 6.7: SEM micrographs of AlCrTi coating deposited on 17/4 PH steel: (a) surface morphology plane as-received, (b) corroded surface morphology plane, c) SEM micrograph of a pit and (d & e) EDX spectrum analysis with inserted table of chemical composition of as-received and corroded coating, respectively.

Figure 6.8 a-d shows the SEM & EDX analysis of AlCrTi coating to distinguish the bimodal phases that constitute the coating structure. Figure 6.8 a shows an SEM micrograph which pointed to an upper surface in the bimodal structure, which revealed Al matrix as can be confirmed by the corresponding EDX spectrum analysis (Figure 6.8 c) whereas very low intensity peak of Ti with low at. % content is revealed. While higher intensity Ti peak with higher at. % content is revealed (Figure 6.7 d) for the lower surface compared to the upper surface which can be attributed to the intermetallic phase $TiAl_3$.
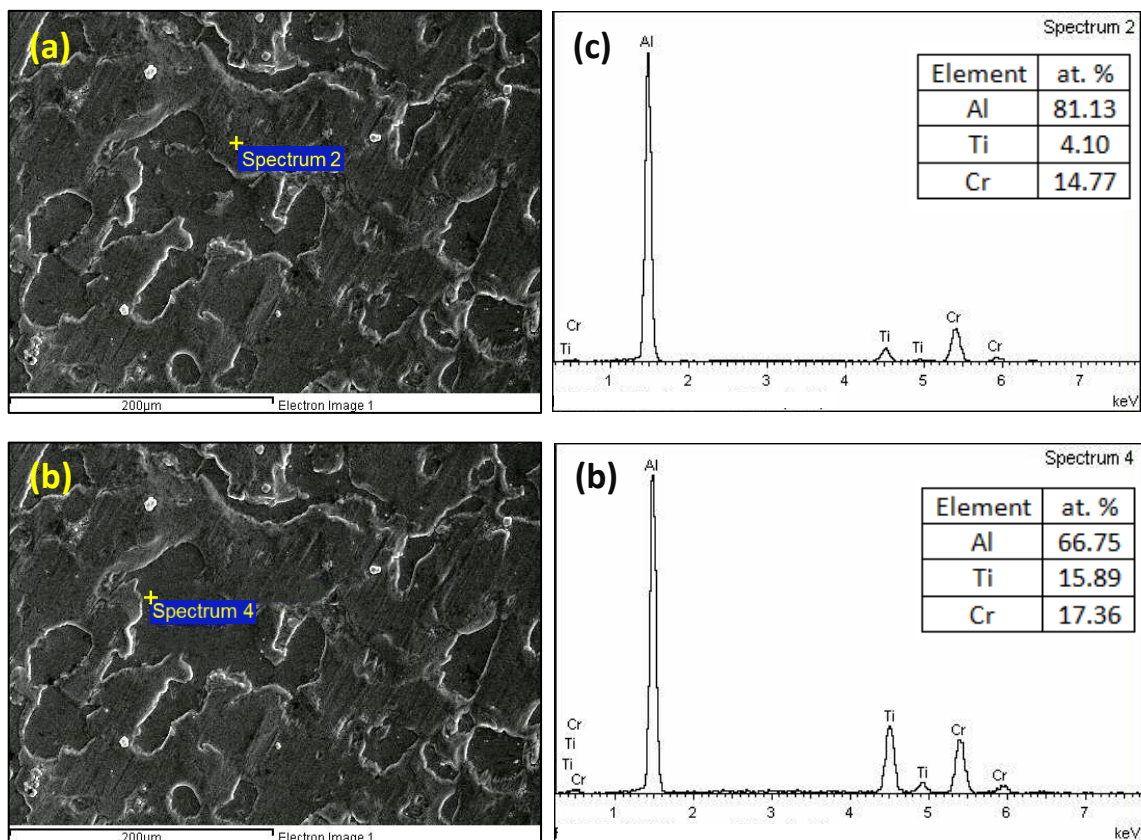
Figure 6.8: SEM & EDX analysis of AlCrTi coating to distinguish bimodal phases; a) SEM micrograph of upper level surface Al matrix and b) SEM micrograph of lower level surface intermetallic phase (c & d) EDX spectrum analysis with inserted table of chemical composition off Al matrix and intermetallic phase respectively.

166

6.4 Electrochemical evaluation techniques

6.4.1 Open circuit potential E_{OCP}

Open circuit potential E_{OCP} curves of 17/4 PH, Al-alloy and PVD Al-based coatings (AlCr, AlCr(N) and AlCrTi) are plotted in Figure 6.9 while the steady-state values after 2 h exposure time in 3.5 wt. % NaCl solution are presented in Table 6.1.

It can clearly be observed that the E_{OCP} values of PVD Al-based coatings and Al 6082 alloy are located at more negative potential compared to the 17/4 PH steel substrate; hence they would be expected to provide a degree of cathodic protection to steel, which means they behave anodicly with respect to the substrate (sacrificial anode).
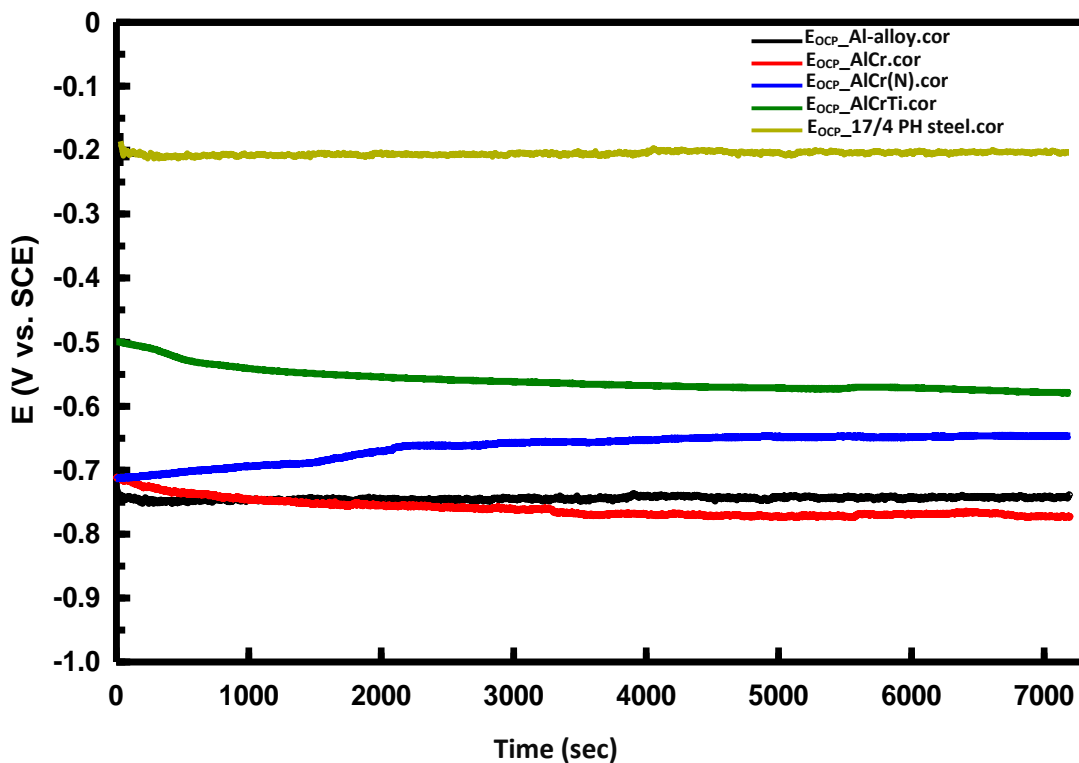
Figure 6.9: Changes of 2 h EOCP exposure to 3.5 wt. % NaCl solution for 17/4 PH substrate, Al 6082 alloy, PVD Al based (AlCr, AlCr(N) and AlCrTi) coatings.

For 17/4 PH steel substrate an E_{OCP} value of -0.252 V vs .SCE was recorded, thus it's cathodic in comparison to the PVD Al-based coatings deposited on it (AlCr, AlCr(N) and AlCrTi). The evolution of E_{OCP} behaviour exhibits a particular trend where the E_{OCP} becomes more noble (-0.646 V vs .SCE) by the addition of nitrogen in AlCr(N) coating compared to E_{OCP} of AlCr coating (-0.773 V vs .SCE) and increasingly noble by addition of titanium in AlCrTi coating (-0.576 V vs. SCE) compared to AlCr and AlCr(N) coatings. It can be observed that the E_{OCP} of Al 6082 alloy is nobler than PVD AlCr coating. This can be related to the addition of ennoblement alloying elements such as Si and Mn to Al.

6.4.2   Potentiodynamic polarisation
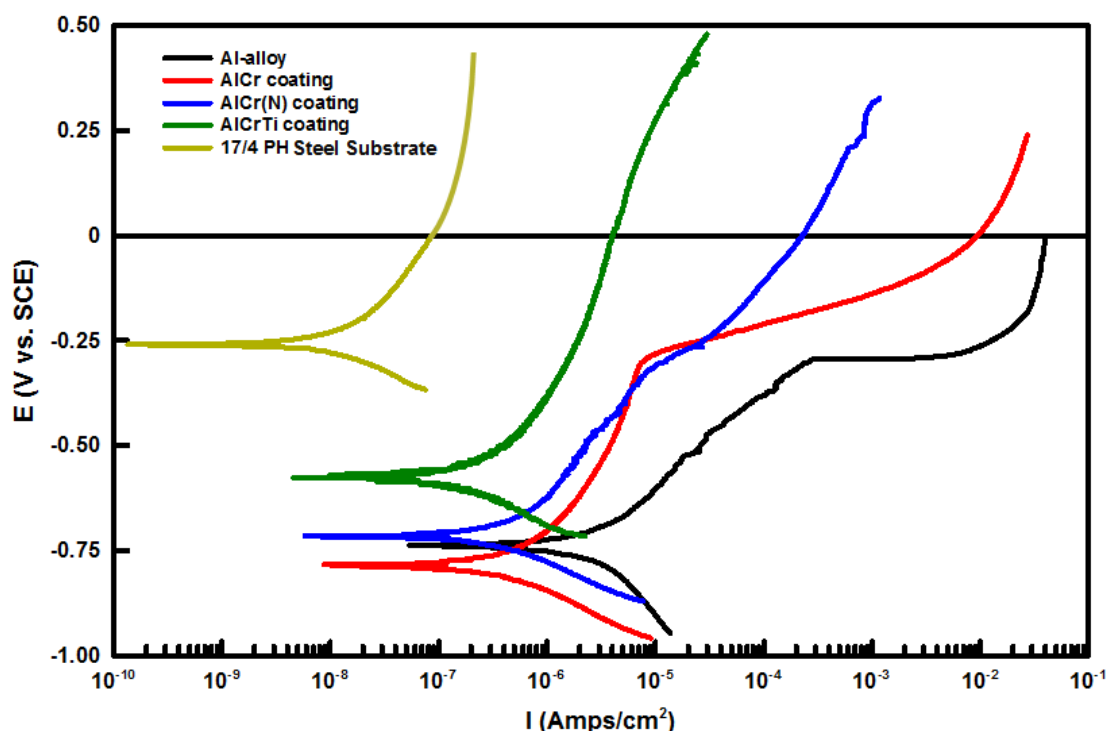
Figure 6.10: Potentiodynamic polarisation curves recorded for 17/4 PH steel substrate, Al 6082 alloy and PVD Al-based coatings (AlCr, AlCr(N) and AlCrTi deposited on 17/4 PH steel.

Figure 6.10 shows typical potentiodynamic polarisation curves obtained after 2 h E_{OCP} exposure to 3.5 wt. % NaCl solution for 17/4 PH steel substrate, Al 6082 alloy and PVD Al-based coatings deposited on 17/4 PH steel. The polarisation curves appear to reveal 17/4 PH steel has the strongest passivation tendency compared to Al 6082 alloy and PVD Al-based coatings. The substrate shows a spontaneous passivation leading to an insignificant increase in anodic current density, suggesting that the 17/4 PH steel substrate is mainly inactive in 3.5 wt. % NaCl solution due to high corrosion resistance induced by the contribution of chromium in its composition. There was no evidence of pitting corrosion potential E_{pit} to be seen in the polarisation curve of 17/4 PH steel.

Table 6.1: E_{OPC}, corrosion potential, corrosion current, pitting and polarisation resistance values of Al 6082 alloy and PVD Al-based coatings deposited on 17/4 PH.

Materials	E_{OCP} (mV)	E_{corr} (mV)	I_{corr} ($\mu A/cm^2$)	E_{pit} (mV)	β_a (mV/decade)	β_b (mV/decade)	R_p (Ωcm^{-2})
Al-alloy	-748	-755	1.084	-295	174.3	164.8	84.7
AlCr	- 775	- 778	0.445	- 300	166.8	126.7	71.15
AlCr(N)	- 646	- 716	0.312	-	180.5	116.2	99.16
AlCrTi	- 576	-579	0.107	-	247.5	166.4	196.64
17/4 PH	- 252	- 252	0.025	-	494	79.7	229.5

The polarisation curve obtained for AlCrTi coating shows a similar behaviour to that of 17/4 PH steel substrate and shows spontaneous passivation of the coating, which continued until the polarisation terminated with slight increase in anodic current density compared to 17/4 PH steel. This relative inactivity can be related to the ennoblement effect due to the combined influence of chromium and titanium that enhanced the corrosion resistance of the coating as well as titanium tending to reduce coating porosity by the relative grains refinement. From Table 6.1, the

relative low corrosion potential difference between AlCrTi coating and 17/4 PH substrate is indicative of a lower driving force for galvanic corrosion.

For AlCr(N) coating the polarisation curve exhibited passive anodic behaviour, which is quite similar to that of AlCrTi coating but, with lower corrosion potential and they are close in anodic current density. This passivity behaviour of the coating appeared to be due to the combined effect of chromium and nitrogen that leads to enhanced corrosion resistance of the coated system as well as nitrogen tending to reduce the coating porosity, as shown in the SEM micrograph of Figure 6.6 a where a relatively dense coating was revealed.

For AlCr coating deposited on 17/4 PH steel substrate the polarisation curve exhibits a typical very active anodic behaviour. An initial passivation period was observed, followed by a gradual increment in corrosion current density at very high anodic overpotential, which can be related to initiation and propagation of pits. According to Table 6.1 a relatively high corrosion potential difference between AlCr coating and 17/4 PH steel substrate demonstrates a strong affinity of the coating for sacrificial protection of the substrate. The onset of coating pitting corrosion potential at -300 mV vs. SCE is observed. The polarisation curve obtained for Al 6082 alloy shows a large passivation period followed by a gradual increment in corrosion current density. The corrosion potential recorded for this alloy was -0.777 V (vs. SCE) . Furthermore, the pitting potential is at about -0.295 V vs .SCE, which is less negative compared to AlCr coating deposited on 14/7 PH steel.

Figure 6.11 shows the initial behaviour of the potential during 2 h E_{OCP} (before application of the potentiodynamic polarisation test cycle and during the 3 h E_{OCP} before application of the (AC)/DC/OCP/AC cyclic test to the three samples of PVD Al-based coatings deposited on 17/4 PH steel substrate are. It can be observed that the initial potential of AlCr during 2 h E_{OCP} decreased from initial potential value of -0.710 V vs. SCE to a value of -0.775 V vs. SCE at 4500 sec. This decrease can be related to the dissolution of the native oxide film, which is probably Al_2O_3 film that formed during sample preparation.
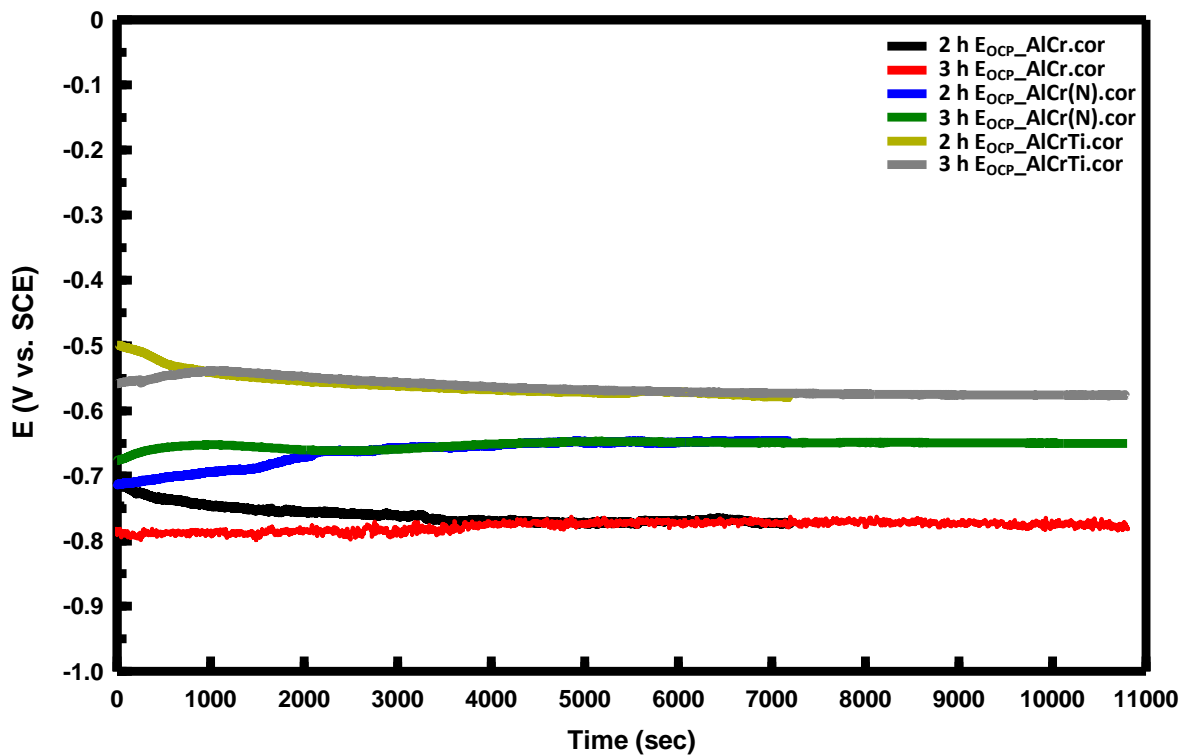
Figure 6.11: the evolution of open circuit potential during 2 h E_{OCP} before application of the potentiodynamic polarisation test and during 3 h E_{OCP} before application of the (AC)/DC/OCP/AC cyclic test to PVD Al-based coatings deposited on 17/4 PH steel.

The evolution of potential during 3 h E_{OCP} appears to exhibit slight increase from initial potential -0.779 V vs. SCE to a value of -0.775 V vs. SCE with only minor fluctuations at 4500 sec. The slight increase can be explained by the growth of an $Al(OH)_3$ layer on the surface of the AlCr coating. The fluctuation is probably attributed to the porosity of the passive film due to the changes in surface morphology. A temporary non-uniform dissolution/recrystallization of $Al(OH)_3$ (because of the high corrosion potential difference between the coating and the substrate), $Al(OH)_3$ may cause to gradually changes to Al_2O_3 with time [161, 168, 169]. This can be consistent with the evolution of solution pH during 3 h E_{OCP} for AlCr (Figure 6.21) that shows minor fluctuations with time. Eventually, the passive film that formed on the surface of AlCr is probably a porous film consisting a combination oxides of $(Al,Cr)_2O_3$.

For AlCr(N) the evolution of potential during 2 h E_{OCP} exhibits a gradual increase from an initial potential value of -0.713 V vs. SCE to -0.646 V vs. SCE at 2000 sec, remaining constant at this value until the end of E_{OCP}. This increase can be attributed to the formation of the $Al(OH)_3$ that gradually changes to Al_2O_3 oxide film on the surface of the AlCr(N) coating. Whilst, the evolution of 3 h E_{OCP} exhibits a slight increase in potential from initial potential value of -0.676 V vs. SCE to value of -0.650 V vs. SCE at 2000 sec, and it remained constant at this value until the end of E_{OCP}. This slight increase in potential at the initial stage attributed to the growth of the $Al(OH)_3$ that changes to Al_2O_3 on the surface of AlCr(N). However, the existence of nitrogen in the AlCr(N) coating tends to reduce the coating porosity as well as the

passive film porosity. Therefore, a dense passive film consisting a mixture of (Al, Cr)$_2$O$_3$ oxides is probably formed on the surface of AlCr(N) coating.

The evolution of potential of AlCrTi during 2 h E_{OCP} exhibits a slight decrease, from an initial potential -0.499 V vs. SCE to -0.576 V vs. SCE at 800 sec, remained constant at this value until the end of E_{OCP} test. The slight decrease can be attributed to the dissolution of the native Al$_2$O$_3$ film that formed during sample preparation. The evolution of potential during 3 h E_{OCP} exhibits an increase in potential from initial potential value of -0.558 V vs. SCE to value of -0.576 V vs. SCE at 800 sec, remained constant at this value until the end of E_{OCP}. This increase can be attributed to the growth of Al(OH)$_3$, which is probably consisting of ternary composition of very protective oxides of Al$_2$O$_3$, Cr$_2$O$_3$ and TiO$_2$ in the form (Al, Cr)$_2$ Ti$_2$ O$_7$ on the surface of the AlCrTi, promotes this film to be more compact and more resistant than that of the AlCr and AlCr(N).

It can be observed that the changes in potential in both 2 h and 3 h E_{OCP} cases occurred at the same time (4500, 2000 and 800 sec) for AlCr, AlCr(N) and AlCrTi respectively. The changes in potential during E_{OCP} of AlCrTi coating occurred in shorter time than for AlCr(N) and AlCr. This can probably be related to the contribution of the relatively small corrosion potential difference between AlCrTi coating coupled to 17/4 PH steel substrate which causes a lower driving force of the galvanic corrosion.

1.1.1 Evolution of EIS spectra after six successive DC/OCP cycles

The characteristic EIS spectra of PVD AlCr, AlCr(N) and AlCrTi coatings deposited on 17/4 PH steel substrate obtained after 2 h E_{OCP} at "EISi" (and after six successive DC/OCP cycles at "EIS1-EIS6") are presented as Nyquist plots in Figure 6.12 a-c and as Bode plots (phase angle vs. frequency) in Figure 6.13 a-c, (impedance modules vs. frequency) in Figure 6.14 a-c.

The Nyquist plots (Figure 6.12 a) for the PVD AlCr coating exhibits an incomplete semicircle for the initial (EISi) spectrum in the high frequency range, which can be attributed to the capacitive behaviour of the passive film that formed during E_{OCP}; however, at low frequencies a diffusional tail is appeared. This can be related to the diffusion process caused by preferential dissolution of the Al that is probably accelerated by the chromium interlayer. Nyquist plots displayed six depressed semicircles of EIS1-EIS6 spectra obtained after six successive DC/OCP cycles. It can be seen that the radius of the depressed semicircle decreased with increasing the number of DC/OCP cycles, which implies a decrease in the charge transfer resistance of the coating due to an increase in coating corrosion rate because of the (sacrificial) galvanic coupling to the substrate.

For the PVD AlCr(N) coating the Nyquist plots in Figure 6.12 b show that the initial EISi spectrum of the coating exhibits a capacitive-resistive behaviour over a wide frequency range, suggesting the presence of a stable dense passive film that formed on the surface of AlCr(N) coating during E_{OCP}.

Figure 6.12: Nyquist plots for PVD Al-based coatings a) AlCr, b) AlCr(N) and c) AlCrTi at E_{OCP} & after six successive DC/OCP cycles.

Nyquist plots for EIS1-EIS6 spectra exhibit incomplete semicircles that can be attributed to a predominantly capacitive behaviour of the AlCr(N) coating. The radii of incomplete semicircle for EIS1, EIS2 and EIS3 decreased with increasing the number of DC/OCP cycles, which can be related to the decrease of the charge transfer resistance of the coating and then increased by DC/OCP cycle 4 (and continues to increase cycles 5 and 6. This can be attributed to increasingly capacitive behaviour that is probably due to the contribution of the chrome oxide layer of 17/4 PH substrate to the overall corrosion resistance of the coating.

The Nyquist plots in Figure 6.12 c show that the initial EISi spectrum of the PVD AlCrTi coating exhibits one depressed semicircle in the high and middle frequency range attributed to the capacitive-resistive behaviour of the passive film that formed on the surface of AlCrTi during E_{OCP}.

In the low frequency range, a diffusional tail appears which can be related to the diffusion of Al^{3+} ions, produced by the anodic reaction from the passive film. Incomplete semicircles are displayed in Nyquist plots for EIS1-EIS6, associated to the capacitive behaviour (like insulator) of AlCrTi coating. This behaviour is likely to be due to a combination of solid solution effects (Al matrix) and grain size refinement (Ti). The radius decreased with increasing DC/OCP cycles, which can be associated to decrease in charge transfer resistance (corrosion resistance) due to the preferential dissolution of Al at the $TiAl_3$/Al interface caused by local galvanic cell interactions between the Al matrix (anode) and $TiAl_3$ intermetallic phase islands (cathode) [78].

Figure 6.13 a-c represents the Bode plots (phase angle vs. frequency) for EIS spectra of PVD AlCr, AlCr(N) and AlCrTi coatings after 3 h E_{OCP} and after six successive DC/OCP cycles. Bode phase angle plots for the AlCr coating in Figure 6.13 a show the initial EISi spectrum featuring two phase angles (two peaks) in the low and middle frequency range; a high phase angle with -65° displayed in the middle frequency range (attributable to a capacitive behaviour of the passive film the formed on the surface of AlCr) and a low phase angle with -52° displayed over the low frequency range, (related to the diffusional process of Al^{3+} ions diffusion from the passive film). The Bode phase angles of spectra EIS1 and EIS2 exhibit typical resistive-capacitive behaviour, featuring one constant phase angle (complete peak) over a wide range of frequency (0.1-100 Hz), suggesting the presence of stable behaviour of AlCr coating. The Bode phase angles of spectra EIS3-EIS6 featuring two peaks, one at intermediate and close to the low frequencies, which relate to the charge transfer resistance and exhibit a small inductive peak a low frequency range, which can be correlated to passivation effects due to the accumulation of corrosion products. The broadening of the EIS spectral peak becomes narrower with increasing number of DC/OCP cycles as well as its phase angle progressively decreasing to lower values. This can be related to a gradual decrease in charge transfer resistance as the corrosion rate of the AlCr coating increases because of the galvanic effect between the coating and 17/4 PH substrate.
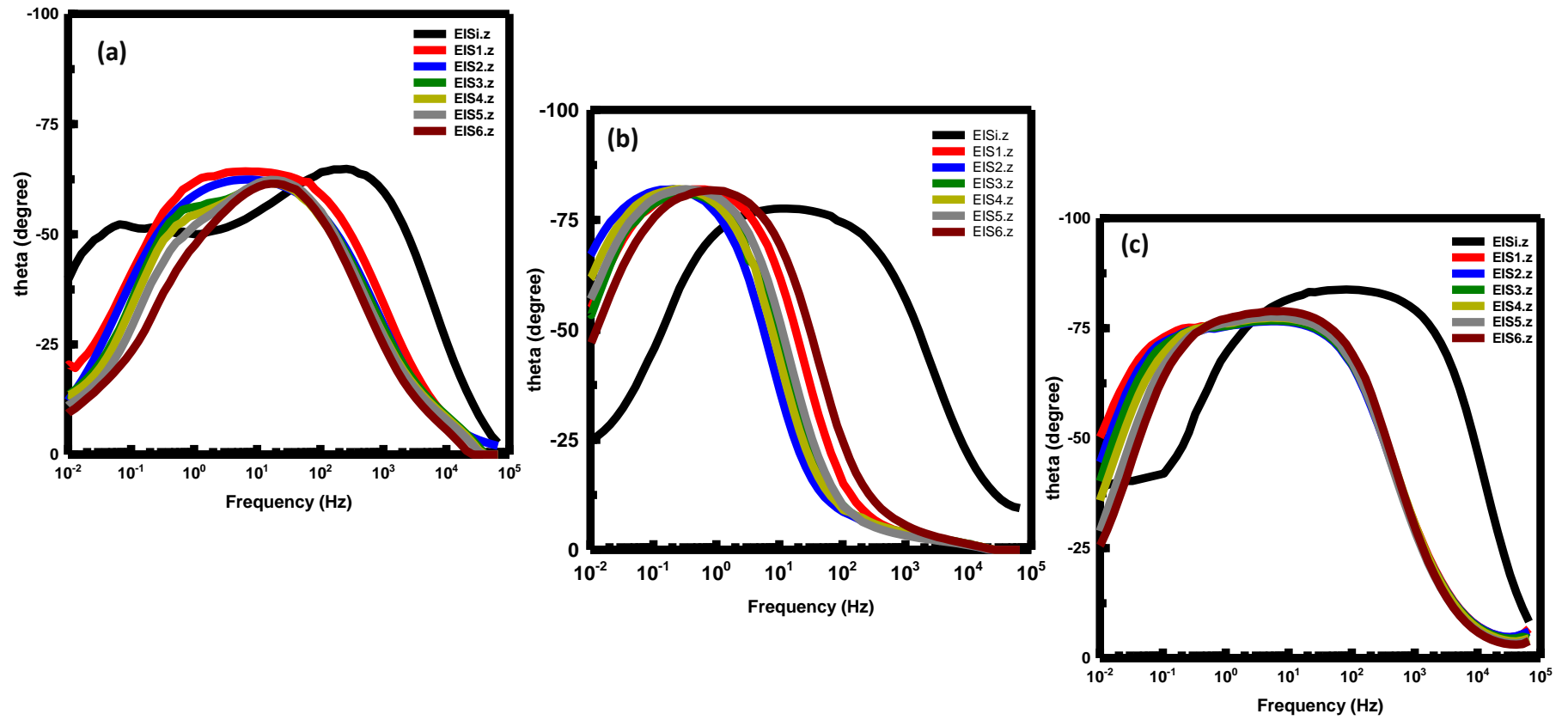
Figure 6.13: Bode plots (phase angle vs. frequency) of PVD Al-based coatings a) AlCr, b) AlCr(N) and c) AlCrTi at E_{OCP} & after six successive DC/OCP cycles.

Figure 6.13 b shows the Bode phase angle plots of the AlCr(N) coating, which exhibits one complete phase angle over a wide range of frequency range (0.1-1000 Hz) for the initial EISi spectrum attributed to the resistive-capacitive behaviour of the passive film that formed on the coating surface. The combination of chromium and nitrogen can enhance the pitting corrosion resistance of the coating as well as addition of nitrogen reducing coating porosity. Bode phase angle spectra of EIS1-EIS6 exhibit one incomplete peak in the middle to low frequency region, indicative of capacitive coating behaviour with insulating properties. It can be seen that the peak deviated towards the middle frequency range after the 4th DC/OCP cycle, which can probably be attributed to a tendency for resistive-capacitive behaviour due to the contribution of the chrome oxide layer of the 17/4 PH steel substrate to the overall barrier protection.

Bode phase angle plots (Figure 6.13 c) of AlCrTi coating exhibit a resistive-capacitive behaviour for the initial EISi over a wide frequency range (0.1-10000 Hz) by phase angle approaching -83°, suggesting the presence of highly stable passive film on the surface of AlCrTi. In the low frequency range (< 0.1Hz), a diffusional process is observed, which caused by the diffusion of Al^{3+} ions, which is produced by the anodic reaction from the passive film.

Bode phase angle plots of spectra EIS1-EIS6 exhibit highly capacitive behaviour, which is indicated at intermediate frequency range (0.01-1000 Hz) by a phase angle approaching -76°. The maximum phase angle reduced from -83° to around -76° and the broadening of the peak becomes narrow with increasing number of DC/OCP cycles, which can be attributed to a decrease of charge transfer resistance of the

coating due to an increase in corrosion rate because of the local galvanic cell interactions between the Al matrix (anode) and $AlTi_3$ intermetallic phase islands (cathode).

Figure 6.14 (a-c) represents the Bode plots (impedance modulus vs. frequency) for EIS spectra after 3 h E_{OCP} and after six successive DC/OCP cycles of PVD AlCr, AlCr(N) and AlCrTi coatings. The Bode modulus of the AlCr coating (Figure 6.14 a) shows the impedance modulus |Z| for the initial EISi is the highest (2.4 x 10^{-4} Ωcm^2), which can be attributed to the high corrosion resistance of the passive film and the coating system. The value of |Z| decreased significantly to 5.3 x 10^{-3} Ωcm^2 after DC/OCP cycle 1 and then it continues to the decrease with increasing DC/OCP cycles until reaching 1.3 x 10^{-3} Ωcm^2 by the 6th DC/OCP cycle. This can be attributed to the decrease in the charge transfer resistance of the coating (increase in corrosion rate) with DC/OCP cycles. For the AlCr(N) coating, the Bode modulus in Figure 6.14 b shows the highest |Z| value for EISi (1.5 x 10^{-5} Ωcm^2) but significantly decreased to 1.4 x 10^{-4} Ωcm^2 after DC/OCP cycle 1, then continues to decrease with increasing DC/OCP cycle to reaching 7.3 x 10^{-3} Ωcm^2 by the 3rd DC/OCP cycle. This can be attributed to a decrease in the charge transfer resistance of the coating due to the increase in corrosion rate of the coating. After application of the 4th DC/OCP cycle, the |Z| value increased to 9.6 x 10^{-3} Ωcm^2 and then continued to increase with DC/OCP cycles to reach 2.5 x 10^{-4} Ωcm^2 by DC/OCP cycle 6. This can be attributed to the increase in charge transfer resistance, which is in this case again probably due to the contribution of the chrome oxide layer on the 17/4 PH steel substrate to the overall barrier protection of the coating system.
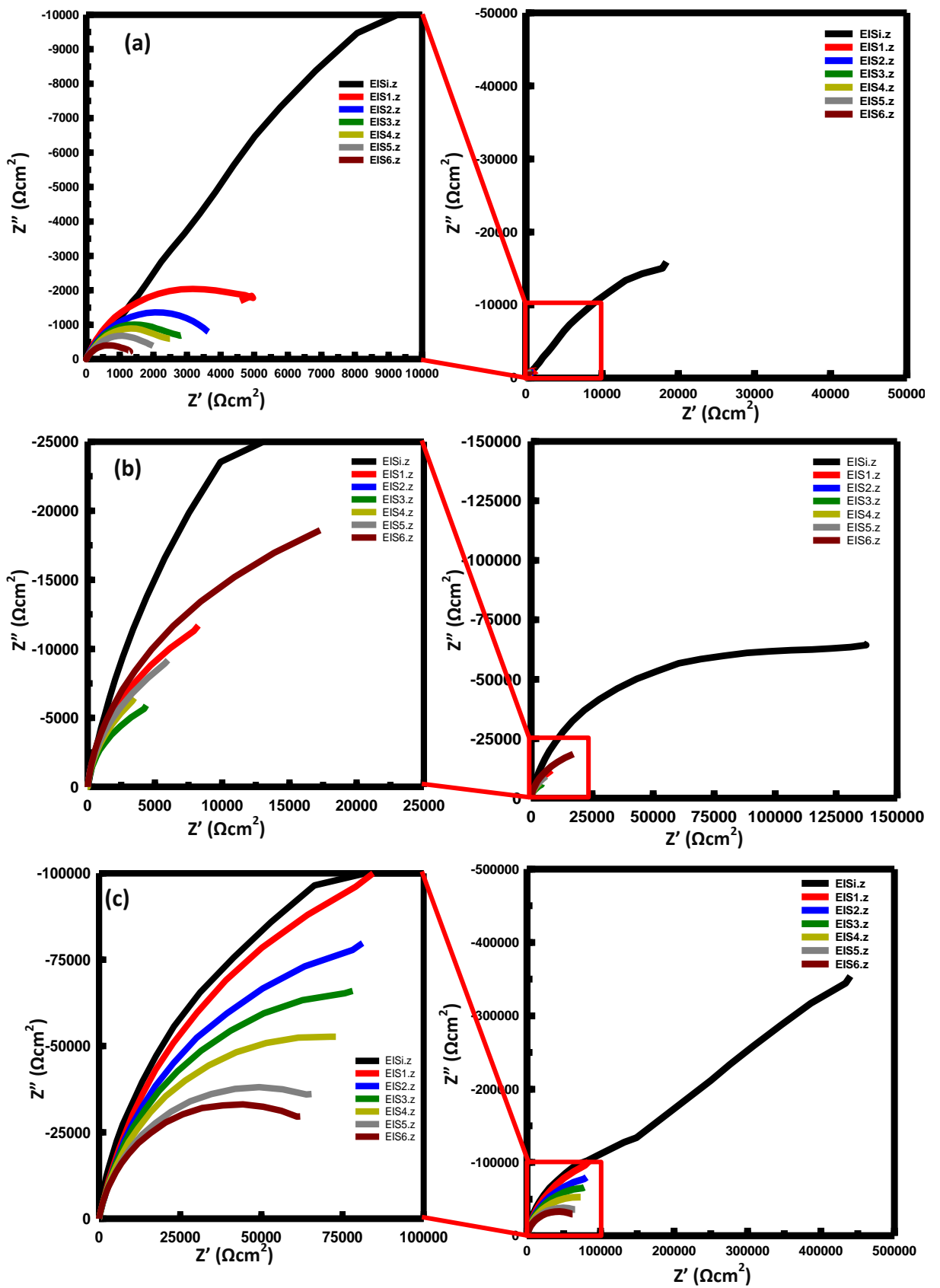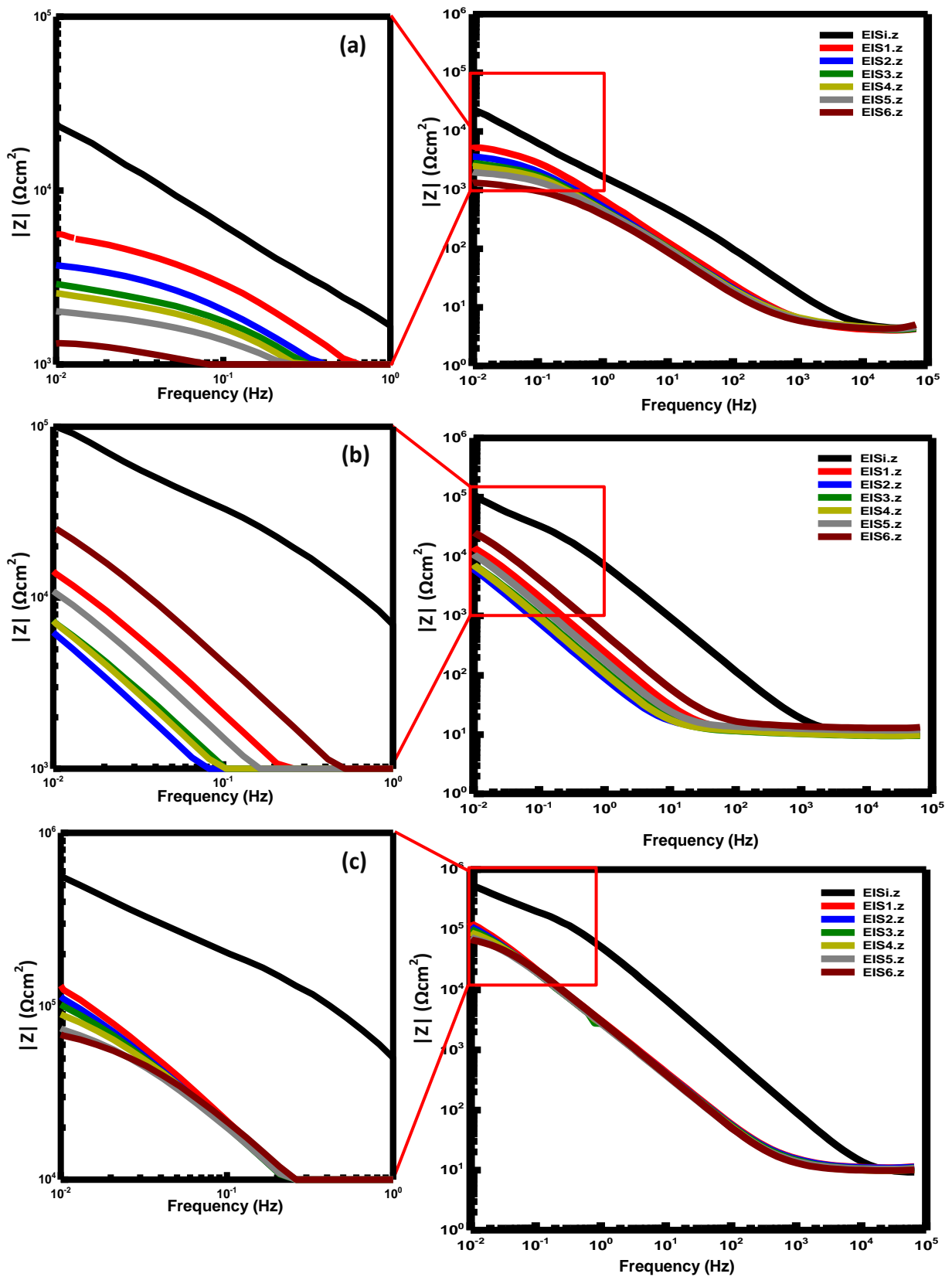
Figure 6.14: Bode plots (impedance modulus vs. frequency) of PVD Al-based coatings a) AlCr, b) AlCr(N) and c) AlCrTi at E_{OCP} & after six successive DC/OCP cycles.

The Bode modulus of the AlCrTi coating presented in Figure 6.14 c shows the highest |Z| for the initial EISi (6.3 x 10^{-5} Ωcm^2), which can be attributed to the high corrosion resistance of the passive film. The value of |Z| decreased significantly to 1.3 x 10^{-5} Ωcm^2 by DC/OCP cycle 1 and then continued to the decrease with DC/OCP cycle to reach 6.8 x 10^{-4} Ωcm^2 by cycle 6. This can be explained by the increase in corrosion rate of the coating due to the dissolution of the Al matrix by accelerated by the $TiAl_3$ intermetallic phase island.

Based on the features of the collected EIS spectra three different equivalent circuits EC can be proposed, as shown in Figure 6.15 a-c below.
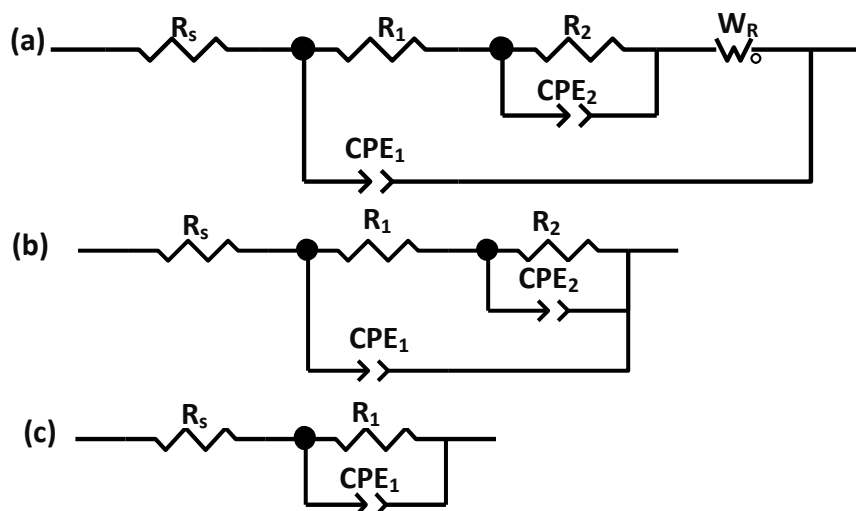
Figure 6.15: Equivalent circuits used to model EIS spectra after a) 3 h E_{OCP} for PVD AlCr and AlCrTi coatings, b) 3 h E_{OCP} for PVD AlCr(N) coating and six successive DC/OCP cycles for PVD AlCr and AlCrTi coatings and c) six successive DC/OCP cycles for PVD AlCr(N) coating.

The equivalent circuit in Figure 6.15 a was employed to model the EIS spectra that obtained after 3 h E_{OCP} at EISi for the AlCr and AlCrTi coatings, which is composed of two time constants (R_1 CPE_1 and R_2 CPE_2) and a Warburg impedance element (W_R),

selected to represent the diffusional process. A pair of time constants in parallel (Figure 6.15 b), comprised of R_1 CPE_1 and R_2 CPE_2 were selected to model the EISi spectrum that obtained after 3 h E_{OCP} the for AlCr(N) coating and the EIS spectra obtained after six successive DC/OCP cycles for AlCr and AlCrTi. In Figure 6.15 c an equivalent circuit with only one time constant (R_1 CPE_1) selected to model the EIS spectra obtained after six successive DC/OCP cycles for AlCr(N).

In the EISi spectrum equivalent circuit of AlCr (Figure 6.15 a), two time constants R_1 CPE_1 and R_2 CPE_2 represent the charge transfer resistance of the passive film and of the AlCr coating, respectively, and a diffusional Warburg impedance, W_R in the low frequency region, attributed to anodic dissolution of Al^{3+} ions from the passive film. The single time constant R_1 CPE_1 circuit (Figure 6.15 c) proposed for EIS1-EIS2 spectra, represents the charge transfer of the AlCr coating. The equivalent circuit presented in Figure 6.15 b was proposed for EIS3-EIS6 spectra where R_1 CPE_1 and R_2 CPE_2 correspond to the charge transfer resistance of the coating and of the chromium interlayer, respectively.

The equivalent circuit presented in Figure 6.15 b for the EISi spectrum of AlCr(N), is comprised of a pair of parallel time constants R_1 CPE_1 and R_2 CPE_2, corresponding to the charge transfer resistance of the passive film and of the AlCr(N) coating, respectively. It can be seen that there appears to be no diffusion element associated to the impedance response of this coating, due to the combined influence of Cr and N that enhanced the corrosion resistance of the coating as well as its densification as revealed by the SEM micrograph shown in Figure 6.5 a.

The single time constant R_1 CPE_1 circuit (Figure 6.14 c) proposed for EIS1-EIS6 spectra, corresponds to the contribution of the chrome oxide layer of the 17/4 PH steel substrate to the overall coating performance.

 The proposed equivalent circuit for the EISi spectrum of the AlCrTi coating shown in Figure 6.14 a, comprises two time constants R_1 CPE_1 and R_2 CPE_2 representing the charge transfer resistance of the passive film and of the AlCrTi coating, respectively. According to the model, a diffusional Warburg impedance element W_R is present in the EC, which is attributed to anodic dissolution of the Al^{3+} ions from the passive film.

For EIS1-EIS6 spectra, the parallel pair of time constants R_1 CPE_1 and R_2 CPE_2 (Figure 6.13 b) represent the charge transfer resistance of the AlCrTi coating in terms of the Al matrix and the intermetallic phase islands of $TiAl_3$, which are cathodic regions of localized galvanic cells inside the Al matrix.

The corresponding values of the individual phase elements of the these proposed equivalent circuits of Figure 6.15 used for fitting the EIS spectra obtained after 2 h E_{OCP} and after six successive DC/OCP cycles for the three PVD AlCr, AlCr(N) and AlCrTi coatings, are collected in Tables 6.2 , 6.3 and 6.4 respectively.

Table 6.2: Fitting results of EIS spectra of PVD AlCr coating obtained after 3 h E_{OCP} & after six successive DC/OCP cycles.

Cycle	R_s $(\Omega\ cm^2)$	CPE_1 $(\mu F/cm^2)$	R_1 $(k\Omega\ cm^2)$	n	CPE_2 $(\mu F/cm^2)$	R_2 $(k\Omega\ cm^2)$	n	W_R $(k\Omega\ cm^2)$
at E_{OCP}	4.3	11.1	23.5	0.93	10.7	22.2	0.85	30.5
1	4.3	38.0	6.2	0.74	-	-	-	-
2	4.3	47.4	4.2	0.73	-	-	-	-
3	4.1	52.4	3.1	0.72	60.1	8.3	0.30	-
4	4.4	55.4	2.8	0.71	74.3	2.4	0.25	-
5	4.4	56.0	2.2	0.71	96.8	1.9	0.26	-
6	4.3	90.6	1.4	0.70	110.5	0.63	0.23	-

Table 6.3: Fitting results of EIS spectra of PVD AlCr(N) coating obtained after 3 h E_{OCP} & after six successive of DC/OCP cycles.

Cycle	R_s (Ω cm^2)	CPE$_1$ (μF/cm^2)	R_1 (KΩ cm^2)	n	CPE$_2$ (μF/cm^2)	R_2 (kΩ cm^2)	n	W_R (kΩ cm^2)
at E_{OCP}	14.2	6.1	215	0.91	16.3	184.2	0.84	-
1	11.6	14.6	27.3	0.93	-	-	-	-
2	11.3	17.7	22.0	0.92	-	-	-	-
3	10.3	25.4	13.7	0.92	-	-	-	-
4	10.5	13.5	18.6	0.93	-	-	-	-
5	12.5	5.1	22.3	0.94	-	-	-	-
6	13.5	2.1	38.4	0.93	-	-	-	-

Table 6.4: Fitting results of EIS spectra of PVD AlCrTi coating obtained after 3 h E_{OCP} & after six successive of DC/OCP cycles.

Cycle	R_s (Ω cm^2)	CPE$_1$ (μF/cm^2)	R_1 (KΩ cm^2)	n	CPE$_2$ (μF/cm^2)	R_2 (kΩ cm^2)	n	W_R (kΩ cm^2)
at E_{OCP}	8.8	2.9	288.5	0.94	9.1	163.3	0.57	50.2
1	10.1	16.6	184.2	0.90	8.3	78.9	0.47	-
2	10.1	17.5	128.1	0.89	10.7	68.1	0.46	-
3	10.1	20.1	125.2	0.86	31.5	12.9	0.46	-
4	10.0	20.6	129.5	0.86	37.8	11.1	0.46	-
5	10.0	21.3	93.1	0.86	70.1	2.9	0.43	-
6	10.1	26.7	79.1	0.86	76.4	1.1	0.43	-

Figure 6.16 a-c shows the EC fitting results (solid green line) with experimental EISi spectrum (dashed red line) obtained after 3 h E_{OCP} of the passive film that formed on the surface of PVD AlCr, AlCr(N) and AlCrTi coatings. The goodness of fit between the proposed model circuit and the experimental values was on the order of 10^{-4}-10^{-3} of chi-squared values (X^2).
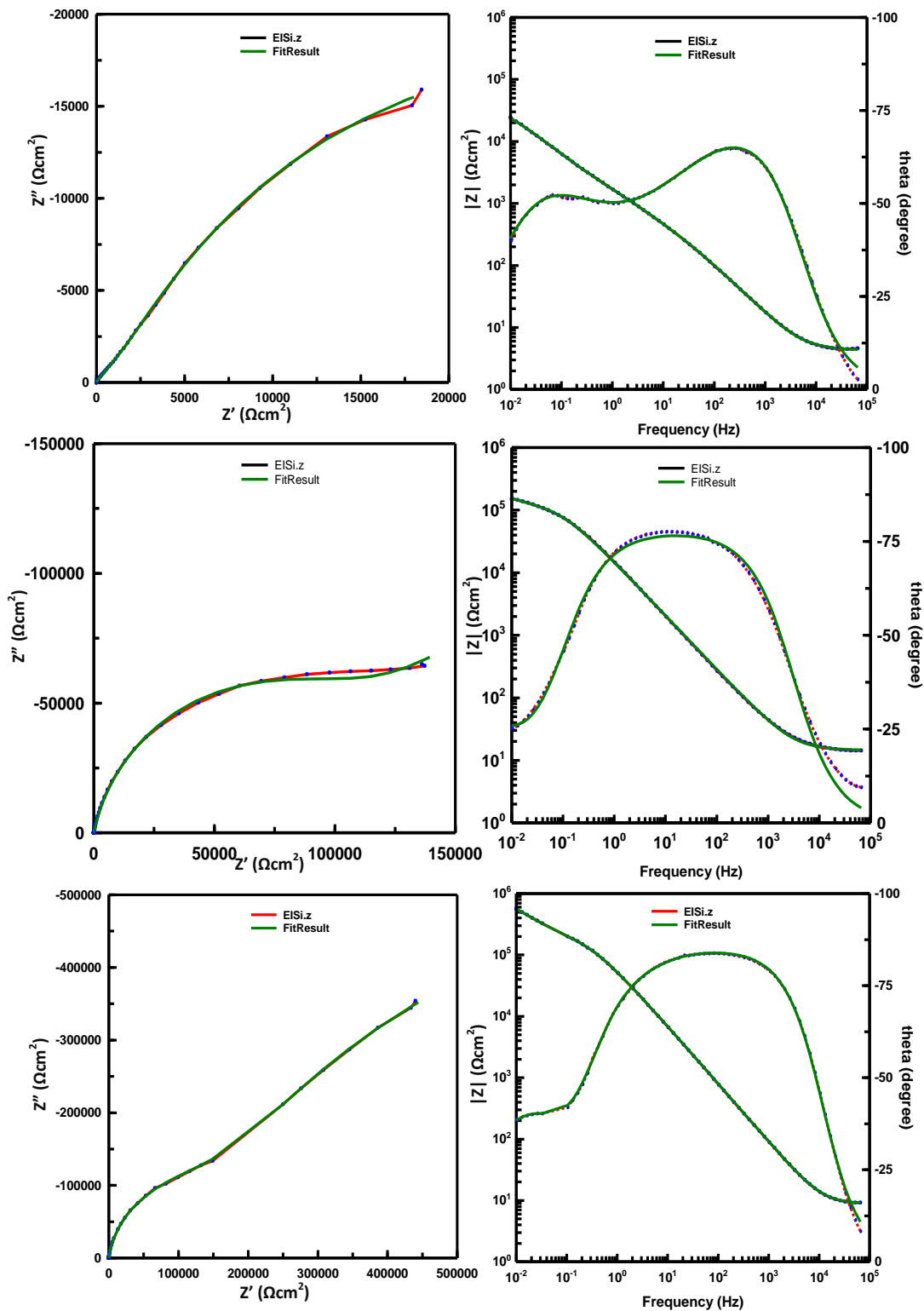
Figure 6.16: The sufficient fitting between the proposed models and experimental values of EISi spectrum after 3 h E_{OCP} for a) AlCr, b) AlCr(N) and c) AlCrTi coatings.

6.4.3 Hydrogen permeation current density during DC cathodic polarisation

Figure 6.17 displays the changes in hydrogen permeation current density with applied -2 V potential vs. SCE during DC1 cathodic polarisation for PVD AlCr, AlCr(N) and AlCrTi coatings. The transients show that the evolution of hydrogen permeation current density appears to be linked directly to the diffusion model D shown in shown Figure 2.14 see section 2.8.1.
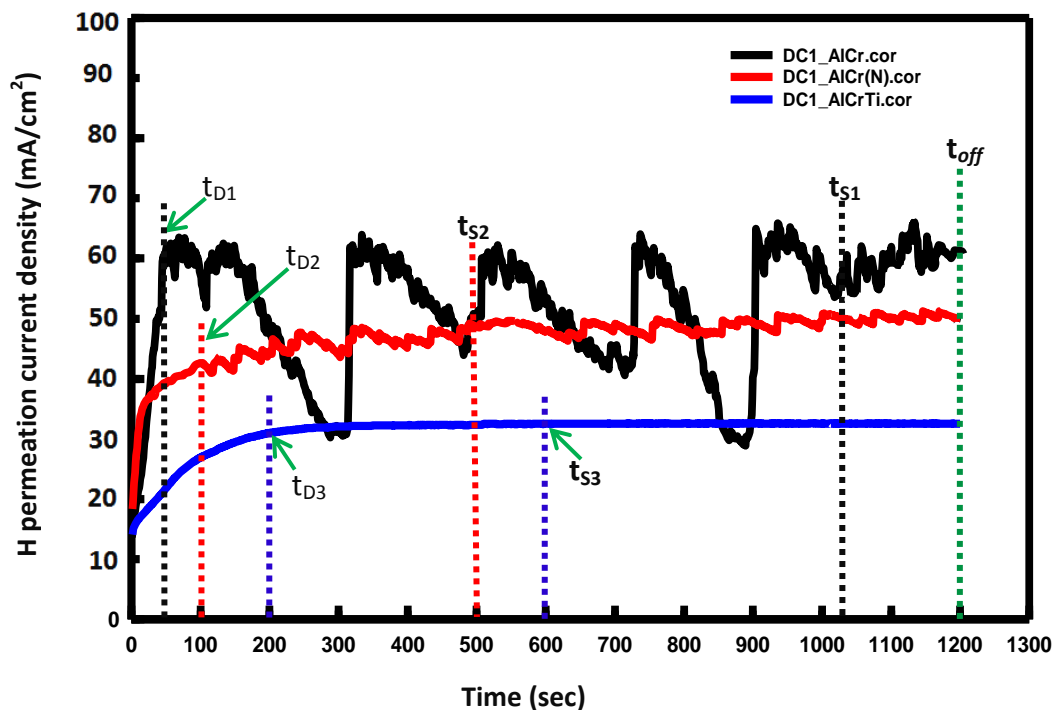
Figure 6.17: Evolution of hydrogen permeation current density curves during DC1 cathodic polarisation for PVD AlCr, AlCr(N) and AlCrTi coatings.

It can be observed that the hydrogen permeation current density transients increase rapidly from a low initial current density (18, 17 and 15 mA/cm^{-2}) to reach a maximum value (59, 43 and 38 mA/cm^{-2}) at diffusion times t_{D1}, t_{D2} and t_{D3} (60, 100 and 200 sec) for PVD AlCr, AlCr(N) and AlCrTi coatings, respectively. This diffusion time is consistent with the time lag in stage (I) at t_1 (60, 100 and 200 sec) of solution

pH evolution during DC1 cathodic polarisation for PVD AlCr, AlCr(N) and AlCrTi coatings respectively (see Figure 6.23 a-c p205), which will be explained broadly later in section 6.4.5.1 p204.

The hydrogen permeation current density transient for the AlCr is high and rapid, which attributed to the high hydrogen permeation rate through the passive film, due to its permeability which is relatively porous. After reaching a maximum diffusion rate value at t_{D1}, hydrogen permeation current density curve is slightly increased with significant fluctuations with time until DC1 cathodic polarisation terminated at t_{off} (1200 sec). The significant fluctuations can be related to the hydrogen instability (permeation and expulsion through the coating) due to changes in surface morphology of the passive film, because of the galvanic coupling effect with the 17/4 PH steel substrate.

For AlCr(N), the hydrogen permeation current density transient is lower and slower than that of AlCr, which can be attributed to the lower hydrogen permeation rate through the passive film due to the lower permeability due to the influence of nitrogen that reduced the coating porosity. After reaching an initial maximum value at t_{D2}, further light increases (with minor fluctuations) in hydrogen permeation current density are observed. This can be explained by the low degradation of the passive film induced by the combined influence of chromium and nitrogen that increased the corrosion resistance.

A much lower and slower hydrogen permeation current density transient for AlCrTi is observed. This can be attributed to the low hydrogen permeation rate through the passive due to the low permeability compared to those of AlCr and AlCr(N)

188

coatings. A very smooth and stable hydrogen permeation current density curve is observed after reaching a maximum diffusion rate value at t_{D3}, which can be related to the interfacial property of the passive (low permeability) film, induced possibly by the formation of a protective mixed oxide film of $(Al, Cr)_2Ti_2O_7$ that promotes the corrosion resistance of the passive film. However, the hydrogen permeation current density curve reaches saturation at time t_{S3} (600 sec) for AlCrTi and remains steady until DC cathodic polarisation terminated at t_{off} (1200 sec). This can be explained by the hydrogen permeation rate through the coating no longer increasing due to the hydrogen ion decay and the contribution of the aluminate ion gel enrichment at the passive film/electrolyte interface. This is consistent with stage (III) of solution pH evolution during DC1 presented in Figure 6.23 c where the increasing in solution pH reached a steady-state at t_2 (600 sec) due to aluminate ion gel enrichment at the passive film/electrolyte interface. Whilst, the effect of aluminate ion gel formed at t_{2a} (1040 and 500 sec) in stage (III) in Figure 6.23 a & b for AlCr and AlCr(N) respectively, can causes a reduction in the fluctuations of hydrogen permeation current density at t_{s1} & t_{s2} (1040 and 500 sec) for AlCr and AlCr(N) respectively.

Figure 6.18 (a-c) shows the hydrogen permeation current density curves during six successive DC cathodic polarisation cycles for PVD AlCr, AlCr(N) and AlCrTi coatings. In Figure 6.18 a it can be observed that the hydrogen permeation current density for AlCr increased with increasing DC cathodic polarisation. This can be related to the increase of hydrogen permeation rate through the coating due to the increase in coating permeability (coating degradation such as porosity).
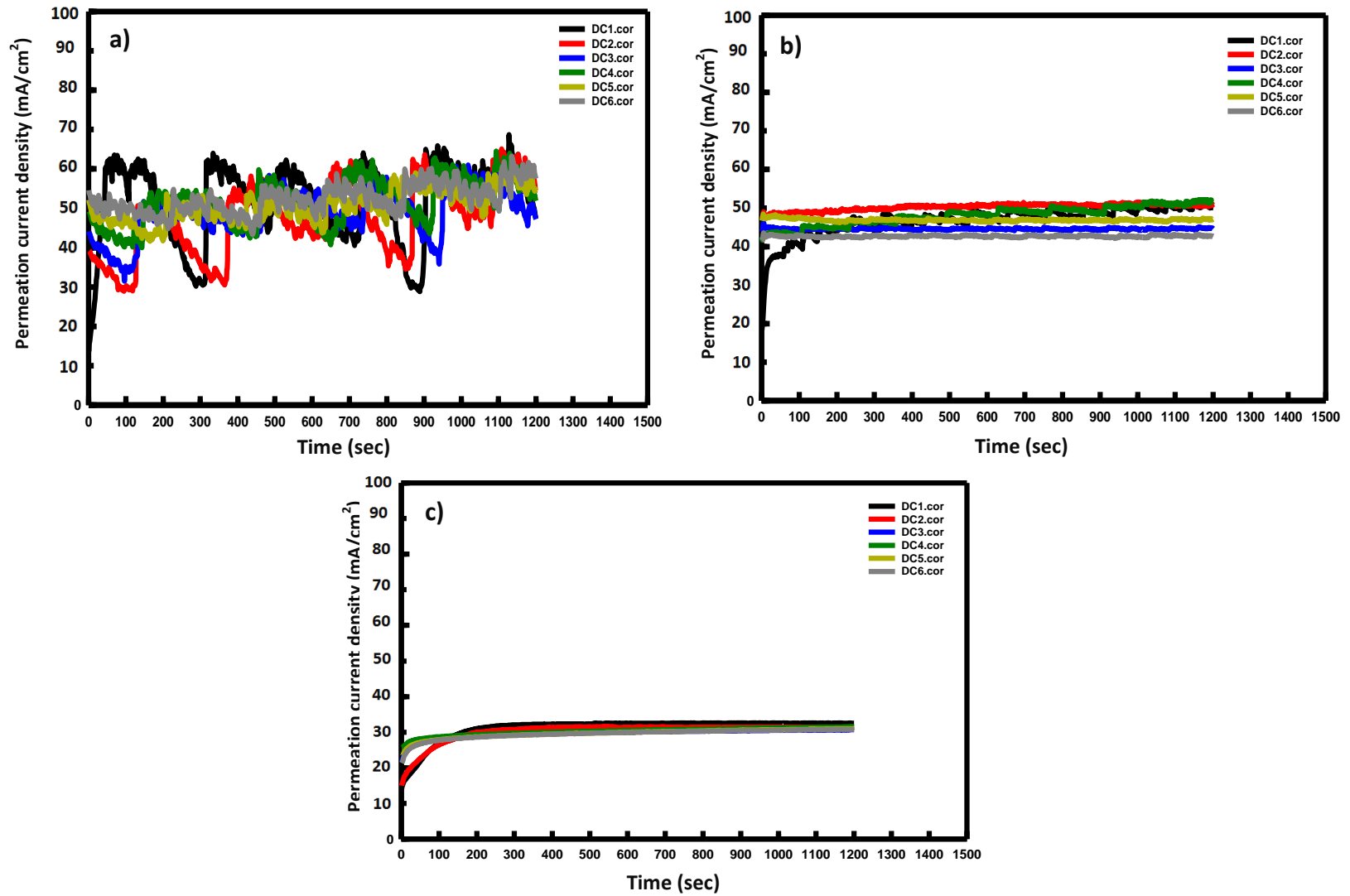
Figure 6.18: Evolution of hydrogen permeation current densities of PVD a) AlCr, b) AlCr(N) and c) AlCrTi coatings during six DC cathodic polarisations .

Large fluctuations in hydrogen permeation current density are observed during DC1-DC6. This can be related to the evolution of hydrogen ion instability (permeation and expulsion through the coating) due to the passive film porosity during DC1 and probably to pitting corrosion, which opens up pores to the substrate with time during DC2-DC6. This can be related to high corrosion potential difference between AlCr coating and 17/4 PH substrate. It can be observed that the intensity of the accompanied fluctuations decreased with increasing the number of DC, which can be related to the hydrogen ion decay at the coating/electrolyte interface.

Figure 6.18 b shows an increase in hydrogen permeation current density for AlCr(N) by applied for the first three DC cathodic polarisation cycles, which can be related to the increase in hydrogen permeation rate through the coating due to the increase in coating permeability because of the coating degradation that caused by galvanic corrosion between the coating and the 17/4 PH substrate. A decrease in hydrogen permeation current density from cycles 4th to 6th is then observed. This can be related to a decrease in hydrogen permeation rate caused by an increasing contribution of the chrome oxide layer of the 17/4 PH steel substrate to the overall protection of the coating system. The hydrogen permeation current density appears to exhibit smaller (and less) fluctuations than that of AlCr with no added nitrogen. It can be seen that during DC2-DC6 there was no increment in hydrogen permeation current density (diffusion rate), which suggests that hydrogen permeation rate through the coating is very low due to the low permeability of

AlCr(N) during DC2-DC3 and due to the chrome oxide layer of the 17/4 PH steel during DC4-DC6.

Figure 6.17 c for AlCrTi exhibits a low and stable hydrogen permeation current density during DC1-DC6 compared to those of AlCr(N) and AlCr. This can be attributed to the low permeability of the coating due to the interfacial property of the coating that induced by the addition of Ti as well as the contribution of the low degradation rate of the coating due to the low electrochemical driving force between AlCrTi coating and 17/4 PH substrate. It can be seen hydrogen permeation current density curve decreased with increasing DC cathodic polarisation, which can be due to hydrogen ion decay.

6.4.4   Evolution of relaxation time OCP after DC cathodic polarisation

Figure 6.19 a-c shows the evolution of six successive relaxation times OCP1-OCP6 of PVD AlCr, AlCr(N) and AlCrTi coatings after six successive DC cathodic polarisations. The observed variation in potential with time for PVD Al-based coating is the galvanic coupling potential with 17/4 PH steel potential.

From the galvanic corrosion properties of PVD Al-based coatings coupled to 17/4 PH steel substrate presented in Figures 6.8 and 6.9 for open circuit potential and potentiodynamic polarisation curves respectively, which appear to be located at higher anodic potentials (-0.785, -0.650 and -0.576 V vs. SCE for AlCr, AlCr(N) and AlCrTi respectively) compared to their respect 17/4 PH steel substrate (-0.252 V (vs. SCE)). However, the galvanic corrosion rate of the anode (PVD Al-based coatings) exceeds that of the cathode (17/4 PH steel), which are inductive of sacrificial protection for the 17/4 PH steel substrate.
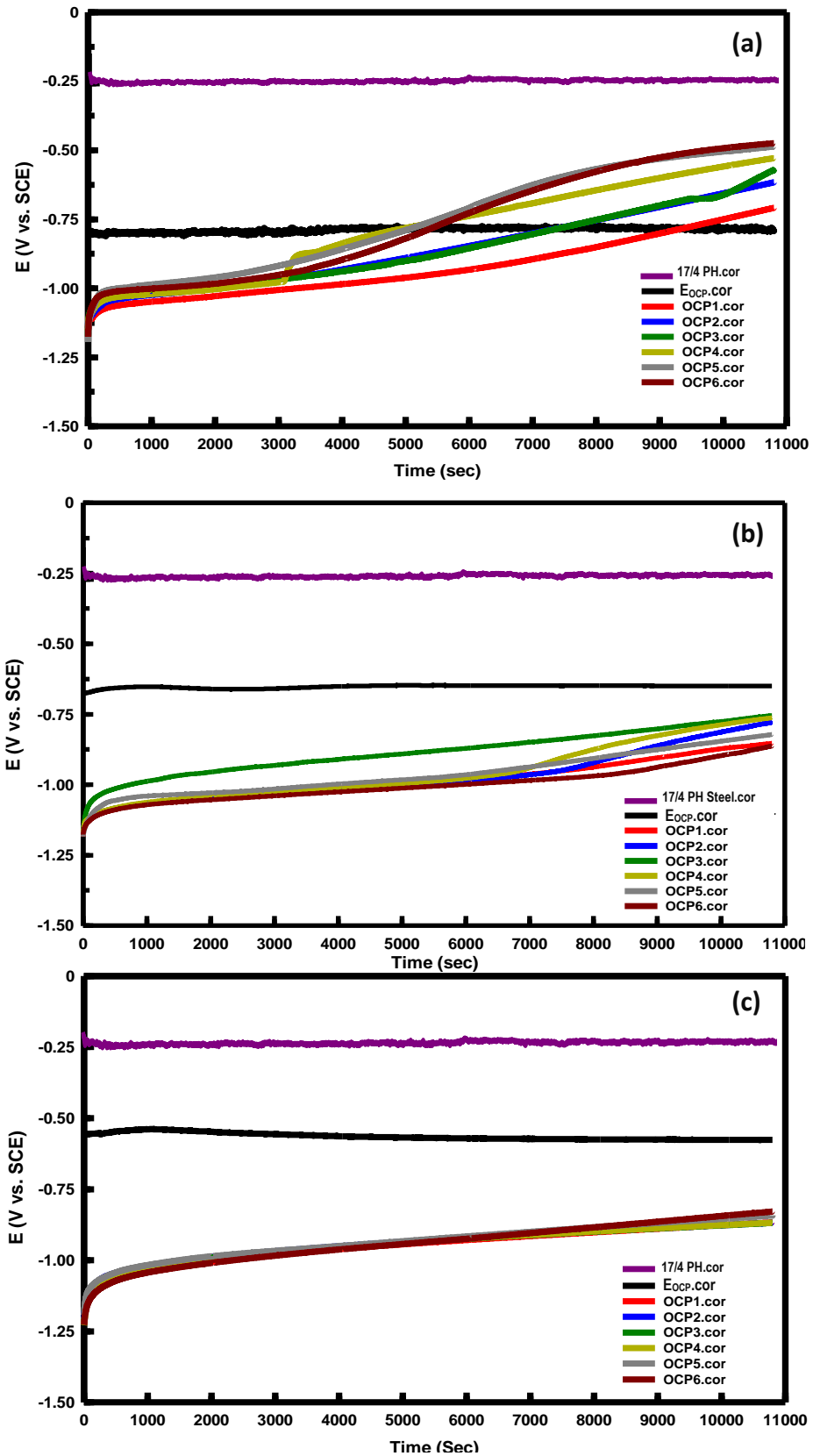
Figure 6.19: Evolution of relaxation time OCP of PVD Al-based coatings a) AlCr, b) AlCr(N) and c) AlCrTi coatings after six successive DC cathodic polarisations.

After DC cathodic polarisation terminated a rapid increase in potential from -2 V vs. SCE to potential beyond -1.2 V vs. SCE which instantaneously observed. During DC cathodic polarisation the standard potential of the cell is -2 V vs. SCE imposed externally by a potentiostat. Once the DC cathodic polarisation terminated the standard potential of the cell c be calculated from the standard reduction potentials at the cathode and anode electrodes. Hence the standard reduction potential at the cathode is $E^{\circ}_{H^+/H_2}$ = 0 V and the standard reduction potential at the anode is $E^{\circ}_{Pt^{3+}/Pt}$ = -1.2 V (see Table 2.1 p35). Therefore, the standard potential for the cell E°_{Cell} can be calculated according to the following equation:

$$E^{\circ}_{Cell} = E^{\circ}_{red,cathode} - E^{\circ}_{red,anode} = E^{\circ}_{H^+/H_2} - E^{\circ}_{Pt^{3+}/Pt} = 0 - 1.2 = \text{-1.2 V}$$

However, the rapid increase in an initial potential beyond -1.2 V. vs SCE is probably due to the standard potential of the cell E°_{Cell}.

However, the continuous increase in potential from beyond -1.2 V vs. SCE in anodic direction during 3 h relaxation time occurs by the driving force of the potential difference between PVD Al-based coating coupled and their 17/4 PH steel substrate. Therefore, it can be said that the electrochemical process during relaxation time is typical a potentiodynamic polarisation scan.

In Figure 6.19 a, the evolution of the relaxation time for the AlCr during OCP1-OCP6 appears to exhibit an increase in anodic potential with time to reach E_{OCP}, but the potential evolution exceeds the initial E_{OCP} of AlCr (-0.8 V) approach the E_{OCP} of the 17/4 PH steel substrate. This can be attributed to partial substrate exposure even after the first DC cathodic polarisation cycle due to the high coating degradation,

which then acts as sacrificial anode for the substrate because of the high galvanic driving force between AlCr coating and 17/4 PH substrate. The SEM micrograph (Figure 6.5 b) of degraded AlCr revealed evidence of alloying elements from the substrate by EDX analysis (Figure 6.5 e). It can be observed that the trend in anodic potential during each relaxation time increases ever closer to the E_{OCP} of the 17/4 PH steel substrate with increasing number of DC polarisation cycles. This can be explained by the increase in coating degradation with increase the number of DC/OCP cycle. A rapid increase in anodic potential during OCP4 at 3300 sec from potential value -0.976 V vs. SCE to a value of -0.878 V vs. SCE is observed. This rapid increase can be probably attributed to localised corrosion attack (pitting corrosion). This can be confirmed by the concurrent rapid decrease in solution pH at 3300 sec during relaxation time OCP4 for AlCr (Figure 6.24 a p210).

The evolution of relaxation time for AlCr(N) in Figure 6.19 b shows an increase in anodic potential during OCP1, OCP2 and OCP3 relaxation times to become closer to E_{OCP} of AlCr(N) with increasing number of DC polarisation cycles. This can be attributed to the lower level of coating degradation due to nitrogen addition with lower potential difference between the coating and the substrate. During OCP4 to OCP6 the anodic potential decreases with relaxation time to be far from the E_{OCP} of the AlCr(N) with increasing the number of DC polarisation cycles. This can be attributed to the contribution of the chrome oxide layer of 17/4 PH steel to the overall corrosion resistance of the coating, which is consistent with the surface

structure as shown in Figure 6.6 b where a layers of chrome oxide with AlCr(N) are seen as well as the high content of Cr revealed by EDX analysis Figure 6.6 e.

The evolution of relaxation times for AlCrTi (Figure 6.19 c) exhibit slight and closer increase in anodic potential curves, which are located quite far from E_{OCP} of the AlCrTi during OCP1-OCP6. This can be attributed to the low coating degradation due to the low galvanic driving force between AlCrTi coating and the 17/4 PH steel substrate.

6.4.5 Evolution of solution pH measurement of PVD Al-based coating

Figures 6.20, 6.21 and 6.22 show the evolution of solution pH that was concurrently monitored during 3 h E_{OCP} and the six successive cycles of (AC)DC/OCP/AC in order to study the effect of the (increasingly alkaline) solution pH on electrochemical corrosion behaviour of the PVD Al-based coatings deposited on 17/4 PH steel substrate.

Figure 6.20 shows a slight decrease with minor fluctuations in solution pH from an initial pH value 6 to value 5.8 is observed during 3 h of E_{OCP} for AlCr coating. This slight decrease can be explained by the initiation of pitting corrosion. The fluctuation can be attributed to the dissolution of Al accelerated by galvanic coupling with chromium interlayer. After wards, a downward "spike" in solution pH is immediately seen with applied -2 V vs. SCE to the electrochemical cell at step DC1. This can be explained by the 'hydrogen charging' of the pH probe, due to the accumulation of H^+ ions at the cathode surface.

However, the intensity of this spike is dependent also on the existing H^+ ions concentration at the coating/electrolyte interface. It can be seen that the spike of solution pH value during DC1 is strongly acidic, which can be related to the high concentration of hydrogen ion at the coating/electrolyte interface while during DC2-DC6 near neutral values of solution pH are observed, which can be attributed to hydrogen ion decay after each applied DC cathodic polarisation. After DC1 cathodic polarisation terminated (starting relaxation time step) an immediate increase of pH can be explained by 'hydroxyl ion charging' of the pH probe. It can clearly be observed that the solution pH then decreases (with significant fluctuations) during the relaxation time of OCP1-OCP4. This gradual acidification of the solution pH is probably due to the production of water and aluminium chloride ($AlCl_4^-$) complex called "Lewis acid" [186] due to the pitting corrosion reactions 2.17-2.21 p22-23 [47].

In contrast, decreases in solution pH with relatively minor fluctuations are observed during OCP5 and OCP6, which can be attributed to the contribution of the (now partially exposed) chrome oxide layer of 17/4 PH steel substrate, that enhanced the overall pitting corrosion resistance.

Figure 6.20: Evolution of solution pH vs. time during 3 h E_{OCP} and applied six of (AC)DC/OCP/AC cyclic testing for PVD AlCr coating.

The evolution of solution pH for the AlCr(N) presented in Figure 6.21 shows a small initial decrease in solution pH (from 5.1 to 5) during E_{OCP} and which remained steady at this value until application of -2 V vs. SCE DC cathodic polarisation, where a sharp downward "spike" in pH value is observed. During DC1 the intensity of the spike appears to be moderately acidic value due to the moderate concentration of H^+ ions at the coating/electrolyte interface, whilst, during DC2-DC6 appears to be near weak alkaline values, which is probably due to hydrogen ion decay due to the evolution of hydrogen gas after applied each DC cathodic polarisation as well as due to OH^- ion decay resulting from the formation of aluminate and high pitting corrosion resistance of the coating. After DC1 cathodic polarisation terminated the solution pH upward "spike" in pH value to the alkalinity is observed (starting relaxation time). This can be explained by 'hydroxyl ion charging' of the pH probe due to the rapid removal of aluminate gel and fast supply of OH^- ions towards the coating. During OCP1 a gradual increase in solution pH is observed immediately after upward spike, which attributed to the increase in aluminate ion formation due to the attack by OH^- ion, which causes the dissolution of the passive film that probably remained from DC1 and then the solution pH deceased slightly with minor fluctuations to reach a weak alkaline values. This decrease is probably due to the water reduction reaction that responsible for the main cathodic partial reaction, which is coupled with the anodic partial reaction of AlCr(N), thereby establishing a short-circuited corrosion cell on AlCr(N) in alkaline solution [44]. Significant fluctuations in solution pH appear to exhibit during OCP2 and OCP3, which probably attributed to the high corrosion rate due to coating breakdown.
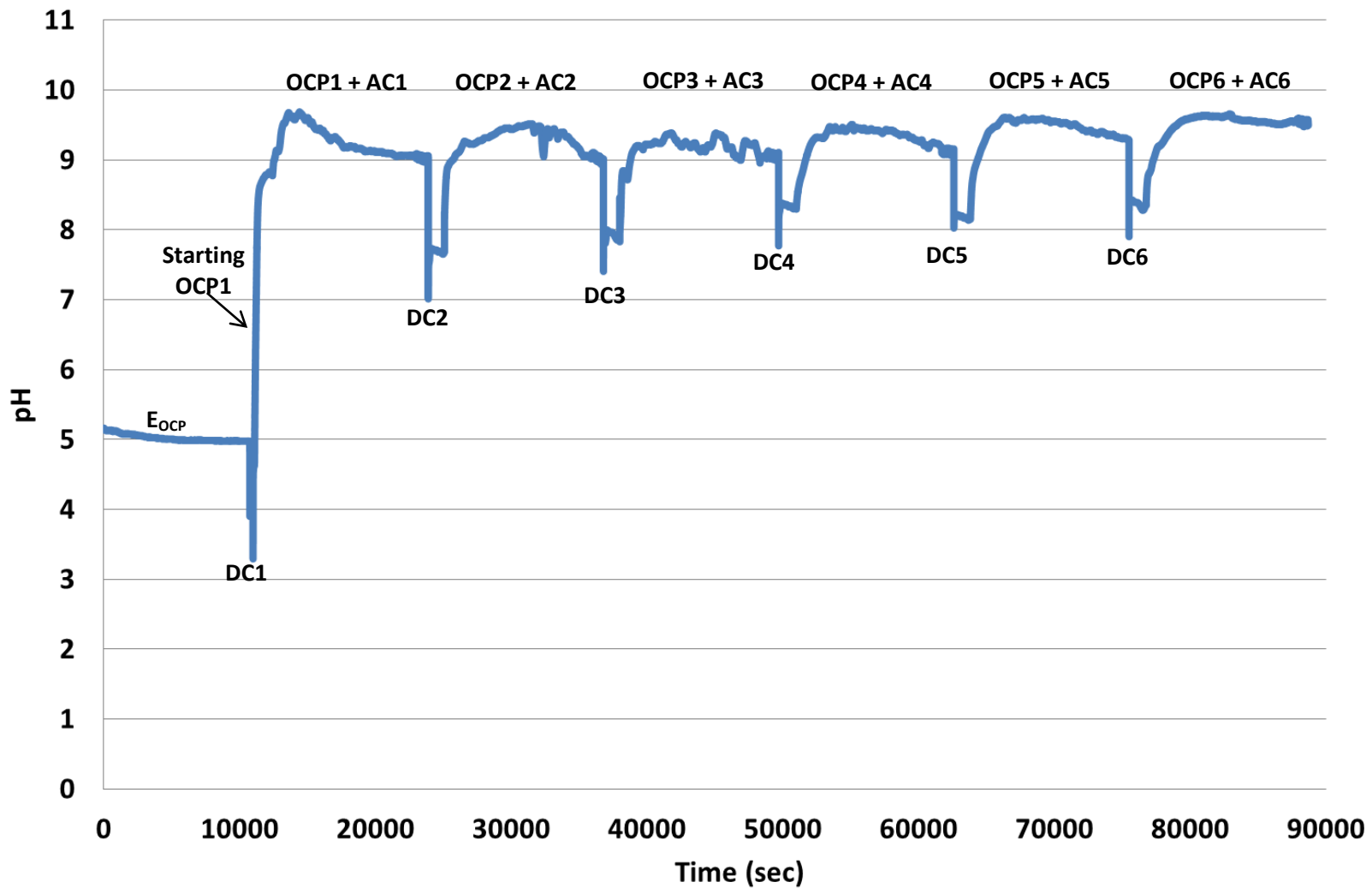
Figure 6.21: Evolution of solution pH vs. time during 3 h E_{OCP} and applied six of (AC)DC/OCP/AC cyclic testing for PVD AlCr(N) coating.

In contrast, slight decrease in solution pH with minor fluctuations during OCP4-OCP6 is observed. The slight decrease can be attributed to the low corrosion rate due to the contribution of the chrome oxide layer of 17/4 PH steel substrate to the overall corrosion resistance of the coating.

The evolution of solution pH during 3 h of E_{OCP} for AlCrTi (Figure 6.22) exhibits a slight decrease with minor fluctuations from an initial value 6.7 to value 6.3 and it remained steady at this value until -2 V. vs SCE (DC1) cathodic polarisation is applied. Immediately a downward in solution pH to reach acidic value up to 3.9 is observed. Whilst, the downward in solution pH during DC2-DC6 is close to the neutrality due to hydrogen ion decay because of the formation of hydrogen gas with applied DC cathodic polarisation. After DC cathodic polarisation terminated the solution pH value instantly increased to the alkalinity value, which can be explained by 'hydroxyl ion charging' of the pH probe.

It can be seen that the evolution of solution pH during six relaxation times OCP1-OCP6 shows a gradual decreased accompanied by minor fluctuations, which can be attributed to the dissolution of Al matrix accelerated by intermetallic phase which probably TiAl$_3$, leading to constructs local pitting corrosion [78]. This is consistent with SEM micrograph of corroded surface morphology as shown in Figure 6.7 c) where a pitting corrosion was revealed.
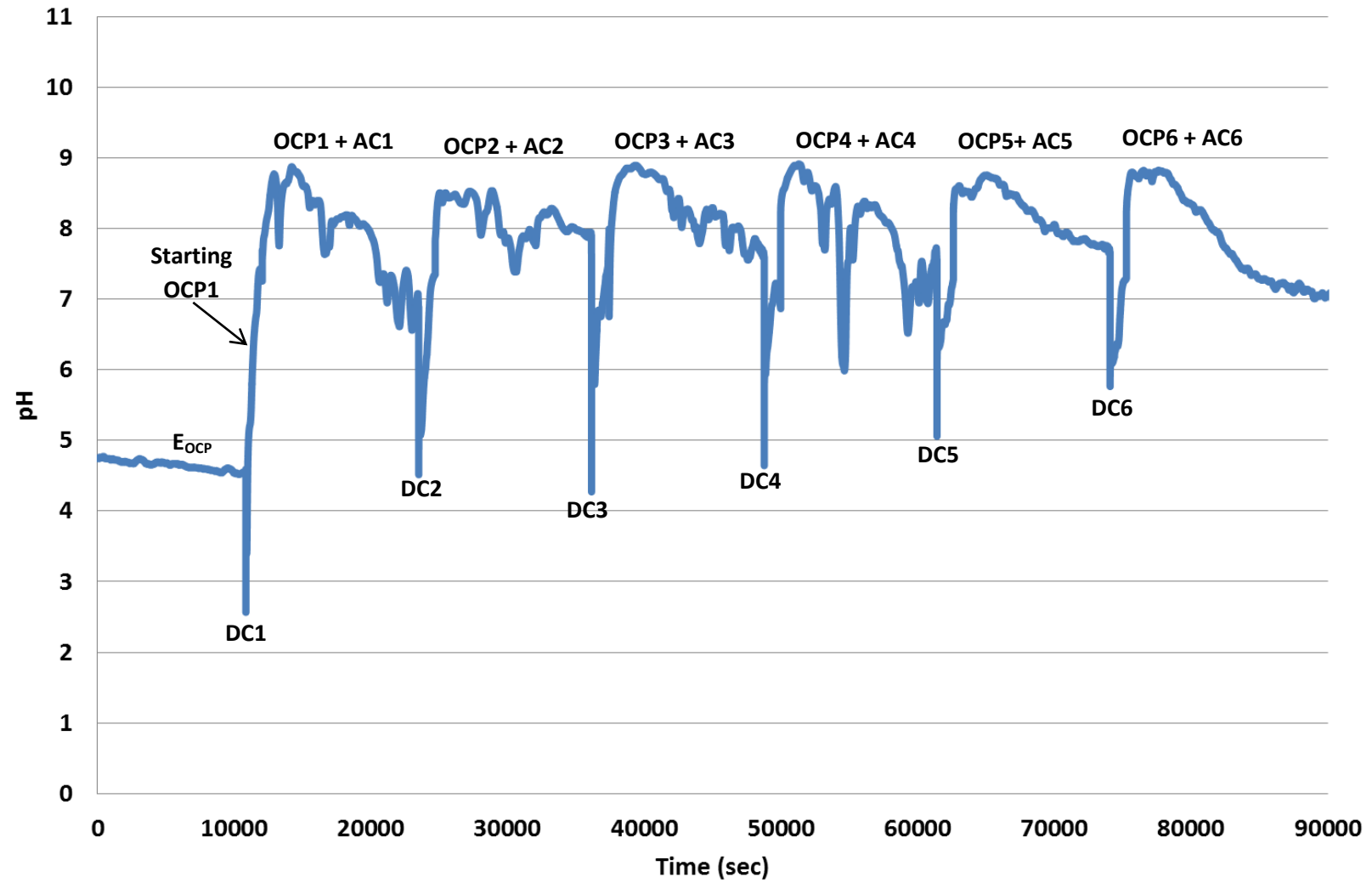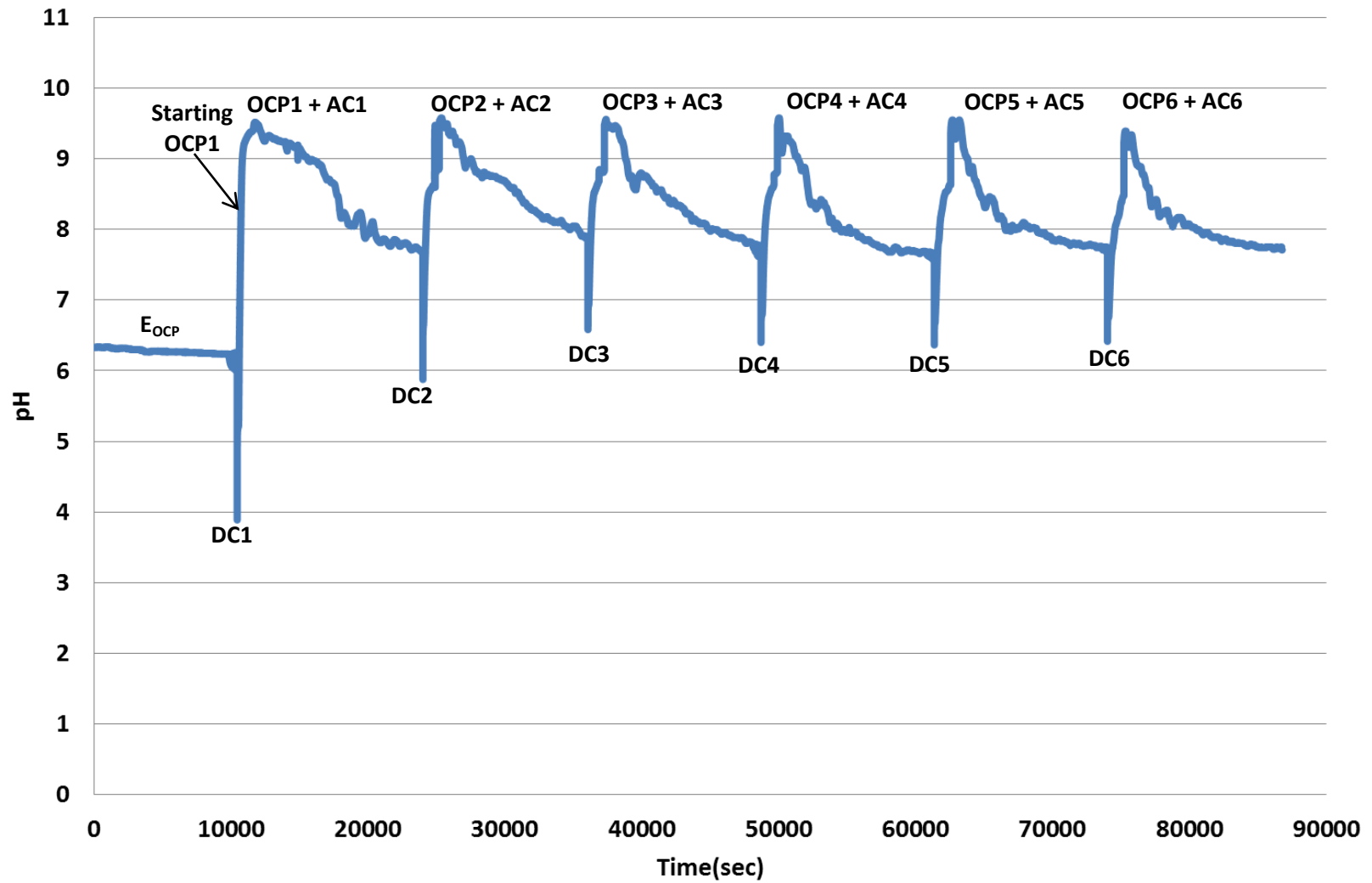
Figure 6.22: Evolution of solution pH vs. time during 3 h E_{OCP} and applied six of (AC)DC/OCP/AC cyclic testing for PVD AlCrTi coating.

However, in order to follow the mechanism underlying the electrochemical corrosion behaviour of PVD Al-based coatings deposited on 17/4 PH steel substrate during six successive DC/OCP cycles, it was necessary to explore the evolution of solution pH during DC cathodic polarisation and during relaxation time to reach E_{OCP} individually in section 6.4.5.1 and 6.4.5.2.

6.4.5.1 *Evolution of solution pH during DC cathodic polarisation*

Figure 6.23 (a-c) shows the evolution of the solution pH, which appears to be composed of three stages of variation during six successive -2 V vs. SCE$_{DC}$ cathodic polarisations of PVD Al-based coatings deposited on 17/4 PH steel substrate.

Figure 6.23a shows the evolution solution pH for AlCr coating during DC cathodic polarisation. It can be seen that during DC1 the stage (I) represents a sudden downward 'spike' in solution followed immediately by a time lag up to t_1 (60 sec) as the -2 V vs. SCE$_{DC}$ cathodic polarisation is initially applied. This time lag can be attributed to the hydrogen permeation rate into the passive film that formed on the surface of AlCr, which can be consistent with hydrogen permeation current density transient to reach a maximum diffusion value at t_{D1} (60 sec) for AlCr in Figure 6.17. Low and rapid increase in solution pH followed the time lag at t_2 (160 sec) in stage (II) is observed. This can be explained by the rapid formation of aluminate ion from the dissolution of the passive film by OH$^-$ ion attack, which probably completely dissolved at t_2.
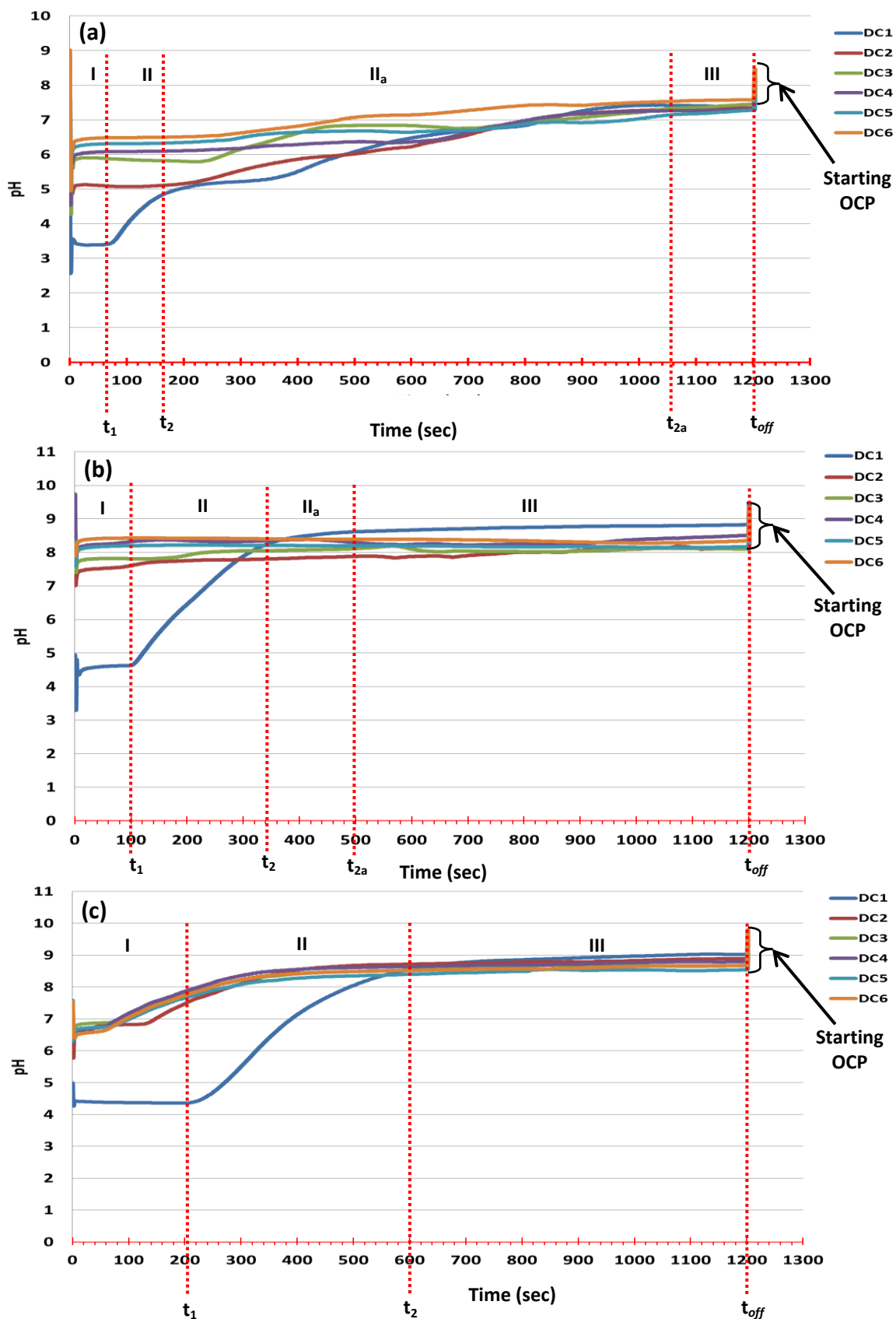
Figure 6.23: Evolution of solution pH curves during six successive DC cathodic polarisation for PVD coatings a) AlCr, AlCr(N) and c) AlCrTi.

An increase in solution pH continues slightly and slowly until reaches a steady-state at t_{2a}. This can be explained by the slow aluminate ion formation, which delayed by the instability of solution pH due to the evolution of hydrogen ion (i.e., permeation as H_{ads} or expulsion as H_2 gas from the coating) that effect on OH^- ion concentration at AlCr/electrolyte interface. This instability in solution pH can be related to the coating degradation because of galvanic effect that led to porous structure.

Stage (III) represents a steady-state in solution pH in the range between t_{2a} (1040 sec) and t_{off}, which can be attributed to the enrichment of aluminate ion gel at the AlCr/electrolyte interface. It can be observed that the time lag during DC2-DC6 increases with increasing the number of DC cathodic polarisation. This can be attributed to low hydrogen permeation rate due to the low permeability in which probably resulting from the AlCr coating as well as the contribution of hydrogen ion decay. Low and slow increase in solution pH followed the time lag during DC2-DC6 is observed. This can be attributed to the low aluminate ion formation. A steady-state at t_{2a} (1040 sec) is observed during DC2-DC6, suggests to the enrichment of aluminate ion gel at the coating/electrolyte interface.

For AlCr(N) the evolution of solution pH during six successive DC cathodic polarisations is presented in Figure 6.23 b. During DC1 the stage (I) represents a sudden downward 'spike' in solution followed immediately by a time lag up to t_1 (100 sec) as the -2 V vs. SCE is initially applied. The time lag for AlCr(N) appears to be longer than that of AlCr during DC1. This can be attributed to the low hydrogen permeation rate through dense passive film that formed on surface AlCr(N)

enhanced its low permeability by the influence of nitrogen, which tends to reduce the passive film porosity. This time lag can be consistent with hydrogen permeation current density transient to reach a maximum diffusion value at t_{D2} (100 sec) for AlCr in Figure 6.17. Stage (II) represents a high and slow increase in solution pH up to t_2 (340 sec). The high increase can be attributed to the high aluminate ion formation by slow dissolution rate of dense passive film by OH^- ion attack, which is probably completely dissolved by t_2. Low and slow increase is observed in stage (II_a), which can be related to the enrichment of aluminate ion at AlCr(N)/electrolyte interface and forms a gel layer that causes a steady-state at t_{2a} (500 sec) in stage (III), and it continues until DC cathodic polarisation terminated at t_{off}.

However, the evolution of solution pH during DC2-DC3 appears to exhibit time lag at about 100 sec and 200 sec. This can be associated to the low hydrogen permeation rate through the coating due to high permeability of AlCr(N) coating as well as the contribution of hydrogen ion decay at AlCr(N)/electrolyte interface, where the solution pH during relaxation time of OCP1 and OCP2 ends with pH value close to the alkalinity (see Figure 6.24 c). After wards a very low increase in solution pH followed the time lag from pH value 7.3 to 7.4 for DC2 and from 3.5 to 3.6 for DC3, and it remains constant with minor fluctuations around this value until DC cathodic polarisation terminated. This very low increase can be explained by the low aluminate ion formation due to the low dissolution rate of AlCr(N), because of the low OH^- ion attack. However, it can be seen in Figure 6.24 b that the solution pH during relaxation time of OCP1 and OCP2 ends with values close to the weak

alkalinity. Suggesting that there is no pitting corrosion reactions occurred, which causes acidification of the solution pH and produces water that supposed to be reduced to H^+ ion and OH^- ion during DC cathodic polarisation. Therefore, hydroxyl ions decay can be expected.

While the evolution of solution pH during DC4-DC6 appears to be no time lag is observed just a steady-state in solution pH value from the initial time until DC cathodic polarisation terminated at t_{off}. This can be attributed to hydrogen permeation through the coating no longer occurred. This can be related to the low permeability of AlCr(N) coating due to the contribution of chrome oxide layer of the 17/4 PH steel to the overall protection of the coating as well as hydrogen ion decay.

In Figure 6.23 c the evolution of solution pH for AlCrTi during DC1 appears to exhibit longest time lag up to t_1 (200 sec) compared to that of AlCr and AlCr (N) coatings as -2 V vs. SCE is initially applied. This can be attributed to the low hydrogen permeation rate through the passive film that formed on the surface of AlCrTi due to low permeability that enhanced by the combination of very protective oxides. High and slow increase in solution pH is observed up to t_2 (600 sec) in the stage (II) attributed to the high aluminate ion formation due to low dissolution rate of the passive film, which is highly corrosion resistance and compact to the coating. The passive film is probably completely dissolved at t_2. A steady-state in solution pH is observed in stage (III), and it continued with time until DC cathodic polarisation terminated at t_{off}. This can be attributed to the aluminate gel that formed at AlCrTi/electrolyte. The evolution in solution pH during DC2 exhibits shorter time lag

than that of DC1 and longer than that of DC3-DC6. This can be explained by the higher permeability of the coating than that of DC1 due to the existing of local pitting corrosion that formed during relaxation time OCP1. While it's longer than that of DC3-DC6 because of the permeability of the coating during DC2 is higher than that of DC3-DC6. A short time lag is observed during DC3-DC6, which can be related to the high hydrogen permeation rate through the coating due high permeability of the coating because of the local pitting corrosion. Slight increase in solution pH is observed during DC2-DC6, which can be explained by the low aluminate ion formation due to low dissolution rate of Al matrix accelerated by intermetallic phase $TiAl_3$ because of OH^- ion decay. A steady-state in solution pH is observed in stage (III), and it continued with time until DC cathodic polarisation terminated at t_{off}, attributed to the aluminate gel that formed at AlCrTi/electrolyte.

6.4.5.2 Evolution of Solution pH during relaxation time to reach E_{OCP}

The evolution of solution pH during six successive relaxation times of OCP1-OCP6 is presented in Figure 6.24 a-c for PVD AlCr, AlCr (N) and AlCrTi coatings. After DC cathodic polarisation terminated, a relaxation time OCP to reach E_{OCP} starts immediately. After DC1 cathodic polarisation terminated (starting relaxation time step) an immediate increase of pH can be explained by 'hydroxyl ion charging' of the pH probe. This can be explained by the rapid increase in potential from -2 V vs. SCE to a standard potential of the cell -1.2 V vs. SCE that caused rapid removal of aluminate gel and fast supply of OH^- ion towards the coting/electrolyte interface.
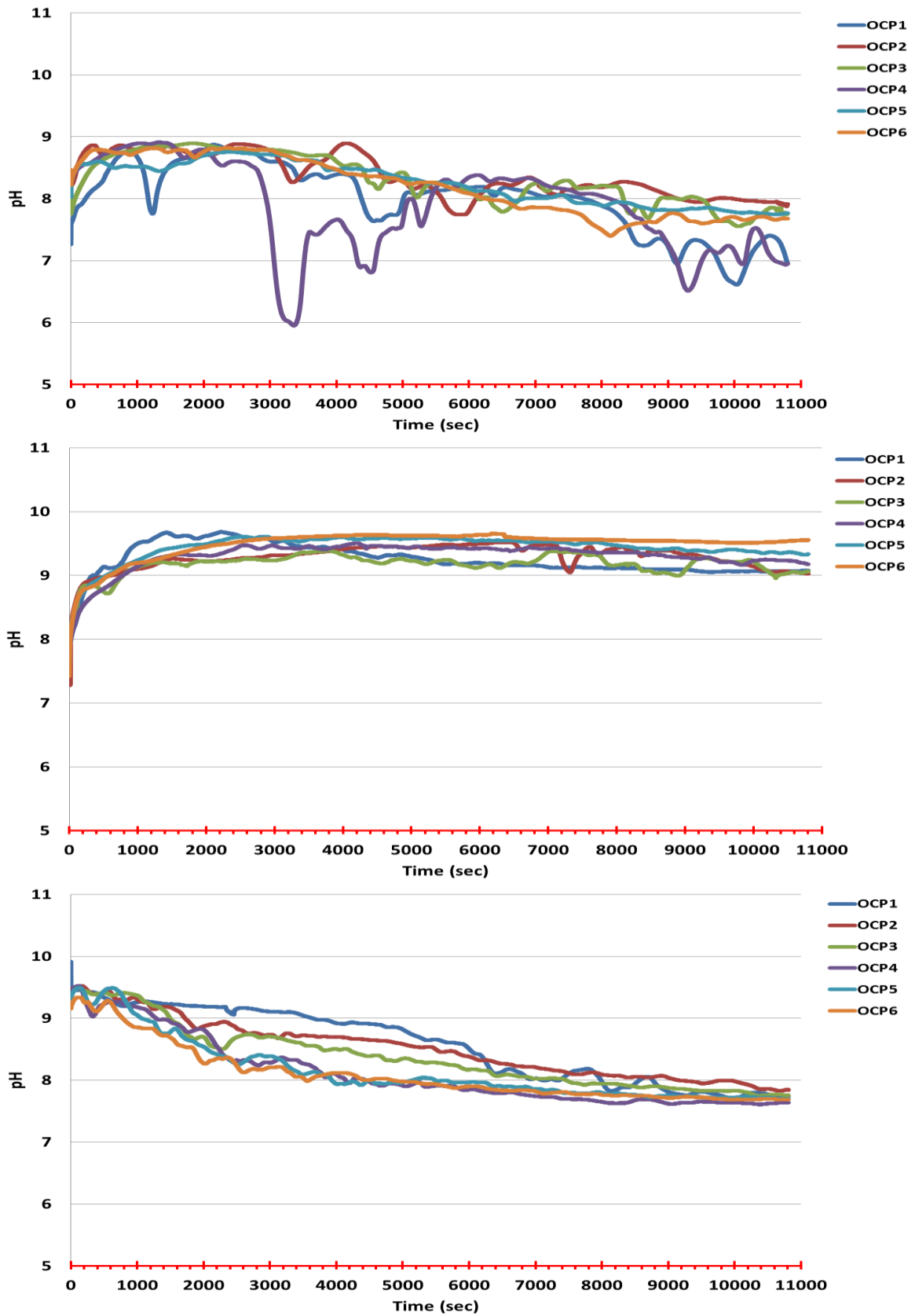
Figure 6.24: Evolution of the pH vs. time during relaxation OCP for PVD a) AlCr, b) AlCr(N) and c) AlCrTi coatings.

Figure 6.24 a shows the evolution of solution pH during six successive relaxation times OCP1-OCP6 for AlCr coating. Immediately, after upward "spike" a gradual increase in solution pH is observed. This can be attributed to the aluminate ion formation due to AlCr dissolution by OH⁻ ions attack. Afterwards a decrease in solution pH with significant fluctuations during OCP1-OCP4 and minor fluctuations during OCP5-OCP6 is observed. This can be due to the acidification in solution pH that probably caused by the production of water and ($AlCl_4^-$) from pitting corrosion. A significant decrease with significant fluctuation in solution pH is observed during OCP4 at about 3300 sec, which can be explained by high pitting corrosion rate.

By contrast, a decrease in solution pH with minor fluctuations during OCP5 and OCP6 is observed, which probably attributed to the contribution of the chrome oxide layer of 17/4 PH steel substrate that enhanced the pitting corrosion resistance. Evolution of solution pH for the AlCr(N) during six relaxation times OCP1-OCP6 that presented in Figure 6.24 b, shows a slight increase in solution pH during OCP1-OCP6 followed by insignificant decrease until the relaxation time terminated.

However, the solution pH became alkaline during DC1 due to high aluminate ion formation by high dissolution of the passive film by OH⁻ ion attack and then it slightly increased during the initial stages of OCP1 due to This slight increase can be related to the slight aluminate ion formation due to low the AlCr(N) dissolution. Afterwards an insignificant decrease in solution pH with time is observed. This insignificant decrease in solution pH attributed to the aluminate ion formation no

more increased due to OH⁻ ions decay at the AlCr(N)/electrolyte interface as well as the contribution of interfacial property of AlCr(N) coating due to the combined influence of Cr and N that enhanced the pitting corrosion resistance. Furthermore, there was no evidence of diffusion process in the impedance spectra of AlCr(N) coating obtained from EIS1-EIS6 is observed, which means no dissociation of coating elements is occurred by the galvanic corrosion. According to the SEM micrograph in Figure 6.6 b of degraded surface after six successive DC/OCP cycles, a spallation at the surface was revealed, which probably caused by the galvanic corrosion. Figure 6.25 shows the visual observation of coating spallation (debris) black scale in electrochemical cell.

Figure 6.25: visual observation of AlCr(N) coating (spallation) after applied six successive DC/OCP cycles

It can be seen that the solution pH during OCP2-OCP6 remained in alkaline level as well as during DC2-DC6 (Figure 6.23 b), which may suggests to no hydrogen permeation, no OH⁻ ions attack, no coating dissolution and no aluminate ion formation. The evolution of solution pH also shows minor fluctuations accompanied

by OCP1-OCP4 and then it became relative stability by OCP5 and OCP6, which attributed to their affinity for passivation as the chrome oxide of 17/4 PH steel forms and increases the overall corrosion resistance of the coating.

In Figure 6.24 c the evolution of solution pH for AlCrTi during six successive relaxation times exhibits slight increase in solution pH immediately after upward spike, which can be attributed to the slight increase in aluminate ion formation. A decrease in solution pH is observed accompanied with minor fluctuations, which can be explained by the acidification of solution pH, which probably caused by the production of water and $AlCl_4^-$ from local pitting corrosion reactions that caused by the local galvanic cell between Al matrix and intermetallic phase $TiAl_3$. It can be observed that the decrease in solution pH increased with increasing DC/OCP cycle. This can be attributed to the increase of local pitting corrosion rate.

6.5   Summary

The results shown in this chapter demonstrate the effectiveness of a developed novel electrochemical technique of (AC)DC/OCP/AC cyclic testing, with concurrent of pH measurement, for evaluating the corrosion behaviour of three different PVD Al-based coatings deposited on 17/4 PH steel, with the (AC)DC/OCP/AC test offering detailed results in a relatively short time (less than 24 h).

According to the galvanic corrosion behaviour of PVD Al-based coatings coupled to 17/4 PH steel, the E_{OCP} and potentiodynamic polarisation curves are located at higher anodic potentials with respect to the substrate. Therefore, PVD Al-based

coatings appear to act as a cathodic protection (sacrificial behaviour) for 17/4 PH steel.

From the obtained results of EIS spectra presented in Figures 6.12-6.14 and Tables 6.2-6.4, it can be concluded that the EIS behaviour of PVD AlCrTi coating showed excellent corrosion resistance with six successive DC/OCP cycles applied compared to PVD AlCr and PVD AlCr(N) coatings. This can be related to the addition of titanium that enhanced the grain refinement, which led to high pitting corrosion resistance of the coating. Meanwhile, this coating exhibited a decrease in the corrosion resistance with increasing number of DC/OCP cycles due to the local galvanic cell between the Al matrix and $TiAl_3$ intermetallic phase islands. According to the small potential difference between AlCrTi and 17/4 PH steel, the driving force of galvanic corrosion potential is very low, which is indicative of reliable cathodic protection for the substrate for long time.

In contrast, PVD AlCr appears to exhibit significant, non-uniform degradation of the coating with applied six successive DC/OCP cycles, which is inductive of sacrificial protection for the 17/14 PH steel substrate, while the PVD AlCr(N) coating showed a decrease in corrosion resistance of the coating after the first three DC cycles, then showed an increase in corrosion resistance of the coating system after the 4th, 5th and 6th cycles, which demonstrated a strong affinity for repassivation behaviour (self-healing) due to the contribution of chrome oxide film of 17/4 PH steel substrate to the overall protection of the coated substrate system.

Based on these results it can be concluded that the AlCrTi coating showed the best corrosion resistance after application of six successive DC/OCP cycles as a sacrificial protection for the substrate, followed by the AlCr(N) and AlCr coatings.

However, the repassivation behaviour exhibited by the AlCr(N) coating after the 4th cycle applied may be suggest an advantage to use this coating preferably in aerospace applications because of its strong ability to self-heal after breakdown during extreme DC polarisation, which might be promising for future coating materials for corrosion protection where cadmium or hard chromium need to be replaced.

Conclusions and Recommendations for Future Work

Conclusions

A brief summary of the key findings resulting from the research undertaken in this thesis (and how they contribute to the field of corrosion testing of engineering coatings) follows below. The main outcome of this work is that it has led to:

1- The successful development of a novel corrosion accelerated electrochemical evaluation technique for electrically-conductive coating materials on metal substrates (for which there is an industrial demand), from which objective results i.e. numerical data values, that can be related directly to coating degradation behaviour can be extracted.

2- After extensive scoping and repeatability trials, to eliminate (or at least reduce the influence of) random variables and reduce 'background noise' in the test procedures, it has been shown that the cyclic test protocol developed can discriminate between the performance of different coatings and (unlike long-term EIS periodic interrogation, or subjective salt spray test evaluation), produce comparative results that can be used to down-select new coatings for corrosion (or combined corrosion and wear) applications in a relatively short time (less than one day).

3- Incorporation of concurrent solution pH measurement with the advanced (AC)DC/OCP/AC technique developed in this work, qualifies this approach to be applied in different industrial applications, such as in aircraft, nuclear and

biomedical sectors (as well as being a useful tool for further academic research into environmentally friendly metallic coatings (PVD-deposited, or otherwise) to replace toxic coatings and processes that currently still need to be used in industry despite legislative pressure to eliminate them.

4- An estimation of the thickness of the passive film formed during 2 h E_{OCP} and six successive DC/OCP cycles has been made from the EIS data (using the capacitance and *n*-exponent data generated after each polarisation cycle). An assumption from *n* of the likely existing porosity in the passive film (and its permittivity relative to the coating material) was used to explore what the 'real' thickness of the passive film might be. The porosity probably somewhat higher, in most cases, since the limited available literature data generally does not take account of porosity.

In summary;

A new electrochemical method (AC)DC/OCP/AC with concurrent solution pH measurement, for accelerated evaluation of the chemical and electrochemical corrosion processes of electrically-conductive coating and/or substrate has been developed and validated as showed in this thesis on uncoated Al 6082 alloy and PVD Al-based coated 17/4PH steel substrate.

- The (AC)DC/OCP/AC method can, with careful control of experimental variables) reproduce the electrochemical corrosion process in the repeated evaluation of (i.e. three repeat tests) uncoated Al 6082 alloy, with sufficient sensitivity to detect changes in the passive film formed on the Al substrate

during 2 h E_{OCP} and after six successive DC/OCP cycles of extreme cathodic polarisation and relaxation/recovery.

- The corrosion behaviour of three prototype PVD Al-based nanostructured coatings (AlCr, AlCr(N) and AlCrTi) deposited on a 17/4 PH steel substrate (a material typically used, either coated or uncoated, for high-strength corrosion applications in demanding, adverse environments in the aerospace and power generation industries) was studied and compared. It was shown that, for AlCrTi, excellent pitting corrosion resistance was exhibited, compared to AlCr(N) and (particularly) AlCr, however AlCr(N) exhibited strong self-healing behaviour after breakdown during extreme DC polarisation, which might be more promising behaviour for future coating materials. The new testing technique developed in this thesis can be used to identify the onset of the degradation more accurately (and in a non-subjective way), with good correlation between characteristic behaviour in solution pH and the corrosion behaviour of the coatings, whilst the EIS interrogation after relaxation provides detailed insights into the coatings' ability to recover and to the rate of degradation likely to occur under adverse conditions in service.

Recommendations for future work

As mentioned above, one of the main scientific outputs of this work was the development of a new electrochemical corrosion evaluation technique for metallic-conductive engineering coatings. In order to make our analysis more robust, certain

variables features that ere noticed in the initial design and experimental conditions (i.e. sample surface pre-conditioning, electrode positioning, electrolyte preparation, etc.) needed to be resolved to allow reliable data to be gathered. From the current findings, a set of logical extensions to this research can be proposed, that allow a systematic exploration for new and useful information about corroding metallic systems as recommended in the following research directions:

- *Improving the sample preparation protocol*: The existence (or not) of a native oxide film on the surface of the substrate or the coating (and its thickness and structure) before conducting any electrochemical experimental work should be taken into account. Actual performance of metallic substrates and coatings can be significantly affected by the native oxide film properties prior to testing, that cause difference in the initial potential behaviour, which ultimately resulting in different corrosion behaviour of the evaluated same sample or could affected even different samples of notionally identical material. This is the most urgent challenge, so the initial potential, since the existence (or not) of native oxide film is a task that cannot be controlled easily, but should be avoided in the first place. Therefore, optimal sample preparation should be further studied. It may be that, in practice, PVD coated structures (particularly when using active metallic films such as the three evaluated here), should be preconditioned electrochemically prior to use, to ensure repeatable in – service performance.

- *Extending the chemistry of the environmental conditions:* The neutral salt solution used in this research represents a significant simplification from the diverse chemical environments (both acidic and alkaline) that could actually be experienced in practical application. In particular, acidic solutions could act as a severe corrosive environment, thereby inducing high corrosion rate during DC cathodic polarisation due to high hydrogen ion concentration. It is, therefore, important to consider these types of solutions in future stages of this research.

- *Improving the aggressive solution conditions:* The effect of using fresh electrolyte solution in each cyclic polarisation test (rather than keeping the same solution for all six cycles) on the corrosion rate under application DC/OCP cycles must be studied in further detail. The chemical composition of the electrolyte after applied six cycles of DC/OCP and after each DC/OCP cycle (for fresh electrolyte solution) should be analyse by Inductively Coupled Plasma Mass Spectroscopy (ICP-MS); to determine the concentration of ionic species (μg/l) that dissolved in the tested electrolyte due to the changes in solution pH. Testing new exposure area could be further explored in future research.

- *Revising the boundary conditions used by current electrochemical cell design:* In particular, the current electrochemical cell design could be improved by adapting a gas collector with stirring mechanism to counteract the evolution of hydrogen gas bubbles over the electrochemical reactions

occurring at the metal/electrolyte interface during DC cathodic polarisation or remove them when formed.

- *Diversity of sampling:* continuation of evaluation of the electrochemical corrosion behaviour of other electrically-conductive substrates and coatings using (AC)DC/OCP/AC cyclic testing to verify their same corrosion behaviour as that evaluated by conventional electrochemical techniques or explore a new corrosion behaviour using our technique.

- *Further validation:* The advanced electrochemical technique developed in this thesis has shown a promising prospect for practical corrosion accelerating and evaluating applications. However, further work is required to validate the correlation between the results obtained electrochemically over (AC)DC/OCP/AC and the actual in-service corrosion rates of the monitored structure. For this purpose, a multiscale approach is recommended that combines tests in small electrochemical cells, large salt spray testing chamber and/or outdoor cyclic testing.

It recommended that the advanced (AC)DC/OCP/AC of all coatings should be repeated several times for statistical reliability; it also need to be performed over different numbers of DC/OCP cycles and at different potentials during DC cathodic polarisation, in order to establish a consistency in the corrosion behaviour of the coatings. An application of (AC) anodic polarisation rather than DC cathodic polarisation cycle should also be considered in future models.

Lastly, multiphysics modelling packages (such as COMSOL) are a powerful tool, which could be used for developing compatible modelling to (AC)DC/OCP/AC cyclic testing, including formation or dissolution of the passive film during DC cathodic polarisation and relaxation time with chemical reaction under solution electrolysis, hydrogen permeation rate, aluminate ion gel formation, growth rate of passivating film, the thickness of the passive, breakdown (transpassive phenomena), and effect of the reduction potential of electrodes.

References

1. Holmberg, K., *Coatings tribology Properties, Mechanisms, Techniques and Applications in Surface Engineering*. 2nd ed, ed. Matthews, A. 18 Mar 2009: Elsevier Science.

2. Robinson, G. C. M. J., *Hydrogen re-embrittlement of high strength steel by corrosion of cadmium and aluminium based sacrificial coatings.* 2005. **40**(1): p. 28-32.

3. Hugh, M. *The environmental and engineering advantages of cadmium coatings, in Sources of cadmium in the environment: .* in *Proceding of the OECD Cadmium Workshop*. 1995. Saltsjöbaden, Sweden, .

4. Liu, C., Leyland, A., Bi, Q., and Matthews, A., *Corrosion resistance of multi-layered plasma-assisted physical vapour deposition TiN and CrN coatings.* Surface and Coatings Technology, 2001. **141**(2–3): p. 164-173.

5. Creus, J., Billard, A., and Sanchette, F., *Corrosion behaviour of amorphous Al–Cr and Al–Cr–(N) coatings deposited by dc magnetron sputtering on mild steel substrate.* Thin Solid Films, 2004. **466**(1–2): p. 1-9.

6. Holmes, L. V., Muehlberger, E. D. E., and and Reilly, J. J., *The Substitution of IVD Aluminum for Cadmium, .* August 1989 Phase I Report, ESL-TR-88-75, Air Force Engineering & Service Center, Engineering and Service Laboratory: Tyndall Air Force Base, Florida.

7. Leyland, A. and Matthews, A., *Design criteria for wear-resistant nanostructured and glassy-metal coatings.* Surface and Coatings Technology, 2004. **177-178**: p. 317-324.

8. Sanchette, F. and Billard, A., *Main features of magnetron sputtered aluminium-transition metal alloy coatings.* Surface and Coatings Technology, 2001. **142-144**: p. 218-224.

9. Park, M. J., Leyland, A., and Matthews, A., *Corrosion performance of layered coatings produced by physical vapour deposition.* Surface and Coatings Technology, 1990. **43-44**(PART 1): p. 481-492.

10.   Buchheit, R. G., Cunningham, M., Jensen, H., Kendig, M. W., and Martinez, M. A., *A Correlation Between Salt Spray and Electrochemical Impedance Spectroscopy Test Results for Conversion-Coated Aluminum Alloys.* Corrosion, 1998. **54**(1): p. 61-72.

11.   Deflorian, F., Fedrizzi, L., Rossi, S., and Buratti, F., *Testing of Protective Organic Coatings on Metals: Comparison of Salt Spray and Electrochemical Impedance Spectroscopy.* Journal of Testing and Evaluation,, 2002. **31**(2): p. 1-7.

12.   Kendig, M., Jeanjaquet, S., Brown, R., and Thomas, F., *Rapid electrochemical assessment of paint.* JCT, Journal of coatings technology, 1996. **68**(39): p. 863-840.

13.   Hollaender, J., Schiller, C. A., and Strunz, W., *Accelerating the Time Scale of Coating Tests - Can the Combination of Linear Small Signal Methods with Electrochemical Stress Improve the Coating Lifetime Prediction* 2001, Fraunhofer - Institut Verfahrenstechnik und Verpakung IVV

14.   Hollaender, J., *Rapid Assessment of Food/Package Interactions by Electrochemical Impedance Spectroscopy (EIS).* Food Additives and Contaminants, 1997. **14**(6-7): p. 617-626.

15.   Suay, J. and García, S. J., *A comparative study between the results of different electrochemical techniques (EIS and AC/DC/AC): Application to the optimisation of the cataphoretic and curing parameters of a primer for the automotive industry.* Progress in Organic Coatings, 2007. **59**(3): p. 251-258.

16.   Puig, M., Cabedo, L., Gracenea, J. J., and Suay, J. J., *The combined role of inhibitive pigment and organo-modified silica particles on powder coatings: Mechanical and electrochemical investigation.* Progress in Organic Coatings, 2015. **80**: p. 11-19.

17.   Suay, J. J., Giménez, E., Rodríguez, T., Habbib, K., and Saura, J. J., *Characterization of anodized and sealed aluminium by EIS.* Corrosion Science, 2003. **45**(3): p. 611-624.

18.   García, S. J. and Suay, J., *Optimization of deposition voltage of cataphoretic automotive primers assessed by EIS and AC/DC/AC.* Progress in Organic Coatings, 2009. **66**(3): p. 306-313.

19. Poelman, M., Olivier, M., Gayarre, N., and Petitjean, J., *Electrochemical study of different ageing tests for the evaluation of a cataphoretic epoxy primer on aluminium.* Progress in Organic Coatings, 2005. **54**(1): p. 55-62.

20. Zhu, C., Xie, R., Xue, J., and Song, L., *Studies of the impedance models and water transport behaviors of cathodically polarized coating.* Electrochimica Acta, 2011. **56**(16): p. 5828-5835.

21. Allahar, K., Upadhyay, V., and Bierwagen, G., *Characterizing the relaxtion of the circuit potential during an AC-DC-AC acceleration test*, in *2009 DoD corrosion conference,*. 2009: Washington, DC, USA.

22. Bierwagen, G., Allahar, K., Su, Q., and Gelling, V., *Electrochemically characterizing the ac–dc–ac accelerated test method using embedded electrodes.* Corrosion Science, 2009. **51**(1): p. 95-101.

23. Olivier, M. and Poelman, M., *Use of Electrochemical Impedance Spectroscopy (EIS) for the Evaluation of Electrocoatings Performances*, in *Recent Researches in Corrosion Evaluation and Protection*, Razavi, R. S., Editor. 2012, InTech: Belgium.

24. Bethencourt, M., Botana, F. J., Cano, M. J., Osuna, R. M., and Marcos, M., *Lifetime prediction of waterborne acrylic paints with the AC–DC–AC method.* Progress in Organic Coatings, 2004. **49**(3): p. 275-281.

25. ISO-17463, *Paints and varnishes -- Guidelines for the determination of anticorrosive properties of organic coatings by accelerated cyclic electrochemical technique*. 2014, The International Organization for Standardization ISO. p. 14.

26. Bowen, C. T., Davis, H. J., Henshaw, B. F., Lachance, R., LeRoy, R. L., and Renaud, R., *Developments in advanced alkaline water electrolysis.* International Journal of Hydrogen Energy, 1984. **9**(1–2): p. 59-66.

27. Marini, S., Salvi, P., Nelli, P., Pesenti, R., Villa, M., Berrettoni, M., Zangari, G., and Kiros, Y., *Advanced alkaline water electrolysis.* Electrochimica Acta, 2012. **82**(0): p. 384-391.

28. Hollingsworth. E.h and Hunsicker. H.Y, *Corrosion of Aluminium and Aluminium Alloys*. Corrosion, ed. 4. Vol. 13. 1992: ASM international, the materials information society. 583-609.

29.   Fasuba, O. A., Yerokhin, A., Matthews, A., and Leyland, A., *Corrosion behaviour and galvanic coupling with steel of Al-based coating alternatives to electroplated cadmium.* Materials Chemistry and Physics, 2013. **141**(1): p. 128-137.

30.   He, J., Wen, J., and Li, X., *Effects of precipitates on the electrochemical performance of Al sacrificial anode.* Corrosion Science, 2011. **53**(5): p. 1948-1953.

31.   Martin, F. J., Cheek, G. T., O'Grady, W. E., and Natishan, P. M., *Impedance studies of the passive film on aluminium.* Corrosion Science, 2005. **47**(12): p. 3187-3201.

32.   Trdan, U. and Grum, J., *Evaluation of corrosion resistance of AA6082-T651 aluminium alloy after laser shock peening by means of cyclic polarisation and EIS methods.* Corrosion Science, 2012. **59**: p. 324-333.

33.   Liu, C., Leyland, A., Lyon, S., and Matthews, A., *Electrochemical impedance spectroscopy of PVD-TiN coatings on mild steel and AISI316 substrates.* Surface and Coatings Technology, 1995. **76–77, Part 2**(0): p. 615-622.

34.   Liu, C., Bi, Q., Leyland, A., and Matthews, A., *An electrochemical impedance spectroscopy study of the corrosion behaviour of PVD coated steels in 0.5 N NaCl aqueous solution: Part I. Establishment of equivalent circuits for EIS data modelling.* Corrosion Science, 2003. **45**(6): p. 1243-1256.

35.   Emregül, K. C. and Aksüt, A. A., *The behavior of aluminum in alkaline media.* Corrosion Science, 2000. **42**(12): p. 2051-2067.

36.   Roberge, P. R., *Corrosion engineering principles and practice*. 2008: McGraw-Hill Professional.

37.   Schweitzer, P. A., *Fundamentals of Metallic Corrosion Atmospheric and Media Corrosion of Metals*. 2006: CRC Press. 1-38.

38.   BOS, W. M., *Prediction of coating durability - Early detection using electrochemical methods*. 2008, Netherlands: Gildeprint drukkerijen B.V., Enschede, .

39.   Christian. V , Michel. J, and Martin. S, *Chapter B.1 - The Corrosion of Aluminium*, in *Corrosion of Aluminium*. 2004, Elsevier: Amsterdam. p. 81-109.

40. David E.J. Talbot and Talbot, J. D. R., *Corrosion Science and Technology,* . Second Edition ed. 2007, USA: Taylor & Francis Group, LLC.

41. Sukiman, N. L., Zhou, X., Birbilis, N., Hughes, A. E., Mol, J. M. C., Garcia, S. J., and Thompson, G. E., *Durability and Corrosion of Aluminium and Its Alloys: Overview, Property Space, Techniques and Developments, Aluminium Alloys - New Trends in Fabrication and Applications*, Ahmad, Z., Editor. 2012.

42. L.L. Shreir, R. A. J., G.T. Burstein, *Corrosion: Metal/environment reactions*. 1994: Butterworth.

43. Hatch, J. E., *Aluminum: Properties and Physical Metallurgy*. 1984: American Society of Metals.

44. Pyun, S. and Moon, S., *Corrosion mechanism of pure aluminium in aqueous alkaline solution.* Journal of Solid State Electrochemistry, 2000. **4**(5): p. 267.

45. Macdonald. D.D, Real. S, and M, U.-M., *Evaluation of alloy anodes for aluminum-air batteries.* J. Electrochem. Soc.,, 1988. **135**: p. 2397–2409.

46. Chu, D. and Savinell, R. F., *Experimental data on aluminum dissolution in KOH electrolytes.* Electrochimica Acta, 1991. **36**(10): p. 1631-1638.

47. Mansouri, K., Ibrik, K., Bensalah, N., and Abdel-Wahab, A., *Anodic Dissolution of Pure Aluminum during Electrocoagulation Process: Influence of Supporting Electrolyte, Initial pH, and Current Density.* Industrial & Engineering Chemistry Research, 2011. **50**(23): p. 13362-13372.

48. Moon, S. M. and Pyun, S. I., *The corrosion of pure aluminium during cathodic polarization in aqueous solutions.* Corrosion Science, 1997. **39**(2): p. 399-408.

49. Mercier, D. and Barthés-Labrousse, M. G., *The role of chelating agents on the corrosion mechanisms of aluminium in alkaline aqueous solutions.* Corrosion Science, 2009. **51**(2): p. 339-348.

50. Boukerche, I., Djerad, S., Benmansour, L., Tifouti, L., and Saleh, K., *Degradability of aluminum in acidic and alkaline solutions.* Corrosion Science, 2014. **78**(0): p. 343-352.

51. Perrault, G. G., *The Role of Hydrides in the Equilibrium of Aluminum in Aqueous Solutions.* Journal of the Electrochemical Society, 1979. **126**(2): p. 199-204.

52. Adhikari, S. and Hebert, K. R., *Factors controlling the time evolution of the corrosion potential of aluminum in alkaline solutions.* Corrosion Science, 2008. **50**(5): p. 1414-1421.

53. Adhikari, S., Ai, J., Hebert, K. R., Ho, K. M., and Wang, C. Z., *Hydrogen in aluminum during alkaline corrosion.* Electrochimica Acta, 2010. **55**(19): p. 5326-5331.

54. Moon, S.-M. and Pyun, S.-I., *The formation and dissolution of anodic oxide films on pure aluminium in alkaline solution.* Electrochimica Acta, 1999. **44**(14): p. 2445-2454.

55. Kim, Y. S., Pyun, S. I., Moon, S. M., and Kim, J. D., *The effects of applied potential and pH on the electrochemical dissolution of barrier layer in porous anodic oxide film on pure aluminium.* Corrosion Science, 1996. **38**(2): p. 329-336.

56. Doche, M. L., Rameau, J. J., Durand, R., and Novel-Cattin, F., *Electrochemical behaviour of aluminium in concentrated NaOH solutions.* Corrosion Science, 1999. **41**(4): p. 805-826.

57. Moon, S.-M. and Pyun, S.-I., *Effects of applied anodic potential and pH on the repassivation kinetics of pure aluminium in aqueous alkaline solution.* Journal of Solid State Electrochemistry, 1999. **3**(2): p. 104-110.

58. Sato, N., *Basics of Corrosion Chemistry*, in *Green Corrosion Chemistry and Engineering*, Sharma, S. K., Editor. 2011, Wiley-VCH Verlag GmbH & Co. KGaA. p. 1-32.

59. Pourbaix, M., *"Atlas of Electrochemical Equilibria in Aqueous Solutions"*. 1974, National Association of Corrosion Engineers.: Houston, TX

60. Perez, N., *Electrochemistry and Corrosion Science (Information Technology: Transmission, Processing & Storage)* Vol. 1. 2004, US: Springer

61. Schweitzer, G. K. and Pesterfield, L. L., *The Aqueous Chemistry of the Elements*. 2010, New York: Oxford University Press, Inc.

62. Cerqueira, A. A. and Marques, M. R., *Electrolytic Treatment of Wastewater in the Oil Industry*, in *New Technologies in the Oil and Gas Industry*, Jorge Salgado Gomes, Editor. 2012, InTech.

63. Szklarska, S. Z., *Pitting corrosion of aluminum.* Corrosion Science, 1999. **41**(9): p. 1743-1767.

64. Foley, R. T., *Localized Corrosion of Aluminum Alloys—A Review.* Corrosion, 1986. **42**(5): p. 277-288.

65. Kaesche, H., *Corrosion of Metals, Physicochemical Principles and Current Problems*. Engineering Materials and Processes. 2003: Springer Berlin Heidelberg.

66. Srinivasa Rao, K. and Prasad Rao, K., *Pitting corrosion of heat-treatable aluminium alloys and welds: A reveiw.* Transactions of the Indian Institute of Metals, 2004. **57**(6): p. 593-610.

67. Mutombo, F. K., *Corrosion Fatigue Behaviour of 5083-H111 and 6061-T651 Aluminium Alloy Welds*. 2011: University of Pretoria.

68. Musa, Y. A., *Corrsion Protection of Al Alloys: Organic Coatings and Inhibitors, Recent Researches in Corrosion Evaluation and Protection*, ed. Razavi.S.R, P. 2012, Malysisa: InTech.

69. Macdonald, D. D., *Passivity–the key to our metals-based civilization.* Pure Appl. Chem, 1999. **71**(6): p. 951-978.

70. McCafferty, E., *Introduction to Corrosion Science*. 2010, New York Dordrecht Heidelberg London: Springer Science+Business Media, LLC.

71. Macdonald. D.D, Urquidi-Macdonald. M, Song. H, Biaggio-Rocha. S, and P., S., *Fundamental studies on passivity and passivity breakdown.* Office of Scientific and Technical Information OSTI, 1991. **23**(12).

72. Soltis, J., *Passivity breakdown, pit initiation and propagation of pits in metallic materials - Review.* Corrosion Science, 2015. **90**: p. 5-22.

73. Baldwin, K. R., Bates, R. I., Arnell, R. D., and Smith, C. J. E., *Aluminium-magnesium alloys as corrosion resistant coatings for steel.* Corrosion Science, 1996. **38**(1): p. 155-170.

74. Akiyama, E., Kawashima, A., Asami, K., and Hashimoto, K., *The effects of alloying elements on the passivity of sputter-deposited amorphous Al-Cr-Mo alloys in 1M HCl.* Corrosion Science, 1996. **38**(8): p. 1281-1294.

75. Chen, G. S., Gao, M., and Wei, R. P., *Microconstituent-Induced Pitting Corrosion in Aluminum Alloy 2024-T3.* Corrosion (Houston), 1996. **52**(1): p. 8-15.

76. Buchheit, R. G., Grant, R. P., Hlava, P. F., McKenzie, B., and Zender, G. L., *Local dissolution phenomena associated with S phase (Al 2CuMg) particles in aluminum alloy 2024-T3.* Journal of the Electrochemical Society, 1997. **144**(8): p. 2621-2628.

77. Juffs, L., Hughes, A. E., and Paterson, P. J. K., *The use of macroscopic modelling of intermetallic phases in aluminium alloys in the study of ferricyanide accelerated chromate conversion coatings.* Micron, 2001. **32**(8): p. 777-787.

78. Zor.S, Zeren.M, Özkazan.H, and Karakulak.H, *Effect of Titanium Addition on Corrosion Properties of Al-Si Eutectic Alloys.* Protection of Metals and Physical Chemistry of Surface, 2012. **48**(5): p. 568–571.

79. Hinds, G. *"The Electrochemistry of Corrosion"*. 1996; Available from: http://www.npl.co.uk/upload/pdf/the_electrochemistry_of_corrosion.pdf (accessed september 14, 2015).

80. Schennach, R. *Electrochemical Kinetics of Corrosion and Passivity.* 2006/2007; Available from: http://www.staff.tugraz.at/robert.schennach/Electrochemical_Kinetics_of_Corrosion_and_Passivity.pdf

81. Baboian.R, *Corrosion tests and standards: application and interpretation*. 2nd ed. 2005, West Conshohocken, USA: ASTM International.

82. Harun, M. K., Marsh, J., and Lyon, S. B., *The effect of surface modification on the cathodic disbondment rate of epoxy and alkyd coatings.* Progress in Organic Coatings, 2005. **54**(4): p. 317-321.

83. Teng, H.-T., Lee, T.-Y., Chen, Y.-K., Wang, H.-W., and Cao, G., *Effect of Al(OH)3 on the hydrogen generation of aluminum–water system.* Journal of Power Sources, 2012. **219**: p. 16-21.

84.   Sørensen, P. A., Dam-Johansen, K., Weinell, C. E., and Kiil, S., *Cathodic delamination: Quantification of ionic transport rates along coating–steel interfaces.* Progress in Organic Coatings, 2010. **68**(1–2): p. 70-78.

85.   Suay, J. J., Rodríguez, M. T., Izquierdo, R., Kudama, A. H., and Saura, J. J., *Rapid assessment of automotive epoxy primers by electrochemical techniques.* Journal of Coatings Technology, 2003. **75**(945): p. 103-111.

86.   Broesder, E. and Stopaq, B. V. *Coatings and Cathodic Disbondment - The True Story*. in *Pipelines 2013*. June 23-26, 2013. Fort Worth, Texas, United States.

87.   Brown, P. *Electrolysis of sodium chloride solution (brine)*. 2000; The electrode reactions and products of the electrolysis of sodium chloride solution (brine).]. Available from: http://www.docbrown.info/page01/ExIndChem/electrochemistry03.htm.

88.   Bodner, R. W. *Electrolytic Cells*. 2009; Available from: http://chemed.chem.purdue.edu/genchem/topicreview/bp/ch20/faraday.php#aq.

89.   Groysman, A. and Groysman, O., *Corrosion for Everybody*. 2009: Springer Dordrecht Heidelberg London New York.

90.   Harrington, D. A. and Conway, B. E., *Kinetic theory of the open-circuit potential decay method for evaluation of behaviour of adsorbed intermediates: Analysis for the case of the H2 evolution reaction.* Journal of Electroanalytical Chemistry and Interfacial Electrochemistry, 1987. **221**(1–2): p. 1-21.

91.   Gouveia, H., Landers, R., and Boodts, J. F. C., *Investigation of the surface properties and the hydrogen evolution reaction, HER, at thermal rhodium oxide electrodes.* Electrochimica Acta, 2007. **52**(7): p. 2359-2369.

92.   Tadeusz, Z., *Electrochemical determination of hydrogen in metals.* Journal of Electroanalytical Chemistry, 1999. **475**(1): p. 82-88.

93.   Pyun, S.-I. and Oriani, R. A., *The permeation of hydrogen through the passivating films on iron and nickel.* Corrosion Science, 1989. **29**(5): p. 485-496.

94.   Fischer, F. D., Mori, G., and Svoboda, J., *Modelling the influence of trapping on hydrogen permeation in metals.* Corrosion Science, 2013. **76**: p. 382-389.

95.   Pérez-Ceballos, A. M., Calderón-Gutierrez, J. A., and Rosa-Mattos, O., *Effect of an electrolyte flow on electrochemical hydrogen permeation.* DYNA, 2014. **81**: p. 152-157.

96.   Zeng, Y., Noël, J. J., Norton, P. R., and Shoesmith, D. W., *Hydrogen transport through thin titanium oxides.* Journal of Electroanalytical Chemistry, 2010. **649**(1–2): p. 277-285.

97.   Taylor, L. M., *Hydrogen Permeation of Alloy-22 Considering The Passive Layer* August, 2007 University of Nevada, Reno

98.   Addach, H., Berçot, P., Rezrazi, M., and Takadoum, J., *Study of the electrochemical permeation of hydrogen in iron.* Corrosion Science, 2009. **51**(2): p. 263-267.

99.   Yan, L., Ramamurthy, S., Noël, J. J., and Shoesmith, D. W., *Hydrogen absorption into alpha titanium in acidic solutions.* Electrochimica Acta, 2006. **52**(3): p. 1169-1181.

100.   Qin, Z., Zeng, Y., and Shoesmith, D. W., *Modeling hydrogen permeation through a thin titanium oxide film and palladium.* Thin Solid Films, 2013. **534**: p. 673-679.

101.   Pound, B. G., *Hydrogen trapping in precipitation-hardened alloys.* Acta Metallurgica et Materialia, 1990. **38**(12): p. 2373-2381.

102.   Bruzzoni, P., Carranza, R. M., Collet Lacoste, J. R., and Crespo, E. A., *Hydrogen diffusion in α-iron studied using an electrochemical permeation transfer function.* Electrochimica Acta, 1999. **44**(16): p. 2693-2704.

103.   Sun, Y., Dai, Y., Liu, Y., and Chen, S., *A rotating disk electrode study of the particle size effects of Pt for the hydrogen oxidation reaction.* Physical Chemistry Chemical Physics, 2012. **14**(7): p. 2278-2285.

104.   Schuman, T. P., *Chapter 17 - Protective coatings for aluminum alloys*, in *Handbook of Environmental Degradation of Materials*, Kutz, M., Editor. 2005, William Andrew Publishing: Norwich, NY. p. 345-366.

105.   Revie, W. R. and Uhlig, H. H., *Corrosion and Corrosion Control: An Introduction to Corrosion Sciencevand Engineering*. 4th ed. 2008: A JOHN WILEY & SONS, INC., PUBLICATION.

106.   Bewilogua, K., Bräuer, G., Dietz, A., Gäbler, J., Goch, G., Karpuschewski, B., and Szyszka, B., *Surface technology for automotive engineering.* CIRP Annals - Manufacturing Technology, 2009. **58**(2): p. 608-627.

107.   Burakowski. T and Wierzchoń.T, *Surface Engineering of Metals: Principles, Equipment, Technologies*. 1999. 177-179.

108.   *Amending Regulation (EC) No 1907/2006 of the European Parliament and of the Council on the Registration, Evaluation, Authorisation and Restriction of of Chemicals (REACH) as regards Annex XVII (Cadmium).* COMMISSION REGULATION (EU) No 835/2012, 18 September 2012.

109.   *Amending Annex XVII to Regulation (EC) No 1907/2006 of the European Parliament and of the Council on the Registration, Evaluation, Authorisation and Restriction of Chemicals (REACH) as regards chromium VI compounds.* COMMISSION REGULATION (EU) No 301/2014., 25 March 2014.

110.   BCC Research LLC. *High-Performance Ceramic Coatings: Markets and Technologies*. 2012; Available from: http://www.bccresearch.com/market-research/advanced-materials/north-american-ceramic-coatings-market-tech-avm015f.html.

111.   Mattox, D. M., *Handbook of Physical Vapor Deposition (PVD) Processing*. 2007: Elsevier.

112.   Holmes, V. L. and Reilly, J. J., *Ion Vapor Deposition Aluminum QualificationTests*, in *Pollution Prevention Project PRJY 921609* June 1995, Environmental ManagementDirectorate: McClellan AFB, CA 95652.

113.   Rickerby, D. S. and Matthews, A., *Advanced Surface Coatings: a Handbook of Surface Engineering*. 1991, Glasgow: Blackie & Sons Limited.

114.   Ohring, M., *Chapter 1 - A Review of Materials Science*, in *Materials Science of Thin Films (Second Edition)*. 2002, Academic Press: San Diego. p. 1-56.

115.   Hill, R. J., ed. *Physical Vapour Deposition*. 1986: Berkeley, CA.

116. Randhawa, H., *TiN-coated high-speed steel cutting tools.* vacum science and technology, 1986. **A4**: p. 2755.

117. Kelly, P. J. and Arnell, R. D., *Magnetron sputtering: a review of recent developments and applications.* Vacuum, 2000. **56**(3): p. 159-172.

118. Kelly, P. J. and Arnell, R. D., *Development of a novel structure zone model relating to the closed-field unbalanced magnetron sputtering system.* Journal of Vacuum Science & Technology A: Vacuum, Surfaces, and Films, 1998. **16**(5): p. 2858-2869.

119. Holmberg, K. and Matthews, A., *Coatings Tribology: Properties, Mechanisms, Techniques and Applications in Surface Engineering*. 2009: Elsevier Science.

120. Martin, P., *Introduction to Surface Engineering and Functionally Engineered Materials*. 2011: Wiley.

121. Messier, R., Giri, A. P., and Roy, R. A., *Revised structure zone model for thin film physical structure.* Journal of Vacuum Science & Technology A, 1984. **2**(2): p. 500-503.

122. Sanchette, F., Tran Huu, L., Billard, A., and Frantz, C., *Structure—properties relationship of metastable Al-Cr and Al-Ti alloys deposited by r.f. magnetron sputtering: role of nitrogen.* Surface and Coatings Technology, 1995. **74–75, Part 2**(0): p. 903-909.

123. Sanchette, F., Czerwiec, T., Billard, A., and Frantz, C., *Sputtering of Al-Cr and Al-Ti composite targets in pure Ar and in reactive Ar-N2 plasmas.* Surface and Coatings Technology, 1997. **96**(2–3): p. 184-190.

124. Creus, J., Berziou, C., Cohendoz, S., Perez, A., Rébéré, C., Reffass, M., Touzain, S., Allely, C., Gachon, Y., Héau, C., Sanchette, F., and Billard, A., *Reactivity classification in saline solution of magnetron sputtered or EBPVD pure metallic, nitride and Al-based alloy coatings.* Corrosion Science, 2012. **57**: p. 162-173.

125. Brennan, P. J., Grossman, S. J., and Harkness, N. R., *The Development and Application of Corrosion/Weathering Cyclic Testing*. 2009, Q Panel Lab Products,Nick Harkness Pty Ltd.

126.   Loveday, D., Peterson, P., and Rodgers, B., *Evaluation of organic coatings with electrochemical impedance spectroscopy, Part1: Fundamentals of Electrochemical Impedance Spectroscopy.* JCT coatings tech, 2004. **8**: p. 46-52.

127.   Loveday, D., Peterson, P., and Rodgers, B., *Evaluation of organic Coatings with Electrochemical Impedance Spectroscopy, part2: Application of EIS to Coatings* JCT coatings tech, 2004. **8**: p. 88-93.

128.   Taylor, S. R., Contu, F., Calle, L. M., Curran, J. P., and Li, W., *Predicting the Long-Term Field Performance of Coating Systems on Steel Using a Rapid Electrochemical Test: The Damage Tolerance Test.* Corrosion, 2012. **68**(3): p. 035007-1-035007-13.

129.   ISSF, I., *The salt spray test and its use in ranking stainless steels, the test and its limits*, in *A technical guide to salt spray test and its interpretation with stainless steel*. May 2008, ISSF.

130.   Floyd, F. L., Avudaiappan, S., Gibson, J., Mehta, B., Smith, P., Provder, T., and Escarsega, J., *Using electrochemical impedance spectroscopy to predict the corrosion resistance of unexposed coated metal panels.* Progress in Organic Coatings, 2009. **66**(1): p. 8-34.

131.   Song. S, Song. G, and S, W., *A Comparative Study on Corrosion Resistance Evaluation Techniques for Coated Magnesium Alloys.* DoD Corrosion Conference, 2011: p. 5.

132.   Mansfeld, F., *Electrochemical impedance spectroscopy (EIS) as a new tool for investigating methods of corrosion protection.* Electrochimica Acta, 1990. **35**(10): p. 1533-1544.

133.   ASTM, *B117-11: Standard Practice for Operating Salt Spray (Fog) Apparatus*, in *Corrosion of metals*. 2011, American Society for Testing and Materials (ASTM), : West Conshohocken, PA, USA.

134.   Olivier.G.M and Poelman.M., *Use of Electrochemical Impedance Spectroscopy (EIS) for the Evaluation of Electrocoatings Performances.* Recent Researches in Corrosion Evaluation and Protection,InTech, 2012.

135.   Allahar, K., Bierwagen, G., and Gelling, V., *Understanding ac–dc–ac accelerated test results.* Corrosion Science, 2010. **52**(4): p. 1106-1114.

136. Treacy, G. M., Wilcox, G. D., and Richardson, M. O. W., *Monitoring the corrosion behaviour of chromate-passivated aluminium alloy 2014 A-T6 by electrochemical impedance spectroscopy during salt fog exposure.* Surface and Coatings Technology, 1999. **114**(2–3): p. 260-268.

137. Macdonald, J. R., *Impedance Spectroscopy* John Wiley & Sons. 1987.

138. Kendig, M. and Scully, J., *Basic aspects of electrochemical impedance application for the life prediction of organic coatings on metals.* Corrosion, 1990. **46**(1): p. 22-29.

139. Bai, Z. Q., Chen, C. F., Lu, M. X., and Li, J. B., *Analysis of EIS characteristics of CO2 corrosion of well tube steels with corrosion scales.* Applied Surface Science, 2006. **252**(20): p. 7578-7584.

140. Liu, C., Leyland, A., Lyon, S., and Matthews, A., *An a.c. impedance study on PVD CrN-coated mild steel with different surface roughnesses.* Surface and Coatings Technology, 1995. **76–77, Part 2**(0): p. 623-631.

141. Bierwagen, G., Tallman, D., Li, J., He, L., and Jeffcoate, C., *EIS studies of coated metals in accelerated exposure.* Progress in Organic Coatings, 2003. **46**(2): p. 149-158.

142. Gambina, F., *Corrosion Resistance Characterization of Coating Systems Used to Protect Aluminum Alloys Using Electrochemical Impedance Spectroscopy and Artificial Neural Networks*. 2010, Ohio State University, : Ohio State

143. Scully.J.R and Taylor.D.W, *Electrochemical Methods of Corrosion Testing, Laboratory Testing*. 9 ed. Corrosion, ed. 4. Vol. 13. 1992: ASM international, the materials information society.

144. Orazem.M.E and B, T., *Electrochemical Impedance Spectroscopy* in *Orazem, M.E. and B. Tribollet, Electrochemical Impedance Spectroscopy* 2008, The Electrochemical Society Series, ed. ECS. p. 155-157.

145. Cole, K. S. and Cole, R. H., *Dispersion and absorption in dielectrics I. Alternating current characteristics.* The Journal of chemical physics, 1941. **9**(4): p. 341-351.

146. Lvovich, V. F., *Impedance Spectroscopy: Applications to Electrochemical and Dielectric Phenomena*. 2012: Wiley.

147.   Orazem, B. M. and Pintauro, T. P., *Tutorials in Electrochemical Technology: Impedance Spectroscopy*. Vol. 13. 2008: The electrochemical Society. .

148.   García, S. J. and Suay, J., *A comparative study between the results of different electrochemical techniques (EIS and AC/DC/AC): Application to the optimisation of the cataphoretic and curing parameters of a primer for the automotive industry.* Progress in Organic Coatings, 2007. **59**(3): p. 251-258.

149.   Gudić, S., Smoljko, I., and Kliškić, M., *Electrochemical behaviour of aluminium alloys containing indium and tin in NaCl solution.* Materials Chemistry and Physics, 2010. **121**(3): p. 561-566.

150.   García, S. J., Rodríguez, M. T., Izquierdo, R., and Suay, J., *Evaluation of cure temperature effects in cataphoretic automotive primers by electrochemical techniques.* Progress in Organic Coatings, 2007. **60**(4): p. 303-311.

151.   Liu, C., Bi, Q., Leyland, A., and Matthews, A., *An electrochemical impedance spectroscopy study of the corrosion behaviour of PVD coated steels in 0.5 N NaCl aqueous solution: Part II.: EIS interpretation of corrosion behaviour.* Corrosion Science, 2003. **45**(6): p. 1257-1273.

152.   Rodríguez, M. T., Gracenea, J. J., García, S. J., Saura, J. J., and Suay, J. J., *Testing the influence of the plasticizers addition on the anticorrosive properties of an epoxy primer by means of electrochemical techniques.* Progress in Organic Coatings, 2004. **50**(2): p. 123-131.

153.   Hinderliter, B., Croll, S., Tallman, D., Su, Q., and Bierwagen, G., *Interpretation of EIS data from accelerated exposure of coated metals based on modeling of coating physical properties.* Electrochimica Acta, 2006. **51**(21): p. 4505-4515.

154.   Kauffman, A. M., *Understanding electrochemical cells- Technical report 17*. 1997, Solartron Instruments- a division of Solartron Group Ltd,: Farnborough, UK.

155.   Autolab.B.V, M., *Autolab Application Note EIS01, Electrochemical Impedance Spectroscopy (EIS), Part 2 – Experimental Setup.* 2011.

156.   Gamry, I. *Rapid Electrochemical Assessment of Paint*. 1997-98; Available from: http://www.gamry.com/application-notes/corrosion-coatings/rapid-electrochemical-assessment-of-paint/ (11 December 2015).

157.   Kendig, M. W. *Rapid electrochemical assessment of paint cell* November 2010; Available from: http://martinkendig.com/15144/15644.html (11 December 2015).

158.   Gamry, I. *Basic of Electrochemical Impedance Spectroscopy* 2016; Available from: www.gamry.com/assets/Application-Notes/Basics-of-EIS.pdf.

159.   Hollaender, J., *Rapid assessment of food/package interactions by electrochemical impedance spectroscopy (EIS).* Food Additives & Contaminants, 1997. **14**(6-7): p. 617-626.

160.   García, S. J. and Suay, J., *Anticorrosive properties of an epoxy-Meldrum acid cured system catalyzed by erbium III trifluromethanesulfonate.* Progress in Organic Coatings, 2006. **57**(4): p. 319-331.

161.   Rosliza, R., *Improvement of Corrosion Resistance of Aluminium Alloy by Natural Products*, in *Corrosion Resistance*, Shih, H., Editor. 2012, InTech. p. 482.

162.   Aalco. M. L. *Aluminium Alloy - Commercial Alloy - 6082 - T6~T651 Plate*. 2016; Available from: http://www.aalco.co.uk/datasheets/Aluminium-Alloy-6082-T6T651-Plate_148.ashx.

163.   ASTM G44 - 99, S., *Practice for Exposure of Metals and Alloys by Alternate Immersion in Neutral 3.5% Sodium Chloride Solution* in *Corrosion Standards and Wear Standards*. 2005, ASTM International

164.   G59-97, A., *Standard Test Method for Conducting Potentiodynamic Polarization Resistance Measurements*. 2014.

165.   García, S. J. and Suay, J., *Application of electrochemical techniques to study the effect on the anticorrosive properties of the addition of ytterbium and erbium triflates as catalysts on a powder epoxy network.* Progress in Organic Coatings, 2006. **57**(3): p. 273-281.

166.   Chao, C. Y., Lin, L. F., and Macdonald, D. D., *A Point Defect Model for Anodic Passive Films I. Film Growth Kinetics.* Journal of the Electrochemical Society, 1981. **128**(6): p. 1187-1194.

167.   Fattah-Alhosseini, A. and Attarzadeh, N., *The Mechanism of Transpassive Dissolution of AISI 321 Stainless Steel in Sulphuric Acid Solution.* International Journal of Electrochemistry, 2011. **2011**.

168. Xiao, Z., Li, Z., Zhu, A., Zhao, Y., Chen, J., and Zhu, Y., *Surface characterization and corrosion behavior of a novel gold-imitation copper alloy with high tarnish resistance in salt spray environment.* Corrosion Science, 2013. **76**: p. 42-51.

169. Schüssler, A. and Exner, H. E., *The corrosion of nickel-aluminium bronzes in seawater—I. Protective layer formation and the passivation mechanism.* Corrosion Science, 1993. **34**(11): p. 1793-1802.

170. Lee, W.-J. and Pyun, S.-I., *Effects of hydroxide ion addition on anodic dissolution of pure aluminium in chloride ion-containing solution.* Electrochimica Acta, 1999. **44**(23): p. 4041-4049.

171. ZRT, G. F. *Anodized aluminium*. 2012   10 January 2017]; Available from: http://www.gorter.hu/en/possibilities/surface_treatment/anodising.

172. Park, I.-S., Ryu, K.-m., Jeong, J., and Ahn, J., *Dielectric Stacking Effect of Al2O3 and HfO2 in Metal–Insulator–Metal Capacitor.* IEEE Electron Device Letters, 2013. **34**(1): p. 120-122.

173. Hyeres, G., *Supermaterials*. Vol. 8. 1999, Dordrecht/ Boston/ London: Kluwer Academic Publishers in coorperation with NATO Scientific Affairs Division.

174. Litvinov, J., Wang, Y. J., George, J., Chinwangso, P., Brankovic, S., Willson, R. C., and Litvinov, D., *Development of pinhole-free amorphous aluminum oxide protective layers for biomedical device applications.* Surface and Coatings Technology, 2013. **224**: p. 101-108.

175. Da-Ming, S., Sun, Z.-Q., and Zhuang, Y.-L., *Microstructure and electrical conductance of AI oxide film anodized in an HF oxygen plasma.* Vacuum, 1997. **48**(2): p. 149-153.

176. Wissling, P., *Metallic Effect Pigments: Fundamentals and Applications*. 2006, Hannover, Germany: Vincentz Network GmbH & Co KG.

177. Bhola, S. M. and Mishra, B., *Effect of ph on the electrochemical properties of oxides formed over β - Ti-15Mo and mixed Ti-6Al-4v alloys.* International Journal of Electrochemical Science, 2013. **8**(5): p. 7075-7087.

178. Hitzig, J., Jüttner, K., Lorenz, W. J., and Paatsch, W., *AC-impedance measurements on porous aluminium oxide films.* Corrosion Science, 1984. **24**(11–12): p. 945-952.

179.   Linardi, E., Collet-Lacoste, J., and Lanzani, L., *Characterization of AA6061 Alloy Oxides Obtained in High Purity Water and in Diluted NaCl Solution.* Procedia Materials Science, 2015. **8**: p. 56-64.

180.   Evertsson, J., Bertram, F., Zhang, F., Rullik, L., Merte, L. R., Shipilin, M., Soldemo, M., Ahmadi, S., Vinogradov, N., Carlà, F., Weissenrieder, J., Göthelid, M., Pan, J., Mikkelsen, A., Nilsson, J. O., and Lundgren, E., *The thickness of native oxides on aluminum alloys and single crystals.* Applied Surface Science, 2015. **349**: p. 826-832.

181.   Klein, I. E., Yaniv, A. E., and White, J. H., *An electrical equivalent for barrier anodic films on aluminium.* Electrochimica Acta, 1972. **17**(12): p. 2231-2237.

182.   Huang, Y., Shih, H., Huang, H., Daugherty, J., Wu, S., Ramanathan, S., Chang, C., and Mansfeld, F., *Evaluation of the corrosion resistance of anodized aluminum 6061 using electrochemical impedance spectroscopy (EIS).* Corrosion Science, 2008. **50**(12): p. 3569-3575.

183.   Oh, H.-J., Jang, K.-W., and Chi, C.-S., *Impedance Characteristics of Oxide Layers on Aluminium.* Bull. Korean Chem. Soc, 1999. **20**(11): p. 1341.

184.   Habib, K. *Measurement of oxide barrier-film thickness of Al alloy by electrochemical impedance spectroscopy at the nanometre scale*. in *NanoScience+ Engineering*. 2008. International Society for Optics and Photonics.

185.   Gavish, N. and Promislow, K., *Dependence of the dielectric constant of electrolyte solutions on ionic concentration: A microfield approach.* Physical Review E - Statistical, Nonlinear, and Soft Matter Physics, 2016. **94**(1).

186.   Schmidbaur, H., *Book Review: Science of Synthesis. (Houben-Weyl, Methods of Molecular Transformations). Category 1: Organometallics. Volume 4: Compounds of Group 15 (As, Sb, Bi) and Silicon Compounds. Edited by Ian Fleming.* Angewandte Chemie International Edition, 2003. **42**(7): p. 715-716.

187.   Tabrizi, M. R., Lyon, S. B., Thompson, G. E., and Ferguson, J. M., *The long-term corrosion of aluminium in alkaline media.* Corrosion Science, 1991. **32**(7): p. 733-742.

Appendix

Appendix A: Research activities during PhD study

Conference Attendance

- **2014 and 2015** Annual University of Sheffield Engineering Symposium USES

- **2013, 2014 & 2016** Annual International Conference on Metallurgical Coatings and Thin Films (ICMCTF), San Diego, California, USA

- **2014 and 2015** Annual SVC Society of Vacuum Coaters, Chicago, Santa Clara, USA

- **2014** The Young Members Committee, IOM3, Loughborough University

- **2013** 40th International Conference on Metallurgical Coatings & Thin Films (ICMCTF), San Diego, California, USA

- **2012** The 3rd International Conference on Fundamentals and Industrial Applications of HIPIMS, Sheffield

Awards

- Best poster presentation at the Young Members Committee, IOM3 at Loughborough University 2014.
- Sponsored student of the Society of Vacuum Coaters Foundation at the 57th Annual Technical Conference, Chicago, USA, 2014.

Publications

- F. Indeir, A. Yerokhin, A. Matthews, A. Leyland. *A comparative study of the corrosion behaviour of PVD Al-based coatings on mild steel by EIS and (AC)DC/AC electrochemical evaluation techniques.* Proceedings of Society of Vacuum Coaters (SVC), 2014.
  DOI: http://dx.doi.org/10.14332/svc14.proc.1888

- F. Indeir, A. Matthews, A. Leyland. *Development of (AC)DC/AC cyclic electrochemical corrosion evaluation protocols for accelerated testing of PVD metallic coatings.* Proceedings of Society of Vacuum Coaters (SVC), 2015.
  DOI: dx.doi.org/10.14332/svc15.proc.1964